The Dissertation Committee for Andrew Chang
certifies that this is the approved version of the following dissertation:

Multiscale Modeling of Thermal Ablation in Fiber Reinforced Composites

Committee:

Eric P. Fahrenthold, Supervisor

Eric M. Taleff

Yuanyue Liu

Kamy Sepehrnoori

Dragan Djurdjanovic

Multiscale Modeling of Thermal Ablation in Fiber Reinforced Composites

by

Andrew Chang, B.S.

DISSERTATION

Presented to the Faculty of the Graduate School of

The University of Texas at Austin

in Partial Fulfillment

of the Requirements

for the Degree of

DOCTOR OF PHILOSOPHY

THE UNIVERSITY OF TEXAS AT AUSTIN

August 2023

Acknowledgments

I wish to thank my advisor Dr. Eric Fahrenthold for his advice, time and patience. I also thank my committee members for their advice and assistance: Dr. Eric Taleff, Dr. Yuanyue Liu, Dr. Kamy Sepehrnoori, and Dr. Dragan Djurdjanovic.

This research was supported by the Army Futures Command. Computer time support was provided by the Texas Advanced Computing Center.

Multiscale Modeling of Thermal Ablation in Fiber Reinforced Composites

Publication No. _____

Andrew Chang, Ph.D.
The University of Texas at Austin, 2023

Supervisor: Eric P. Fahrenthold

The development of improved numerical methods and physical models of thermal ablation is necessary for reducing uncertainties in the prediction of Thermal Protection System (TPS) performance and hence the reduction of TPS weight and the maximization of aerospace vehicle payloads. Models simulating ablation must address significantly disparate temporal and spatial scales, including molecular scale chemical physics of resin pyrolysis and macroscale resin and fiber ablation. Numerical methods must also be able to account for solid erosion effects and the resulting geometry evolution.

This research has developed the first discrete nonholonomic Hamiltonian approach for the multiscale modeling of thermal ablation. The model incorporates three scales of interest, including a reacting molecular dynamics model at the nanoscale and hybrid particle element models at the meso and macro scales. Unlike all previous works in literature, the disparate temporal and spatial scales of the ablation problem are addressed, in part, by

incorporating a fully coupled chemical-thermomechanical ablation model at the mesoscale. The research builds on previous work on the hybrid particle element method by the addition of variable mass particles at the meso and macro scales, as well as a description of the resin and fiber composite architecture in the macroscale model. Solid erosion effects and the resulting surface recession are accounted for explicitly in the particle-element kinematics. The presented methodology improves on existing macroscale models in three main respects: first, the solid dynamics is modeled explicitly with full chemical-thermomechanical coupling at the mesoscale and thermomechanical coupling at the macroscale, second mass and energy is rigorously conserved in the formulation of the state space equations, and third a general method of accounting for solid erosion effects and geometry evolution is included. The formulation is validated by comparison with published ablation experiments on fiber reinforced phenolic and cyanate ester composites.

Table of Contents

Glossary

Acronyms

CFD	Computational Fluid Dynamics
CHAR	CHarring Ablator Response
CHyPS	Coupled Hypersonic Protection System
CMA	Charring Materials Ablation
CVFEM	Control Volume Finite Element
DG	Discontinuous Galerkin
FEATS	Finite Element based Ablative and Thermal response Simulator
FEM	Finite Element Method
FIAT	Fully Implicit Ablation and Thermal response
FV	Finite Volume
HERO	Heat transfer and Erosion Analysis
MOPAR	Modeling of Pyrolysis and Ablation Response
PATO	Porous Materials Analysis Toolbox based on OpenFoam
PICA	Phenolic Impregnated Carbon Ablator
SCMA	Super Charring Materials Ablation
TACOT	Theoretical Ablative Composite for Open Testing
TGA	Thermogravimetric Analysis
TPS	Thermal Protection System
VANS	Volume Averaged Navier Stokes

Nomenclature

$E^{(j)}$, $\mathbf{E}^{(j)}$	matrix element deviatoric strain
$E^{e(j)}$, $\mathbf{E}^{e(j)}$	matrix element elastic strain
$E^{p(j)}$, $\mathbf{E}^{p(j)}$	matrix element plastic strain
$E^{(i,j)}$	fiber element modulus (N)
E_g	total gas internal energy (J/kg)
e_g	gas internal energy (J/kg)
$C_j^{(i)}$	concentration of species j in particle i (mol/m^3)
$c^{(i)}$, $\mathbf{c}^{(i)}$	particle center of mass (m)
c_p	specific heat (J/kg-K)
c_{sf}	fiber sound speed (m/s)
c_{sr}	resin sound speed (m/s)
c_{vf}	fiber specific heat (J/kg-K)
c_{vr}	resin specific heat (J/kg-K)
$D^{(i)}$	fiber element damage variable
$d^{(j)}$	matrix element damage variable
$\mathbf{e}^{(i)}$	particle Euler parameters
f	mass fraction
$f^{vis(i)}$, $\mathbf{f}^{vis(i)}$	particle viscous force (N)
$\mathbf{g}^{(i)}$	particle four component angular momentum vector (kg-m^2/s)
H_{eff}	effective heat of ablation (J/kg)
H_g	total gas enthalpy (J/kg)
H_{py}	resin heat of pyrolysis in a resin and fiber composite (J/kg)
h	enthalpy (J/kg)
$h^{ext(i)}$	particle external total enthalpy (J/kg)
h_{dec}	resin decomposition enthalpy (J/kg)
$\bar{h}$	partial heat of charring (J/kg), defined in equation 1.14
$h_k^{(i)}$	particle semi-major axes lengths (m)

$\mathbf{h}^{(i)}$	particle body fixed co-rotating angular momentum vector (kg-m^2/s)
$\mathbf{J}$, J	diffusive mass flux kg/m^2-s
$\mathbf{J}^{(i)}$	particle moment of inertia tensor (kg-m^2)
$J_c^{(j)}$	maximum matrix element compression
$\mathbf{K}$	permeability (m^2)
$k^{(k)}$	reaction rate constant for reaction k $(1/s)(mol/m^3)^{1-m^{(k)}}$, see Tables 2.10, 2.14, 2.19, 2.23, 2.28, 2.32, 2.37 and 2.41
k, $\mathbf{k}$	thermal conductivity (W/m-K)
L	heating profile propagation distance (m), see equation 3.25
ℓ	heating profile depth (m), see equations (2.31), (3.28) and (3.29)
M_{frg}	system fragmented mass loss (kg)
$\mathbb{M}_j$	molar mass of species j (mol/kg)
$\mathbf{M}^{vis(i)}$	particle viscous torque (N-m)
$\dot{m}_c$	char mass flux (kg/m^2-s)
$\dot{m}_g$	pyrolysis gas flux (kg/m^2-s)
$m^{(i)}$	particle masses (kg)
N_r	number of reactions
N_s	number of chemical species
n_e	number of matrix elements
n_p	number of particles
P	pressure (Pa)
$P^{(i)}$	particle pressure (Pa)
$p^{(i)}$, $\mathbf{p}^{(i)}$	particle translational momenta (kg-m/s)
Q	total system heat input (J)
Q_{cw}	cold wall heat load (J)
Q_{rr}	re-radiated heat load (J)
$\mathbf{q}_{\text{cond}}$, q_{cond}	conductive heat flux (W/m^2)

q_{conv}	convective heat flux (W/m^2)
q_{cw}	cold wall heat flux (W/m^2)
q_{rad}	radiative heat flux (W/m^2)
q_{rr}	re-radiated heat flux (W/m^2)
R	ideal gas constant $(J/mol\text{-}K)$
S, $\mathbf{S}$	matrix element stress tensor (Pa)
s	surface recession (m)
$s_j^{(i)}$	mass of species j in particle i (kg)
$\dot{s}_j^{cvc(i)}$	rate of convection of gas species j out of gas control volume in particle i (kg/s)
$\dot{s}_j^{reac(i)}$	evolution of species j in particle i due to pyrolysis reactions (kg/s)
T	kinetic energy (J)
T^*	kinetic co-energy (J)
t	time (s)
$U^{(i)}$	particle internal energy (J)
$\dot{U}^{con(i)}$	particle numerical heat conduction (J/s)
$\dot{U}^{ele(i)}$	particle power flow due to element deviatoric deformation (J/s)
$\dot{U}^{inp(i)}$	particle heat input (J/s)
$\dot{U}^{irr(i)}$	particle irreversible power flow (J/s)
$\dot{U}^{trc(i)}$	particle transpiration cooling (J/s)
$\dot{U}^{wrk(i)}$	particle power flow due to volumetric compression (J/s)
$\hat{u}$	unit step function
$u^{(i)}$	particle specific internal energy (J/kg)
$u_f^{(j)}$	matrix element failure internal energy (J/kg)
$u_f^{fib(i)}$	fiber element failure internal energy (J/kg)
V	system potential energy (J)

$V_0^{e(j)}$	matrix element volume in reference configuration (m^3)
$V_g^{(i)}$	particle gas control volume (m^3)
v, $\mathbf{v}$	velocity (m/s)
α_{ij}	boolean matrix for fiber elements connectivities
$\alpha^{(j,k)}$	reaction exponent for species j in reaction k
$\Gamma^{D(i)}$	fiber element strain energy release variable (J), see Equation 3.65
$\Gamma^{d(j)}$	matrix element strain energy release variable (J), see Equation 3.64
γ	Grüneisen parameter
ϵ	emissivity
$\epsilon^{(i,j)}$	fiber element strain
$\epsilon^{p(j)}$	matrix element accumulated plastic strain
$\epsilon_f^{p(j)}$	matrix element failure plastic strain
$\zeta^{(i,j)}$	ellipsoidal distance metric for particles i, j
θ	temperature (K)
$\kappa^{(i)}$	particle heat input decay constant ($1/m$)
$\lambda^{(i)}$	particle resin extent of pyrolysis
$\lambda_f^{(j)}$	matrix element failure ablation progress
μ	dynamic viscosity (kg/ms)
$\mu^{(j)}$	element shear modulus (Pa)
$\nu^{(i)}$	particle volume (m^3)
$\nu_0^{(i)}$	particle volume in reference configuration (m^3)
ν_{RF}	reference particle volume (m^3)
$\nu^{(j,k)}$	product stoichiometric coefficient for species j in reaction k
$\hat{\nu}^{(j,k)}$	reactant stoichiometric coefficient for species j in reaction k
$\xi^{(i,k)}$	reaction rate for reaction k in particle i (mol/m^3-s)
ρ	density (kg/m^3)

$\bar{\rho}$	true density (kg/m^3)
$\rho^{(i)}$	particle density (kg/m^3)
$\rho_0^{(i)}$	particle reference density (kg/m^3)
σ	Stefan-Boltzmann's constant (W/m^2-K^4)
$\sigma^{(i,j)}$	fiber element stress (N)
$\sigma_s^{(j)}$	matrix element spall stress (Pa)
τ	resin mass loss time constant (s)
ϕ	volume fraction
$\phi^{(i,j)}$	fraction of power flow in matrix element j given to particle i
$\psi^{(i)}$	matrix element strain energy density (J/m^3)
$\psi^{(i,j)}$	fiber element strain energy density (J/m)
ω^{pyr}	gas mass source due to resin pyrolysis (kg/m^3-s)
ω_i^{pyr}	gas mass source due to pyrolysis of resin constituent i (kg/m^3-s)
$\boldsymbol{\omega}^{(i)}$	particle body fixed co-rotating angular velocity ($1/s$)

Subscripts

c	char
f	fiber
g	gas
m	mesh
R	resin species index
r	resin
s	solid
v	virgin
w	wall

List of Tables

List of Figures

Chapter 1

Introduction

1.1 Background and Motivation

During hypersonic flight, vehicles are subject to intense aerodynamic heating. A Thermal Protection System (TPS) is required to protect the vehicle from the thermal loads. TPS materials fall into two categories: reusable and nonreusable. Reusable materials operate by re-radiating the absorbed heat back into the environment. The tiles on the underside of the Space Shuttle are an example of such a material. Reusable TPS, while more costly to develop, can be employed on multiple missions as long as their integrity has not been compromised. Ablative materials reject heat through an additional process of mass discard, the working principle being that the energy rejected by mass removal does not propagate further into the structure. The most common form of ablative materials is polymeric ablatives, which consist of a fiber reinforcement with a resin infiltrant. Mass loss generally proceeds from pyrolysis of the resin, chemical erosion of the matrix and fibers, and mechanical removal. The modeling of these processes constitutes a coupled chemical-thermomechanical problem that spans multiple temporal and spatial scales. Ablative TPS are often designed with large safety margins due to uncertainties in the prediction of the TPS performance, resulting in a higher TPS weight. Improved numer-

ical methods for ablation modeling are thus important for further optimizing TPS design.

The following sections provide a review of the current ablation literature. A review of macroscale ablation models is given first, followed by a review of meso and nanoscale models.

1.2 Review of Thermal Ablation Modeling

Ablation models in literature model the material as a charring and conducting continuum. The solid decomposes from a virgin to charred material generating pyrolysis gases that percolate through the material and are ejected at the surface. A schematic of the ablation problem is shown below in Figure 1.1.

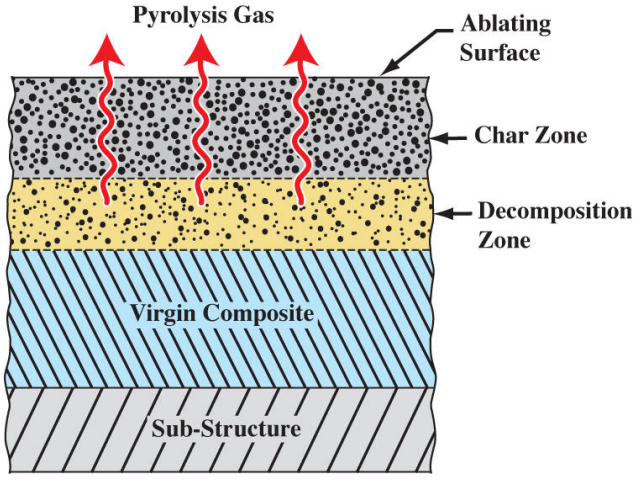

Figure 1.1: Schematic of a charring ablator. Image is from Ref [3].

The solid is typically treated as a rigid and immobile entity, neglecting strength

and mechanical effects. At the surface, ablation causes the surface to recede due to erosion of the charred material.

Early work on ablation was done in the 1960s by Kendall et al. [87] and Moyer and Rindal [118] on the 1-D Charring Materials Ablation (CMA) program, described in a series of six NASA reports [14, 84–86, 118, 134]. Some simplifying assumptions were employed in the CMA model, including excluding chemical kinetics and assuming that the pyrolysis gas generated from resin decomposition was instantaneously ejected from the material. Later work was done by Clark [41] in the 1970s on the development of a 1-D model accounting for gas pressure due to pyrolysis gas accumulation, homogeneous and heterogeneous chemical kinetics, and separate temperatures for solid and gas. Much of recent work, however, is largely derivative of the CMA model. This was noted in a review by Lachaud et al. [97] in 2011, in which the author noted that ablation models were mostly replicas or parallel developments of the CMA ablation model. Laub et al. [99] also emphasized a stagnation in the ablation literature in a presentation at NASA in 2011 titled "Ablator Modeling: Why Not Much Has Changed Over the Past 45+ Years". In particular, the author noted that since the 1960s ablation modeling has benefited from advancements in parallel computing and improved numerical methods, which has since resulted in the replacement of CMA with more recent Finite Volume and Finite Element codes [13], including extensions to 2-D [28, 46] and 3-D [5, 35, 95, 139]. Models describing internal gas pressure due to pyrolysis, such as Darcy's law [5, 35, 46, 95, 139], more detailed descriptions of pyroly-

sis decomposition [155], and empirical estimates of mechanical erosion [113] have been added to address specific cases. Authors have recently introduced (or re-introduced) capabilities to account for homogeneous and heterogeneous chemical kinetics [112, 138]. Efforts have also considered coupling ablation models to Computational Fluid Dynamics (CFD) solvers [47, 138]. However, the fundamental ablation modeling has not evolved.

This dissertation introduces a new integrated multiscale approach to ablation modeling that departs sharply from current methods. However, the following paragraphs describe a summary of the current modeling landscape in the ablation literature for comparison and review of existing work. Since the ablation literature has a strong historical development, a description of the CMA model is given first, followed by more recent advancements.

1.2.1 Charring Materials Ablation Model

The energy balance in CMA is formulated in one dimension as [118]

$$\frac{\partial}{\partial t}(\rho_s h_s A) = \frac{\partial}{\partial y}\left(kA\frac{\partial \theta}{\partial y}\right) + \frac{\partial}{\partial y}(\dot{m}_g h_g) \tag{1.1}$$

where ρ_s is the solid density, h_s the solid enthalpy, h_g the gas enthalpy, $\dot{m}_g$ the gas mass flux, k thermal conductivity, θ temperature, y the spatial coordinate, and A a variable cross sectional area. The solid consists of resin and fiber:

$$\rho_s = \Gamma\rho_r + (1-\Gamma)\rho_f \tag{1.2}$$

where Γ is a resin volume fraction and ρ_r and ρ_f are the resin and fiber densities respectively. The fiber is assumed not to decompose in-depth and erodes only

at the surface. The decomposition model for the resin is based on laboratory pyrolysis data obtained from thermogravimetric analysis (TGA). Reflective of TGA experimental data, the resin is assumed to consist of multiple pyrolyzing constituents which undergo parallel irreversible pyrolysis reactions. The decomposition of each constituent is modeled with an Arrhenius form:

$$\rho_r = \sum_{i=1}^{N_p} \rho_i \tag{1.3}$$

$$\frac{\partial \rho_i}{\partial t} = -k_i \exp\left(\frac{-E_i}{R\theta}\right) \rho_i^{\nu} \left(\frac{\rho_i - \rho_i^c}{\rho_i^{\nu}}\right)^{m_i} \tag{1.4}$$

where N_p is the number of pyrolyzing constituents, ρ_i^{ν} and ρ_i^c a constituent virgin and char density, and R the universal gas constant. The constants ρ_i^{ν}, ρ_i^c, k_i, E_i and m_i are obtained from fit to TGA data.

The decomposition of the resin generates pyrolysis gases. The gas source due to resin pyrolysis ω^{pyr} is thus

$$\omega^{\text{pyr}} = \sum_{i=1}^{N_p} \omega_i^{\text{pyr}}, \quad \omega_i^{\text{pyr}} = -\frac{\partial \rho_i}{\partial t} \tag{1.5}$$

The CMA model assumes the pyrolysis gas is instantaneously ejected from the material. Based on this assumption, the gas mass balance is expressed as [118]

$$\frac{\partial \dot{m}_g}{\partial y} = -A\, \omega^{\text{pyr}} \tag{1.6}$$

where the gas flux $\dot{m}_g$ is defined as positive when flowing towards the surface in the $-y$ direction. The local gas flux is obtained by integration assuming an impermeable back wall:

$$\dot{m}_g = \int_y^{y_b} A\, \omega^{\text{pyr}} dy \tag{1.7}$$

where y_b is the backwall spatial coordinate.

For the solid thermal model, material properties are interpolated between a fully virgin and fully charred state. For performing interpolation, an extent of decomposition variable α is introduced as

$$\alpha = \frac{\rho_r - \rho_c}{\rho_v - \rho_c} \tag{1.8}$$

$$\rho_v = \sum_{i=1}^{N_p} \rho_i^v, \quad \rho_c = \sum_{i=1}^{N_p} \rho_i^c \tag{1.9}$$

Fictitious virgin and char mass fractions are then defined by

$$f_v = \frac{\alpha \rho_v}{\rho_s}, \quad f_c = \frac{(1-\alpha)\rho_c}{\rho_s} \tag{1.10}$$

The specific enthalpy of the solid (h) is then defined as a mass weighted average of the virgin and char specific enthalpies (h_v and h_c) [118]:

$$h(\theta) = f_v h_v(\theta) + f_c h_c(\theta) \tag{1.11}$$

where $h_v(\theta)$ and $h_c(\theta)$ are expressed as tabulated functions of temperature. Substituting equations 1.2 to 1.11 into the energy balance (equation 1.1), the energy balance can be written [118]

$$\rho c_p \frac{\partial \theta}{\partial t} = \frac{1}{A}\frac{\partial}{\partial y}\left(kA\frac{\partial \theta}{\partial y}\right) - (h_g - \bar{h})\omega^{\text{pyr}} + \frac{1}{A}\dot{m}_g \frac{\partial h_g}{\partial y} \tag{1.12}$$

where

$$c_p = f_v c_v + f_c c_c, \quad c_v = \frac{\partial h_v}{\partial \theta}, \quad c_c = \frac{\partial h_c}{\partial \theta} \tag{1.13}$$

$$\bar{h} = \frac{\rho_v h_v - \rho_c h_c}{\rho_v - \rho_c} \tag{1.14}$$

To account for recession, a translating spatial coordinate x is introduced as

$$x = y - s \tag{1.15}$$

where s is the recession depth. The energy and mass balance equations in the translating frame are then written [118]

$$\rho_s c_p \frac{\partial \theta}{\partial t} = \frac{1}{A}\frac{\partial}{\partial x}\left(kA\frac{\partial \theta}{\partial x}\right) - (h_g - \bar{h})\omega^{\text{pyr}} + \frac{1}{A}\dot{m}_g \frac{\partial h_g}{\partial x} + \dot{s}\rho c_p \frac{\partial \theta}{\partial x} \tag{1.16}$$

$$\frac{\partial \rho_i}{\partial t} = -\omega_i^{\text{pyr}} + \dot{s}\frac{\partial \rho_i}{\partial x} \tag{1.17}$$

The conducted heat flux and surface recession rate are imposed as boundary conditions at the ablating surface. To determine these quantities, the CMA model introduced the thermochemical ablation approach, still widely used in current models, to describe the mass and energy balance between an ablating surface and an external fluid environment. It is worth noting that the existing literature has not properly addressed jump conditions at the fluid–solid interface in the thermochemical ablation model in CMA. Typical in the literature is the formulation of a "thin control volume" [45, 71, 95, 106, 111, 115, 138] fixed to the receding surface, which is used to postulate the balance of mass and energy fluxes. However, the size of the thin control volume is not stated. Some authors [7, 26, 53, 127] have instead described the thermochemical ablation model using control surfaces, which is adopted in the following description. For the surface energy balance, it is assumed that the incoming and outgoing

fluxes at the fluid-solid surface sum to zero [7, 71, 96, 111, 171]:

$$q_{conv} - (\rho v)_w h_w - \sum_{i=1}^{N_s} J_{i,w} h_{i,w} + \alpha q_{\text{rad}} - \epsilon\sigma\theta_w^4 = \dot{m}_c h_c + \dot{m}_g h_g - q_{\text{cond}} \quad (1.18)$$

where the subscript w denotes that quantities are evaluated in the fluid at the wall. On the left hand side, q_{conv} is the convective flux, $(\rho v)_w$ is the total convective mass flux away from the wall, h_w is the wall enthalpy, $J_{i,w}$ is the diffusive flux of species i away from the wall, $h_{i,w}$ is the enthalpy of species i at the wall, αq_{rad} is the radiative flux, and $\epsilon\sigma\theta_w^4$ is the re-radiated flux. On the right hand side, $\dot{m}_g$ is the pyrolysis gas flux entering the fluid-solid surface, h_c and h_g are the char and pyrolysis gas enthalpies respectively, q_{cond} is the heat flux conducted into the solid, and $\dot{m}_c$ is the char mass flux resulting from erosion of the solid material, which is related to the surface recession velocity as $\dot{m}_c = \dot{s}\,\rho_c$. Figure 1.2 shows a schematic of the surface energy balance.

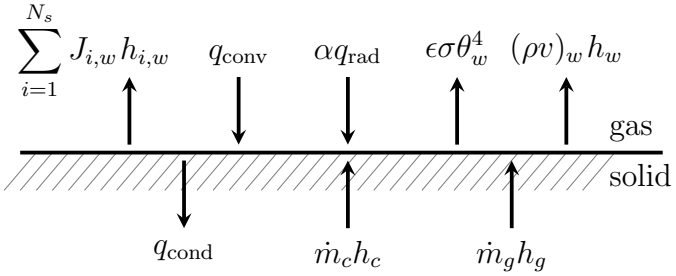

Figure 1.2: Energy balance at an ablating surface, adapted from Refs [7, 71, 96, 111].

For the surface mass balance, it is assumed that the incoming and outgoing chemical element mass fluxes at the fluid-solid surface sum to zero where a

discontinuity is permitted in the chemical composition [7, 71, 96, 111, 171]:

$$\sum_{i=1}^{N_s} m_{k,i} J_{i,w} + (\rho v)_w f_{k,w} = \dot{m}_c f_{k,c} + \dot{m}_g f_{k,g} \tag{1.19}$$

In the above, $m_{k,i}$ is the mass fraction of chemical element k in the ith species, and $f_{k,w}$, $f_{k,c}$ and $f_{k,g}$ are the mass fraction of element k in the fluid at the wall, in the solid char, and in the pyrolysis gas respectively. Figure 1.3 shows a schematic of the surface mass balance.

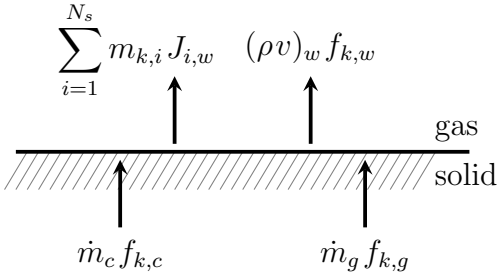

Figure 1.3: Elemental mass balance at an ablating surface, adapted from [7, 71, 96, 111].

The CMA model estimates the convective heat and diffusive mass fluxes from a boundary layer approximation. The convective heat flux is estimated as: $q_{conv} = \rho_e u_e C_H (h_e - h_w)$, where ρ_e and u_e are a boundary layer edge density and edge velocity, h_e a boundary layer edge enthalpy, and C_H a heat transfer coefficient [87]. The diffusive mass flux is estimated as: $J_{i,w} = \rho_e u_e C_M (f_{i,w} - f_{i,e})$ where C_M is a mass transfer coefficient, and $f_{i,e}$ is the mass fraction of species i at the boundary layer edge. Other expressions were also developed for the case of unequal diffusion coefficients [87]. Finally, the char mass flux and fluid

composition at the wall were determined by assuming chemical equilibrium between the fluid and solid surface subject to the chemical elemental constraints described in equation 1.19 and equal temperatures between the fluid and solid [87]. The surface recession rate and other fluid thermodynamic quantities were then computed from the char mass flux and wall composition.

The thermochemical ablation approach is added to the CMA model to provide boundary conditions for the heat flux conducted into the material and the surface recession rate. In particular, the material solver outputs a pyrolysis gas flux and surface temperature and a chemistry solver then returns a char flux and fluid thermodynamic quantities at the wall, from which the recession velocity and conducted heat flux are then computed. Often, the chemistry solver is not run concurrently with the ablation simulation but is used to tabulate a table beforehand which is then interpolated by the ablation solver (e.g., $\dot{m}_c, h_w = f(\dot{m}_g, \theta_w, P)$, where P is an environmental pressure [38, 52]). Current ablation models continue to use the thermochemical ablation approach introduced by CMA when assuming equilibrium surface chemistry, though chemistry solvers have since been updated with improved algorithms. Scoggins et al. [140] describes the implementation of a chemical equilibrium solver based on the Gibbs function continuation method which has been used by recent works in literature [38, 47, 96, 110].

The CMA model discretizes the energy and mass balance equations using the finite difference method [118]. Since the pyrolysis reactions tend to create a sharp pyrolysis front with steep density gradients, each node in the

finite difference grid was additionally subdivided into nodelets for finer resolution of the density. The grid translates with surface recession (equation 1.15) with the exception of the back boundary node, which shrinks with recession (see Figure 1.4).

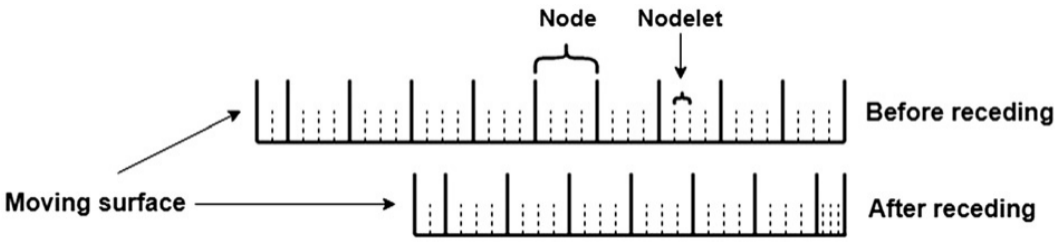

Figure 1.4: Finite difference grid used in Refs [83, 116, 152] in implementing the CMA model. Image is from Ref [152].

The last node is deleted once a critical thickness is reached. [118]. For the temporal discretization, the energy and mass balance equations are coupled explicitly.

The CMA model has seen recent use in performing 1-D analysis. Tahmsabi et al. (2020) [152] used the CMA model in performing inverse estimation of the time dependent heating environment and temperature dependent specific heat $c_p(\theta)$ (equation 1.14) and thermal conductivity as tabulated functions of temperature or time. In particular, hypothetical temperature versus time curves were assumed at various spatial locations, and a nonlinear least squares optimization algorithm was then used to determine the tabulated functions for matching ablation simulation results to the hypothetical curves. A similar analysis was done by Kato et al. [83] using experimental arc-jet test data.

1.2.2 Fully Implicit Ablation and Thermal (FIAT) response model

The CMA program explicitly couples the energy balance equation to the mass balance and surface mass and energy balance equations. FIAT (Ref [33]) was developed as a more numerically stable replacement for CMA by, as the name suggests, employing a fully implicit solution scheme. The main differences between the FIAT and CMA model may be listed as: FIAT uses finite volume for discretization, it includes an additional term to account for internal radiation in the energy balance, the mesh is uniformly contracted rather than translated to account for recession, and a unit cross sectional area is assumed.

NASA recently used FIAT for extensive analysis of the Mars Perseverance rover heat shield in 2022 [2, 117]; however, existing publications on the FIAT model in literature is rather sparse. The FIAT model is described in Ref [33], in which the energy balance is stated as

$$\rho c_p \frac{\partial \theta}{\partial t} = \frac{\partial}{\partial x}\left(k\frac{\partial \theta}{\partial x} - q_R\right) - (h_g - \bar{h})\omega^{\text{pyr}} + \dot{m}_g \frac{\partial h_g}{\partial x} + \dot{s}\rho c_p \frac{\partial \theta}{\partial x} \tag{1.20}$$

which, with the exception of the internal radiation term q_R, is a copy of that in the CMA model. It is noted, however, that the coordinate movement term has not been corrected to account for a contracting mesh movement scheme. The finite volume discretization is also excluded in the paper. Subsequent publications on FIAT have described the incorporation of equilibrium chemistry solvers into the FIAT program ([113]), which simplifies the user interface but has not further addressed the formulation. In Ref [33], the authors compare

FIAT simulation temperature predictions with arc-jet thermocouple data for PICA (Phenolic Impregnated Carbon Ablator). Predictions of char and gas mass flux were compared with the CMA model.

1.2.3 CHarring Ablator Response (CHAR) model

In higher dimensions, the 1-D pyrolysis gas flow model in CMA cannot be directly extended to higher dimensions due to the flow direction being ill-defined (though limited attempts have been made [31]), not to mention that the assumption of 1-D flow and instantaneous ejection may not be valid [169]. Authors have thus incorporated models describing pyrolysis gas transport. Amar et al. [3, 5] developed CHAR, a 1, 2, and 3-D ablation program, using the continuous Galerkin finite element method in an Arbitrary Lagrangian-Eulerian (ALE) frame. They include a pyrolysis gas mass balance as [5]:

$$\frac{\partial}{\partial t}(\phi_g \rho_g) + \nabla \cdot (\phi_g \rho_g \mathbf{v}_g) = \omega^{\text{pyr}} + \mathbf{v}_m \cdot \nabla(\phi_g \rho_g) \tag{1.21}$$

where ϕ_g is porosity (assumed to be the gas volume fraction), ρ_g the gas density, $\mathbf{v}_g$ the gas velocity, and $\mathbf{v}_m$ the mesh velocity. The gas velocity is obtained from the steady form of Darcy's law, describing fluid flow in a porous medium:

$$\mathbf{v}_g = -\frac{1}{\phi_g \mu} \mathbf{K} \nabla P \tag{1.22}$$

where P is the gas pressure, computed from the ideal gas law, μ is the dynamic viscosity, and $\mathbf{K}$ is the permeability tensor. The energy balance is stated as

[5]:

$$\frac{\partial}{\partial t}(\rho_s h_s + \phi_g \rho_g E_g) + \nabla \cdot (\phi_g \rho_g H_g \mathbf{v}_g) = \nabla \cdot (\mathbf{k} \nabla \theta) + \nabla(\rho_s h_s + \phi_g \rho_g E_g) \cdot \mathbf{v}_m \tag{1.23}$$

where $\mathbf{k}$ is the thermal conductivity tensor, and E_g and H_g are the gas specific total internal energy and total enthalpy:

$$E_g = h_g - \frac{P}{\rho_g} + \frac{1}{2}\mathbf{v}_g^T \mathbf{v}_g \tag{1.24}$$

$$H_g = h_g + \frac{1}{2}\mathbf{v}_g^T \mathbf{v}_g \tag{1.25}$$

For surface recession, CHAR uses the thermochemical ablation model developed in CMA [5]. Mesh movement was based on treating the mesh as a fictitious linear elastic solid that is deformed to conform to the computed normal recession. The mesh velocity was computed by performing finite differencing between mesh configurations. This method of using spring penalties for moving the mesh has also been used by other authors [46, 153] in recent literature.

For developing the finite element equations, the mass and energy balance equations were stated in the weak form as [5]:

$$\int_{\Omega(t)} \left[\frac{\partial}{\partial t}(\phi_g \rho_g)\psi - \nabla\psi \cdot \phi_g \rho_g \mathbf{v}_g - \omega^{\text{pyr}}\psi - \psi \nabla(\phi_g \rho_g) \cdot \mathbf{v}_m \right] d\mathbf{x} + \int_{\partial\Omega(t)} \psi \phi_g \rho_g \mathbf{v}_g \cdot \hat{\mathbf{n}} \, ds = 0 \tag{1.26}$$

$$\int_{\Omega(t)} \Big[\frac{\partial}{\partial t}(\rho_s h_s + \phi_g \rho_g E_g)\psi - \nabla\psi \cdot \phi_g \rho_g H_g \mathbf{v}_g + \nabla\psi \cdot \mathbf{k}\nabla\theta - \psi_m \nabla(\rho_s h_s + \phi_g \rho_g E_g) \cdot \mathbf{v}_m \Big] \mathbf{dx} + \int_{\partial\Omega(t)} (\psi \phi_g \rho_g H_g \mathbf{v}_g + \mathbf{q}_{\text{cond}}) \cdot \hat{\mathbf{n}}\, ds = 0 \tag{1.27}$$

where ψ is a test function and $\mathbf{q}_{\text{cond}}$ is the boundary heat flux.

For the finite element approximation, the authors employed first order Lagrange shape functions for the test functions and finite element basis. The nodal temperatures and gas pressures were chosen as the system unknowns [3, 5]:

$$\theta_h = \sum_{i=1}^{N} \theta_i \psi_i \tag{1.28}$$

$$P_h = \sum_{i=1}^{N} P_i \psi_i \tag{1.29}$$

where N is the total number of nodes, and θ_i and P_i are the nodal temperatures and pressures.

The authors employed two significant simplifying approaches to reduce computational cost and handle sharp density profiles. First, for the solid density, the authors integrated the Arrhenius decomposition equations (equation 1.4) as a set of ordinary differential equations (ODEs) at each node, excluding the formulation of a solid mass balance equation. Since equation 1.4 is formulated for a fixed Eulerian frame, the temperature profile was interpolated onto a fixed mesh for integrating the ODEs. Second, an inconsistent finite element

interpolation is used in that a linear interpolation is assumed for all quantities [3]:

$$(\rho_s h_s)_h = \sum_{i=1}^{N} (\rho_s h_s)_i \psi_i \tag{1.30}$$

$$(\phi_g \rho_g E_g)_h = \sum_{i=1}^{N} (\phi_g \rho_g E_g)_i \psi_i \tag{1.31}$$

$$(\phi_g \rho_g H_g)_h = \sum_{i=1}^{N} (\phi_g \rho_g H_g)_i \psi_i \tag{1.32}$$

where the above nodal quantities are computed from the nodal temperatures, pressures and solid densities. The authors performed verification [3] using the method of manufactured solutions for problems in an Eulerian frame without thermal decomposition. A discussion on errors arising from the discretization of the mesh movement terms and the effects of the simplifying approaches described above was not included.

1.2.4 Modeling of Pyrolysis and Ablation Response (MOPAR) model

The MOPAR ablation program was developed at the University of Michigan, which has received recent attention in the literature on the coupling of material response solvers to CFD [46, 47]. The constitutive model is similar to CHAR. The balance equations are discretized in 2-D using the Control Volume Finite Element Method (CVFEM) on an ALE frame. In CVFEM, the balance equations are formulated in integral form and applied to control volumes defined on a finite element mesh. The control volumes are defined around each mesh vertice by joining element centers and side midpoints. A

linear finite element interpolation is employed for the temperature, gas density, and solid density, which is then used to define fluxes at the control volumes interfaces [75, 82]. The gas mass balance is stated as [46]:

$$\frac{d}{dt}\int\limits_{\Omega(t)} \phi_g \rho_g \, d\mathbf{x} + \int\limits_{\partial\Omega(t)} \phi_g \rho_g \mathbf{v}_g \cdot \hat{\mathbf{n}} \, ds = \int\limits_{\Omega(t)} \omega^{\text{pyr}} \, d\mathbf{x} + \int\limits_{\partial\Omega(t)} \phi_g \rho_g \mathbf{v}_m \cdot \hat{\mathbf{n}} \, ds \quad (1.33)$$

where the steady form of Darcy's law is used for computing the gas velocity (equation 1.22). For the solid mass balance, the authors employed a similar approach to Amar et al. [5] in the CHAR ablation program where the solid density at each node is obtained by integrating the Arrhenius decomposition equations (equation 1.4) as a set of ODEs in an Eulerian frame, excluding the formulation of a solid mass balance equation. The energy balance is stated as [46]:

$$\frac{d}{dt}\int\limits_{\Omega(t)} (\rho_s h_s + \phi_g \rho_g e_g) \, d\mathbf{x} + \int\limits_{\partial\Omega(t)} \phi_g \rho_g h_g \mathbf{v}_g \cdot \hat{\mathbf{n}} \, ds = \\ - \int\limits_{\partial\Omega(t)} \mathbf{q}_{\text{cond}} \cdot \hat{\mathbf{n}} \, ds + \int\limits_{\partial\Omega(t)} (\rho_s h_s + \phi_g \rho_g h_g) \mathbf{v}_m \cdot \hat{\mathbf{n}} \, ds \quad (1.34)$$

where the gas kinetic energy is neglected in the energy balance. In discretizing the mass and energy balance equations, the nodal gas density and temperatures were chosen as the solution variables.

The authors considered several methods for computing surface recession, including the thermochemical ablation model in CMA and coupling to CFD. The mesh is moved to account for recession by treating it as a linear elastic solid that is deformed to conform to the receding surfaces. However,

details on how the mesh movement velocity is defined and the discretization of the mesh movement terms are not described.

The authors performed 2-D simulations of the ablation of carbon phenolic in a rocket motor nozzle [46]. Results were compared to recession predictions at selected locations. The simulation overpredicted recession by about a factor of two.

There is a point of concern in the energy balance in MOPAR. In particular, the gas enthalpy rather than the gas internal energy is convected with the grid motion [46]. This differs from other work in literature employing the finite volume method [153] in which the gas internal energy is the convected quantity. Also, if the energy balance (equation 1.34) is written point-wise:

$$\frac{\partial}{\partial t}(\rho_s h_s + \phi_g \rho_g e_g) + \nabla \cdot (\phi_g \rho_g h_g \mathbf{v}_g) = \\ -\nabla \cdot \mathbf{q}_{\text{cond}} + \phi_g \rho_g (h_g - e_g) \nabla \cdot \mathbf{v}_m + \mathbf{v}_m \cdot \nabla(\rho_s h_s + \phi_g \rho_g h_g) \tag{1.35}$$

it can be seen that the energy balance in MOPAR differs from CHAR (equation 1.23) regarding the mesh movement term. The two agree if the gas enthalpy and gas internal energy are equal. MOPAR was developed based on work at Sandia National Laboratories by Amar and Blackwell et al. [4] in which the same issue is also present.

1.2.5 Porous Materials Analysis Toolbox (PATO) based on OpenFoam

Lachaud et al. [92, 95] considered including homogeneous and heterogeneous reactions in modeling the decomposition kinetics and pyrolysis gas

chemistry. The model was implemented using the finite volume method in the ablation program PATO [95] (Porous-material Analysis Toolbox based on OpenFOAM) in 1-D, 2-D and 3-D. The balance equations are presented in a fixed frame, neglecting surface recession. The total gas mass balance is [92]

$$\frac{\partial}{\partial t}(\phi_g \rho_g) + \nabla \cdot (\phi_g \rho_g \mathbf{v}_g) = \omega^{\text{pyr}} + \sum_{j=1}^{N_g} \omega_j^{\text{het}} \tag{1.36}$$

where N_g is the number of gas species and ω_j^{het} accounts for gas source terms for species j due to heterogeneous reactions with the solid. The steady form of Darcy's law was used for computing the gas velocity. An individual mass balance is included for each gas species:

$$\frac{\partial}{\partial t}(\phi_g \rho_g f_j) + \nabla \cdot (\phi_g \rho_g \mathbf{v}_g f_j) + \nabla \cdot \mathbf{J}_j = \sum_{i=1}^{N_p} m_{j,i} \omega_i^{\text{pyr}} + \omega_j^{\text{het}} + \omega_j^{\text{hom}} \tag{1.37}$$

where f_j is the gas mass fraction of species j, $m_{j,i}$ the mass fraction of species j in the pyrolysis products of pyrolyzing constituent i, $\mathbf{J}_j$ the diffusive flux, and ω_j^{hom} accounts for gas source terms due to homogeneous reactions. The solid mass balance is

$$\frac{\partial \rho_s}{\partial t} = -\omega^{\text{pyr}} - \sum_{j=1}^{N_g} \omega_j^{\text{het}} \tag{1.38}$$

The energy balance is formulated as [92]

$$\begin{aligned} \frac{\partial}{\partial t}(\phi_g \rho_g e_g + \rho_s h_s) + \nabla \cdot (\phi_g \rho_g h_g \mathbf{v}_g) + \nabla \cdot \sum_{j=1}^{N_g} h_j \mathbf{J}_j = \\ - \nabla \cdot \mathbf{q}_{\text{cond}} + \mu \phi_g^2 \mathbf{v}_g^T \mathbf{K}^{-1} \mathbf{v}_g \end{aligned} \tag{1.39}$$

where h_j is the enthalpy of gas species j, and the last term accounts for viscous heating associated with Darcian flow. The authors performed a comparison

of 1-D simulation results with a replica of the CMA model on a hypothetical material called TACOT (Theoretical Ablative Composite for Open Testing) described by a properties database developed for purposes of performing code to code comparisons [91]. Compared to the CMA model, PATO predicted a lower pyrolysis gas enthalpy in the presence of homogeneous finite rate chemistry, resulting in a less endothermic resin pyrolysis [91]. Validation of PATO with experimental data was not performed. The authors have noted in a previous publication [95] that validated finite rate chemistry models are generally absent in the literature.

Meurisse et al. [110, 111] performed 2-D [110] and 3-D [111] simulations of PICA (phenolic impregnated carbon ablator) using PATO. The authors employed the thermochemical ablation model developed in CMA for computing recession, and mentioned that PATO supports an unstructured moving mesh algorithm to account for recession. However, a description of the mesh movement algorithm was not included, and the mass and energy balance equations were formulated for a fixed mesh. Available works in the literature using PATO have also not included a description of the finite volume discretization [92, 95, 110, 111].

1.2.6 Incorporation of Ablation into CFD Models

The chart below shows a survey on published research topics in hypersonics conducted in U.S. universities in 2017, presented by Boyd [23] at the Hypersonics Weapons Summit in 2021. One of the main points made by the

author was the presence of a heavy imbalance in the academic literature towards aerothermodynamics research, with relatively significantly less attention paid to materials response.

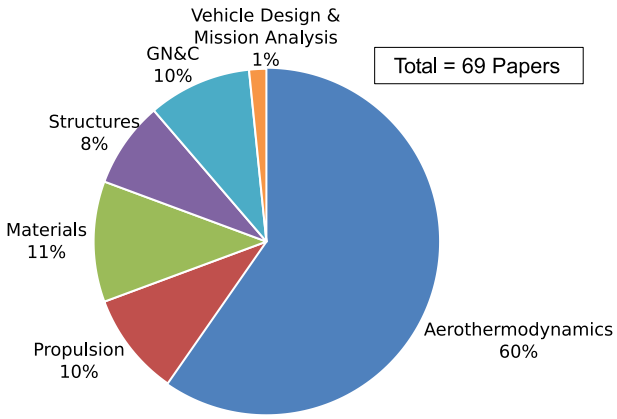

Figure 1.5: U.S. universities published research topics in hypersonics in 2017 [23]

Investigators have incorporated ablation by loosely coupling CFD models to ablation solvers [29, 30, 34, 47, 64, 90, 108]. A time transient ablation solution is typically coupled to a steady state CFD solution in loosely coupled methods. The CFD solution is then sequentially re-computed based on some update criteria. Authors have also performed Volume Averaged Navier Stokes (VANS) simulations where the solid is implied as an immobile phase in a fluid simulation [42, 50, 112, 138, 153, 168]. Since the ratio of flow to thermal time constants in hypersonic flight conditions is on the order of 10^{-9} [175], VANS simulations have been limited to laboratory scale experiments, excluding hypersonic conditions.

Schrooyen et al. [138] performed 2-D VANS simulations of porous flow

through a carbon fiber pre-form where the solid was implied as a rigid immobile phase in the fluid simulation. The model includes a mass balance of individual chemical species and accounts for homogeneous and heterogeneous reactions. The solid-fluid interface was implied by a strong ramping of the gas volume fraction and the permeability, effectively imposing a drag force on the fluid inside the solid. The fluid momentum balance can be stated as [138]:

$$\frac{\partial}{\partial t}(\phi_g \rho_g \mathbf{v}_g) + \nabla \cdot (\phi_g \rho_g \mathbf{v}_g \mathbf{v}_g) = -\phi_g \nabla P + \nabla \cdot \boldsymbol{\tau} - \mu \mathbf{K}^{-1} \phi_g^2 \mathbf{v}_g \tag{1.40}$$

where $\boldsymbol{\tau}$ is a viscous stress tensor. The permeability was defined as a function of the gas volume fraction [138]:

$$\mathbf{K}^{-1} = k \frac{S_{f,0}^2 (1-\phi_g)^2}{\phi_g^3} \mathbf{I} \tag{1.41}$$

where $S_{f,0}$ is an initial fiber volume specific surface area, and k a dimensionless proportionality constant. The solid density evolved due to oxidation of the carbon preform as:

$$\frac{\partial \rho_s}{\partial t} = -S_f k_f \rho_g f_{O_2} \tag{1.42}$$

where S_f is an estimated fiber surface area, k_f an oxidation rate, and f_{O_2} the gas mass fraction of oxygen. For estimating S_f, a simple fiber geometry was assumed consisting of infinitely long cylinders:

$$S_f = \frac{2}{r_0} (\phi_s \phi_{s0})^{1/2} \tag{1.43}$$

where r_0 is an initial fiber radius, ϕ_s the solid volume fraction, and ϕ_{s0} the initial solid volume fraction. The solid volume fraction was computed assuming

a rigid immobile solid phase:

$$\phi_s = \frac{\rho_s}{\rho_{s0}} \phi_{s0} \tag{1.44}$$

where ρ_{s0} is the initial solid density. The gas volume fraction was then computed as:

$$\phi_g = 1 - \phi_s \tag{1.45}$$

The solid volume fraction was initialized as a sharp hyperbolic tangent function, and the mesh was refined around the interface. During the simulation, the interface became more diffuse, which the authors [138] stated corresponds to the presence of volumetric oxidation. The authors also considered more complex functional forms for S_f to describe fiber pitting. The resulting simulations were relatively sensitive to the associated geometric assumptions. The governing balance equations were discretized using the discontinuous Galerkin finite element method. The convective terms were discretized using the advection upstream splitting method; diffusive terms were discretized using symmetric interior penalties. The resulting equations were integrated using a fully implicit scheme [138].

Miccoli et al. [112], who performed 2-D VANS simulations of TACOT [91] in a plasmatron torch, extended the model by Schrooyen et al. [138] to include a resin matrix where the fibers were permitted to ablate after the matrix had fully pyrolyzed [112], describing the case where the matrix coats the fibers and prevents oxidation. The simulation results were qualitatively

compared to experimental data on char depth [112], though the authors noted that the simulations were not run long enough to reproduce experimental results.

Tahmasbi et al. [153] performed 2-D VANS simulations of pyrolysis gas flow inside of an orthotropic ablator. Recession was imposed as a boundary condition, and the mesh was moved to conform to the receding surfaces. Weng et al. [168] performed 3-D simulations of pyrolysis gas flow inside of an orthotropic ablator and neglected recession.

For loosely coupled methods, a time transient ablation model is typically coupled to a steady state CFD solver with an exchange of selected surface quantities [29, 30, 34, 47, 64, 90, 108]. During the ablation simulation, the CFD domain may be re-meshed and the solution updated based upon some update criteria. In the fluid solver, an injection of gas species into the fluid domain occurs at the surface due to erosion of the solid and ejection of pyrolysis gases from the ablating material. Authors have considered non-equilibrium [29, 34] and equilibrium [21] surface chemistry. The boundary conditions can generally be described as [21, 29, 34]:

$$(\rho \mathbf{v} f_i + \mathbf{J}_i) \cdot \hat{\mathbf{n}} = \dot{m}_i^{\text{het}} + \dot{m}_g f_{i,g}, \qquad \text{non-equilibrium} \tag{1.46}$$

$$(\rho \mathbf{v} f_i + \mathbf{J}_i) \cdot \hat{\mathbf{n}} = (\dot{m}_c + \dot{m}_g) f_{i,w}, \qquad \text{equilibrium} \tag{1.47}$$

where $\hat{\mathbf{n}}$ is the surface normal pointing outwards from the solid, ρ and $\mathbf{v}$ are the fluid density and velocity, f_i the gas mass fraction of species i, and $\mathbf{J}_i$, the diffusive flux of species i. For the non-equilibrium case, the right-hand

side includes sources due to heterogeneous surface chemistry ($\dot{m}_i^{\text{het}}$) and the ejection of pyrolysis gas, where $f_{i,g}$ is the mass fraction of species i in the pyrolysis gas. For computing surface recession, the char mass flux is related to the heterogeneous reaction terms as [34]

$$\dot{m}_c = \sum_{i=1}^{N_g} \dot{m}_i^{\text{het}} \tag{1.48}$$

For the equilibrium chemistry case, the gas composition at the wall $f_{i,w}$ is computed using the thermochemical ablation model in CMA [21, 47]. Compared to the uncoupled case, the elemental diffusive flux in the thermochemical ablation model can be obtained from the fluid solver rather than a boundary layer approximation [34]. In both cases, the total surface mass balance is [29]

$$\rho \mathbf{v} \cdot \hat{\mathbf{n}} = \dot{m}_c + \dot{m}_g \tag{1.49}$$

since the diffusive fluxes are assumed to sum to zero.

For the fluid velocity at the solid surface, various boundary conditions exist. For example, Bianchi et al. [21] uses

$$\mathbf{v} = \frac{1}{\rho}(\dot{m}_c + \dot{m}_g)\hat{\mathbf{n}}, \quad \frac{\partial P}{\partial n} = 0 \tag{1.50}$$

where P is pressure, while Martin et al. [108] employs:

$$\frac{\partial}{\partial n}(\rho v_n^2 + P) = 0 \tag{1.51}$$

where v_n is the velocity normal component, and the tangential components are assumed zero.

For the surface energy balance, the fluid temperature at the wall is prescribed by the solid material response solver [34]. The surface energy balance used in the CMA model is then employed for computing the heat flux conducted into the solid material (equation 1.18) [34]. Compared to the uncoupled case, the convective and radiative heat flux in the thermochemical ablation model can be obtained from the CFD solution [34].

During the ablation simulation, the CFD domain may be re-meshed and the solution updated based upon some update criteria. Chen et al. [34] remeshed the fluid domain and updated the CFD solution whenever the surface temperature or surface recession had changed beyond some specified threshold. Cross et al. [47] selected a certain number of time points in a rocket motor firing to update the CFD solution.

For performing coupling, Kuntz et al. [90], who performed ablation simulations in 2-D, considered a coupling scheme where the CFD solution was held constant between updates; however, "large instabilities" were encountered in the surface heating rates. The author attributed these instabilities to the "highly nonlinear nature of the ablation process. Small changes in heating rate and surface temperature result in large changes in ablation and surface blowing rate. The large changes in the blowing rate cause significant changes in subsequent heating rates ..." [90], where surface blowing refers to the ejection of mass from the ablating material into the fluid domain due to pyrolysis gas ejection and erosion of the solid. The authors adopted an alternative method where the CFD solution was linearly interpolated between updates. Since

this required that the CFD solution be known at a future trajectory point, iteration was required. Cross et al. [47], who coupled a CFD model to the 2-D MOPAR ablation program, noted that the simulation results by Kuntz "suggest that the instability was not completely eliminated, and might have become problematic again if the simulation was extended further in time" [47]. Cross et al. [47] employed a similar interpolation method but also spatially smoothed the material response solution before passing it to the CFD solver. The additional smoothing helped further suppress the instability, but was still insufficient to remove it entirely. The authors note that such instabilities are a common characteristic of loosely coupled ablation simulations which update a flow domain with changes in geometry due to ablation [47].

More simple forms of coupling also exist. Chen et al. [32] proposed a scheme in which the fluid solver neglected mass injection, and an engineering correction was subsequently applied to the convective heat flux. In another approach, Meurrise et al. [110] computed the CFD solution once using the unablated shape and then interpolated the CFD solution onto the ablated shape as the simulation progressed.

1.2.7 Summary

Macroscale ablation modeling has a strong historical development largely based on the CMA model developed in the 1960s. Authors have added models describing pyrolysis gas pressure, such as Darcy's law, the inclusion of homogeneous and heterogeneous chemistry, and coupling to CFD. The fundamental

ablation modeling, however, has not evolved significantly. The solid thermal model in CMA describes the material as a fictitious mixture of fully virgin and fully charred material. This description may be partly due to the fact that it is difficult to obtain material properties during thermal decomposition [118]. Beck [18] has noted that the thermal conductivity of the charred material cannot be measured in laboratory experiments. Laboratory produced chars are generally prepared by baking the material in an oven. The resulting microstructure, however, differs from that produced in ground tests or flight. Efforts have thus been made in estimating material properties via inverse estimation [18, 116, 152]. In particular, material properties, usually expressed as tabulated functions of temperature, are varied using a nonlinear least squares algorithm to match simulation results to experimental data [116, 152]. However, Beck [18] stated that properties derived via iterative correlation to experimental data ought not to be considered material properties as they compensate for "the uncertainties in all of the other properties/parameters in the material thermal model" [18].

To perform code to code comparison, a public database TACOT [91] (Theoretical Ablative Composite for Open Testing) has been compiled based on experimentally derived material properties in literature, including arc-jet ablation tests [44], which aims to represent the material PICA (phenolic impregnated carbon ablator) [158]. Wang et al. conducted oxyacetylene torch ablation tests of PICA and compared experimental surface temperature, recession, and in-depth thermocouple data to a replica of the CMA model using

TACOT material properties. The authors observed severe disagreement between simulation and experiment on all measured quantities, with surface recession rates being "6.38 times (equilibrium) and 14.08 times (frozen) higher than experimental data" [164], where the range occurred over various estimates of the heat transfer coefficient $\rho_e u_e C_H$ in the thermochemical ablation model. To help determine the source of the discrepancy, the authors conducted a steady state ablation analysis in which they noted that the experimental recession rates and surface temperatures could not be simultaneously met using TACOT material properties and the CMA thermochemical ablation model. Possible causes that the authors considered included TACOT properties being poorly representative of PICA, multi-dimensional effects, experimental errors, and non-equilibrium surface thermochemistry.

Most ablation models attempt to account for geometry evolution by moving the mesh [6, 31, 46, 153]. For moving frame problems, however, care must be taken that quantities are properly convected with grid motion and that mass and energy are conserved [59, 63, 153]. These issues are often left unaddressed [31, 35, 46, 95, 139]. Authors have also considered solving the governing equations in a stationary frame, re-meshing the domain, and interpolating quantities to the new mesh [52, 131, 150].

Strength and mechanical effects are typically ignored in modeling the solid material, and the solid is implied as a rigid and immobile entity. Mechanical analysis is performed in an uncoupled manner where the temperature profile from an ablation solver is used to analyze thermal stresses and strains

[60, 61, 131]. Quinn et al. [131] considered modeling the solid explicitly in a Lagrangian frame. Recession was approximated by re-meshing the material in the reference configuration and interpolating quantities onto the new mesh. Fu et al. [60, 61] also considered modeling the solid in a Lagrangian frame but neglected recession. In both cases, the solid dynamics were limited to small strain mechanical equilibrium and uncoupled from the rest of the ablation kinematics. The models thus differed little from an uncoupled mechanical analysis. The absence of mechanical coupling may be due to the disparity between mechanical and thermal conduction time constants, requiring that thermal conduction models exclude an explicit representation of the solid material. This dissertation considers a mirrored approach in which the solid is modeled explicitly, including strength effects and material erosion, while conduction is kept to a minimum.

A summary of ablation models in the literature is listed in Tables 1.1 to 1.3. Five components are listed for each model: first is the model dimensionality (1D, 2D, or 3D), second is the numerical method used, third is whether the discretization is presented, fourth is whether the model conserves mass and energy, and the last is whether a solid model is included.

Table 1.1: Summary of ablation models in literature in use by NASA.

	FIAT	TITAN	3-D FIAT	CHAR	ICARUS	PATO
Reference	[33]	[28]	[35]	[5]	[139]	[95]
Dimensionality (n-D)	1	2	3	1-3	3	1-3
Numerical method	FV	FV	FV	FEM	FV	FV
Describes discretization						
Conserves mass and energy						
Models solid						

Discretization:
- green - Numerical discretization included
- yellow - Essential components of the numerical discretization, such as formulation of the mesh movement terms, are missing
- red - No description of numerical discretization

Conservation:
- green - Conserves mass and energy
- yellow - Insufficient description of formulation to determine if mass and energy are conserved
- red - Mass and energy not conserved

Solid model:
- green - Solid is explicitly modeled
- red - Solid is implied

Table 1.2: Summary of replicas or simplifications of NASA ablation models in literature.

	MOPAR	HERO	FEATS	CHyPS	Dec et al.	Appar et al.
Reference	[46, 107]	[52]	[20]	[38]	[49]	[8]
Dimensionality (n-D)	2	2	2	2	1	2
Numerical method	CVFEM	FEM	FEM	DG	FEM	FV
Describes discretization						
Conserves mass and energy						
Models solid						

Table 1.3: Summary of ablation models in literature including extension beyond the NASA models.

	SCMA	Micc-oli et al.	Schr-ooyen et al.	Tahm-asbi et al.	Weng et. al	Quinn et al.
Reference	[150]	[112]	[138]	[153]	[168]	[131]
Dimensionality (n-D)	2	2	2	2	3	2-3
Numerical method	FV	DG	DG	FV	FV	DG
Describes discretization						
Conserves mass and energy						
Models solid						

1.3 Review of Subscale Analysis

Recent literature has seen an increasing interest in analyzing the composite material at the meso and nanoscales [13] to support the development of higher fidelity ablation models. At the nanoscale, reactive molecular dynamic (RMD) simulations of resin pyrolysis are performed [17, 36, 68, 172]. Nanoscale simulations have typically focused on identifying resin decomposition pathways [17, 36, 68, 172] with limited extension to higher scales. To estimate composite properties for ablation models, authors have analyzed the composite architecture at the mesoscale to estimate macrostructural properties such as thermal conductivity, porosity, and permeability [56, 79, 137, 141, 174]. An explicit representation of the fiber and resin is employed in analyzing the composite architecture, and composite properties are estimated by averaging over a representative volume. Such models operate as addendums to existing ablation modeling methodologies. Current ablation models account for spallation by scaling the thermochemical mass loss by a constant empirical factor [113, 128]. Fiber oxidation simulations [56, 93, 94, 161] have thus also been performed at the mesoscale to improve understanding of spallation causes, where it is understood that oxidation may lead to a weakening of the fibers at the surface [94]. Authors have also studied the formation of surface roughness patterns due to fiber oxidation since surface roughness may increase heating by inducing turbulence [161].

The following sections describe recent work in the literature at each scale with a focus on the applicability of current methods toward multiscale

ablation modeling.

1.3.1 Review of Nanoscale Modeling

Nanoscale models generally focus on molecular dynamic simulations of resin pyrolysis [17, 19, 36, 68, 105, 172]. For the extension to multiscale modeling, the extraction of decomposition and chemical kinetics is of primary interest [19, 68]. During resin pyrolysis, the solid material is subject to changes in chemical composition. Authors have employed various methods for defining the extent of pyrolysis, with methods centered around defining a representative system reactant. Chen et al. [27], who simulated the pyrolysis of various engineering polymers, chose the number of backbone monomers as the representative system reactant. In the presented simulation results, the backbone monomer population was observed to spike at the start of the simulation due to the disassociation of the polymer chains, after which it gradually decreased with the formation of subsequent pyrolysis products. The backbone monomer population in the latter portion of the simulation was used for kinetics fitting. Harpale et al. [68] conducted simulations of phenolic pyrolysis where the phenolic rings were first cross linked to create an interconnecting net work of C–C bonds during an initial curing simulation. The number of intact C–C bonds was then used to define a representative system reactant during the pyrolysis simulation. Bhesania et al. [19] used a dimensional reduction technique introduced by Sakano et al. [136] for reaction course graining to define a representative system reactant. The authors first formulated a vector represen-

tation of the system where each timeframe was described by a numerical vector describing the coordination geometry of the chemical species. From the simulation results, a matrix was constructed where the matrix rows corresponded to selected timeframes during the pyrolysis simulation. A dimensional reduction was then performed, using non-negative matrix factorization, to reduce the matrix column space to three principal components. In the presented simulation results, the time evolution of the three components qualitatively produced the expected behaviors of a reactant, product and intermediate in a decomposition reaction. The component that most behaved like a reactant was then used to define the extent of pyrolysis. In each case, the selected reactant variable χ is fit assuming a reaction rate of Arrhenius form:

$$\frac{d\chi}{dt} = -k\chi^n, \quad k = A\exp\left(\frac{-E}{R\theta}\right) \tag{1.52}$$

where a first order reaction ($n = 1$) is typically used. Validation of the kinetics is based on matching the Arrhenius constants to TGA derived values [27, 68]. Chen et al. [27] ran a series of isothermal simulations, from which the pre-exponential factor A and activation energy E were obtained by fitting to the curve

$$\ln(k_i) = \ln(A) - \frac{E}{R}\left(\frac{1}{\theta_i}\right) \tag{1.53}$$

where k_i was obtained by fitting to the simulation results at each temperature θ_i. This method is also employed by other authors in literature [65, 68, 163]. Bhesania et al. [19] performed non-isothermal simulations. In doing fitting, an

instantaneous reaction rate $k(t)$ was calculated assuming the following relation

$$\chi(t) = \chi_0 \exp(-kt) \tag{1.54}$$

The same equation 1.53 was used to determine the Arrhenius constants. The authors did not present results on reaction rate versus temperature during the non-isothermal simulations.

In order to incorporate the RMD simulation results into a resin pyrolysis model, Harpale et al. [68] used an engineering control volume formulation to estimate a resin charring velocity, which was then used to model the pyrolysis of phenolic micro balloons. Bhesania et al. [19] related the MD reactant variable to the remaining resin mass fraction in a 1-D phenolic pyrolysis simulation. Chen et al. [27] considered the reproduction of differential thermogravimetric curves (derivative of mass loss in TGA with respect to temperature) for various engineering polymers. Authors generally employ the following relation [19, 27, 68]

$$\frac{\partial}{\partial t}\left(\frac{\rho}{\rho_0}\right) = -k\left(\frac{\rho}{\rho_0}\right)^n \tag{1.55}$$

where ρ is the solid density, ρ_0 the starting solid density, and k is obtained from the MD simulation results. Authors have employed inconsistent values for the exponent n in formulating pyrolysis models. Harpale et al. [68] and Bhesania et al. [19] used a value of one for n to fit the RMD simulation results but used a value of zero in the pyrolysis simulations. Chen et al. [27] did not specify the exponent value.

It is worth noting that existing extensions of RMD simulation results to pyrolysis modeling provide limited fidelity. MD derived pyrolysis models in literature assume a single constituent resin decomposition [19, 27, 68]. A coarsened representation of the RMD system is also employed, excluding chemical kinetics. Current MD derived pyrolysis models thus do not pose an advantage over TGA based models and have not seen incorporation into ablation models in literature.

An approach that has not been taken in the current ablation literature is the extension of the RMD chemical kinetics to higher scales. The most significant difficulty to such an approach is the requirement of a multiscale integration strategy, as the RMD chemical kinetics occur on a far smaller time scale than macroscale simulations. The current literature may thus benefit from new methods that leverage the chemical fidelity of RMD simulations and provide an extension to higher scales.

1.3.2 Review of Mesoscale Modeling

Mesoscale simulations typically employ an explicit representation of the composite fiber and resin architecture. The microscale structure can be generated algorithmically [78, 141, 174] or from experimental computed tomography data [57, 58, 123, 160]. Mesoscale simulations fall into two categories: (1) estimation of composite properties [78, 79, 123, 137, 141, 174], and (2) oxidation simulations [9, 57, 93, 102, 130, 160].

For the first category, mesoscale analysis aims to estimate compos-

ite properties from the material microstructure to support ablation modeling [79, 123, 137, 141, 174]. Properties extracted from mesoscale composite models include thermal conductivity, permeability, tortuosity, porosity, and specific surface area. Thermal conductivity is typically estimated by solving a steady state heat equation from which a bulk conductivity is extracted [56, 141, 174]. Permeability and tortuosity can be obtained by stochastic methods, such as Direct Simulation Monte Carlo or Monte Carlo Random Walk [22, 56]. Porosity and specific surface area are calculated directly from the mesoscale geometry [56]. These quantities are then input into ablation models [13, 95].

Semeraro et al. [141] estimated the thermal conductivity of short fiber and woven carbon materials where the fiber structures were obtained from experimental computed tomography (CT) scans. CT scans return a voxel representation of the material, which consists of a Cartesian grid where each grid is associated with a scalar value describing a mean X-ray attenuation. For estimating thermal conductivity, the authors used the voxel-based representation to construct a Cartesian grid which was then discretized using Finite Volume. An anisotropic thermal conductivity tensor was associated with each grid, accounting for the anisotropic thermal conductivity of the carbon fibers and carbon fiber tows, where the orientation of the thermal conductivity tensor was estimated from the CT scan data [141, 142]. The effective thermal conductivity was then obtained by solving a steady state heat equation over a representative volume. Zhou et al. [174] estimated the thermal conductivity of a silica reinforced phenolic composite where the resin and fiber structures

were generated algorithmically, and the resin was assumed to fill the volume between the fibers. Thermal conductivity was also estimated by solving a steady state heat equation, where a finite element discretization was employed using the commercial software ABAQUS, and isotropic thermal conductivity was assumed for the fiber and resin constituents. For the resin thermal conductivity, the authors performed a parametric study on the effects of matrix porosity, assuming a random ellipsoidal pore distribution in the matrix constituent.

Borner et al. [22] estimated the permeability of FiberForm, a commercial short chopped carbon fiber material that has been used as the fiber reinforcement in ablative materials such as PICA (phenolic impregnated carbon ablator [158]). The fiber structure of FiberForm was obtained from CT scan data. Direct Simulation Monte-Carlo (DSMC), a stochastic method that tracks the movement and collisions of a set of representative particles, was then used to simulate gas transport through the material. Permeability was then estimated based on the average mass flow rate and pressure drop across a representative volume. The authors also performed studies on the effect of temperature, porosity, and orientation on the permeability of FiberForm. Jambunathan et al. [79] studied the permeability of FiberForm and a commercial carbon felt material. The fiber structures were also obtained from CT scan data, and DSMC was used to simulate gas transport through the material.

For the second category, mesoscale oxidation simulations attempt to reproduce the oxidized composite geometries observed under Scanning Electron

Microscopy (SEM), modeling surface roughening [102, 160, 161] and volumetric oxidation [57, 93, 123]. Regarding motivation, surface roughening promotes the transition from laminar to turbulent flow, increasing heating, and may also increase the effective reactive surface area, accelerating recession [161]. For volumetric oxidation, it is suggested that oxygen penetration may weaken the material in the surface layers leading to spallation [94].

For modeling oxidation, mesoscale models track the solid surfaces explicitly. The surfaces evolve as [93]

$$\frac{\partial S}{\partial t} + \mathbf{v} \cdot \nabla S = 0 \tag{1.56}$$

where S is a scalar level-set function defining the surface position, and $\mathbf{v}$ is the surface velocity due to oxidation. The oxidation rate is modeled with a simple first order form

$$\mathbf{v} = -\Omega k C \hat{\mathbf{n}}, \quad k = k_0 \exp(-E/R\theta) \tag{1.57}$$

where k is the gasification rate (m/s), C the molar oxygen concentration, Ω the solid molar volume and $\hat{\mathbf{n}}$ the surface normal. The oxygen concentration is modeled as

$$\frac{\partial C}{\partial t} + \nabla \cdot (C\mathbf{v}_g) = \nabla \cdot (D \nabla C), \qquad \text{in the fluid} \tag{1.58}$$

$$D \nabla C \cdot \hat{\mathbf{n}} = kC, \qquad \text{at fluid-solid interface} \tag{1.59}$$

where D is a diffusion coefficient. For the bulk gas velocity $\mathbf{v}_g$ and temperature θ, current models typically assume isothermal conditions and zero bulk velocity [57, 93, 102, 123, 160, 161] or a fixed temperature profile and constant gas

velocity [94]. For numerical discretization, a Cartesian Eulerian background grid is employed with a surface tracking algorithm, including volume of fluid [9, 160] and level set [130]. Authors have also used stochastic methods with Monte Carlo Random Walk to model oxygen diffusion and a sticking probability for the surface reactions; the solid surface evolves based on a marching cube algorithm [93]. Model validation is based on the reproduction of solid morphologies observed under SEM.

Aspa et al. [9] developed a surface tracking algorithm based on the volume of fluid method to simulate the oxidation of carbon-carbon composites. The authors performed simulations of a single fiber coated in a carbon matrix with the aim being to reproduce a conical shaped morphology observed under SEM (see Figure 1.6), where the conical shape was suggested to develop due to differential oxidation of the carbon fibers and the surrounding matrix. Mesoscale simulations were also conducted on the formation of cavities in the space shuttle thermal protection system due to damage to the SiC coating, exposing the underlying carbon-carbon composite. Isothermal conditions and zero convective mass transport were assumed for all simulations. Qin et al. [130] also performed oxidation simulations of a carbon-carbon composite assuming isothermal conditions and zero convection. A level-set algorithm was used for tracking fiber and matrix surfaces. The authors performed simulations of a fiber array immersed in a surrounding matrix, aiming to reproduce a conical shaped fiber morphology observed under SEM. Simulations were also performed for the recession of the carbon-carbon composite in the throat of a

solid rocket motor, where environmental parameters, such as temperature and oxidative species concentration, were obtained from a CFD solution. Simulation results were qualitatively compared to SEM images of the ablated throat in a solid rocket motor.

Lachaud et al. [92] performed oxidation simulations of PICA (phenolic impregnated carbon ablator), a carbon fiber reinforced phenolic composite with a short chopped fiber architecture [158]. Oxygen diffusion was simulated using a Monte Carlo random walk algorithm. Oxidation of the matrix and fibers was estimated using a sticking probability for the surface reactions, and the surfaces were tracked using a marching cube approximation (see Figure 1.7).

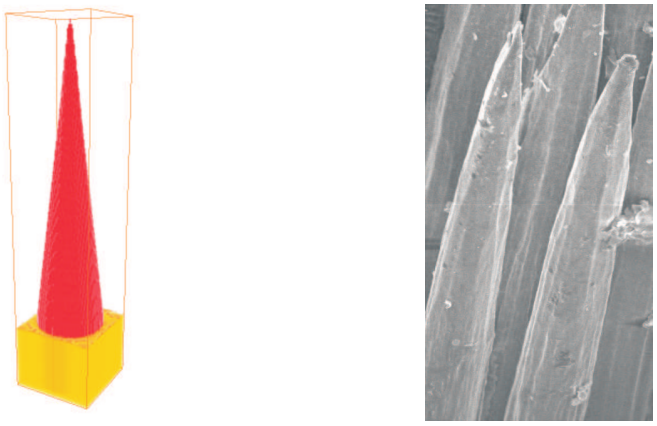

(a) Simulated fiber oxidation in Ref [9].

(b) SEM image of oxidized carbon fiber surface in Ref [9].

Figure 1.6: Simulation of carbon fiber oxidation by Aspa et al. [130] using the volume of fluid method on a Eulerian Cartesian grid. The authors perform qualitative comparison of simulation results to SEM images of oxidized carbon fibers.

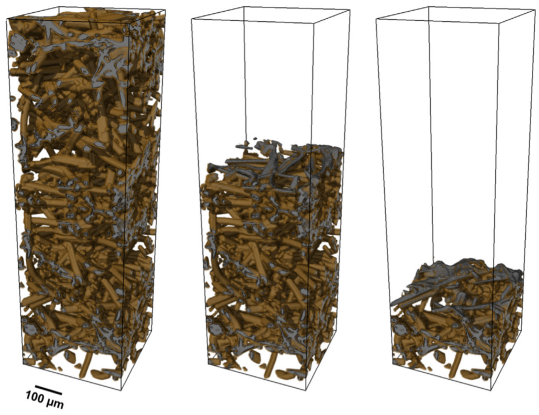

Figure 1.7: Simulation in Ref [92] on the oxidation of FiberForm (a short carbon fiber composite) coated with phenolic. The fiber structure is obtained from CT scan data. Oxygen diffusion is modeled using a random walk algorithm on a 3-D Cartesian grid, and a sticking probability law is used to estimate oxidation.

1.3.3 Summary

Current ablation models are based on methodologies developed in the 1960s. This stagnation has also been marked in recent literature [97, 99]. The current avenue of improvement, as recently described by Barnhardt et al. [13], is to construct microscale composite models for estimating composite properties, such as thermal conductivity, porosity, and permeability, from the material microstructure for input into ablation models [13, 95]. However, such methods do not fundamentally extend existing ablation modeling methodologies. Mesoscale oxidation simulations also lack meaningful extension to higher scales and generally support phenomenological spallation models [94]. Current nanoscale models also lack an extension of the chemical kinetics to higher scales. The literature may thus benefit from a new integrated multiscale ap-

proach that includes the integration of pyrolysis and ablation models at the nano and meso scales.

1.4 Objective

This research develops the first integrated multiscale ablation model spanning three levels of interest, as indicated in Table 1.4: nano, meso, and macro scale. In particular, the mesoscale model serves as a link to integrate the nanoscale RMD chemistry and the macroscale ablation model. The formulation extends current ablation models in literature by addressing four main issues. First, it develops a multiscale strategy for coupling the three scales of interest: nano, meso, and macro scale. Second, as part of the multiscale strategy, it incorporates a mesoscale model which simulates the fully coupled chemical-thermomechanical ablation problem. Third, it enforces the conservation of mass and energy in formulating the state variable evolution equations at each scale. Fourth, it explicitly models solid erosion effects for composite geometries in the macroscale ablation model.

The formulation is discrete nonholonomic Hamiltonian at all scales. It is pure particle at the nanoscale and hybrid particle element at the meso and macroscale. Hamilton's equations are formulated at each scale without reference to partial differential equations (PDE). This differs from the literature in that it separates the discretization process (e.g., finite element) from the solution method (e.g., weighted residuals for PDE). The benefit of this approach is that it allows for seamless element and particle based description of

the material in an energy conserving formulation. A schematic of the multi-scale structure is shown in Figure 1.8. RMD simulations are performed at the nanoscale to obtain chemical kinetics models of the resin decomposition process and pyrolysis gas reactions. The mesoscale model incorporates the RMD chemical kinetics into a 1-D fully coupled chemical-thermomechanical simulation of resin pyrolysis in a fiber and resin composite. From the mesoscale simulation results, the energy required to pyrolyze the resin in the composite material is computed and input into the macroscale model. The macroscale model then simulates in three dimensions the thermomechanical response of the composite to the applied mechanical and thermal loads. Included are the effects of transpiration cooling, ablation of both the resin and fiber reinforcement and evolution of the TPS geometry. The macroscale simulation incorporates a resin mass loss model obtained from the mesoscale simulation results since the short time constants of the RMD kinetics preclude direct simulation of transient chemical processes at the macroscale. The mechanical time constant generally determines the macroscale time constant, which is typically much shorter than conduction time constants. In order to directly simulate the solid dynamics of surface erosion processes at the macro scale, two assumptions are made: (1) heat conduction is limited to that which is numerically required to obtain smooth solutions, and (2) the externally applied loading rates are amplified (on the order of 10^4) so that the total applied thermal load occurs over a much shorter time than is typical of ablation experiments. These assumptions are similar to those adopted, for example, in

molecular dynamics simulations of plastic deformation mechanisms [62] and macroscale shock compression processes [167], where accessible molecular scale simulation times are much smaller than that representative of corresponding macroscale experiments. As in the latter case, the validity of the numerical modeling assumptions is evaluated by comparison of the simulation results to experiment.

This research builds on previous research on the hybrid particle element method [73, 101, 124, 145] by the addition of variable mass particles for simulating mass loss due to resin pyrolysis. In the macroscale model, the fiber reinforcement is represented by a set of tension only bar elements whose nodes are located at the particle centers of mass. This builds on previous research on the simulation of fabrics [132, 144] by combining particles, finite elements and tension only bar elements to produce a composite description of the material. Surface recession at the macroscale is captured by failing the elements and fibers once specific thermal, mechanical, and ablation criteria are reached. Since the failure criteria for the elements and fibers are distinct, the TPS erosion is not limited by the requirement to follow a single recession surface. This scheme also avoids the requirement of an adaptive mesh algorithm typically employed in current literature.

1.5 Organization

This dissertation describes a three level multiscale modeling approach to thermal ablation. The nanoscale RMD pyrolysis chemical kinetics was taken

from previous work [162]. A full description of the nanoscale model is thus not included here, and only the details of the incorporation of the RMD chemical kinetics into the mesoscale model are included. Chapter 2 describes the 1-D mesoscale formulation, including the linking of the thermomechanical and chemical kinetics models. Simulations are presented for two resin systems, phenolic and cyanate ester. Chapter 3 describes the 3-D macroscale formulation, including the incorporation of a resin mass loss model obtained from the mesoscale simulation results. Simulations presented in Chapter 3 include models of three fiber reinforcement architectures: 3-D, 2-D, and short fiber architecture. Finally, Chapter 4 summarizes the main contributions of this research.

Table 1.4: Comparison of the three scales.

Scale	Spatial Unit	Temporal Unit	Application
Molecular	nm	ps	resin pyrolysis chemistry
Meso	μm	ns	resin pyrolysis in fiber composite
Macro	mm	μs	ablation and shape change

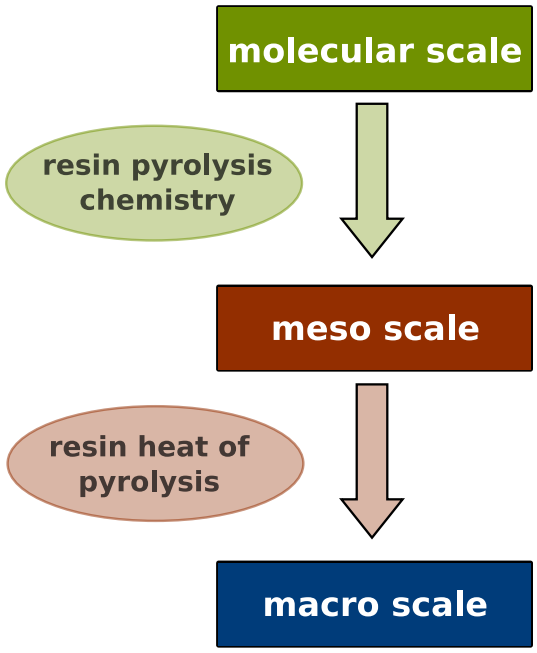

Figure 1.8: Multiscale model structure.

Chapter 2

Mesocale Model

2.1 Introduction

The 1-D mesoscale model presented in this chapter extends previous research on hybrid particle-element with chemical reactions [101] to include variable mass particles. It fully couples the RMD chemical kinetics with the thermomechanical response. The model uses 1-D linear finite elements, which model the elastic response in tension and plastic strain evolution. The particles, located at the nodes of the elements, capture the compressive response and are modeled as a mixture of fiber and resin. The particle mass evolution is coupled to the RMD chemical kinetics to account for mass loss due to resin pyrolysis. The principle purpose of the mesoscale simulation is to compute a resin heat of pyrolysis within a fiber reinforced composite, which is a required input to the macroscale simulation.

2.2 Chemical Kinetics Model

The RMD formulation and chemical kinetics models are not developed in this dissertation but are taken from previous research [15, 16, 162]. The RMD model is based on a nonholonomic formulation that differs from conven-

tional molecular dynamics in that rate equations rather than analytic functions determine the bond orders and bonding-debonding process. Readers interested in the RMD formulation are directed to previous works by Bass et al. [15, 16]. For the resin pyrolysis simulations and the pyrolysis chemistry models, readers are directed to previous work by Wang [162]. The RMD simulations of resin pyrolysis [162] start with an initial NVE interval where the number of atoms, volume, and energy are held constant, allowing for the disassociation of the resin species. Following the NVE interval, a thermostat is applied, gradually reducing the simulation temperature to a target thermostat temperature while holding the number of atoms and volume constant, allowing recombination reactions to occur. Accordingly, the kinetic modeling of the pyrolysis chemistry is split into two parts: (a) fit to the disassociation portion of the simulation and (b) fit to the recombination portion. The kinetic models have the functional form:

$$\dot{C}_j^{(i)} = \sum_{k=1}^{N_r} \left(\nu^{(j,k)} - \hat{\nu}^{(j,k)}\right) \xi^{(i,k)} \tag{2.1}$$

where $C_j^{(i)}$ is the molar concentration of species j in particle i, N_r is the number of reactions, $\xi^{(i,k)}$ is the reaction rate for reaction k in particle i, and $\nu^{(j,k)}$ and $\hat{\nu}^{(j,k)}$ are the stoichiometric coefficients for the products and reactants of species j in reaction k respectively.

The disassociation reactions rates have the functional form

$$\xi^{(i,k)} = k^{(k)} \left(\frac{\rho^{(i)}}{\rho_0^{(i)}}\right)^{1-m^{(k)}} \prod_{j=1}^{N_s} \left(C_j^{(i)}\right)^{\alpha^{(j,k)}} \hat{u}\left(u^{(i)} - u_{ign}\right) \tag{2.2}$$

where $k^{(k)}$ are the reaction rate constants, $\rho^{(i)}$ the density of particle i, $\rho_0^{(i)}$ a reference particle density, N_s the number of species, $\alpha^{(j,k)}$ the rate exponents, $u^{(i)}$ the particle specific internal energy density, u_{ign} the ignition internal energy density, and $\hat{u}$ the unit step function. The disassociation reactions occurred rapidly in the early stages of the RMD simulation resulting in very high reaction rates. The disassociation reaction rate constants $k^{(k)}$ used in the mesoscale model were thus reduced by a constant factor from the RMD-derived values to help mitigate time step constraints. Reflective of the RMD simulations, the recombination reactions are initiated after the disassociation reactions are complete. The recombination reaction rates have the form:

$$\xi^{(i,k)} = k^{(k)} \left(\frac{\rho^{(i)}}{\rho_0^{(i)}} \right)^{1-m^{(k)}} f^{(k)}(\theta) \prod_{j=1}^{N_s} \left(C_j^{(i)} \right)^{\alpha^{(j,k)}} \hat{u}(\lambda^{(i)} - \lambda_{max}) \tag{2.3}$$

where $\lambda^{(i)}$ is the extent of resin pyrolysis computed as:

$$\lambda^{(i)} = 1 - \frac{C_R^{(i)}}{C_{R0}^{(i)}} \tag{2.4}$$

The constant index R denotes the resin species index, and $C_{R0}^{(i)}$ denotes the starting resin species concentration. The recombination reactions are initiated once $\lambda^{(i)}$ reaches a critical value λ_{max}, which was set to 0.99 for all simulations in this thesis. A dependence on temperature (θ) is also included through the temperature dependent function $f^{(k)}$, which is modeled as having one of two

forms,

$$f^{(k)}(\theta) = \frac{1}{1+\exp\left(\frac{\theta-\theta^{(k)}}{\theta^{(k)}}\right)}, \quad \text{or} \tag{2.5}$$

$$f^{(k)}(\theta) = 1 - \frac{1}{1+\exp\left(\frac{\theta-\theta^{(k)}}{\theta^{(k)}}\right)} \tag{2.6}$$

where the forms were chosen in Ref [162] from fitting to the RMD simulation results.

2.3 Species Masses Evolution

In the mesoscale model, the particle mass $m^{(i)}$ and the vector of species masses $s_j^{(i)}$ constitute part of the system generalized coordinates. The species concentrations are related to the species masses as:

$$C_j^{(i)} = \frac{s_j^{(i)}}{\phi_r^{(i)} \nu^{(i)} \mathbb{M}_j} \tag{2.7}$$

where $\nu^{(i)}$ is the particle volume, $\phi_r^{(i)}$ the resin volume fraction, $\mathbb{M}$ denotes molar mass, and $s_{R0}^{(i)}$ is the initial resin mass in particle i. The starting resin mass $s_{R0}^{(i)}$ in a particle is calculated by

$$s_{R0}^{(i)} = \rho_0^{(i)} f_r^{(i)} \nu_0^{(i)} \tag{2.8}$$

where $f_r^{(i)}$ is the resin mass fraction, and $\nu_0^{(i)}$ is the particle volume in the reference configuration. The mesoscale simulation initializes the resin and gas species masses with the same molar ratios as the RMD simulation. For pyrolysis in air, the RMD simulations were initialized with the resin species

and the air species nitrogen and oxygen. The nitrogen and oxygen quantities were initialized with a ratio of 4:1, representing an air atmosphere. Sufficient oxygen was supplied to achieve an oxygen balance of zero, corresponding to all carbon being converted to carbon dioxide and all hydrogen being converted to water. For pyrolysis in vacuum, the RMD simulations were initialized with only the resin species [162].

The pyrolysis reactions act as source terms for the evolution of the particle masses. The reaction source terms are:

$$\dot{s}_j^{reac(i)} = \dot{C}_j^{(i)} \, \phi_r^{(i)} \, \nu^{(i)} \, \mathbb{M}_j \tag{2.9}$$

The evolution of the particle mass is modeled as equal to the resin mass evolution:

$$\dot{s}_R^{(i)} = \dot{s}_R^{reac(i)} \tag{2.10}$$

$$\dot{m}^{(i)} = \dot{s}_R^{reac(i)} \tag{2.11}$$

It is assumed in the mesoscale model that the fiber remains chemically inert. This is consistent with the purpose of the mesoscale model to compute a resin heat of pyrolysis. It is noted, however, that the fiber, while chemically inert, still affects the thermomechanical response.

The particle mass includes only the resin and fiber masses. For the gas species, a gas control volume is associated with each particle in which the gas species are assumed to reside. For simulations in air, the size of the control volume V_g is calculated from the initial nitrogen and oxygen content. For

simulations in vacuum, an air to resin mass ratio is used. V_g is computed as

$$V_g^{(i)} = \frac{1}{\rho_{\text{air}}}(s_{N_20}^{(i)} + s_{O_20}^{(i)}) \qquad \text{(in air)} \tag{2.12}$$

$$V_g^{(i)} = \frac{1}{\rho_{\text{air}}} s_{R0}^{(i)} \xi \qquad \text{(in vacuum)} \tag{2.13}$$

where ρ_{air} is an air density, which is simply set to the density of air at sea level (1.2254 kg/m^3), $s_{N_20}^{(i)}$ and $s_{O_20}^{(i)}$ are the initial nitrogen and oxygen masses for simulations in air, and ξ is an air to resin mass ratio. For simulations in vacuum, ξ is set to the equivalent value for simulations in air. The gas species masses evolution include two contributions: one from the pyrolysis reactions, and the second from convection out of the gas control volume:

$$\dot{s}_j^{(i)} = \dot{s}_j^{reac(i)} + \dot{s}_j^{cvc(i)}, \quad j \in gas \tag{2.14}$$

The rate of convection ($\dot{s}^{cvc(i)}$) is modeled as proportional to the gas pressure:

$$\dot{s}_j^{cvc(i)} = -k_g^{(i)} \frac{s_j^{(i)}}{V_g^{(i)}} P_g^{(i)} \frac{\nu_0^{(i)}}{\nu_{RF}} \hat{u}(C_R^f - C_R^{(i)}), \quad j \in gas \tag{2.15}$$

where $P_g^{(i)}$ is the gas pressure, and ν_{RF} is a reference volume. $k_g^{(i)}$ is a constant which scales as:

$$k_g^{(i)} = \hat{k} \frac{1}{\rho_{\text{air}}} \frac{V_g^{(i)2/3}}{c_{sr}} \tag{2.16}$$

where c_{sr} is the resin sound speed, and $\hat{k}$ is a non-dimensional gas convection coefficient. The pressure of the gas within this control volume is computed from the ideal gas law. An initial ambient pressure P_{g0} is computed as:

$$P_{g0}^{(i)} = \left(\frac{s_{N_20}^{(i)}}{\mathbb{M}_{N_2}} + \frac{s_{O_20}^{(i)}}{\mathbb{M}_{O_2}} \right) R\theta_0 \frac{1}{V^{g(i)}} \tag{2.17}$$

where R is the ideal gas constant. The gas pressure is then calculated by,

$$P_g^{(i)} = \left\langle R\theta^{(i)} \frac{1}{V_g^{(i)}} \sum_{j \in gas} \frac{s_j^{(i)}}{\mathbb{M}_j} - P_{g0}^{(i)} \right\rangle \tag{2.18}$$

where the summation is done over the gas species, and the Macaulay brackets $\langle x \rangle$ denote

$$\langle x \rangle = \begin{cases} x & x > 0 \\ 0 & x \leq 0 \end{cases} \tag{2.19}$$

2.4 Equations of State

Each particle is assumed to consist of a mixture of fiber and resin. The mixture equation of state is formulated as [133]

$$P = f_f P_f \frac{\rho_0}{\rho_{f0}} + f_r P_r \frac{\rho_0}{\rho_{r0}} \tag{2.20}$$

$$\theta = f_r \frac{c_{v_r}}{c_v} \theta_r + f_f \frac{c_{v_f}}{c_v} \theta_f, \quad c_v = c_{v_r} f_r + c_{v_f} f_f \tag{2.21}$$

where P_f and P_r are fiber and resin pressures, ρ_{f0} and ρ_{r0} are fiber and resin reference densities, c_{v_f} and c_{v_r} are fiber and resin specific heats, θ_f and θ_r are fiber and resin temperatures, f_f and f_r are fiber and resin mass fractions, and ρ_0 is a composite reference density. The fiber and resin equations of state take a Mie-Grüneisen form:

$$P_f = \rho_{f0} c_{s_f}^2 \left(\frac{\rho}{\rho_0} - 1 \right) + \gamma_f \rho_{f0} (u - u_0) \tag{2.22}$$

$$P_r = \rho_{r0} c_{s_r}^2 \left(\frac{\rho}{\rho_0} - 1 \right) + \gamma_r \rho_{r0} (u - u_0) \tag{2.23}$$

where c_{s_f} and c_{sr} are fiber and resin sound speeds, γ_f and γ_r fiber and resin Grüneisen parameters, u_0 a reference internal energy density, and ρ a composite density. In the absence of experimental data, a rough average of the Grüneisen parameter may be estimated as [69]

$$\gamma = \frac{\alpha K_s}{c_p \rho_0} \tag{2.24}$$

where α is a volumetric thermal expansion coefficient, K_s a bulk modulus and c_p a specific heat. The fiber and resin temperatures are computed from the fiber and resin specific heats:

$$\theta_f = \frac{1}{c_{v_f}}(u - u_0) + \theta_0 \tag{2.25}$$

$$\theta_r = \frac{1}{c_{vr}}(u - u_0) + \theta_0 \tag{2.26}$$

where θ_0 is a reference temperature. For the pyrolysis reactions, the disassociation chemistry begins once an ignition internal energy is reached (see Equation (2.2)). The ignition internal energy is calculated from a resin pyrolysis temperature θ_{pyr} by

$$u_{ign} = c_{vr}(\theta_{pyr} - \theta_0) + u_0 \tag{2.27}$$

In modeling a given composite material, typical experimental quantities that can be obtained are the true fiber and resin densities $\bar{\rho}_f$ and $\bar{\rho}_r$, reference composite density ρ_0, and the resin and fiber mass fractions f_r and f_f. From

these quantities, the fiber and resin reference densities are calculated as

$$\rho_{f0} = \bar{\rho}_f \left(\frac{f_r}{\bar{\rho}_r} + \frac{f_f}{\bar{\rho}_f} \right) \rho_0 \tag{2.28}$$

$$\rho_{r0} = \bar{\rho}_r \left(\frac{f_r}{\bar{\rho}_r} + \frac{f_f}{\bar{\rho}_f} \right) \rho_0 \tag{2.29}$$

which scales the true fiber and resin densities to account for composite porosity.

2.5 Heat Input Formulation

An external heat input is applied on the particles. The heat input formulation adopted in this work is taken from the optical literature describing the attenuation of a radiant flux in an absorbing body [121, 170]. In particular, the flux q in an absorbing medium is assumed to decay according to the Bouger-Lambert law ([170])

$$dq = -\kappa q \, ds \tag{2.30}$$

where ds is the optical path length and κ an absorption coefficient. This heat input form has also been employed in literature on the simulation of resin pyrolysis in fiber composites under radiative heating [80, 121, 173]. In this research, while the above form is employed for the heat input, the absorption coefficient κ is formulated such that the heat input profile moves through the material with resin pyrolysis and is not meant to be reflective of any material absorption properties. The absorption coefficient is formulated for each particle as:

$$\kappa^{(i)} = \left(1 - \lambda^{(i)}\right) \hat{u} \left(\lambda_{max} - \lambda^{(i)}\right) \frac{1}{\ell} \tag{2.31}$$

where ℓ is an absorption depth, and $\kappa^{(i)}$ evolves from $1/\ell$ to zero with resin pyrolysis in particle i. The heat flux attenuation in the particles can be described by the following schematic:

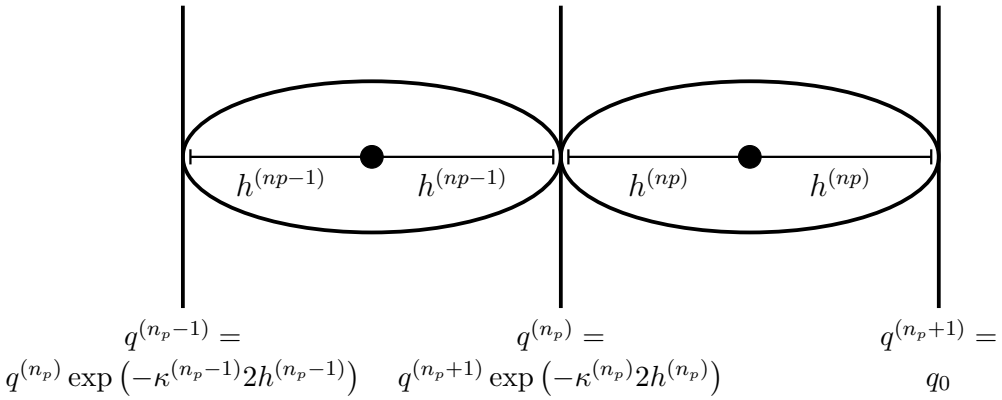

Figure 2.1: Schematic of heat flux attenuation in the particles in the mesoscale model.

where n_p is the total number of particles, $h^{(i)}$ a particle radius, and q_0 the heat flux impinging on the material. The heat flux at the particle interfaces can then be defined as

$$\begin{aligned} q^{(n_p+1)} &= q_0 \\ q^{(i)} &= q_0 \prod_{j=i}^{n_p} \exp(-\kappa^{(j)} 2h^{(j)}) \quad 1 \leq i \leq n_p \end{aligned} \tag{2.32}$$

The heat flux in the particles is then calculated by

$$\dot{U}^{inp(i)} = q^{(i+1)} - q^{(i)} \tag{2.33}$$

Summing across the particles, the total system heating rate $\dot{Q}$ is

$$\dot{Q} = \sum_{i=1}^{n_p} \dot{U}^{inp(i)} = q_0 - q^{(1)} \tag{2.34}$$

$$\dot{Q} = q_0 \left[1 - \exp\left(- \sum_{i=1}^{n_p} \kappa^{(i)} 2h^{(i)} \right) \right] \tag{2.35}$$

As seen in equation 2.35, variations in the total system heating rate are dependent on the variable $q^{(1)}$ associated with the back most particle. As seen in Figure 2.2, the heating depth ℓ is chosen to be reflective of a sharp heating profile resulting in the heat flux being negligibly small at the backside of the domain. Figure 2.3 shows the particle heat input $\dot{U}^{inp(i)}$ versus particle position as well as the heating rate Q versus time, in which a constant total system heating rate is observed.

It is noted, however, that $q^{(1)}$ depends on the discretization and is not non–negligible in general. Cases in which the total system heating rate may vary include: (1) the pryolysis front progresses to the backside of the domain, (2) ℓ is large relative to the domain size, and (3) a very course particle resolution is used. For the mesoscale simulations conducted in this thesis, care was taken to avoid the three aforementioned cases.

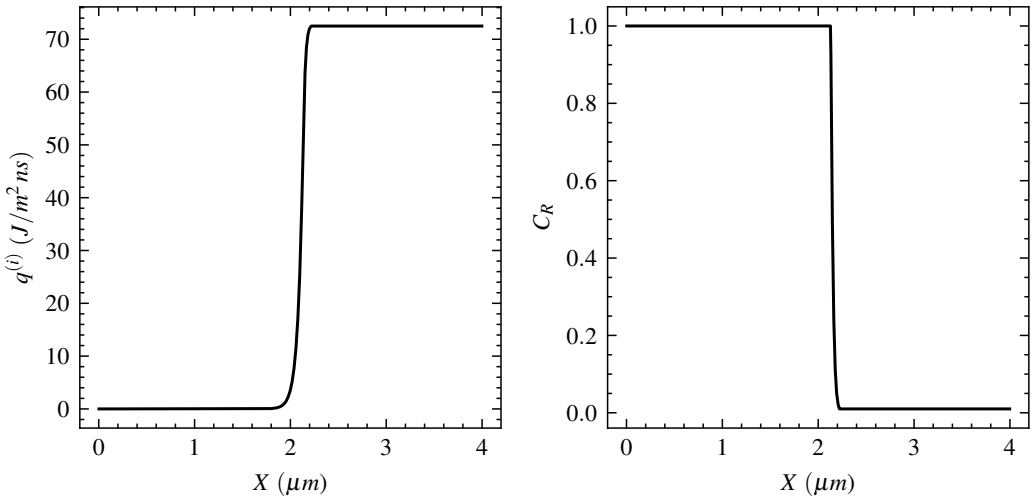

Figure 2.2: Heat flux profile for the ablation simulation of a carbon fiber reinforced phenolic composite at 20 ns, showing the heat flux attenuation modulated by resin pyrolysis in the particles.

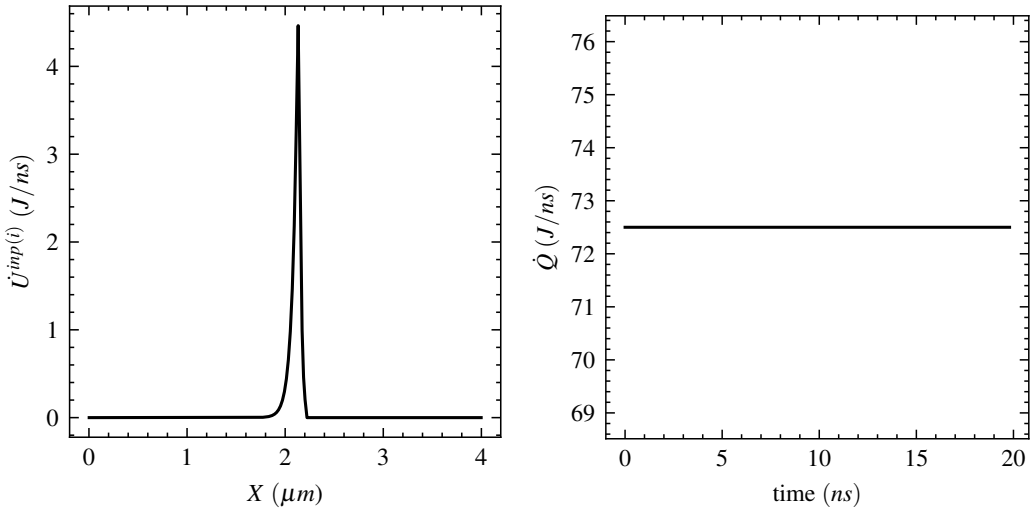

Figure 2.3: Heat input profile at 20 ns and total system heating rate for the ablation simulation of a carbon fiber reinforced phenolic composite.

2.6 Particle and Element Kinematics

The hybrid particle element interpolation builds upon previous work [73, 124]. In the 1-D mesoscale formulation, a particle based density interpolation is used for calculating volumetric change in the particles, which is formulated as

$$\frac{\rho^{(i)}}{\rho_0^{(i)}} = 1 + \frac{1}{2}\sum_{j=1}^{n_p}\left(\frac{\zeta_0^{(i,j)}}{\zeta^{(i,j)}} - 1\right) W^{(i,j)}, \quad \zeta^{(i,j)} = \frac{|c^{(i)} - c^{(j)}|}{2h^{(i)}} \tag{2.36}$$

where $c^{(i)}$ is the center of mass of a particle, $\rho^{(i)}$ and $\rho_0^{(i)}$ a particle density and reference density, $h^{(j)}$ a particle radius, and $\zeta_0^{(i,j)}$ is the value of $\zeta^{(i,j)}$ in the reference configuration. The weighting function $W^{(i,j)}$ is defined by

$$W^{(i,j)} = (1 - \delta_{ij})u_s\left(1 - \zeta^{(i,j)}\frac{\rho^{(j)}}{\rho_0^{(j)}}\right) \tag{2.37}$$

Similar to past work [124] which avoids the requirement for a differentiable density interpolation, the time derivative of the particle density is defined by

$$\frac{\dot{\rho}^{(i)}}{\rho_0^{(i)}} = -\frac{1}{2}\sum_{j=1}^{n_p}\frac{\dot{\zeta}^{(i,j)}}{\zeta^{(i,j)2}}\zeta_0^{(i,j)}W^{(i,j)} \tag{2.38}$$

The density interpolation Equation (2.36) is used for computing the particle density while the density time derivative Equation (2.38) will be used for computing generalized forces.

The particle centers of mass $c^{(i)}$ are the nodes of large strain finite elements used to model the tensile response and elastic plastic evolution. A deviatoric strain tensor is computed for each element, having the functional

form

$$E^{(j)} = E^{(j)}(c^{(i)}), \quad \dot{E}^{(j)} = \dot{E}^{(j)}(c^{(i)}, \dot{c}^{(i)}) \tag{2.39}$$

The strain is additively decomposed into elastic and plastic parts [73, 124]

$$E^{(j)} = E^{e(j)} + E^{p(j)}, \quad \dot{E}^{p(j)} = \dot{E}^{p(j)}(c^{(i)}, E^{p(j)}, \epsilon^{p(j)}, u^{(i)}, d^{(j)}) \tag{2.40}$$

where $E^{e(j)}$ and $E^{p(j)}$ are the elastic and plastic strain tensors respectively, $d^{(j)}$ describes element damage, having a value of zero for intact elements and one for failed elements, and $\epsilon^{p(j)}$ is an accumulated plastic strain obtained by integrating

$$\dot{\epsilon}^{p(j)} = |\dot{E}^{p(j)}| \tag{2.41}$$

An element stress $S^{(j)}$ is calculated from the elastic strain by

$$S^{(j)} = (1 - d^{(j)})\mu^{(j)} \frac{1 - \rho_{r0}/\bar{\rho}_r}{1 + \rho_{r0}/\bar{\rho}_r} E^{e(j)} \tag{2.42}$$

where $\mu^{(j)}$ is a matrix modulus. The factor $(1 - \rho_{r0}/\bar{\rho}_r)/(1 + \rho_{r0}/\bar{\rho}_r)$ accounts for matrix porosity [120]. Element failure in the mesoscale model is modeled on three criteria: (1) a maximum historic element internal energy calculated from its associated particles, (2) a maximum accumulated plastic strain, and (3) a maximum historic element stress. The element fails when any three exceed certain values. The damage variable is formulated as

$$d^{(j)} = \max\left\{\hat{u}(\epsilon^{p(j)} - \epsilon_f^{p(j)}), \hat{u}(u_{max}^{(j)} - u_f^{(j)}), \hat{u}(S_{max}^{(j)} - \sigma_s^{(j)})\right\} \tag{2.43}$$

where $u_{max}^{(j)}$ is a maximum historic element internal energy, $S_{max}^{(j)}$ a maximum historic element stress, and $\epsilon_f^{p(j)}$, $u_f^{(j)}$, and $\sigma_s^{(j)}$ are a failure plastic strain, failure internal energy, and failure spall stress respectively.

2.7 Hamiltonian Formulation

The system kinetic co-energy T^* and system potential energy V are simply the sum of the particle kinetic co-energies and internal energies respectively:

$$T^*(m^{(i)}, \dot{c}^{(i)}) = \sum_{i=1}^{n_p} \frac{1}{2} m^{(i)} \dot{c}^{(i)2} \tag{2.44}$$

$$V(U^{(i)}) = \sum_{i=1}^{n_p} U^{(i)} \tag{2.45}$$

The particle momenta $p^{(i)}$ are

$$p^{(i)} = \frac{\partial T^*}{\partial \dot{c}^{(i)}} = m^{(i)} \dot{c}^{(i)} \tag{2.46}$$

The system kinetic energy is then defined via the Legendre Transform

$$T = \sum_{i=1}^{n_p} p^{(i)} \dot{c}^{(i)} - T^* \tag{2.47}$$

which has the canonical form

$$T(m^{(i)}, p^{(i)}) = \sum_{i=1}^{n_p} \frac{p^{(i)2}}{2m^{(i)}} \tag{2.48}$$

The total differential of the kinetic co-energy is

$$dT^* = \sum_{i=1}^{n_p} \left(p^{(i)} d\dot{c}^{(i)} + \frac{\partial T^*}{m^{(i)}} dm^{(i)} \right) \tag{2.49}$$

From the Legendre Transform (equation 2.47), the kinetic energy has the total differential

$$dT = \sum_{i=1}^{n_p} \left(dp^{(i)} \dot{c}^{(i)} + p^{(i)} d\dot{c}^{(i)} \right) - dT^* \tag{2.50}$$

$$dT = \sum_{i=1}^{n_p} \left(dp^{(i)} \dot{c}^{(i)} - \frac{\partial T^*}{\partial m^{(i)}} dm^{(i)} \right) \tag{2.51}$$

From the canonical form (equation 2.48), the total differential can also be expressed as

$$dT = \sum_{i=1}^{n_p} \left(\frac{\partial T}{\partial p^{(i)}} dp^{(i)} + \frac{\partial T}{\partial m^{(i)}} dm^{(i)} \right) \tag{2.52}$$

from which the following relations are obtained

$$\frac{\partial T}{\partial m^{(i)}} = - \frac{\partial T^*}{\partial m^{(i)}} = -\frac{1}{2} \dot{c}^{(i)2} \tag{2.53}$$

$$\dot{c}^{(i)} = \frac{\partial T}{\partial p^{(i)}} \tag{2.54}$$

The system Hamiltonian is simply the sum of the total system kinetic and potential energies

$$H = T + V \tag{2.55}$$

2.7.1 Virtual Work

Forces that arise due to the particle mass evolution must be accounted for in the formulation of the virtual work. The presence of additional forces due to mass evolution has appeared in previous research on the application of Hamilton's equations to ALE frame reacting fluid simulations [70, 89]. The treatment is adapted here for Lagrangian frame hybrid particle-element. The system virtual work (δW) is expressed as the sum of an internal (δW^{int}) and external (δW^{ext}) portion:

$$\delta W = \delta W^{int} + \delta W^{ext} \tag{2.56}$$

The internal virtual work accounts for the particle mass evolution and is formulated as

$$\delta W^{int} = \sum_{i=1}^{n_p} \left(\dot{m}^{(i)} \dot{c}^{(i)} \delta c^{(i)} - \dot{c}^{(i)2} \delta m^{(i)} \right) \tag{2.57}$$

which balances the rate of change of kinetic energy in the particles due to mass loss. It is noted that the internal virtual work performs no net work on the system, as the above yields zero when the variations are taken to be physical ($\delta c^{(i)} = \dot{c}^{(i)} dt$, $\delta m^{(i)} = \dot{m}^{(i)} dt$). The external virtual work is

$$\delta W^{ext} = \sum_{i=1}^{n_p} \left(h^{ext(i)} \, \delta m^{(i)} + f^{ext(i)} \, \delta c^{(i)} \right) \tag{2.58}$$

where $h^{ext(i)}$ is a total external enthalpy and $f^{ext(i)}$ accounts for external loading on the particles. In the mesoscale model, the gas pressure is applied as an external mechanical loading,

$$f^{ext(i)} = -P^{g(i)} \frac{\nu_0^{(i)}}{\nu_{RF}} + f^{mech(i)} \tag{2.59}$$

Additional external loads $f^{mech(i)}$ may also be included.

2.7.2 Nonholonomic Constraints

The nonholonomic constraints include the evolution of the particle internal energy, which is

$$\dot{U}^{(i)} = \dot{U}^{ele(i)} + \dot{U}^{wrk(i)} + \dot{U}^{irr(i)} - \dot{U}^{con(i)} + \dot{U}^{inp(i)} + \dot{U}^{trc(i)} \tag{2.60}$$

where $\dot{U}^{ele(i)}$ is associated with deviatoric deformation in the elements, $\dot{U}^{wrk(i)}$ with volumetric deformation of the particles, $\dot{U}^{irr(i)}$ with viscous dissipation in

the particles, $\dot{U}^{con(i)}$ with heat conduction between the particles, $\dot{U}^{inp(i)}$ with external heating of the particles, and $\dot{U}^{trc(i)}$ with transpiration cooling in the particles. Power flow in the elements due to deviatoric deformation is [73, 124]

$$\dot{U}^{ele(i)} = \sum_{j=1}^{n_e} \phi^{(i,j)} V_0^{e(j)} S^{(j)} \left(\dot{E}^{(j)} - \dot{E}^{p(j)} \right) \tag{2.61}$$

where n_e is the number of elements, $\phi^{(i,j)}$ is the fraction of the power in element j transmitted to particle i and $V_0^{e(j)}$ is an element volume. Power flow in the particles due to volumetric deformation is

$$\dot{U}^{wrk(i)} = m^{(i)} \frac{P^{(i)}}{\rho^{(i)2}} \dot{\rho}^{(i)} \tag{2.62}$$

and the irreversible power is

$$\dot{U}^{irr(i)} = \sum_{j=1}^{n_e} \phi^{(i,j)} V_0^{e(j)} S^{(j)} \dot{E}^{p(j)} + f^{v(i)} \dot{c}^{(i)}, \tag{2.63}$$

$$f^{v(i)} = \sum_{j=1}^{n_p} \tau^{(i,j)} \left(\dot{c}^{(i)} - \dot{c}^{(j)} \right) \tag{2.64}$$

where $\tau^{(i,j)}$ is a numerical damping coefficient. The interparticle conduction is

$$\dot{U}^{con(i)} = \sum_{j=1}^{n_p} \kappa^{(i,j)} \left(\theta^{(i)} - \theta^{(j)} \right) \tag{2.65}$$

where $\kappa^{(i,j)}$ is a conduction coefficient. Transpiration cooling in the particles is formulated as

$$\dot{U}^{trc(i)} = \left(u^{(i)} + \frac{P^{(i)}}{\rho^{(i)}} + h_{dec} \right) \dot{m}^{(i)} \tag{2.66}$$

where the energy ejected from the particle is defined as the sum of a particle enthalpy and a decomposition enthalpy h_{dec}. The decomposition enthalpy

quantifies the energy required to drive the resin pyrolysis reactions and is taken from the literature. A positive value corresponds to an endothermic decomposition and a negative value to an exothermic decomposition. The energy ejected from the particle includes a chemical term in the form of the decomposition enthalpy h_{dec} and a dependence on the thermomechanical response through the particle enthalpy.

2.7.3 Hamilton's Equations

The system level model is obtained by combining the mesoscale Hamiltonian with the canonical Hamilton's equations, virtual work expression, and nonholonomic constraints describing the evolution of the particle internal energies and particle masses. The canonical Hamilton's equations are

$$\begin{aligned} \dot{p}^{(i)} &= -\frac{\partial H}{\partial c^{(i)}} + q^{c(i)}, \quad \dot{c}^{(i)} = \frac{p^{(i)}}{m^{(i)}}, \\ 0 &= -\frac{\partial H}{\partial U^{(i)}} + q^{U(i)}, \quad 0 = -\frac{\partial H}{\partial m^{(i)}} + q^{m(i)} \end{aligned} \tag{2.67}$$

where $q^{c(i)}$, $q^{U(i)}$, and $q^{m(i)}$ are generalized nonconservative forces determined by the nonholonomic constraints and virtual work. Introducing Lagrange multipliers $\gamma^{U(i)}$, and $\gamma^{m(i)}$ for the nonholonomic constraints, the generalized forces can be written

$$\begin{aligned} q^{c(i)} =& \frac{1}{2}\sum_{j=1}^{n_p}\left(\frac{m^{(i)}\rho_0^{(i)}\zeta_0^{(i,j)}}{(2h^{(i)})^2}\frac{P^{(i)}}{\rho^{(i)2}}\frac{W^{(i,j)}}{\zeta^{(i,j)3}}\gamma^{U(i)} + \right. \\ & \left. \frac{m^{(j)}\rho_0^{(j)}\zeta_0^{(j,i)}}{(2h^{(j)})^2}\frac{P^{(j)}}{\rho^{(j)2}}\frac{W^{(j,i)}}{\zeta^{(j,i)3}}\gamma^{U(j)}\right)\left(c^{(i)} - c^{(j)}\right) \end{aligned}$$

$$- \sum_{j=1}^{n_e} V_0^{e(j)} S^{(j)} \frac{\partial E^{(j)}}{\partial c^{(i)}} \sum_{k=1}^{n_p} \phi^{(k,j)} \gamma^{U(k)} - f^{v(i)} + \dot{m}^{(i)} \dot{c}^{(i)} + f^{ext(i)} \quad (2.68)$$

$$q^{U(i)} = \gamma^{U(i)} \quad (2.69)$$

$$q^{m(i)} = - \left(u^{(i)} + \frac{P^{(i)}}{\rho^{(i)}} + h_{dec} \right) \gamma^{U(i)} + h^{ext(i)} - \dot{c}^{(i)2} + \gamma^{m(i)} \quad (2.70)$$

Substituting the above into the degenerate Hamilton's equations, the Lagrange multipliers can then be solved for in closed form:

$$\gamma^{U(i)} = 1 \quad (2.71)$$

$$\gamma^{m(i)} = u^{(i)} + \frac{P^{(i)}}{\rho^{(i)}} + h_{dec}^{(i)} + \frac{1}{2} \dot{c}^{(i)2} - h^{ext(i)} \quad (2.72)$$

Now that the Lagrange multipliers are known, the momentum balance equations can be derived as

$$\dot{p}^{(i)} = \frac{1}{2} \sum_{j=1}^{n_p} \left(\frac{m^{(i)} \rho_0^{(i)}}{(2h^{(j)})^2} \frac{P^{(i)}}{\rho^{(i)2}} \frac{W^{(i,j)}}{\zeta^{(i,j)3}} + \frac{m^{(j)} \rho_0^{(j)}}{(2h^{(i)})^2} \frac{P^{(j)}}{\rho^{(j)2}} \frac{W^{(j,i)}}{\zeta^{(j,i)3}} \right) \left(c^{(i)} - c^{(j)} \right)$$
$$- \sum_{j=1}^{n_e} V_0^{e(j)} S^{(j)} \frac{\partial E^{(j)}}{\partial c^{(i)}} - f^{v(i)} + \dot{m}^{(i)} \dot{c}^{(i)} + f^{ext(i)} \quad (2.73)$$

$$\dot{c}^{(i)} = \frac{p^{(i)}}{m^{(i)}} \quad (2.74)$$

which combined with the evolution equations for the internal state variables constitute the system level equations.

2.8 Ablation Simulations

The simulations presented in this section proceed first with a verification of the proper implementation of the mesoscale code, followed by validation

simulations. After model validation, ablation simulations of three materials are presented for incorporation into the macroscale model: a high and low density carbon phenolic material and a carbon cyanate ester material. The one-dimensional mesoscale program has a relatively low computational cost and runs comfortably on a single thread, although the program also supports OpenMP parallelization. A plot of run time versus thread count is shown in Figure 2.6 for the ablation simulation of carbon reinforced phenolic presented in section 2.8.1.

The first simulation verifies the proper implementation of the mesoscale code by comparison with a wall shock problem for an inert material. Validation of the hybrid particle element method in 1-D with test problems with known exact solutions has been done in previous work [100, 124]. Park et al. [124] verified the method for the wall shock problem of Noh [122] consisting of a fluid stream colliding with a rigid wall, and for the bar impact problem of Kolsky [88] consisting of an elastic bar subject to a sudden tensile pressure. Verification is performed here for a 5 km/s wall shock problem to ensure proper implementation of the code. For the verification simulation, the material is assumed to have a composite density of 1450 kg/m^3 and a fiber and resin mass fractions of 0.625 and 0.375 respectively. The fiber and resin Mie-Grüneisen equations of state parameters are those of carbon fiber (Table 2.5) and phenolic resin (Table 2.3). The simulation results are in good agreement with the exact solution obtained from solving the Rankine-Hugoniot equations (Figure 2.5).

The second simulation presents validation with published experimental

data by Ladacki et al. [98] on the heat of pyrolysis of phenolic in a silica fiber reinforced phenolic composite with 1790 kg/m^3 composite density and 0.3 resin weight loading. The authors measured the heat of pyrolysis by measuring the standard (298 K) heat of formation of the virgin and charred composite by bomb calorimetry, where the charred material was prepared by heating in a nitrogen environment. The composition of the pyrolytic volatiles was measured by mass spectrometry and used to calculate the heat of formation for the pyrolysis gas. The heat of pyrolysis H_{py} was then calculated as

$$f_r H_{py} = f_{vol} H_f \text{ volatiles} + (1 - f_{vol}) H_f \text{ char} - H_f \text{ resin} \tag{2.75}$$

which assumes the following decomposition representation

$$\text{virgin} \rightarrow f_{vol} \text{ volatiles} + (1 - f_{vol}) \text{ char} \tag{2.76}$$

where f_r is the resin composite mass fraction, f_{vol} the fraction of the composite mass lost in the form of pyrolytic volatiles, and H_f denotes heat of formation. It is noted that while the authors express the heat of pyrolysis H_{py} as per unit mass of resin, all experiments were conducted on the composite material. For measuring the heat of formation in Ref [98], a sample was first sealed in a fixed volume container (called a bomb) and then burned in a pure oxygen environment. Measured quantities were the heat of reaction, calculated from the temperature change of the bomb, and the combustion products water and carbon dioxide. A heat of formation of the sample H_f(sample) was then calculated as [98]:

$$H_f(\text{sample}) = H_f(CO_2) + H_f(H_2O) - H_f(O_2) - H_c \tag{2.77}$$

where H_c is the measured heat of reaction. This method was used to measure the heat of formation of the virgin and char composites. The silica fiber was present in all the bomb calorimetry experiments and was assumed to be chemically inert. The composite properties and experimental results in Ref [98] are summarized in Table 2.2.

Reflective of the charred material being produced by heating in an inert environment, comparison with the experimental results is made using the chemical kinetics for phenolic pyrolysis in vacuum. In Ref [162], the disassociation chemistry for phenolic pyrolysis in vacuum consists of a single reaction:

$$\begin{aligned} C_6H_6O \rightarrow 5.225H + 5C + 0.9O+ \\ 0.1C_2 + 0.625CH + 0.1CO + 0.075CH_2 \end{aligned} \tag{2.78}$$

The recombination reactions consist of four reactions:

$$\begin{aligned} C + O \rightarrow CO \\ 2C \rightarrow C_2 \\ H + C \rightarrow CH \\ H + CH \rightarrow CH_2 \end{aligned} \tag{2.79}$$

All of the chemistry model parameters, including the reaction rate constants $k^{(j)}$, rate exponents $\alpha^{(i,j)}$, temperature functions $f^{(j)}$, and stoichiometric coefficients $\nu^{(i,j)}$ and $\hat{\nu}^{(i,j)}$ for the disassociation and recombination reactions, are provided in Tables 2.25 to 2.33. The material properties for phenolic resin

and silica fiber used in the mesoscale model and their associated experimental references are provided in Table 2.3 and Table 2.6.

Simulation results are compared to the experimental value for the heat of pyrolysis [98]. The mesoscale model computes a heat of pyrolysis as the total energy input into the system Q divided by the total mass lost from the system M.

$$H_{py} = \frac{Q}{M}, \quad \dot{Q} = \sum_{i=1}^{n_p} \dot{U}^{inp(i)}, \quad \dot{M} = \sum_{i=1}^{n_p} \dot{m}^{(i)} \tag{2.80}$$

Figure 2.7 shows the mesoscale simulation results. The plot shows good agreement between simulation (1.72 MJ/kg) and experiment (1.73 MJ/kg). The particle density, particle reaction progress, particle internal energy, particle pressure, element accumulated plastic strain, element damage, and element stress are shown in Figures 2.7 to 2.10.

Since the particle heating produces mechanical waves which may reflect off the back wall and interact with the pyrolysis front, the simulation domain is enlarged with a buffer region. To reduce computational cost, larger particles are employed in the buffer region resulting in a coarser particle resolution in the buffer. Figure 2.12 show the particle diameters versus particle position and particle index. The domain consists of two regions with uniform particle diameters: a high resolution region, and a low resolution region. The high resolution region is joined to the low resolution region by a graded segment, where the diameter of each successive particle is increased by a constant factor. A factor of 1.1 was employed for all simulations in this thesis. Figure 2.13

shows a comparison of the element stress and particle compression profiles in the high resolution region with and without particle grading in the buffer. In the case without particle grading, a high particle resolution is employed for the entire domain. For the case with particle grading, the particle diameter differs by a factor of a hundred between the high and low resolution regions, reducing the number of particles in the buffer region by a factor of seventy. Negligible difference is observed in the simulation results, indicating that the particle grading does not result in any reflection of mechanical waves.

As described in section 2.5, the heating of the particles is modulated by the reaction progress and approximates a spacially exponentially decaying heating profile which follows the reaction front. The heat input formulation has two adjustable parameters: a heating rate, and heating depth (see equations (2.31) and (2.32)). It is of interest as to whether these parameters affect the heat of pyrolysis computed by the mesoscale simulation as a dependence on these parameters would introduce artifacts in the mesoscale simulation results. For a factor of four difference in both the heating depth and total system heating rate, the heat of pyrolysis has minimal change, as shown in Table 2.1. Convergence with respect to particle count is shown in Figure 2.11. The simulation is observed to show good numerical convergence.

2.8.1 Ablation Simulation for a Carbon Fiber Reinforced Phenolic Composite

This section presents the simulation of resin pyrolysis in a carbon reinforced phenolic composite with a resin weight loading of 0.375 and composite density of 1450 kg/m^3. The purpose of this simulation is to compute a resin heat of pyrolysis in the resin fiber composite for input into a macroscale model. The composite parameters are representative of the material tested by Pesci et al. [125], who conducted experimental plasma torch ablation testing of a carbon fiber reinforced phenolic composite under various heat fluxes and exposure times (see Appendix A). Reflective of the experimental environment, the chemical kinetics for phenolic pyrolysis in air is used. In Ref [162], the dissociation chemistry for phenolic pyrolysis in air consists of a single reaction:

$$C_6H_6O + 24N_2 + 7O_2 \rightarrow \tag{2.81}$$
$$5.833H + 4.833C + 48N + 13.5O + 0.167OH + CO + 0.167CO_2$$

The recombination reactions consist of five reactions:

$$2N \rightarrow N_2$$
$$OH + H \rightarrow H_2O$$
$$O + H \rightarrow OH$$
$$C + O \rightarrow CO$$
$$CO + O \rightarrow CO_2 \tag{2.82}$$

All of the chemistry model parameters, including the reaction rate constants $k^{(j)}$, rate exponents $\alpha^{(i,j)}$, temperature functions $f^{(j)}$, and stoichiometric coef-

ficients $\nu^{(i,j)}$ and $\hat{\nu}^{(i,j)}$ for the disassociation and recombination reactions, are provided in Tables 2.25 to 2.33. The material properties for phenolic resin and carbon fiber used in the mesoscale model along with their associated experimental references are provided in Table 2.3 and Table 2.5. Figure 2.14 shows the mesoscale simulation results for the heat of pyrolysis, having a value of 1.42 MJ/kg. The particle density, particle reaction progress, particle internal energy, particle pressure, element accumulated plastic strain, element damage, and element stress are shown in Figures 2.14 to 2.17.

Mesoscale simulations were also conducted for pyrolysis in vacuum. The chemistry model for phenolic pyrolysis in vacuum is described in section 2.8 and listed in Tables 2.25 to 2.33. The particle density, particle reaction progress, particle internal energy, particle pressure, element accumulated plastic strain, element damage, and element stress are shown in Figures 2.27 to 2.30. The simulation results have minimal difference from the air case.

2.8.2 Ablation Simulation for PICA (Phenolic Impregnated Carbon Ablator)

This section presents the simulation of resin pyrolysis in a high porosity carbon fiber reinforced phenolic composite with a resin weight loading of 0.38 and composite density of 274 kg/m^3. The purpose of this simulation, similar to the preceding section, is to compute a resin heat of pyrolysis in the resin fiber composite for input into a macroscale model. The composite parameters are representative of the material called PICA, a light weight material that was

first used as the forebody heat shield on the Stardust Sample Return Capsule [147], the Mars Science Lander, and most recently on the Mars Perseverance rover in 2020 [117]. Available experimental data on PICA is described in a series of arc-jet tests done by Tran et al. [158], who conducted arc-jet testing of PICA in air under various heat fluxes and exposure times with varying sample geometries (see Appendix B). The mesoscale simulation results for resin pyrolysis in air for PICA is shown in Figures 2.18 to 2.21.

The heat of pyrolysis for PICA computed from the mesoscale simulation results is 1.41 MJ/kg, which is similar to the fully dense carbon phenolic composite described in the preceding section. The fully dense material and PICA are similar in terms of composite constituents and resin weight loading. They differ in their fiber architecture, which is discussed in greater detail in the macroscale model, and in their composite porosity. The fully dense material supports significantly higher stresses than the high porosity PICA as shown in Figures 2.17 and 2.21. However, the difference in porosity is observed to have little effect on the heat of pyrolysis in the mesoscale simulation, with both materials having a heat of pyrolysis of about 1.4 MJ/kg.

Mesoscale simulations were also conducted for PICA in vacuum (Figures Figures 2.31 to 2.34). Similar to the fully dense material described in the preceding section, minimal difference is observed between the air and no air cases.

2.8.3 Ablation Simulation for a Carbon Fiber Reinforced Cyanate Ester Composite

This section presents the simulation of resin pyrolysis in a carbon fiber reinforced cyanate ester composite with a resin weight loading of 0.114 and composite density of 1710 kg/m^3. The purpose of this simulation, like the preceding sections, is to compute a resin heat of pyrolysis in the resin fiber composite for input into a macroscale model. The composite parameters are representative of the material tested by Nahar [119], who conducted oxyacetylene torch ablation tests of a carbon reinforced cyanate ester material on an oxyacetylene test bed (OTB) (see Appendix C).

Reflective of the experimental environment, the chemical kinetics for cyanate ester pyrolysis in air is used. In Ref [162], the disassociation chemistry for cyanate ester pyrolysis is modeled as a single reaction:

$$C_{17}H_{14}N_2O_2 + 61.5N_2 + 19.5O_2 \rightarrow \tag{2.83}$$
$$13.5H + 13.5C + 125.0N + 36.5O + 0.5OH + 3.0CO + 0.5CO_2$$

The recombination reactions consist of five reactions, identical to those for phenolic pyrolysis in air:

$$2N \rightarrow N_2 \tag{2.84}$$

$$OH + H \rightarrow H_2O \tag{2.85}$$

$$O + H \rightarrow OH \tag{2.86}$$

$$C + O \rightarrow CO \tag{2.87}$$

$$CO + O \rightarrow CO_2 \tag{2.88}$$

All of the chemistry model parameters, including the reaction rate constants $k^{(j)}$, rate exponents $\alpha^{(i,j)}$, temperature functions $f^{(j)}$, and stoichiometric coefficients $\nu^{(i,j)}$ and $\hat{\nu}^{(i,j)}$ for the disassociation and recombination reactions are provided in Tables 2.16 to 2.24. The material properties for cyanate ester and carbon fiber used in the mesoscale model along with the associated experimental references are provided in Table 2.4 and Table 2.5. Figures 2.22 to 2.25 shows the mesoscale simulation results. The heat of pyrolysis is 4.32 MJ/kg,which is higher than the carbon phenolic materials in the preceding sections, which were around 1.4 MJ/kg. It is noted that the cyanate ester material has a very small resin weight loading of 0.114. A significant portion of the energy input into the material is thus spent heating carbon with relatively little mass being lost due to the small resin weight loading.

For comparison of phenolic to cyanate ester, a simulation was conducted with a 0.38 resin mass fraction, similar to the resin mass fraction of the carbon phenolic composites presented in the preceding sections (sections 2.8.1 and 2.8.2), which yields a heat of pyrolysis of 1.33 MJ/kg (Figure 2.26). This is slightly lower than the carbon phenolic composites, which are around 1.4 MJ/kg. In terms of resin properties, cyanate ester has a higher pyrolysis temperature (700 K [119]) than phenolic (500 K [98]) which results in a higher ignition internal energy for the pyrolysis reactions. This, however, is off balanced by the fact that cyanate ester decomposes exothermically (-47 kJ/kg [35, 103]) in comparison to phenolic which decomposes endothermically (293 kJ/kg [151]). The mesoscale model predicts cyanate ester to have a slightly

lower heat of pyrolysis H_{py} in comparison to phenolic at a similar composite resin mass fraction.

Mesoscale simulations were also conducted for pyrolysis in vacuum. In Ref [162], the disassociation chemistry for cyanate ester pyrolysis in vacuum is

$$C_{17}H_{14}N_2O_2 \rightarrow 12.375H + 13C + 1.75N + 1.75O + \\ 1.0625C_2 + 0.125N_2 + 1.625CH + 0.25CO \tag{2.89}$$

The recombination reactions are:

$$C + O \rightarrow CO$$
$$2C \rightarrow C_2$$
$$H + C \rightarrow CH$$
$$H + CH \rightarrow CH_2$$
$$2N \rightarrow N_2 \tag{2.90}$$

The chemistry model parameters for cyanate ester pyrolysis in vacuum are listed in Tables 2.34 to 2.42. Similar to the phenolic cases, minimal difference is observed between the air and vacuum simulation cases (Figures 2.35 to 2.38).

2.8.4 Summary

The purpose of the mesoscale model is to compute a resin heat of pyrolysis in a fiber composite for input into the macroscale model. Validation of the model was done by comparison to bomb calorimetry experiments on

silica fiber reinforced phenolic. The inert pyrolysis chemistry model from Ref [162] was used, reflective of the decomposed composite having been prepared in a nitrogen environment. For extension to the macroscale model, simulations of three materials were performed: a fully dense carbon phenolic, a low density carbon phenolic (PICA), and a fully dense carbon cyanate ester material. Reflective of the experimental environments, all simulations employed the pyrolysis in air chemistry models.

Separate from extension to the macroscale model, simulations were also performed for the three materials using the inert environment pyrolysis chemistry models. Minimal difference was observed in comparison to the air cases. This result is comparable to thermogravimetric analysis experiments in literature conducted in air and nitrogen environments in which the main difference observed was the presence of carbon oxidation in air [37, 77]. At lower temperatures ($< 630\ K$) prior to significant carbon mass loss, the total mass loss behaviors were observed to be the same. In regards to the pyrolysis chemistry, Chiantore et al. [37], who identified phenolic pyrolysis volatiles using gas chromatography, noted that the principle pyrolysis volatile products did not differ between a nitrogen and air environment, though the relative amounts varied. The mesoscale simulation assumes the fibers to be chemically inert in computing a resin heat of pyrolysis. Excluding carbon oxidation, existing experimental works suggest that the resin mass loss kinetics have little dependence on the degradation environment, which qualitatively support the mesoscale simulation results.

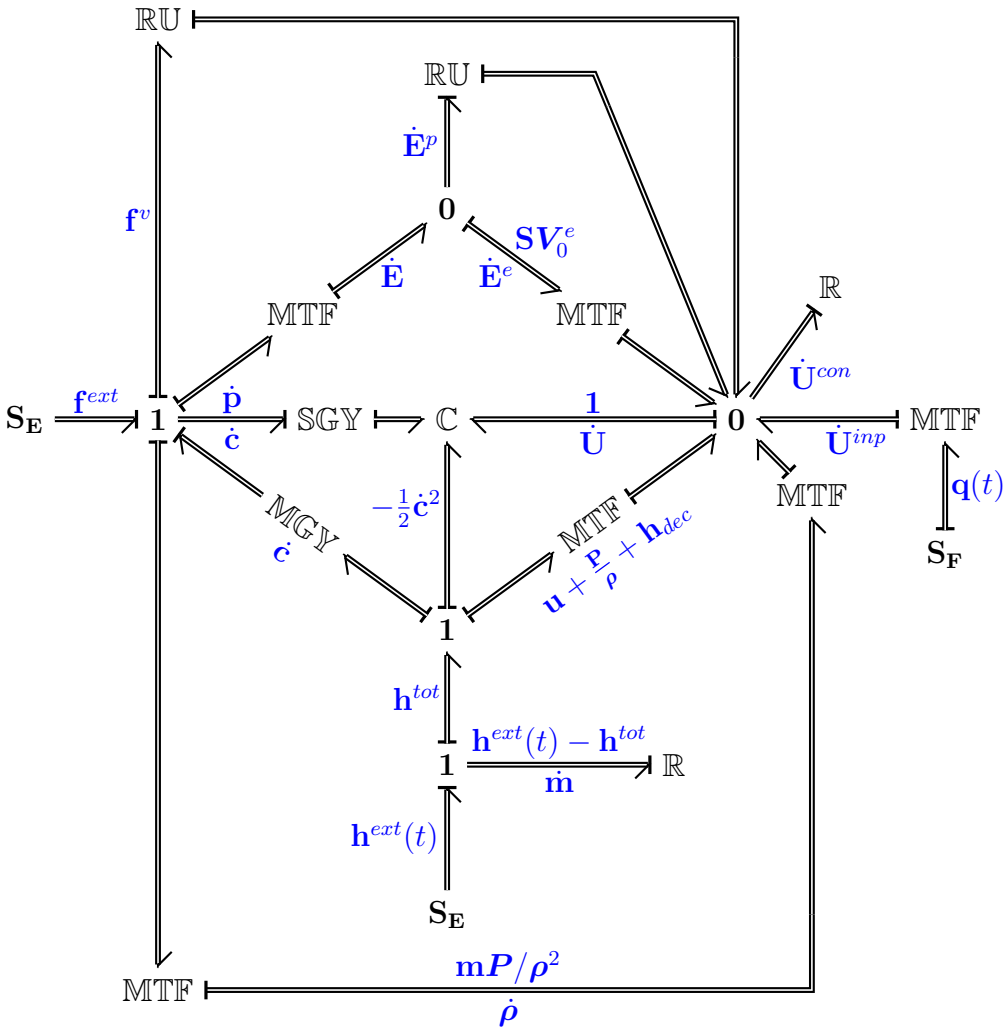

Figure 2.4: Mesoscale model bond graph. The particle internal energies are treated as generalized coordinates where the associated efforts are unity. This has also been employed in previous work by Hean and Fahrenthold [54, 70].

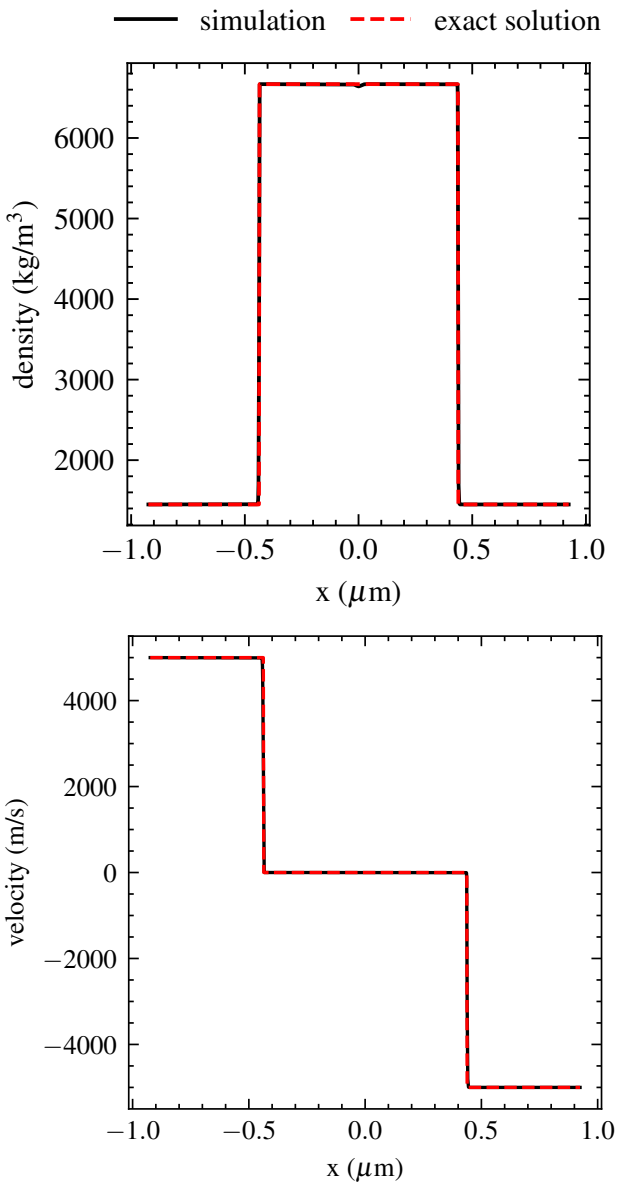

Figure 2.5: Mesoscale simulation of a 5 km/s wall shock at 0.315 ns in an inert carbon fiber reinforced phenolic material with composite density of 1450 kg/m^3 and resin weight loading of 0.375. The dotted lines show the exact solution obtained from solving the Rankine-Hugoniot equations. Validation of the hybrid particle element method in 1-D with wall shock problems has also been done in previous work [100, 124], and is presented here for verification of the mesoscale code implementation.

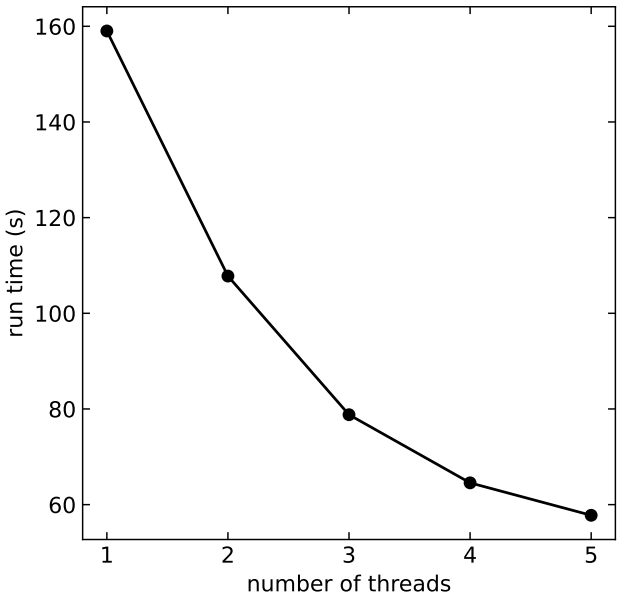

Figure 2.6: Mesoscale program run time versus thread count for the ablation simulation of carbon reinforced phenolic presented in section 2.8.1 (ran with a 900 particle count).

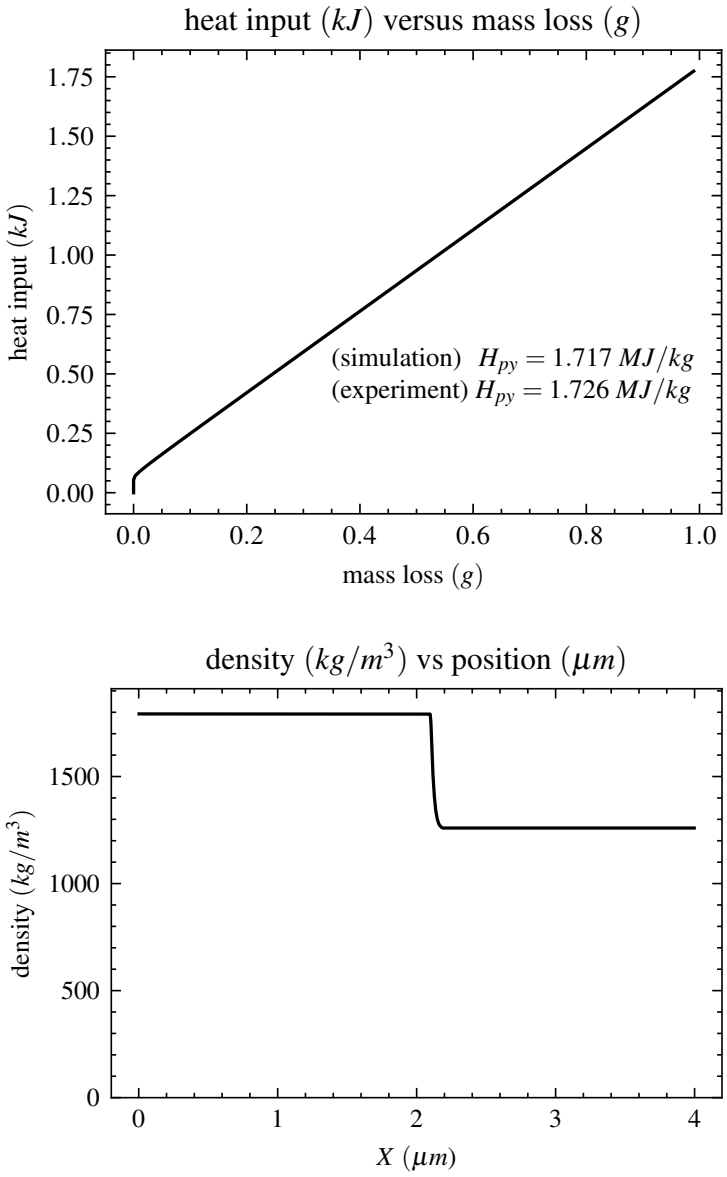

Figure 2.7: Mesoscale simulation of phenolic pyrolysis in vacuum for a silica fiber reinforced phenolic composite with 1790 kg/m^3 composite density and 0.3 resin weight loading, showing the heat input versus mass loss and the density spacial profile at 20 ns. The simulation heat of pyrolysis is computed from the slope of the heat input versus mass loss curve, excluding the region with transient start up effects. The experimental value is from Ref [98].

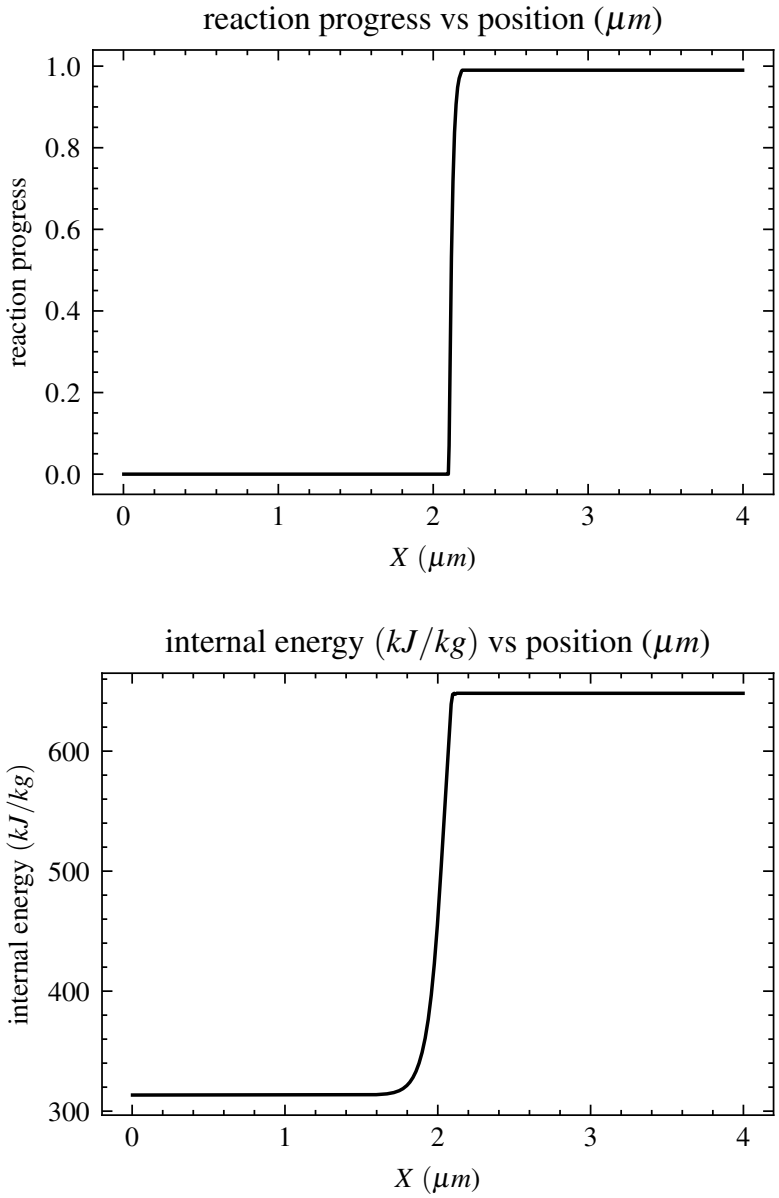

Figure 2.8: Mesoscale simulation of phenolic pyrolysis in vacuum for a silica fiber reinforced phenolic composite with 1790 kg/m^3 composite density and 0.3 resin weight loading, showing the particle reaction progress and particle internal energy profiles at 20 ns.

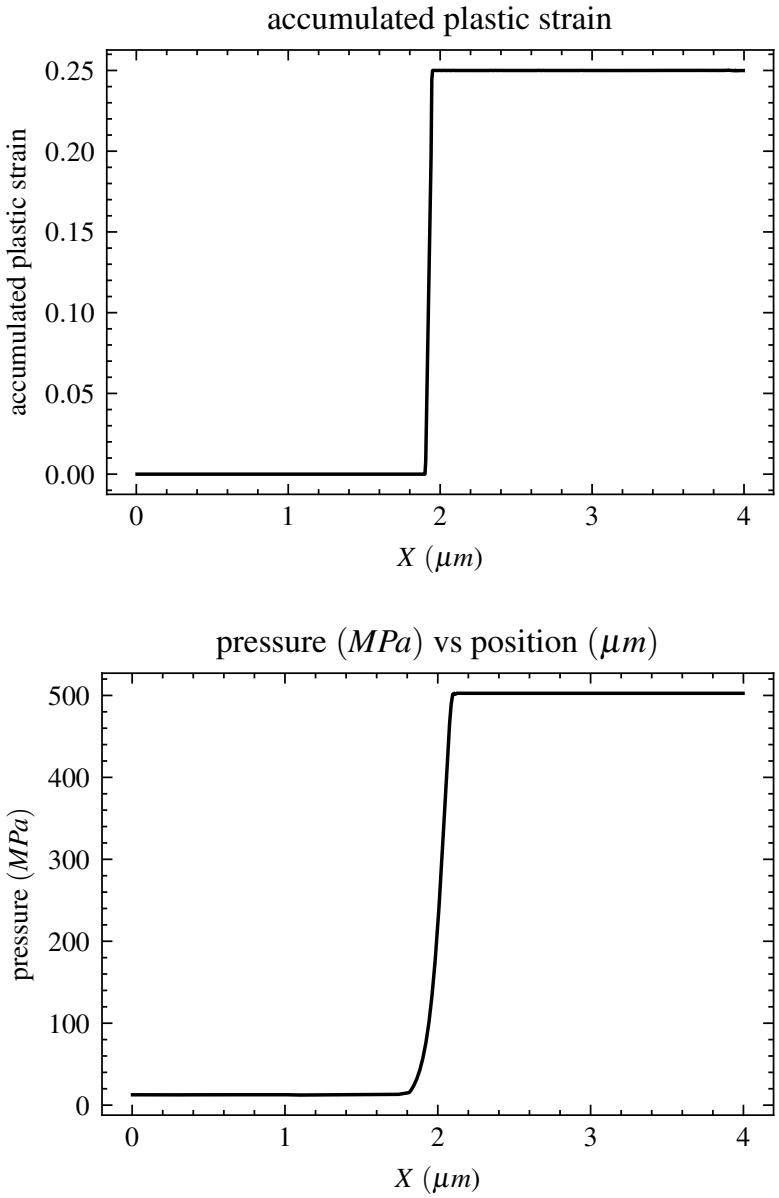

Figure 2.9: Mesoscale simulation of phenolic pyrolysis in vacuum for a silica fiber reinforced phenolic composite with 1790 kg/m^3 composite density and 0.3 resin weight loading at 20 ns, showing the element accumulated plastic strain and particle pressure profiles at 20 ns.

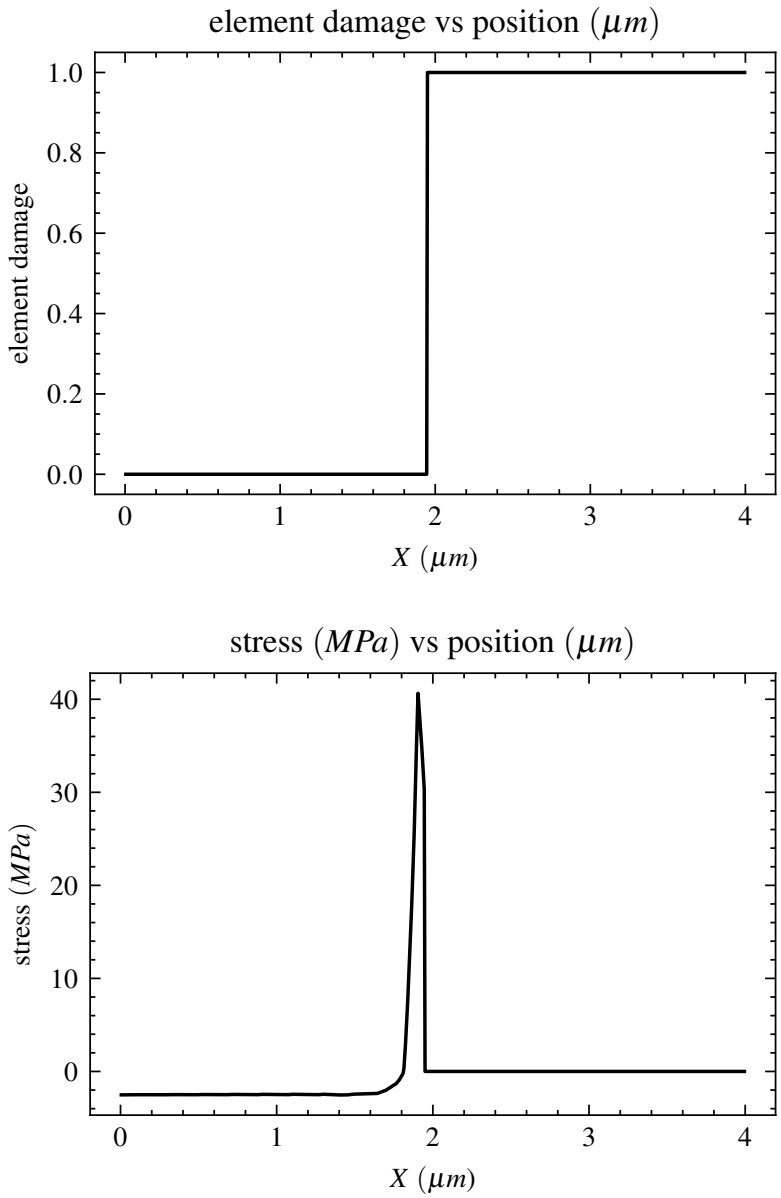

Figure 2.10: Mesoscale simulation of phenolic pyrolysis in vacuum for a silica fiber reinforced phenolic composite with 1790 kg/m^3 composite density and 0.3 resin weight loading, showing the element damage and element stress profiles at 20 ns.

Table 2.1: Heat of pyrolysis H_{py} versus system heating rate and heating depth. The table below shows a set of 16 simulations where the system heating rate and heating depth are both varied by a factor of four.

H_{py} (MJ/kg)	Heating Depth (nm)			
Heating rate (J/ns)	20	40	60	80
22.394	1.703	1.706	1.707	1.708
44.788	1.707	1.709	1.710	1.710
67.182	1.713	1.712	1.711	1.710
89.577	1.716	1.712	1.712	1.713

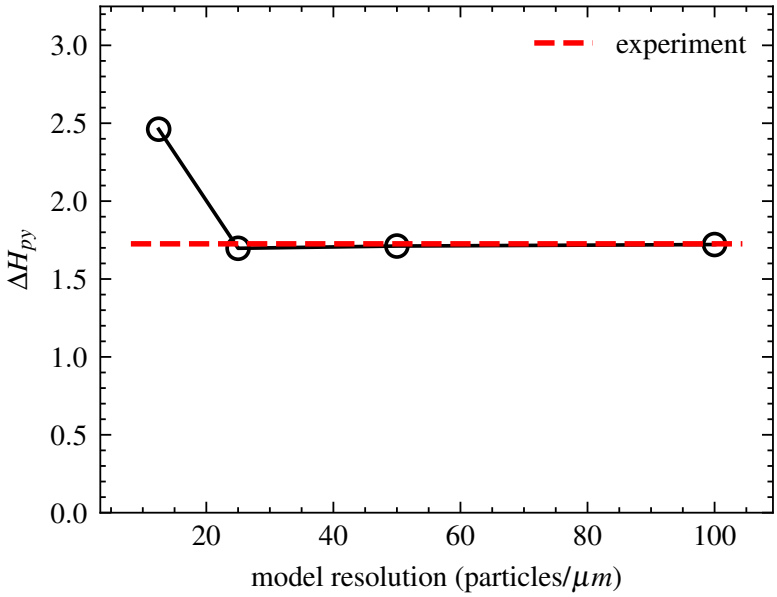

Figure 2.11: Convergence with respect to particle count for a mesoscale simulation of phenolic pyrolysis in vacuum for a silica fiber reinforced phenolic composite with 1790 kg/m^3 composite density and 0.3 resin weight loading, showing the computed H_{py} at 20 ns.

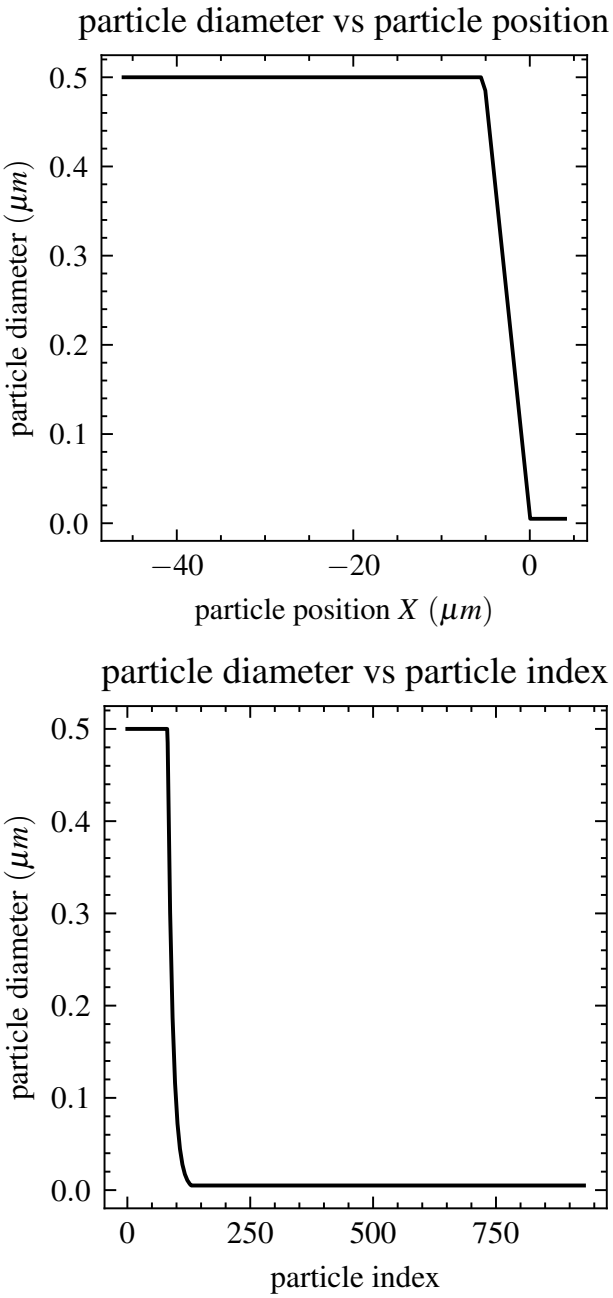

Figure 2.12: Graded mesh employed in the mesoscale simulations. The mesh is split into a course and fine region where the spatial resolutions differ by a factor of a hundred. The regions are joined by a graded region where the particle sizes are gradually changed.

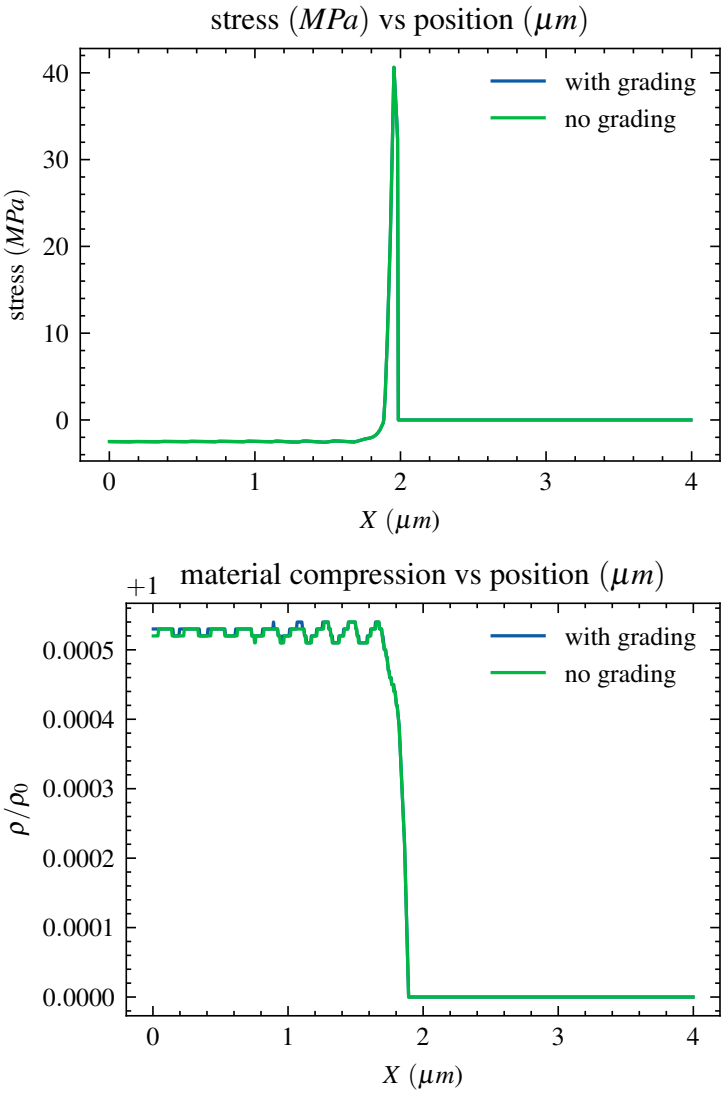

Figure 2.13: Comparison of element stress and particle compression for simulations conducted with and without particle grading in the buffer region. The particle diameters are shown in Figure 2.12. The number of particles in the buffer region differ by a factor of seventy.

Table 2.2: Heat of pyrolysis of phenolic in a silica fiber reinforced phenolic composite (Ladacki et al. 1966 [98]).

composite density ρ_0	1790[a] kg/m^3
composite resin mass fraction f_r	0.30
$(1/f_r)H_f$ char	2.45 MJ/kg
$(1/f_r)H_f$ virgin	-2.44 MJ/kg
$(1/f_r)H_f$ volatiles	-3.97 MJ/kg
H_{py}	1.73 MJ/kg

[a] The authors only report resin weight loading. The density is calculated assuming a composite porosity of zero, in light of the material being a high density material for use in the ablative nozzle extension of the Apollo system.

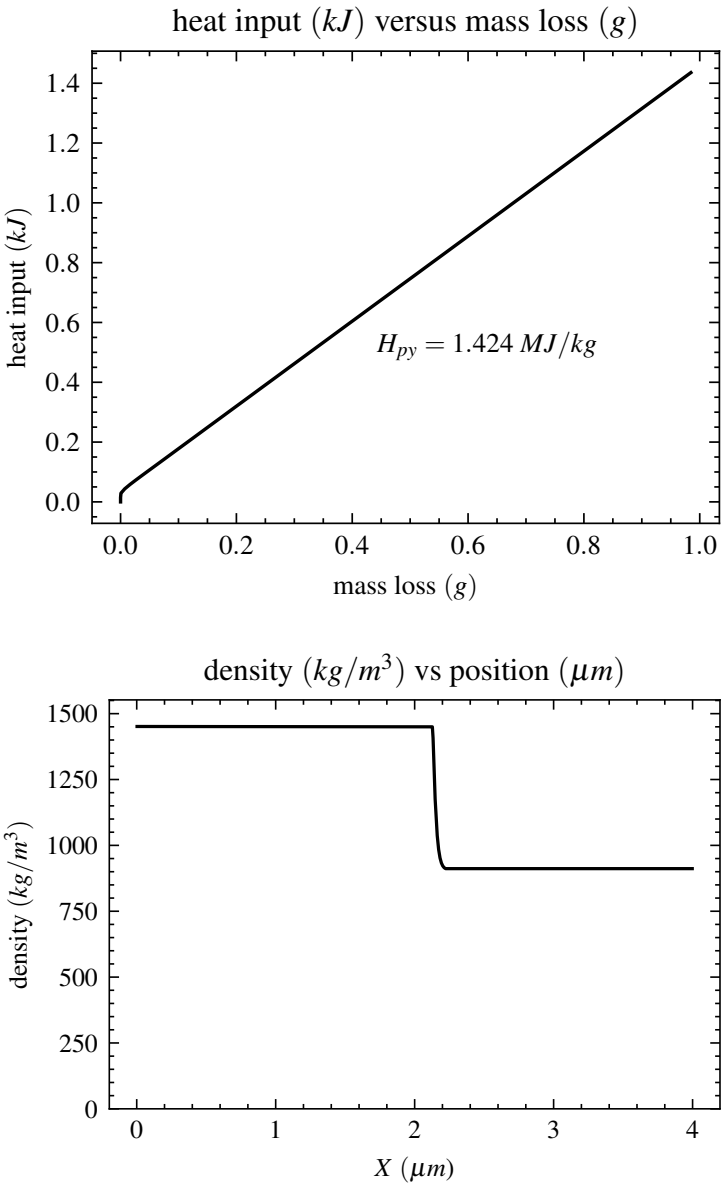

Figure 2.14: Mesoscale simulation of phenolic pyrolysis in air for a carbon fiber reinforced phenolic composite with 1450 kg/m^3 composite density and 0.375 resin weight loading, showing the heat input versus mass loss and the density spacial profile at 20 ns. The simulation heat of pyrolysis is computed from the slope of the heat input versus mass loss curve, excluding the region with transient start up effects.

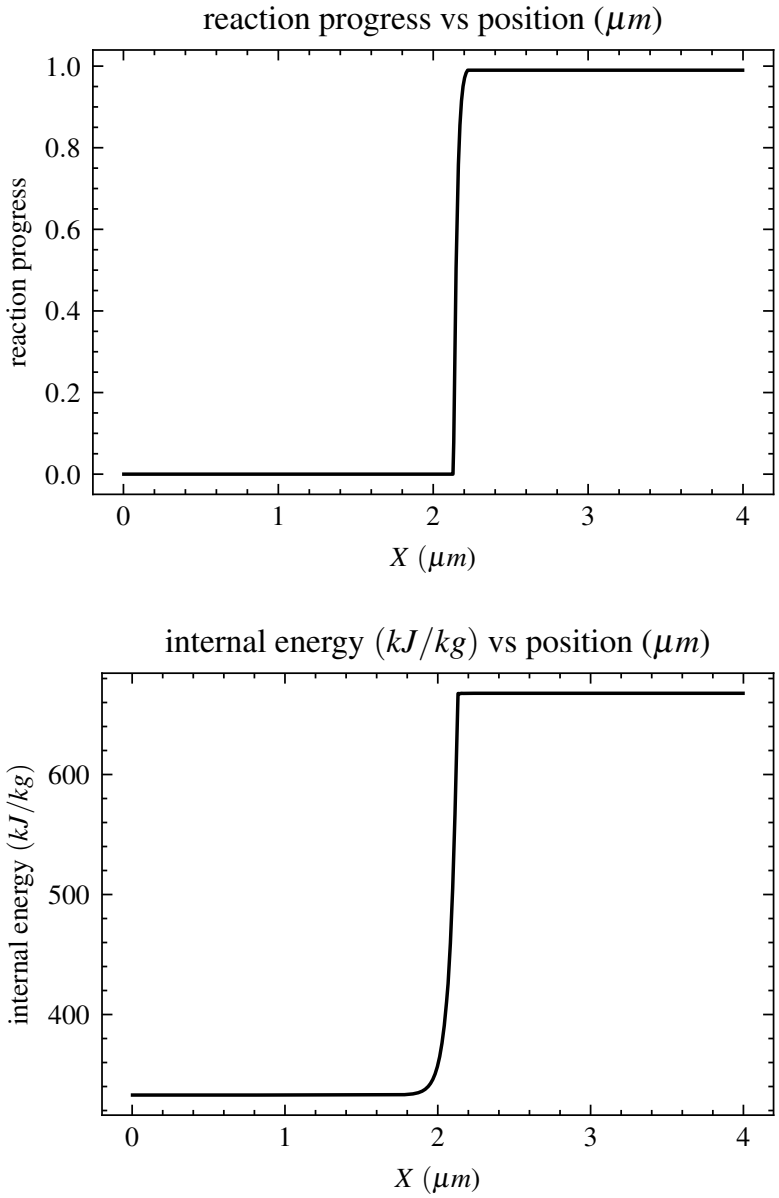

Figure 2.15: Mesoscale simulation of phenolic pyrolysis in air for a carbon fiber reinforced phenolic composite with 1450 kg/m^3 composite density and 0.375 resin weight loading, showing the particle reaction progress and particle internal energy profiles at 20 ns.

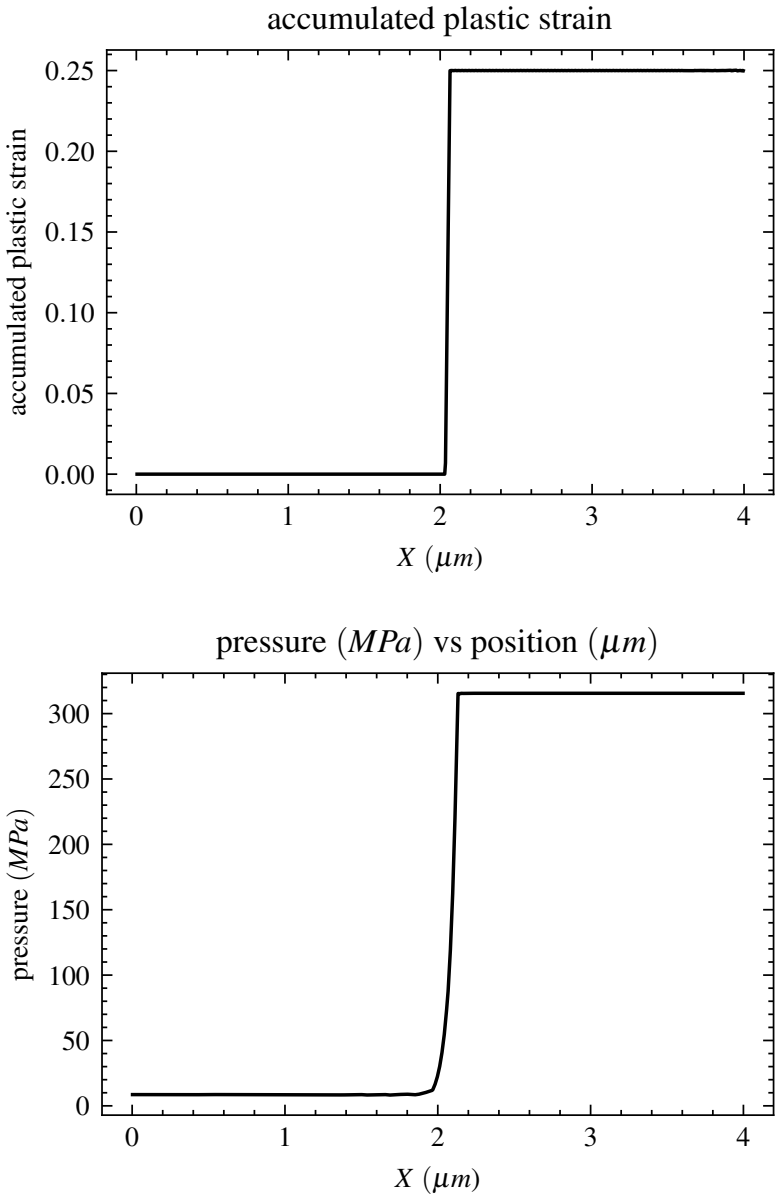

Figure 2.16: Mesoscale simulation of phenolic pyrolysis in air for a carbon fiber reinforced phenolic composite with 1450 kg/m^3 composite density and 0.375 resin weight loading, showing the element accumulated plastic strain and particle pressure profiles at 20 ns.

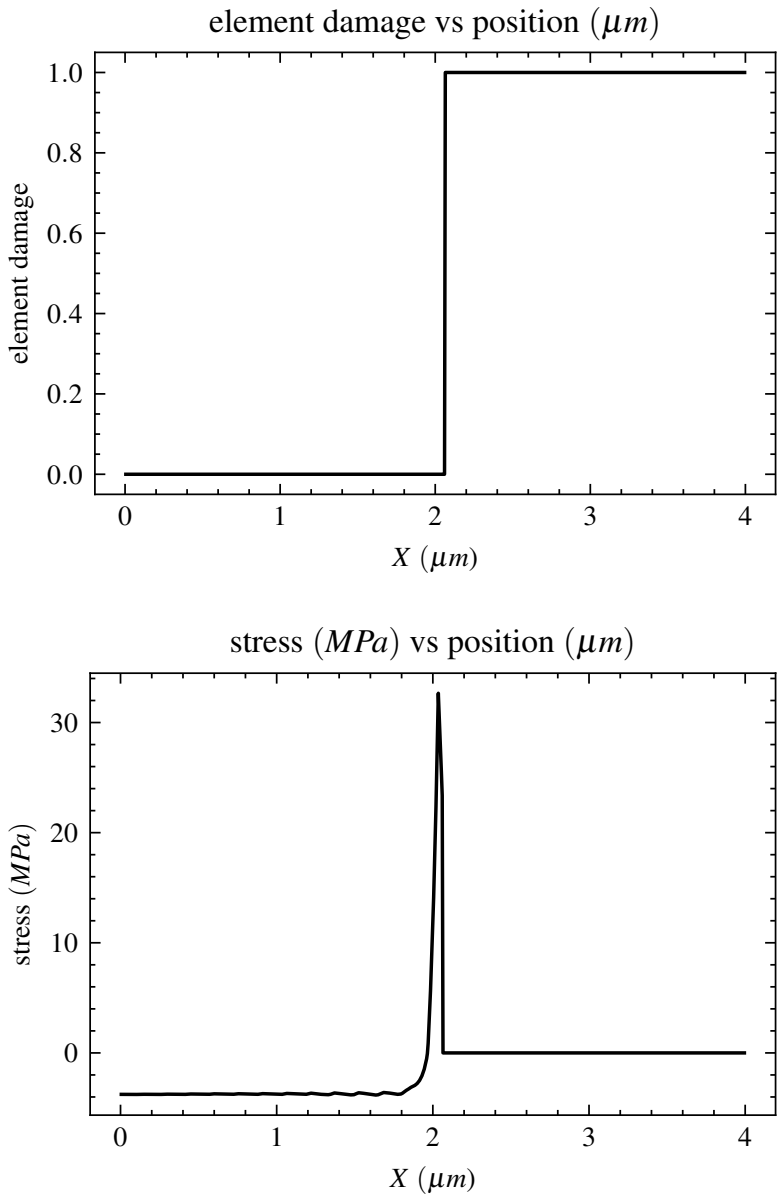

Figure 2.17: Mesoscale simulation of phenolic pyrolysis in air for a carbon fiber reinforced phenolic composite with 1450 kg/m^3 composite density and 0.375 resin weight loading, showing the element damage and element stress profiles at 20 ns.

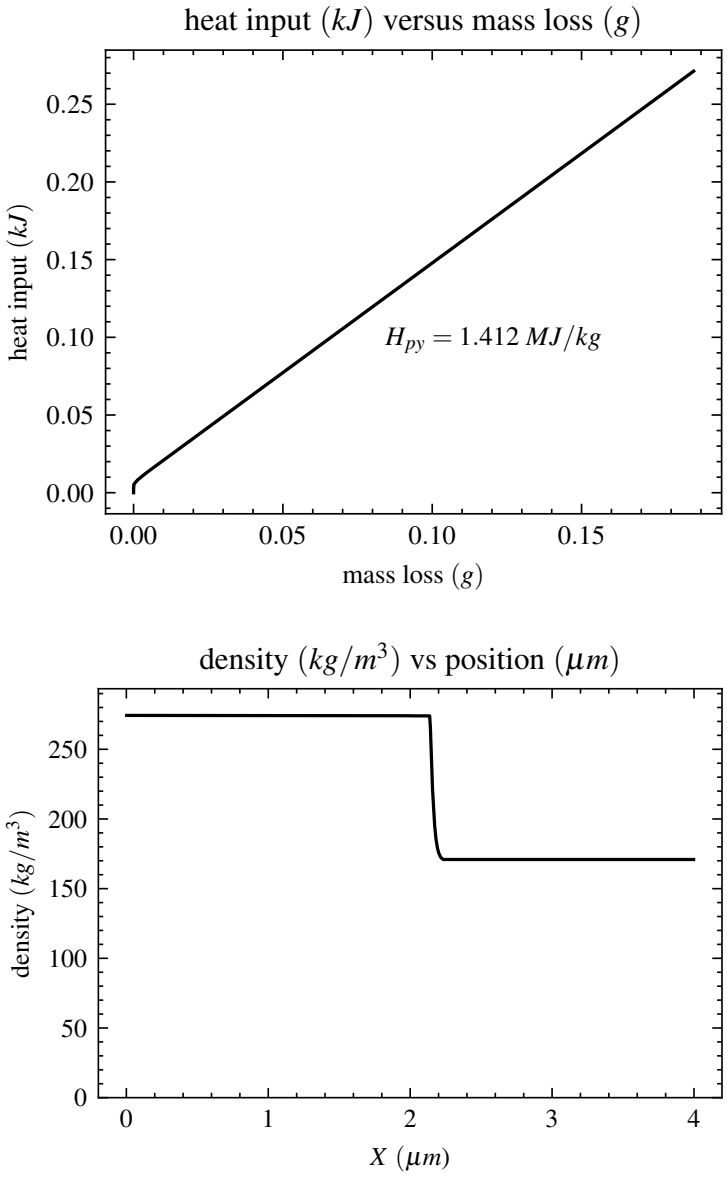

Figure 2.18: Mesoscale simulation of phenolic pyrolysis in air for PICA, showing the heat input versus mass loss and the density spacial profile at 20 ns. The simulation heat of pyrolysis is computed from the slope of the heat input versus mass loss curve, excluding the region with transient start up effects.

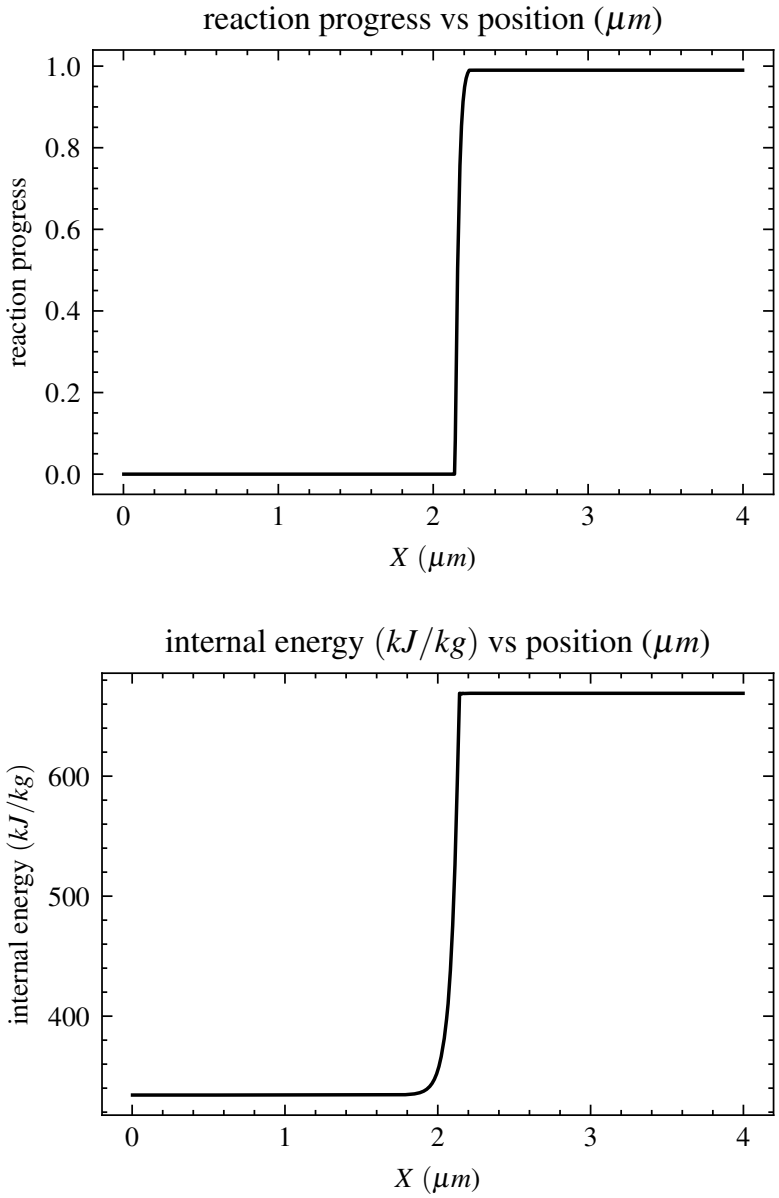

Figure 2.19: Mesoscale simulation of phenolic pyrolysis in air for PICA at 20 ns, showing the particle reaction progress and particle internal energy profiles.

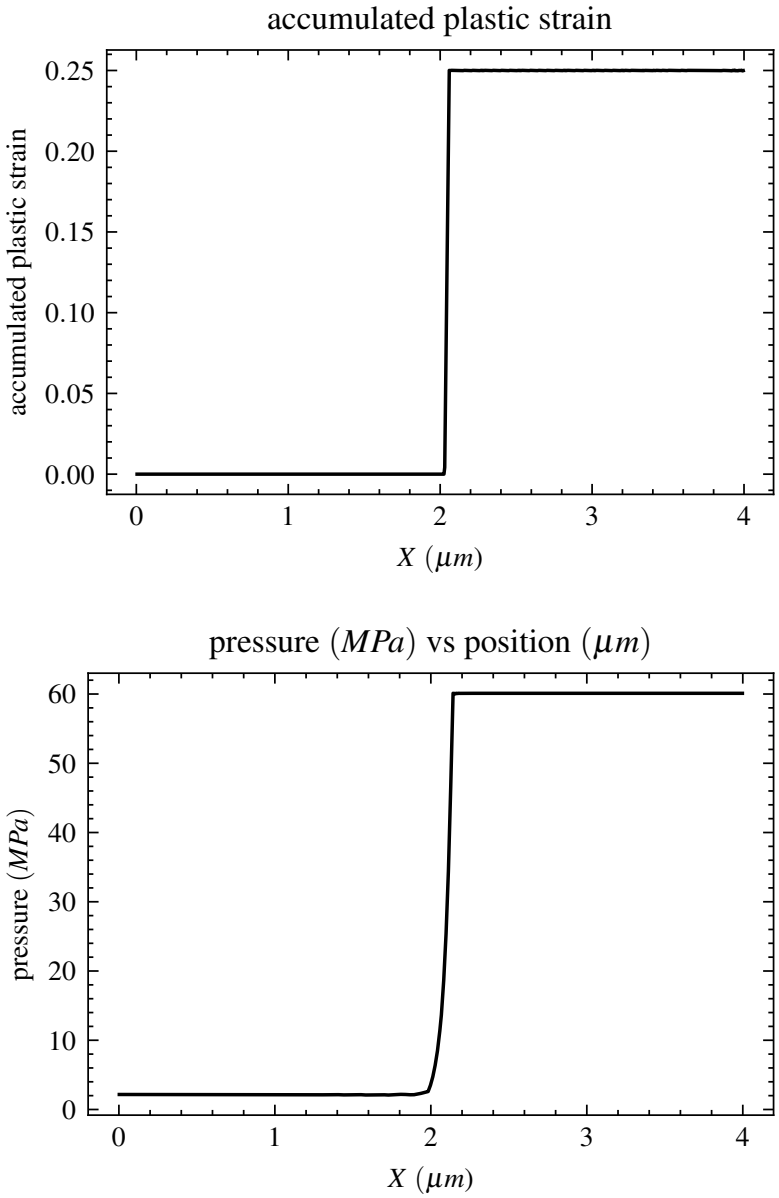

Figure 2.20: Mesoscale simulation of phenolic pyrolysis in air for PICA at 20 ns, showing the element accumulated plastic strain and particle pressure profiles.

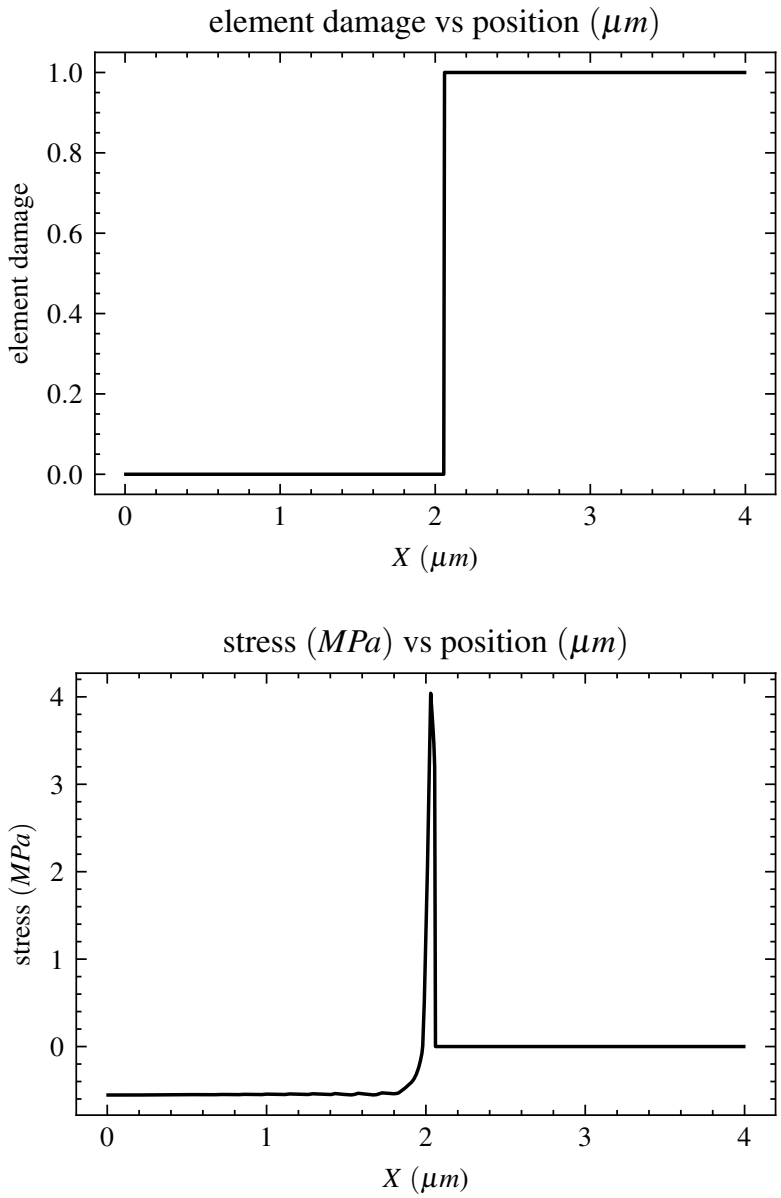

Figure 2.21: Mesoscale simulation of phenolic pyrolysis in air for PICA at 20 ns, showing the element damage and element stress profiles.

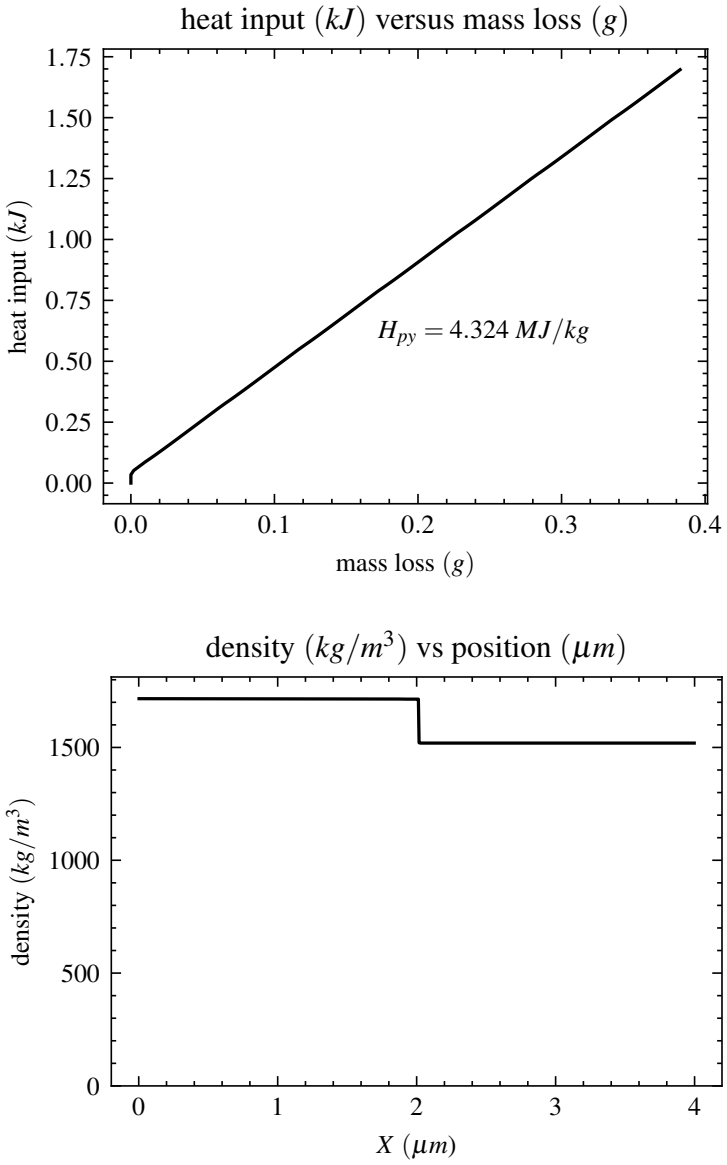

Figure 2.22: Mesoscale simulation of cyanate ester pyrolysis in air for a carbon fiber reinforced cyanate ester composite with 1710 kg/m^3 composite density and 0.114 resin weight loading, showing the heat input versus mass loss and the density spacial profile at 20 ns. The simulation heat of pyrolysis is computed from the slope of the heat input versus mass loss curve, excluding the region with transient start up effects.

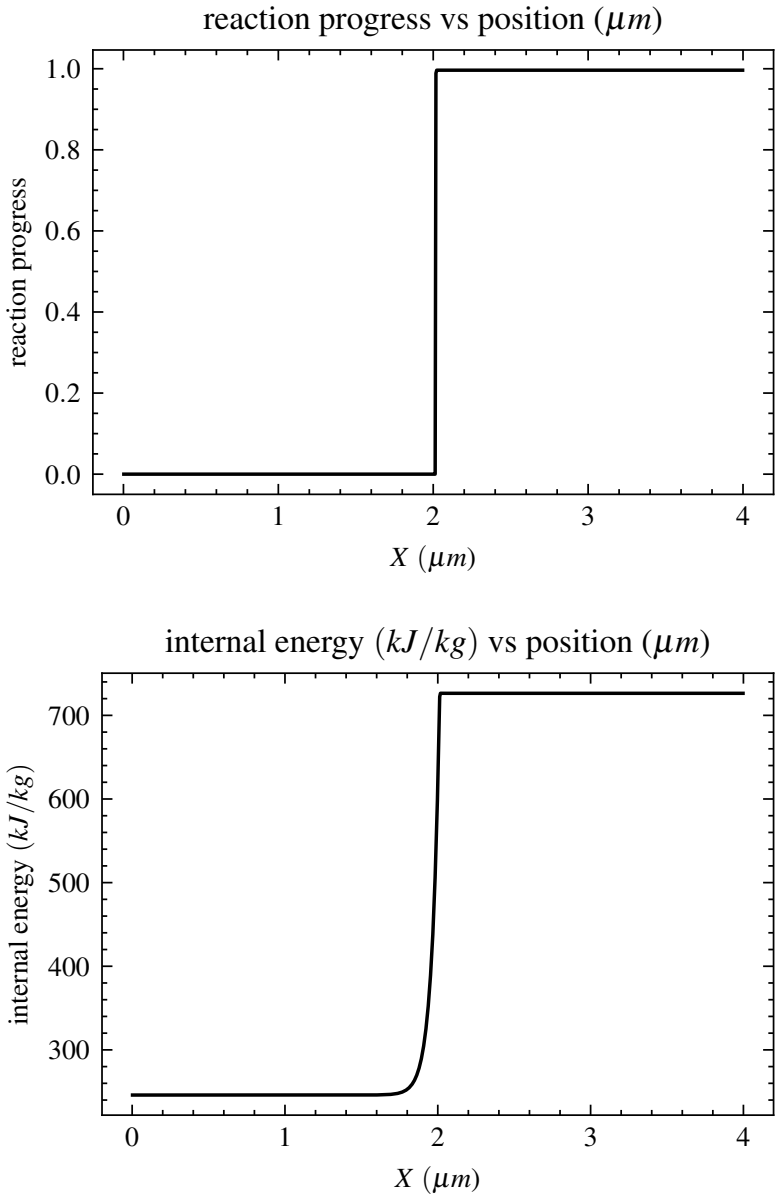

Figure 2.23: Mesoscale simulation of cyanate ester pyrolysis in air for a carbon fiber reinforced cyanate ester composite with 1710 kg/m^3 composite density and 0.114 resin weight loading, showing the particle reaction progress and particle internal energy profiles at 20 ns.

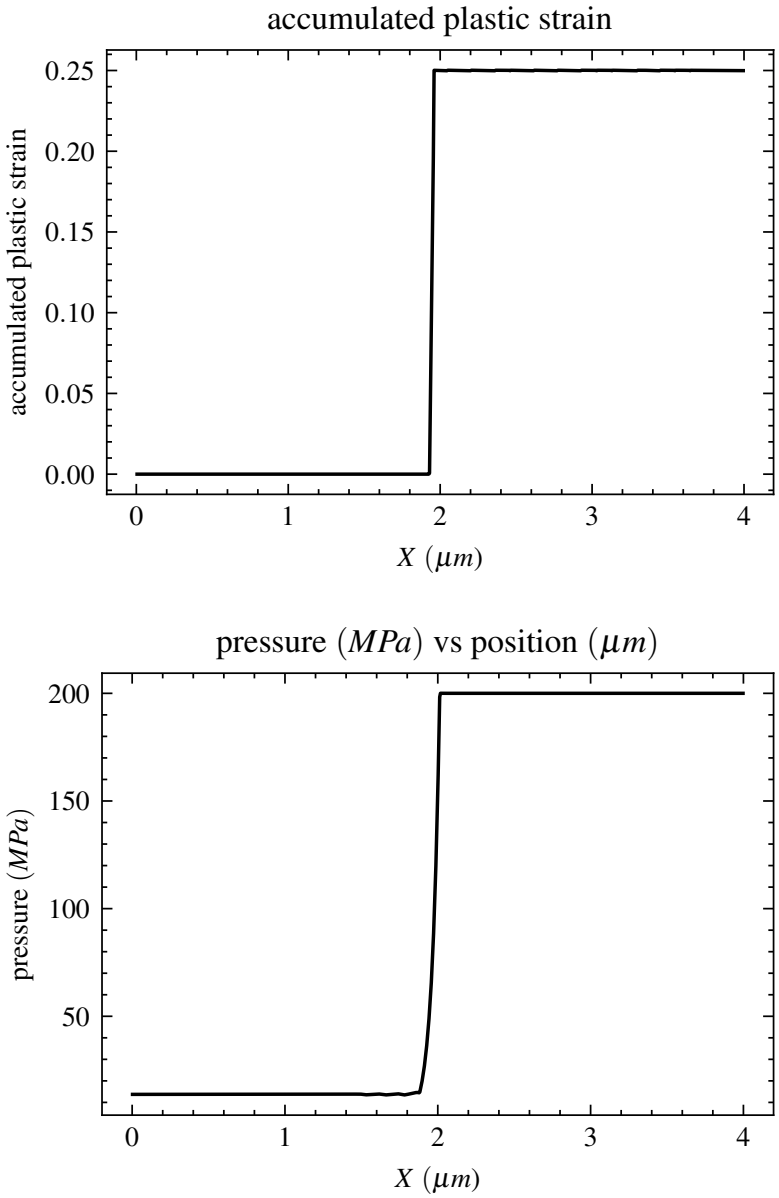

Figure 2.24: Mesoscale simulation of cyanate ester pyrolysis in air for a carbon fiber reinforced cyanate ester composite with 1710 kg/m^3 composite density and 0.114 resin weight loading, showing the element accumulated plastic strain and particle pressure profiles at 20 ns.

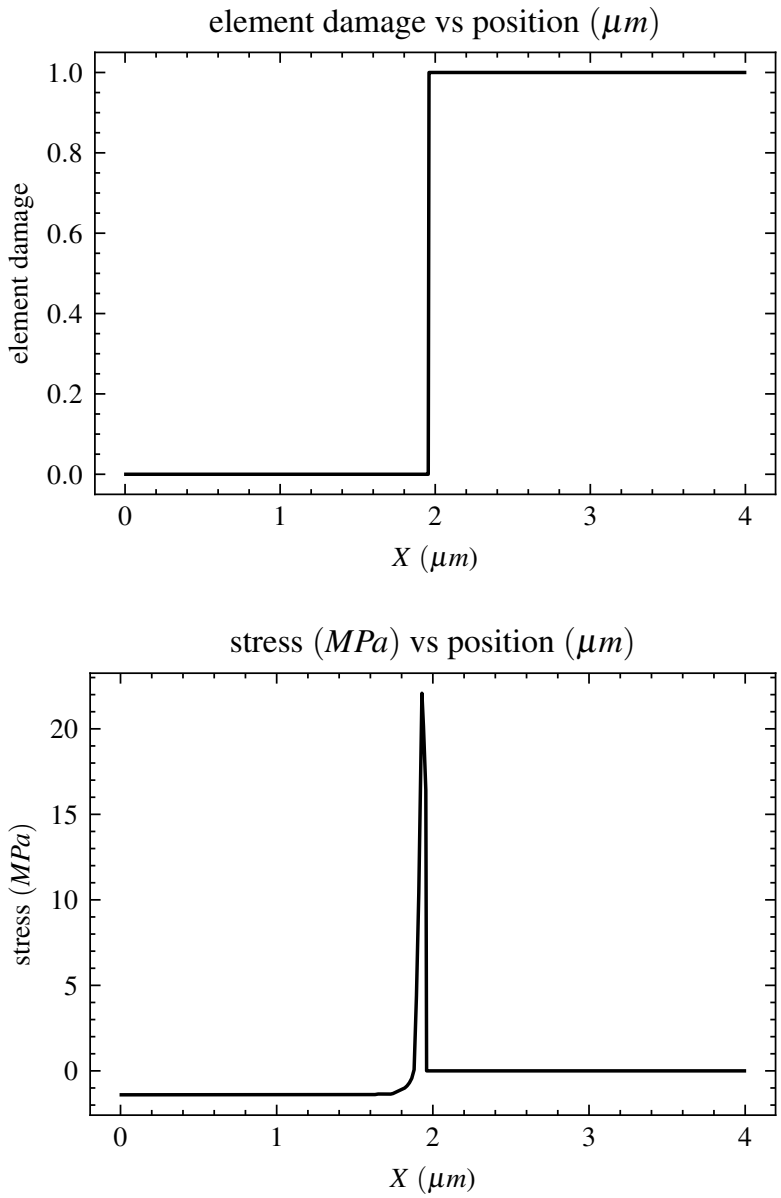

Figure 2.25: Mesoscale simulation of cyanate ester pyrolysis in air for a carbon fiber reinforced cyanate ester composite with 1710 kg/m^3 composite density and 0.114 resin weight loading, showing the element damage and element stress profiles at 20 ns.

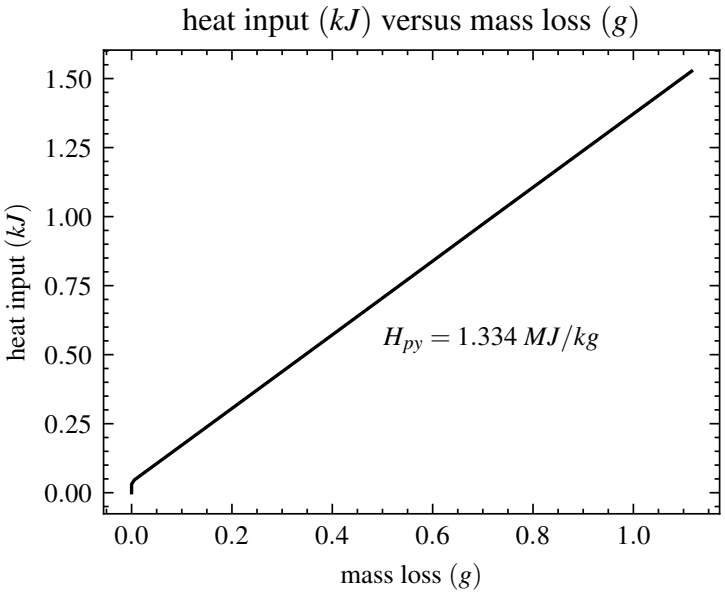

Figure 2.26: Mesoscale simulation of cyanate ester pyrolysis in air for a carbon fiber reinforced cyanate ester composite with 1540 kg/m^3 composite density and 0.38 resin weight loading, showing the heat input versus mass loss and the density spacial profile at 20 ns. The simulation heat of pyrolysis is computed from the slope of the heat input versus mass loss curve, excluding the region with transient start up effects.

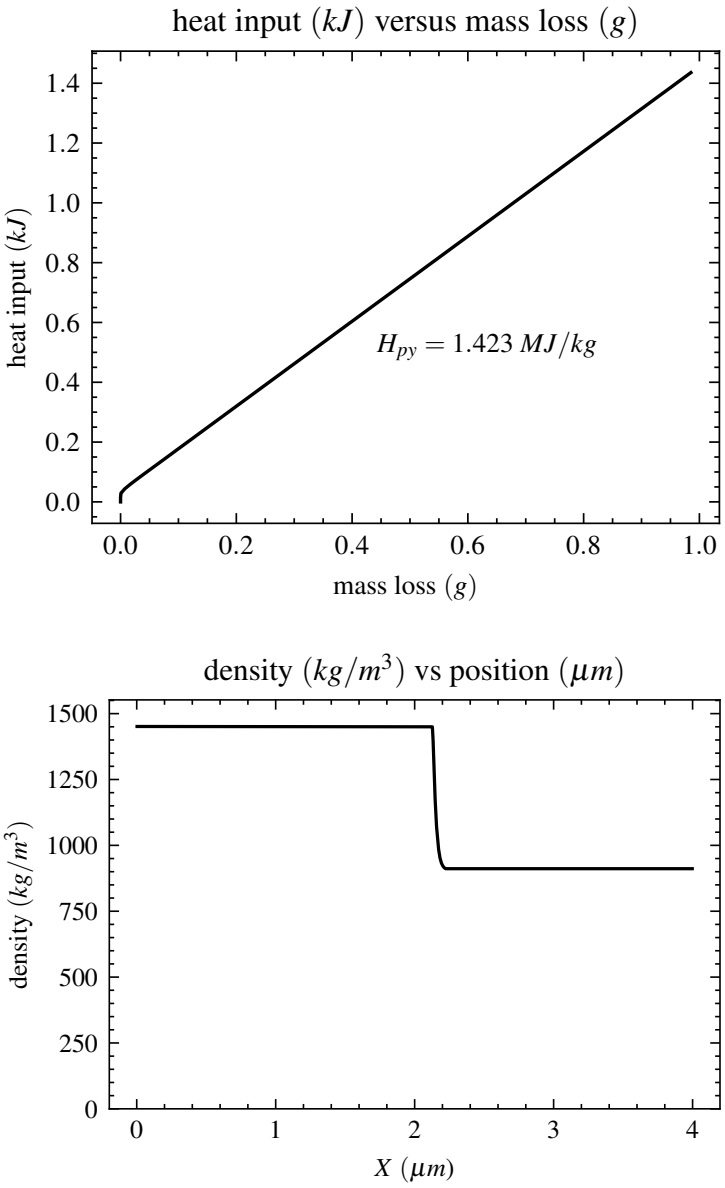

Figure 2.27: Mesoscale simulation of phenolic pyrolysis in vacuum for a carbon fiber reinforced phenolic composite with 1450 kg/m^3 composite density and 0.375 resin weight loading, showing the heat input versus mass loss and the density spacial profile at 20 ns. The simulation heat of pyrolysis is computed from the slope of the heat input versus mass loss curve, excluding the region with transient start up effects.

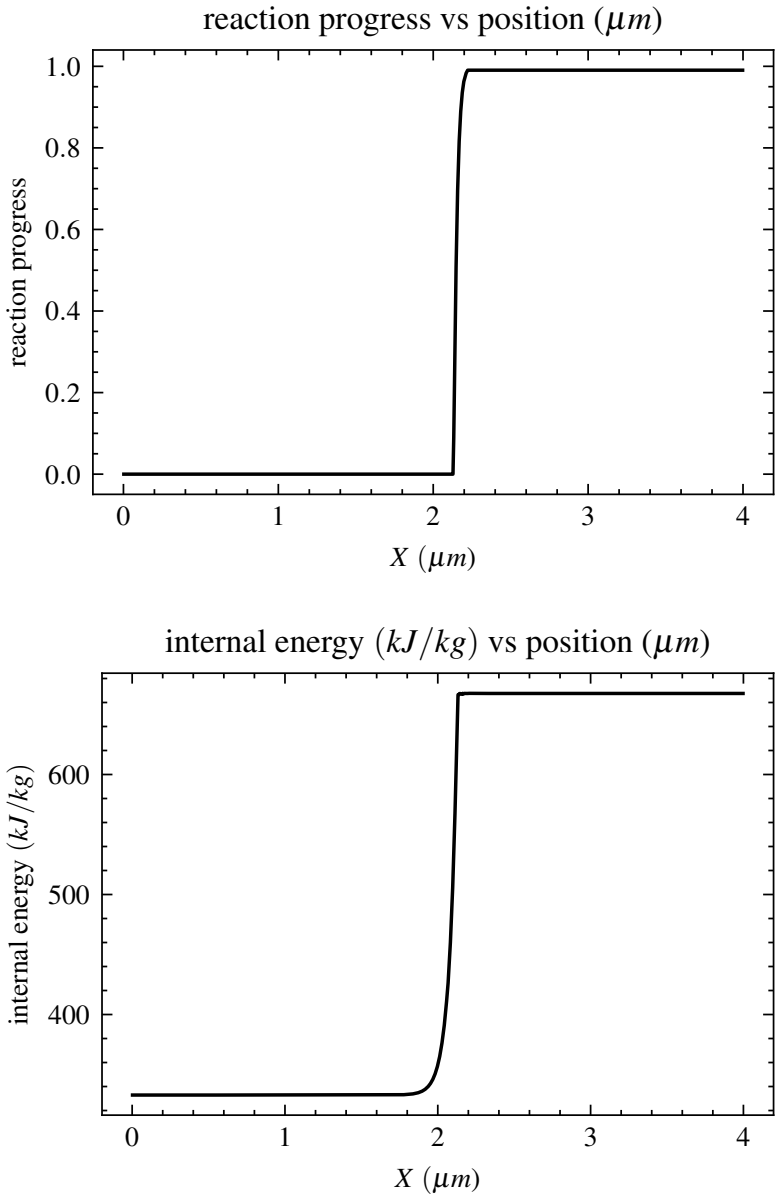

Figure 2.28: Mesoscale simulation of phenolic pyrolysis in vacuum for a carbon fiber reinforced phenolic composite with 1450 kg/m^3 composite density and 0.375 resin weight loading, showing the particle reaction progress and particle internal energy profiles at 10 ns.

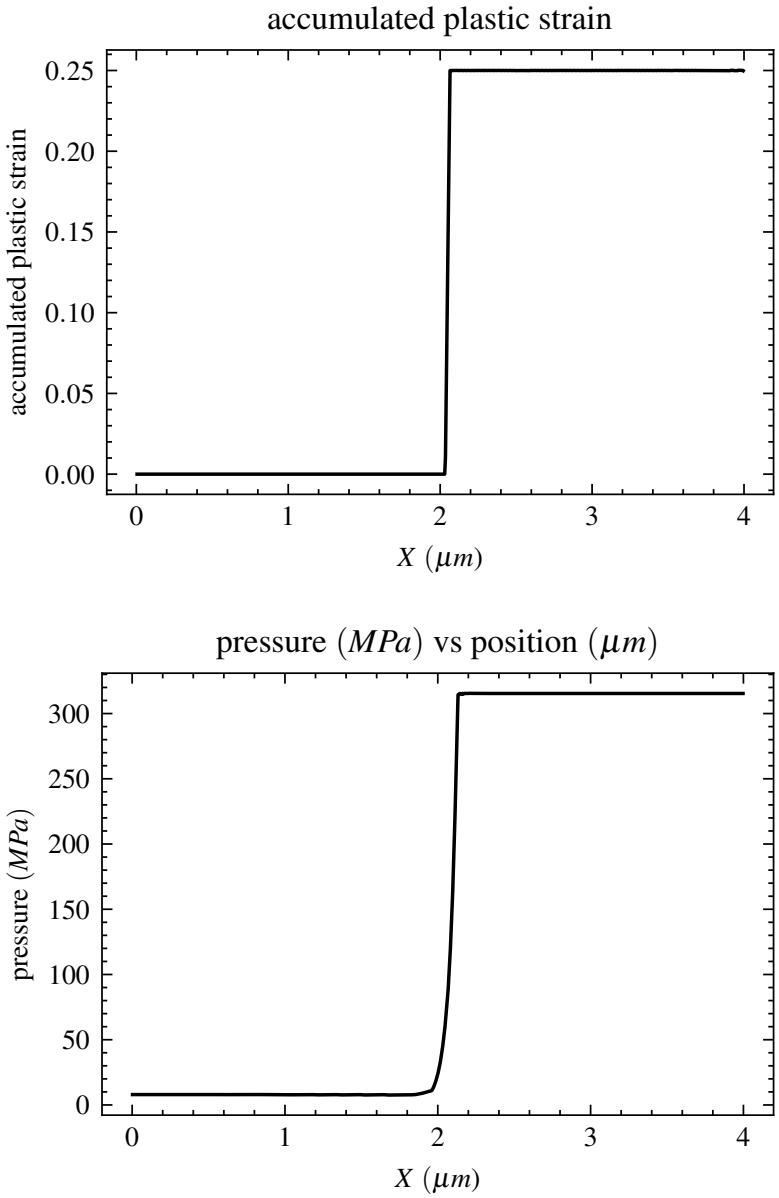

Figure 2.29: Mesoscale simulation of phenolic pyrolysis in vacuum for a carbon fiber reinforced phenolic composite with 1450 kg/m^3 composite density and 0.375 resin weight loading, showing the element accumulated plastic strain and particle pressure profiles at 20 ns.

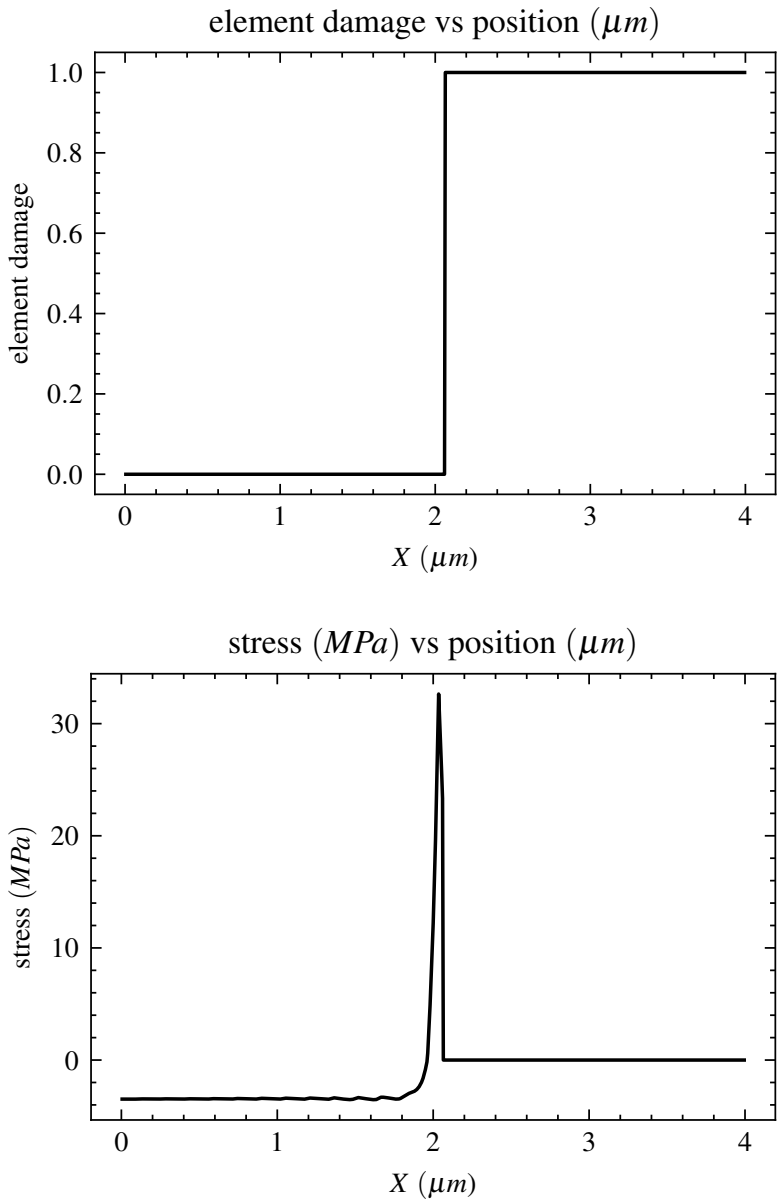

Figure 2.30: Mesoscale simulation of phenolic pyrolysis in vacuum for a carbon fiber reinforced phenolic composite with 1450 kg/m^3 composite density and 0.375 resin weight loading, showing the element damage and element stress profiles at 20 ns.

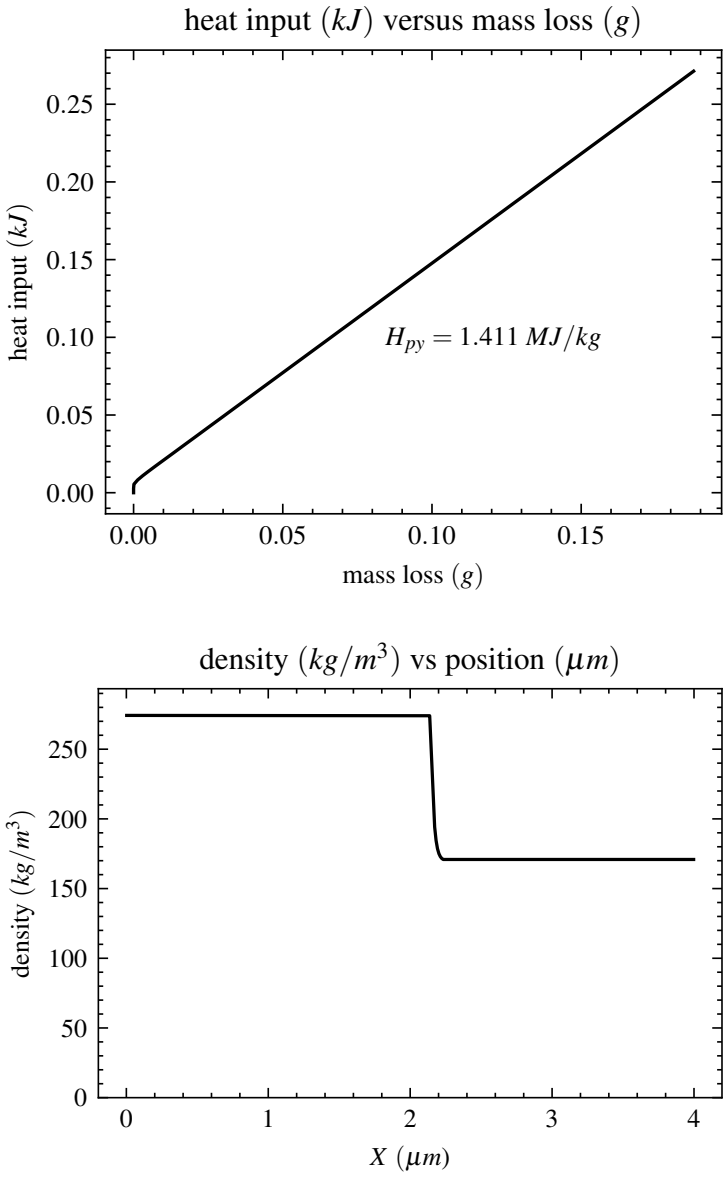

Figure 2.31: Mesoscale simulation of phenolic pyrolysis in vacuum for PICA, showing the heat input versus mass loss and the density spacial profile at 20 ns. The simulation heat of pyrolysis is computed from the slope of the heat input versus mass loss curve, excluding the region with transient start up effects.

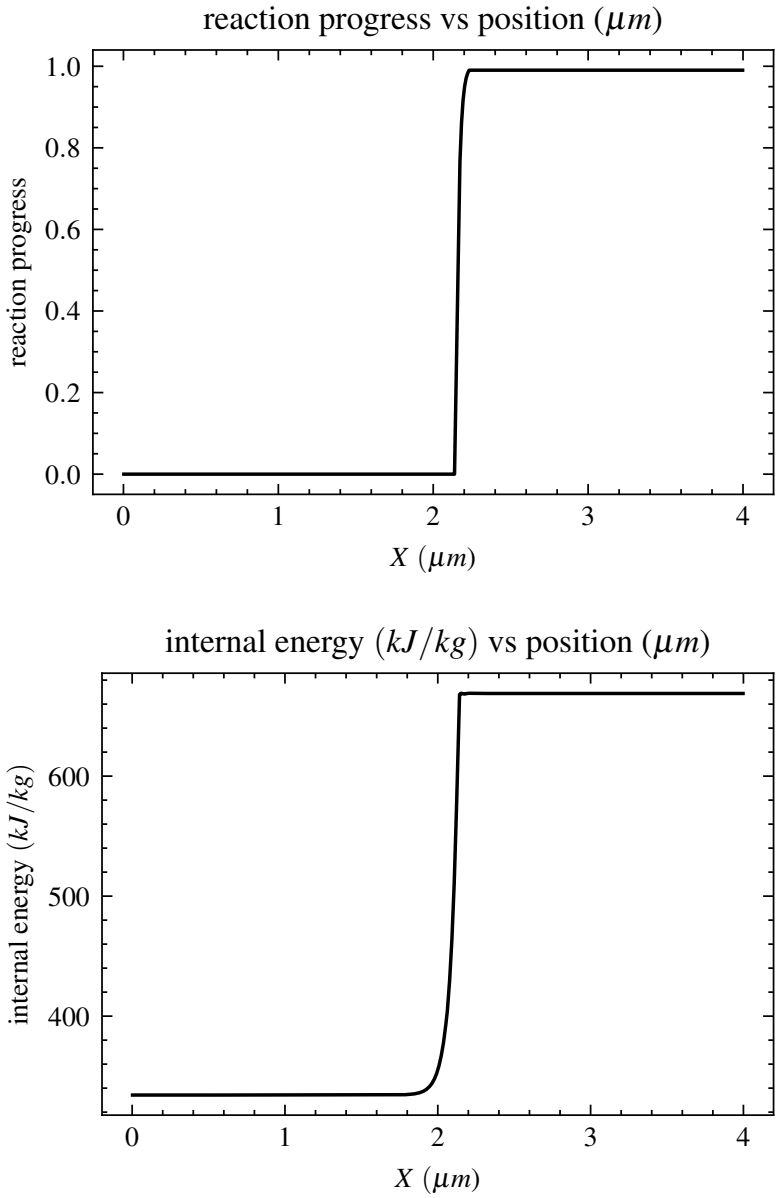

Figure 2.32: Mesoscale simulation of phenolic pyrolysis in vacuum for PICA at 20 ns, showing the particle reaction progress and particle internal energy profiles.

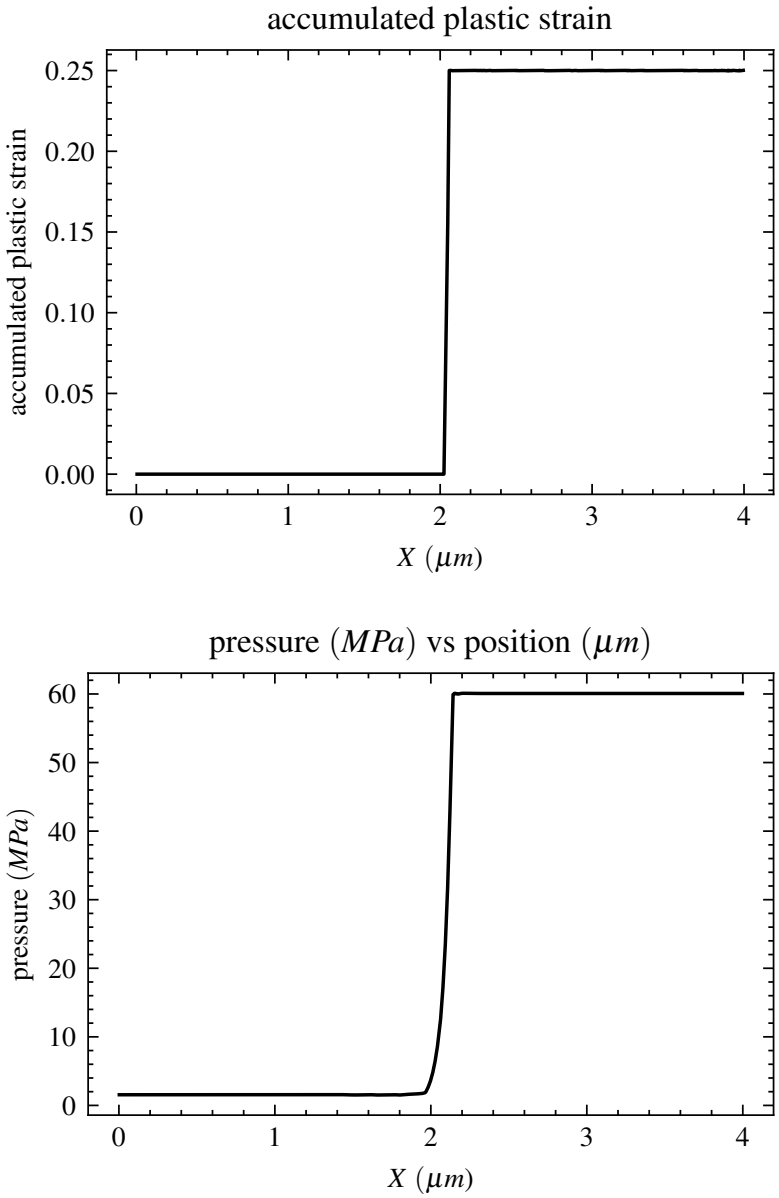

Figure 2.33: Mesoscale simulation of phenolic pyrolysis in vacuum for PICA at 20 ns, showing the element accumulated plastic strain and particle pressure profiles.

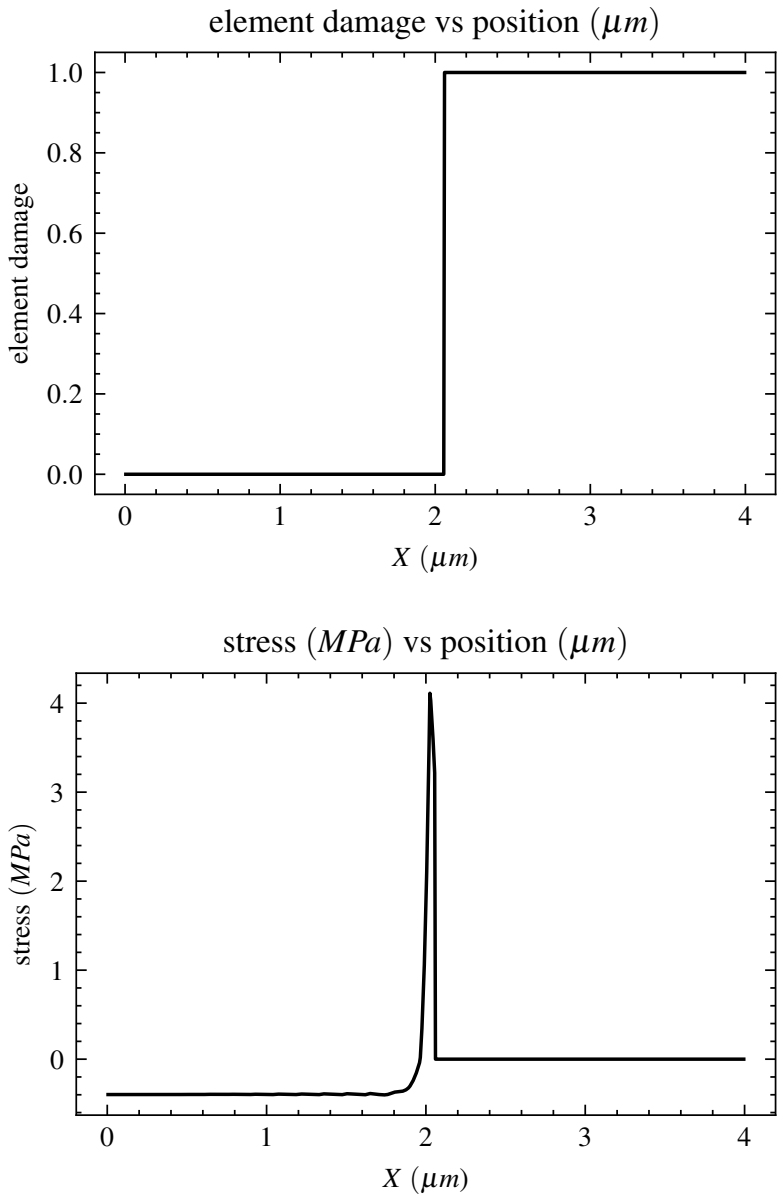

Figure 2.34: Mesoscale simulation of phenolic pyrolysis in vacuum for PICA at 20 ns, showing the element damage and element stress profiles.

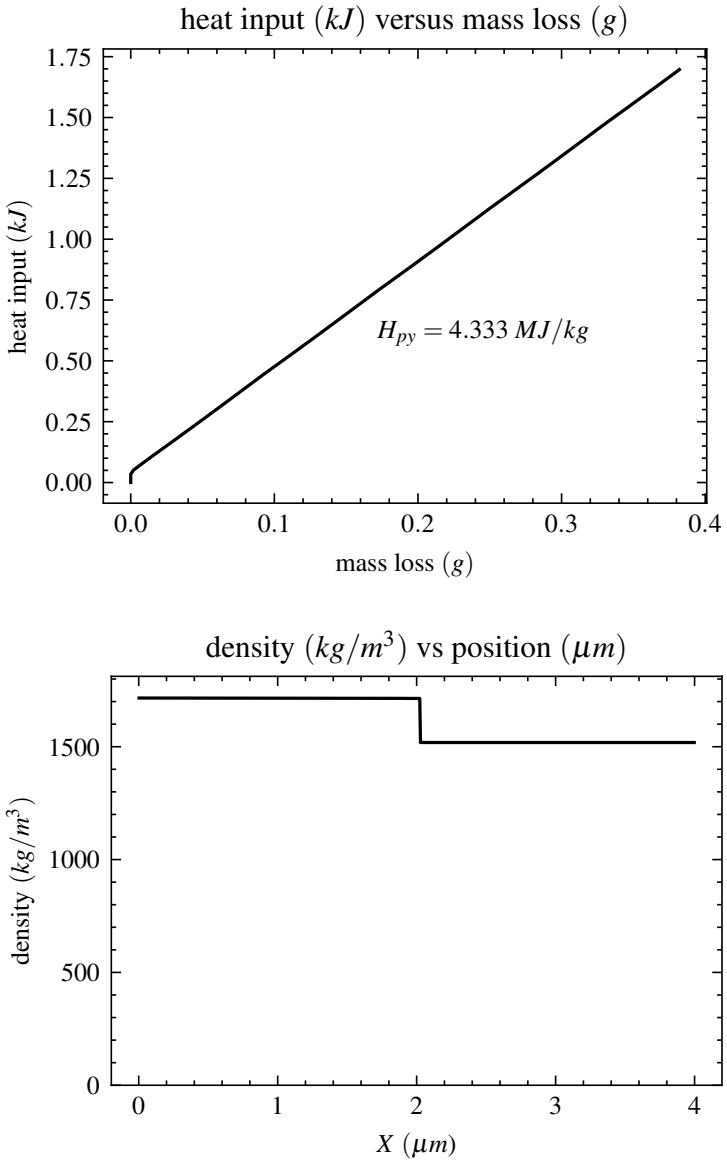

Figure 2.35: Mesoscale simulation of cyanate ester pyrolysis in vacuum for a carbon fiber reinforced cyanate ester composite with 1710 kg/m^3 composite density and 0.114 resin weight loading, showing the heat input versus mass loss and the density spacial profile at 20 ns. The simulation heat of pyrolysis is computed from the slope of the heat input versus mass loss curve, excluding the region with transient start up effects.

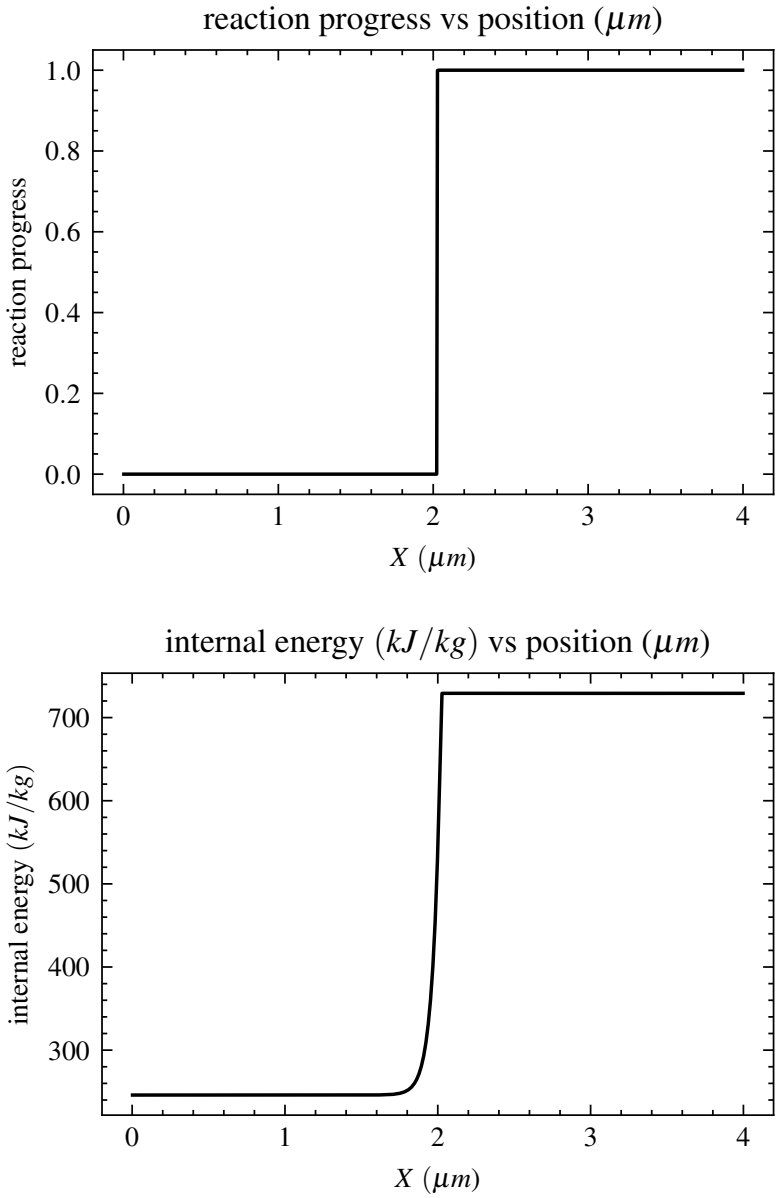

Figure 2.36: Mesoscale simulation of cyanate ester pyrolysis in vacuum for a carbon fiber reinforced cyanate ester composite with 1710 kg/m^3 composite density and 0.114 resin weight loading at 20 ns, showing the particle reaction progress and particle internal energy profiles at 20 ns.

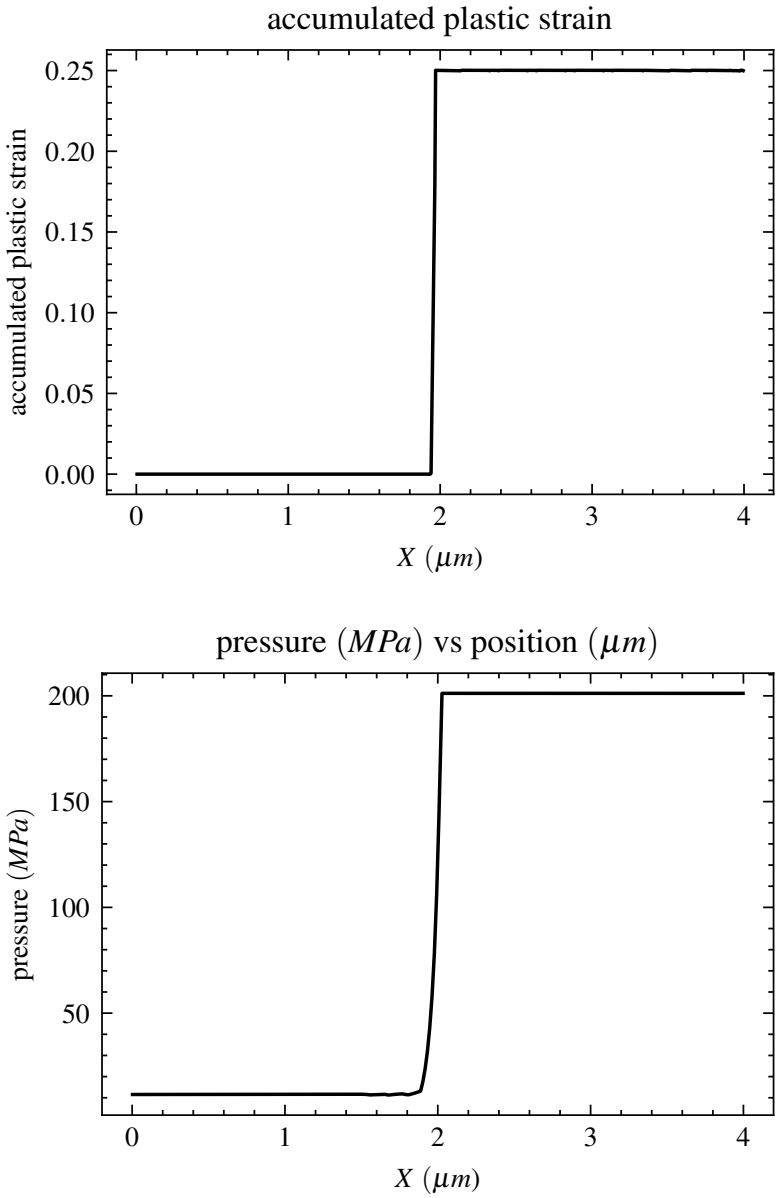

Figure 2.37: Mesoscale simulation of cyanate ester pyrolysis in vacuum for a carbon fiber reinforced cyanate ester composite with 1710 kg/m^3 composite density and 0.114 resin weight loading, showing the element accumulated plastic strain and particle pressure profiles at 20 ns.

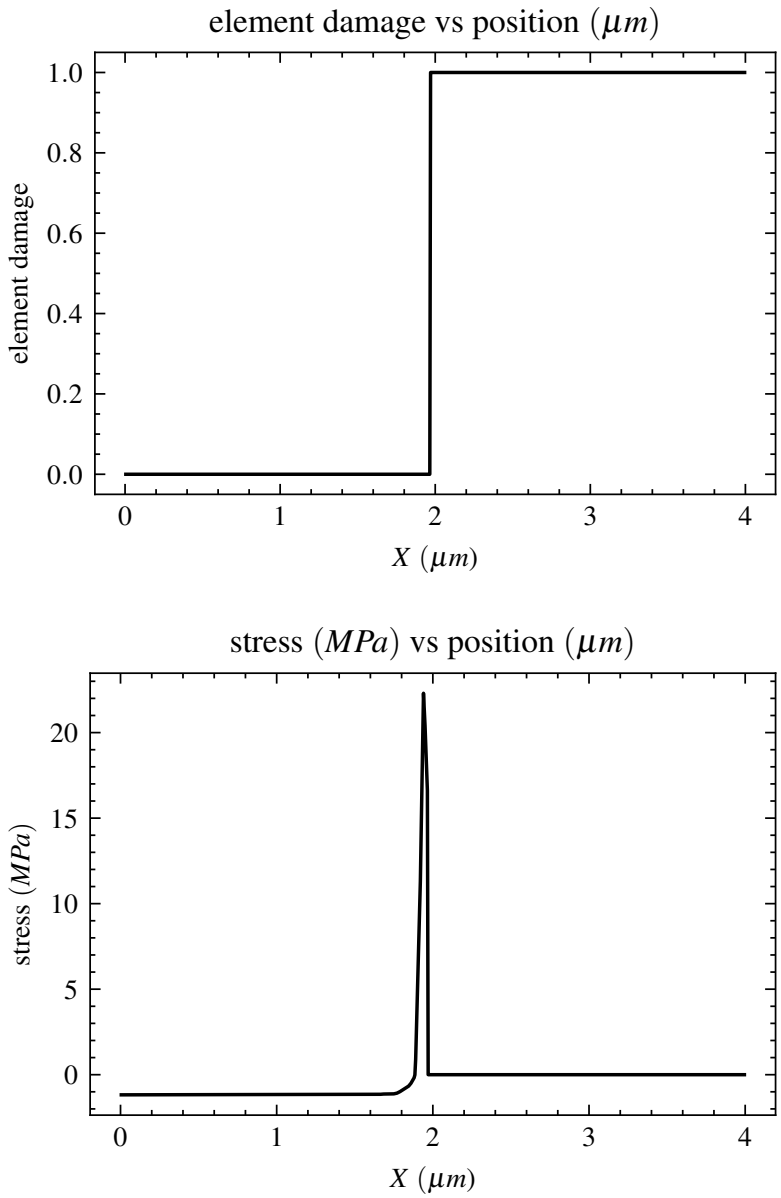

Figure 2.38: Mesoscale simulation of cyanate ester pyrolysis in vacuum for a carbon fiber reinforced cyanate ester composite with 1710 kg/m^3 composite density and 0.114 resin weight loading, showing the element damage and element stress profiles at 20 ns.

Table 2.3: Phenolic material properties

	Value	Reference
density $\bar{\rho}_{res}$	1250 kg/m^3	[17, 51]
pyrolysis temperature θ_{pyr}	500 K	[98, 156]
heat of decomposition h_{dec}	293 kJ/kg	[151]
specific heat c_{v_r}	1674 J/kgK	[166]
sound speed c_{s_r}	2370 m/s	[69]
Grüneisen γ_{res}	1.3	[69]
Young's modulus	5.79 GPa	[69]
Yield stress	136 MPa	[165]

Table 2.4: Cyanate Ester material properties

density $\bar{\rho}_{res}$	1250 kg/m^3	[119]
pyrolysis temperature	700 K	[119]
heat of decomposition	280 kJ/kg	[103]
specific heat c_{v_r}	1200 J/kgK	[25]
sound speed c_{s_r}	1425 m/s	[11]
Grüneisen γ_{res}	0.11[a]	
Young's modulus	1.16 GPa	[11]
Yield stress	55 MPa	[11]

[a] Grüneisen γ_{res} is estimated from equation 2.24 where the volumetric thermal expansion coefficient α is 62.6×10^{-6} K^{-1} [11].

Table 2.5: Carbon fiber material properties

	Value	Reference
density $\bar{\rho}_{fib}$	1800 kg/m^3	[39]
specific heat c_{v_f}	771 J/kgK	[81]
sound speed c_{s_f}	2687 m/s	[149]
Grüneisen γ_{fib}	0.26	[148]
Young's modulus	28 GPa	[149]
Yield stress	76 MPa	[81]
melt temperature	3895[a] K	[1]

[a] Carbon sublimation temperature used in place for melt temperature.

Table 2.6: Silica fiber material properties

density $\bar{\rho}_f$	2200 kg/m^3	[66]
specific heat c_{v_f}	775 J/kgK	[76]
sound speed c_{s_f}	4084 m/s	[67]
Grüneisen γ_f	0.64	[109]
Young's modulus	73 GPa	[67]
Yield stress	160 MPa	[40]
melt temperature	1740 K	[143]

Table 2.7: Species indices and molar masses for the pyrolysis chemistry model for phenolic pyrolysis in air [162].

Species	Index i	Molar mass $\mathbb{M}^{(i)}$ $(g/mole)$
C_6H_6O	1	94.1112
H	2	1.00794
C	3	12.0107
N	4	14.0067
O	5	15.9994
N_2	6	28.0134
O_2	7	31.9988
OH	8	17.0073
CO	9	28.0101
CO_2	10	44.0095
H_2O	11	18.0153

Table 2.8: Stoichiometric coefficients $\nu^{(i,j)}$ for the disassociation chemistry model for phenolic pyrolysis in air [162].

$\nu^{(i,j)}$	Reaction (j)
i	1
1	0
2	5.833
3	4.833
4	48
5	13.5
6	0
7	0
8	0.167
9	1
10	0.167
11	0

Table 2.9: Stoichiometric coefficients $\hat{\nu}^{(i,j)}$ for the disassociation chemistry model for phenolic pyrolysis in air [162].

$\hat{\nu}^{(i,j)}$	Reaction (j)
i	1
1	1
2	0
3	0
4	0
5	0
6	24
7	7
8	0
9	0
10	0
11	0

Table 2.10: Rate law constants for the disassociation chemistry model for phenolic pyrolysis in air [162].

Reaction (j)	Rate constant $(k^{(j)})$ $(1/s)(mol/m^3)^{1-m^{(j)}}$	$m^{(j)}$
1	1.02×10^9	1.5029

Table 2.11: Rate law exponents for the dissasociation chemistry model for phenolic pyrolysis in air [162].

Reaction (j)	Species (i)	$\alpha^{(i,j)}$
1	1	0.5013
1	6	0.5002
1	7	0.5014

Table 2.12: Stoichiometric coefficients $\nu^{(i,j)}$ for the recombination chemistry model for phenolic pyrolysis in air [162].

$\nu^{(i,j)}$	Reaction (j)				
i	1	2	3	4	5
1	0	0	0	0	0
2	0	0	0	0	0
3	0	0	0	0	0
4	0	0	0	0	0
5	0	0	0	0	0
6	1	0	0	0	0
7	0	0	0	0	0
8	0	0	1	0	0
9	0	0	0	1	0
10	0	0	0	0	1
11	0	1	0	0	0

Table 2.13: Stoichiometric coefficients $\hat{\nu}^{(i,j)}$ for the recombination chemistry model for phenolic pyrolysis in air [162].

$\hat{\nu}^{(i,j)}$	Reaction (j)				
i	1	2	3	4	5
1	0	0	0	0	0
2	0	1	1	0	0
3	0	0	0	1	0
4	2	0	0	0	0
5	0	0	1	1	1
6	0	0	0	0	0
7	0	0	0	0	0
8	0	1	0	0	0
9	0	0	0	0	1
10	0	0	0	0	0
11	0	0	0	0	0

Table 2.14: Recombination chemistry model for phenolic pyrolysis in air [162].

Reaction (j)	Rate constant ($k^{(j)}$) $\frac{1}{s}\left(\frac{mol}{m^3}\right)^{1-m^{(j)}}$	$m^{(j)}$	Temperature function $f^{(j)}(\theta)$	$\theta^{(j)}$ (K)
1	6.9555×10^7	1.7596	$\frac{1}{1+\exp\left(\frac{\theta-\theta^{(j)}}{\theta^{(j)}}\right)}$	2118.3
2	1.0217×10^3	2.9686	$\frac{1}{1+\exp\left(\frac{\theta-\theta^{(j)}}{\theta^{(j)}}\right)}$	1641.1
3	1.9673×10^6	2.0617	$\frac{1}{1+\exp\left(\frac{\theta-\theta^{(j)}}{\theta^{(j)}}\right)}$	3166.0
4	4.4733×10^5	2.2083	$\frac{1}{1+\exp\left(\frac{\theta-\theta^{(j)}}{\theta^{(j)}}\right)}$	3166.0
5	2.0923	3.5070	$\frac{1}{1+\exp\left(\frac{\theta-\theta^{(j)}}{\theta^{(j)}}\right)}$	1641.1

Table 2.15: Rate law exponents for the recombination chemistry model for phenolic pyrolysis in air [162].

$\alpha^{(i,j)}$	Reaction (j)				
i	1	2	3	4	5
1	0	0	0	0	0
2	0	1.3069	1.1893	0	0
3	0	0	0	0.2886	0
4	1.7596	0	0	0	0
5	0	0	0.8724	1.9198	1.5637
6	0	0	0	0	0
7	0	0	0	0	0
8	0	1.6617	0	0	0
9	0	0	0	0	1.9433
10	0	0	0	0	0
11	0	0	0	0	0

Table 2.16: Species indices and molar masses for the pyrolysis chemistry model for cyanate ester pyrolysis in air [162].

Species	Index i	Molar mass $\mathbb{M}^{(i)}$ $(g/mole)$
$C_{17}H_{14}N_2O_2$	1	278.30526
H	2	1.00794
C	3	12.0107
N	4	14.0067
O	5	15.9994
N_2	6	28.0134
O_2	7	31.9988
OH	8	17.0073
CO	9	28.0101
CO_2	10	44.0095
H_2O	11	18.0153

Table 2.17: Stoichiometric coefficients $\hat{\nu}^{(i,j)}$ for the disassociation chemistry model for cyanater ester pyrolysis in air [162].

$\hat{\nu}^{(i,j)}$	Reaction (j)
i	1
1	1
2	0
3	0
4	0
5	0
6	61.5
7	19.5
8	0
9	0
10	0
11	0

Table 2.18: Stoichiometric coefficients $\nu^{(i,j)}$ for the disassociation chemistry model for cyanater ester pyrolysis in air [162].

$\nu^{(i,j)}$	Reaction (j)
i	1
1	0
2	13.5
3	13.5
4	125.0
5	36.5
6	0
7	0
8	0.5
9	3.0
10	0.5
11	0.0

Table 2.19: Rate law constants for the disassociation chemistry model for cyanate ester pyrolysis in air [162].

Reaction (j)	Rate constant $(k^{(j)})$ $(1/s)(mol/m^3)^{1-m^{(j)}}$	$m^{(j)}$
1	8.2985×10^9	1.5171

Table 2.20: Rate law exponents for the disassociation chemistry model for cyanate ester pyrolysis in air [162].

Reaction (j)	Species (i)	$\alpha^{(i,j)}$
1	1	0.5527
1	6	0.4407
1	7	0.5237

Table 2.21: Stoichiometric coefficients $\nu^{(i,j)}$ for the recombination chemistry model for cyanate ester pyrolysis in air [162].

$\nu^{(i,j)}$	Reaction (j)				
i	1	2	3	4	5
1	0	0	0	0	0
2	0	0	0	0	0
3	0	0	0	0	0
4	0	0	0	0	0
5	0	0	0	0	0
6	1	0	0	0	0
7	0	0	0	0	0
8	0	0	1	0	0
9	0	0	0	1	0
10	0	0	0	0	1
11	0	1	0	0	0

Table 2.22: Stoichiometric coefficients $\hat{\nu}^{(i,j)}$ for the recombination chemistry model for cyanate ester pyrolysis in air [162].

$\hat{\nu}^{(i,j)}$	Reaction (j)				
i	1	2	3	4	5
1	0	0	0	0	0
2	0	1	1	0	0
3	0	0	0	1	0
4	2	0	0	0	0
5	0	0	1	1	1
6	0	0	0	0	0
7	0	0	0	0	0
8	0	1	0	0	0
9	0	0	0	0	1
10	0	0	0	0	0
11	0	0	0	0	0

Table 2.23: Recombination chemistry model for cyanate ester pyrolysis in air [162].

Reaction (j)	Rate constant $(k^{(j)})$ $\frac{1}{s}\left(\frac{mol}{m^3}\right)^{1-m^{(j)}}$	$m^{(j)}$	Temperature function $f^{(j)}(\theta)$	$\theta^{(j)}$ (K)
1	3.1901×10^{10}	1.2473	$\frac{1}{\exp\left(\frac{\theta-\theta^{(j)}}{\theta^{(j)}}\right)}$	3625.1
2	7.4324×10^{9}	1.2822	$\frac{1}{\exp\left(\frac{\theta-\theta^{(j)}}{\theta^{(j)}}\right)}$	2350.3
3	1.1821×10^{2}	2.8715	$\frac{1}{\exp\left(\frac{\theta-\theta^{(j)}}{\theta^{(j)}}\right)}$	3331.0
4	5.0899×10^{6}	2.1191	$\frac{1}{\exp\left(\frac{\theta-\theta^{(j)}}{\theta^{(j)}}\right)}$	3331.0
5	9.5821×10^{6}	1.9644	$\frac{1}{\exp\left(\frac{\theta-\theta^{(j)}}{\theta^{(j)}}\right)}$	2350.3

Table 2.24: Rate law exponents for the recombination chemistry model for cyanate ester pyrolysis in air [162].

$\alpha^{(i,j)}$	Reaction (j)				
i	1	2	3	4	5
1	0	0	0	0	0
2	0	0.6249	1.8920	0	0
3	0	0	0	1.1321	0
4	1.2473	0	0	0	0
5	0	0	0.9795	0.9870	1.4584
6	0	0	0	0	0
7	0	0	0	0	0
8	0	0.6573	0	0	0
9	0	0	0	0	0.5060
10	0	0	0	0	0
11	0	0	0	0	0

Table 2.25: Species indices and molar masses for the pyrolysis chemistry model for phenolic pyrolysis in vacuum [162].

Species	Index i	Molar mass $\mathbb{M}^{(i)}$ $(g/mole)$
C_6H_6O	1	94.11124
H	2	1.00794
C	3	12.01070
O	4	15.99940
C_2	5	24.02140
CH	6	13.01864
CO	7	28.01010
CH_2	8	14.02658

Table 2.26: Stoichiometric coefficients $\nu^{(i,j)}$ for the disassociation chemistry model for phenolic pyrolysis in vacuum [162].

$\nu^{(i,j)}$	Reaction (j)
i	1
1	0.0
2	5.225
3	5.0
4	0.9
5	0.1
6	0.625
7	0.1
8	0.075

Table 2.27: Stoichiometric coefficients $\hat{\nu}^{(i,j)}$ for the disassociation chemistry model for phenolic pyrolysis in vacuum [162].

$\hat{\nu}^{(i,j)}$	Reaction (j)
i	1
1	1
2	0
3	0
4	0
5	0
6	0
7	0
8	0

Table 2.28: Rate law constants for the disassociation chemistry model for phenolic pyrolysis in vacuum [162].

Reaction (j)	Rate constant $(k^{(j)})$ $(1/s)(mol/m^3)^{1-m^{(j)}}$	$m^{(j)}$
1	1.0504×10^{13}	0.5687

Table 2.29: Rate law exponents for the dissasociation chemistry model for phenolic pyrolysis in vacuum [162].

Reaction (j)	Species (i)	$\alpha^{(i,j)}$
1	1	0.5687

Table 2.30: Stoichiometric coefficients $\nu^{(i,j)}$ for the recombination chemistry model for phenolic pyrolysis in vacuum [162].

$\nu^{(i,j)}$	Reaction (j)			
i	1	2	3	4
1	0	0	0	0
2	0	0	0	0
3	0	0	0	0
4	0	0	0	0
5	0	1	0	0
6	0	0	1	0
7	1	0	0	0
8	0	0	0	1

Table 2.31: Stoichiometric coefficients $\hat{\nu}^{(i,j)}$ for the recombination chemistry model for phenolic pyrolysis in vacuum [162].

$\hat{\nu}^{(i,j)}$	Reaction (j)			
i	1	2	3	4
1	0	0	0	0
2	0	0	1	1
3	1	2	1	0
4	1	0	0	0
5	0	0	0	0
6	0	0	0	1
7	0	0	0	0
8	0	0	0	0

Table 2.32: Recombination chemistry model for phenolic pyrolysis in vacuum [162].

Reaction (j)	Rate constant $(k^{(j)})$ $\frac{1}{s}\left(\frac{mol}{m^3}\right)^{1-m^{(j)}}$	$m^{(j)}$	Temperature function $f^{(j)}(\theta)$	$\theta^{(j)}$ (K)
1	1.7679×10^6	1.9758	$\frac{1}{1+\exp\left(\frac{\theta-\theta^{(j)}}{\theta^{(j)}}\right)}$	2000.0
2	1.3371×10^7	1.6300	$\frac{1}{1+\exp\left(\frac{\theta-\theta^{(j)}}{\theta^{(j)}}\right)}$	2000.0
3	1.4190×10^8	1.1596	$1-\frac{1}{1+\exp\left(\frac{\theta-\theta^{(j)}}{\theta^{(j)}}\right)}$	2000.0
4	8.3811×10^5	2.0234	$\frac{1}{1+\exp\left(\frac{\theta-\theta^{(j)}}{\theta^{(j)}}\right)}$	2000.0

Table 2.33: Rate law exponents for the recombination chemistry model for phenolic pyrolysis in vacuum [162].

$\alpha^{(i,j)}$	Reaction (j)			
i	1	2	3	4
1	0.0	0.0	0.0	0.0
2	0.0	0.0	0.6634	0.0234
3	1.4697	1.6300	0.4962	0.0
4	0.5061	0.0	0.0	0.0
5	0.0	0.0	0.0	0.0
6	0.0	0.0	0.0	2.000
7	0.0	0.0	0.0	0.0
8	0.0	0.0	0.0	0.0

Table 2.34: Species indices and molar masses for the pyrolysis chemistry model for cyanate ester pyrolysis in vacuum [162].

Species	Index i	Molar mass $\mathbb{M}^{(i)}$ $(g/mole)$
$C_{17}H_{14}N_2O_2$	1	278.30526
H	2	1.00794
C	3	12.01070
N	4	14.00670
O	5	15.99940
C_2	6	24.02140
N_2	7	28.01340
CH	8	13.01864
CO	9	28.01010
CH_2	10	14.02658

Table 2.35: Stoichiometric coefficients $\hat{\nu}^{(i,j)}$ for the disassociation chemistry model for cyanater ester pyrolysis in vacuum [162].

$\nu^{(i,j)}$	Reaction (j)
i	1
1	0.0
2	12.375
3	13.0
4	1.75
5	1.75
6	1.0625
7	0.125
8	1.625
9	0.25
10	0.0

Table 2.36: Stoichiometric coefficients $\nu^{(i,j)}$ for the disassociation chemistry model for cyanater ester pyrolysis in vacuum [162].

$\hat{\nu}^{(i,j)}$	Reaction (j)
i	1
1	1
2	0
3	0
4	0
5	0
6	0
7	0
8	0
9	0
10	0

Table 2.37: Rate law constants for the disassociation chemistry model for cyanate ester pyrolysis in vacuum [162].

Reaction (j)	Rate constant $(k^{(j)})$ $(1/s)(mol/m^3)^{1-m^{(j)}}$	$m^{(j)}$
1	3.8844×10^{12}	0.5

Table 2.38: Rate law exponents for the disassociation chemistry model for cyanate ester pyrolysis in vacuum [162].

Reaction (j)	Species (i)	$\alpha^{(i,j)}$
1	1	0.5

Table 2.39: Stoichiometric coefficients $\nu^{(i,j)}$ for the recombination chemistry model for cyanate ester pyrolysis in vacuum [162].

$\nu^{(i,j)}$	Reaction (j)				
i	1	2	3	4	5
1	0	0	0	0	0
2	0	0	0	0	0
3	0	0	0	0	0
4	0	0	0	0	0
5	0	0	0	0	0
6	0	1	0	0	0
7	0	0	0	0	1
8	0	0	1	0	0
9	1	0	0	0	0
10	0	0	0	1	0

Table 2.40: Stoichiometric coefficients $\hat{\nu}^{(i,j)}$ for the recombination chemistry model for cyanate ester pyrolysis in vacuum [162].

$\hat{\nu}^{(i,j)}$	Reaction (j)				
i	1	2	3	4	5
1	0	0	0	0	0
2	0	0	1	1	0
3	1	2	1	0	0
4	0	0	0	0	2
5	1	0	0	0	0
6	0	0	0	0	0
7	0	0	0	0	0
8	0	0	0	1	0
9	0	0	0	0	0
10	0	0	0	0	0

Table 2.41: Recombination chemistry model for cyanate ester pyrolysis in vacuum [162].

Reaction (j)	Rate constant $(k^{(j)})$ $\frac{1}{s}\left(\frac{mol}{m^3}\right)^{1-m^{(j)}}$	$m^{(j)}$	Temperature function $f^{(j)}(\theta)$	$\theta^{(j)}$ (K)
1	9.7359×10^4	2.5781	$\frac{1}{1+\exp\left(\frac{\theta-\theta^{(j)}}{\theta^{(j)}}\right)}$	1002.0
2	5.1752×10^6	1.9907	$\frac{1}{1+\exp\left(\frac{\theta-\theta^{(j)}}{\theta^{(j)}}\right)}$	1002.0
3	4.9200×10^6	1.4597	$1-\frac{1}{1+\exp\left(\frac{\theta-\theta^{(j)}}{\theta^{(j)}}\right)}$	998.6
4	3.9367×10^3	4.0	$\frac{1}{1+\exp\left(\frac{\theta-\theta^{(j)}}{\theta^{(j)}}\right)}$	998.6
5	1.1267×10^7	1.9759	$\frac{1}{1+\exp\left(\frac{\theta-\theta^{(j)}}{\theta^{(j)}}\right)}$	1000.1

Table 2.42: Rate law exponents for the recombination chemistry model for cyanate ester pyrolysis in vacuum [162].

$\alpha^{(i,j)}$	Reaction (j)				
i	1	2	3	4	5
1	0.0	0.0	0.0	0.0	0.0
2	0.0	0.0	0.3791	2.000	0.0
3	0.5785	1.9907	1.0806	0.0	0.0
4	0.0	0.0	0.0	0.0	1.9759
5	1.9996	0.0	0.0	0.0	0.0
6	0.0	0.0	0.0	0.0	0.0
7	0.0	0.0	0.0	0.0	0.0
8	0.0	0.0	0.0	2.000	0.0
9	0.0	0.0	0.0	0.0	0.0
10	0.0	0.0	0.0	0.0	0.0

Chapter 3

Macroscale Model

3.1 Introduction

The macroscale model simulates in three dimensions the thermomechanical response of the composite material to applied mechanical and thermal loads, including the effects of transpiration cooling, ablation of both resin and fiber, and evolution of the TPS geometry. The resin mass loss model is derived from the mesoscale simulation results, since the small time constants of the RMD kinetics preclude direct simulation of the chemical kinetics at the macroscale. The macroscale model developed in this chapter builds upon previous work on the hybrid particle element method [73, 101, 124, 145] by the addition of variable mass particles for simulating resin pyrolysis and by the addition of a fiber reinforcement model. The fiber reinforcement is represented as a set of tension only bar elements whose nodes are located at the particle centers of mass. This builds on previous research on the simulation of fabrics [132, 144] by combining particles, finite elements, and tension only bar elements to produce a composite description of the material. Mass loss at the macroscale includes mass loss in the particles due to resin ablation and bulk material removal from failure of the elements and fibers. The total simulated mass loss as a function of total heat input into the material is compared to

published experimental results to validate the method.

The following sections describe the macroscale model formulation. To exclude reiteration of previous work, focus is given on the extensions of existing formulations.

3.2 Mass Kinetics

As mentioned, the macroscale model incorporates a resin ablation model from the mesoscale simulation results for the heat of pyrolysis. The particle mass evolution at the macroscale takes a simple first order form

$$\dot{m}^{(i)} = -\frac{1}{\tau}\left\langle m^{(i)} - m_0 + \frac{1}{H_{py}}\langle u^{(i)} - u_0\rangle m^{(i)} \right\rangle \hat{u}\left(m^{(i)} - m_0^{(i)} f_f\right) \tag{3.1}$$

where τ is a time constant describing the rate at which the particle mass relaxes to a target value computed from the resin heat of pyrolysis and the particle internal energy. The particle fiber mass content is treated as constant in the macroscale model; however, fiber ablation is still accounted for in the composite model by the failure of the fiber elements and bulk mass removal. A particle ablation progress variable $\lambda^{(i)}$ is defined in the macroscale model as

$$\lambda^{(i)} = 1 - \frac{m^{(i)}}{m_0^{(i)}} \tag{3.2}$$

3.3 Composite Model

The macroscale model builds on previous research on the hybrid particle element method [73, 124, 132, 144, 145] by combining particles, finite elements,

and tension only bar elements to produce a composite description of the material. The ellipsoidal particle centers of mass are the nodes of large strain finite elements used to model the tensile response and elastic plastic evolution. Similar to the mesoscale model, a deviatoric strain is computed for each element having the functional form

$$\mathbf{E}^{(j)} = \mathbf{E}^{(j)}\left(\mathbf{c}^{(i)}\right), \quad \dot{\mathbf{E}}^{(j)} = \dot{\mathbf{E}}^{(j)}\left(\dot{\mathbf{c}}^{(i)}, \mathbf{c}^{(i)}\right) \tag{3.3}$$

The strain is additively decomposed into elastic and plastic parts

$$\mathbf{E}^{(j)} = \mathbf{E}^{e(j)} + \mathbf{E}^{p(j)}, \quad \dot{\mathbf{E}}^{p(j)} = \dot{\mathbf{E}}^{p(j)}(\mathbf{c}^{(i)}, \mathbf{E}^{p(j)}, \epsilon^{p(j)}, u^{(i)}, d^{(j)}) \tag{3.4}$$

The accumulated plastic strain $\epsilon^{p(j)}$ is obtained by integrating

$$\dot{\epsilon}^{p(j)} = \left(\frac{1}{2} tr\left(\dot{\mathbf{E}}^{p(j)^T}\dot{\mathbf{E}}^{p(j)}\right)\right)^{1/2} \tag{3.5}$$

An elastic strain energy density $\psi^{(j)}$ is associated with each element and is defined as

$$\psi^{(j)} = (1 - d^{(j)})\mu^{(j)} tr\left(\mathbf{E}^{e(j)^T}\mathbf{E}^{e(j)}\right) \tag{3.6}$$

from which a deviatoric stress is calculated as

$$\mathbf{S}^{(j)} = \frac{\partial \psi^{(j)}}{\partial \mathbf{E}^{e(j)}} = (1 - d^{(j)})2\mu^{(j)}\mathbf{E}^{e(j)} \tag{3.7}$$

where $\mu^{(j)}$ is a shear modulus and $d^{(j)}$ models the transition from an intact to failed element. The element damage evolution used here is

$$\dot{d}^{(j)} = \frac{\Lambda^{(j)}}{\hat{n}\Delta t}\hat{u}(1 - d^{(j)}) \tag{3.8}$$

where Δt is the time step, $\hat{n}$ the number of steps used to model transition from an intact to failed element, and

$$\Lambda^{(j)} = \max\Big\{ \hat{u}(\epsilon^{p(j)} - \epsilon_f^{p(j)}),\, \hat{u}(u_{max}^{(j)} - u_f^{(j)}), \\ \hat{u}(J_c^{(j)} - J_{min}^{(j)}),\, \hat{u}(\sigma_{max}^{(j)} - \sigma_s^{(j)}),\, \hat{u}(\lambda_f^{(j)} - \lambda^{(j)}) \Big\} \tag{3.9}$$

The above function initiates element failure when the accumulated plastic strain $\epsilon^{p(j)}$, maximum historic element internal energy $u_{max}^{(j)}$, minimum element Jacobian $J_{min}^{(j)}$, maximum eigenvalue of the deviatoric stress $\sigma_{max}^{(j)}$, and element ablation progress $\lambda^{(j)}$ reach associated critical values for the failure plastic strain $\epsilon_f^{p(j)}$, failure internal energy $u_f^{(j)}$, maximum compression $J_c^{(j)}$, spall stress $\sigma_s^{(j)}$, or failure ablation progress $\lambda_f^{(j)}$. The element maximum historic internal energy $u_{max}^{(j)}$ and ablation progress $\lambda^{(j)}$ are computed from its associated particles.

The ellipsoidal particle centers of mass also define a set of tension only bar elements used to model the fiber reinforcement. A strain is computed for each bar element, having the functional form [144]

$$\epsilon^{(i,j)} = \epsilon^{(i,j)} \left(\mathbf{c}^{(i)}, \mathbf{c}^{(j)}, \mathbf{e}^{(i)}, \mathbf{e}^{(j)} \right) \tag{3.10}$$

where $\epsilon^{(i,j)}$ is the strain of the bar element with vertices defined by the centers of mass of particles i and j, and the euler parameters $\mathbf{e}^{(i)}$ describe the angular orientation of the ellipsoidal particles [73, 144]. An elastic strain energy density $\psi^{(i,j)}$ is associated with each bar element and is defined as

$$\psi^{(i,j)} = \frac{1}{2} E^{(i,j)} (1 - D^{(i,j)}) \langle \epsilon^{(i,j)} \rangle^2 \tag{3.11}$$

from which a fiber stress $\sigma^{(i,j)}$ is derived

$$\sigma^{(i,j)} = \frac{\partial \psi^{(i,j)}}{\partial \langle \epsilon^{(i,j)} \rangle} = E^{(i,j)}(1 - D^{(i,j)})\langle \epsilon^{(i,j)} \rangle \tag{3.12}$$

where $E^{(i,j)}$ is an average Young modulus and $D^{(i,j)}$ models the transition from an intact to failed bar element. The modulus and damage for each bar element are computed from the particles as

$$E^{(i,j)} = \frac{1}{2}\left(E^{(i)} + E^{(j)}\right) \tag{3.13}$$

$$D^{(i,j)} = \frac{1}{2}\left(D^{(i)} + D^{(j)}\right) \tag{3.14}$$

The fiber damage evolution used here has the same form as the element damage evolution:

$$\dot{D}^{(i)} = \frac{\Lambda_f^{(i)}}{\hat{n}\Delta t}\hat{u}(1 - D^{(i)}) \tag{3.15}$$

$\Lambda_f^{(i)}$ is formulated as

$$\Lambda_f^{(i)} = \hat{u}(u_{max}^{(i)} - u_f^{fib(i)}) \tag{3.16}$$

where fiber failure is initiated when the maximum historic internal energy $u_{max}^{(i)}$ exceeds a fiber failure internal energy $u_f^{fib(i)}$.

3.4 Equations of State

The mixture equation of state at the macroscale is the same as that in the mesoscale, and briefly restated here:

$$P = f_f P_f \frac{\rho_0}{\rho_{f0}} + f_r P_r \frac{\rho_0}{\rho_{r0}}$$

$$\theta = f_r \frac{c_{vr}}{c_v}\theta_r + f_f \frac{c_{v_f}}{c_v}\theta_f, \quad c_v = c_{vr} f_r + c_{v_f} f_f$$

Since the macroscale model does not directly incorporate the RMD chemistry, the macroscale formulation has no explicit dependence on temperature which is treated only as a model output. The constituent temperatures in the macroscale are calculated by

$$\theta_f = \min\left(\frac{1}{c_{v_f}}(u - u_0) + \theta_0, \theta_f^{max}\right) \tag{3.17}$$

$$\theta_r = \min\left(\frac{1}{c_{v_r}}(u - u_0) + \theta_0, \theta_r^{max}\right) \tag{3.18}$$

where θ_f^{max} and θ_r^{max} are a maximum fiber and resin temperature. For the resin, the maximum temperature is set to the pyrolysis temperature. An oxidation temperature of 1000 K is used for the fiber [126].

3.5 Heat Input

The macroscale model employs a simple heat input formulation where a per unit mass heat input is applied to the particles residing inside a cylindrical control volume. Inside the volume, the heat input has an exponentially decaying spacial profile described by a moving surface. The surface has either a planar or radial geometry. As ablation proceeds, the surface descends through the cylindrical volume, propagating the heat input profile.

For convenience, the following description assumes that the cylindrical control volume is centered along the y–axis. A radial distance for each particle is then calculated as:

$$r^{(i)} = \left[\left(\mathbf{c}^{(i)} - \mathbf{c}^{(i)^T}\hat{\mathbf{y}}\hat{\mathbf{y}}\right)^T\left(\mathbf{c}^{(i)} - \mathbf{c}^{(i)^T}\hat{\mathbf{y}}\hat{\mathbf{y}}\right)\right]^{1/2} \tag{3.19}$$

where $\hat{\mathbf{y}}$ is the unit y basis vector. The bottom of the control volume is defined as the xz plane containing the point $\mathbf{b}_0$:

$$\mathbf{b}_0 = \{0, -s_0, 0\} \tag{3.20}$$

where s_0 is a constant. The upper surface of the control volume consists of either a planar or hemispherical surface. Relative to $\mathbf{b}_0$, a particle distance $R_0^{(i)}$ and height $H_0^{(i)}$ are calculated as:

$$R_0^{(i)} = \left[\left(\mathbf{c}^{(i)} - \mathbf{b}_0 \right)^T \left(\mathbf{c}^{(i)} - \mathbf{b}_0 \right) \right]^{1/2} \tag{3.21}$$

$$H_0^{(i)} = \left(\mathbf{c}^{(i)} - \mathbf{b}_0 \right)^T \hat{\mathbf{y}} \tag{3.22}$$

A particle then resides within the control volume based upon the following boolean variables:

$$\eta_H^{(i)} = \hat{u}^{(i)} \left(R_c - r^{(i)} \right) \hat{u} \left(H_0^{(i)} \right) \hat{u} \left(R_s - R_0^{(i)} \right) \tag{3.23}$$

$$\eta_P^{(i)} = \hat{u}^{(i)} \left(R_c - r^{(i)} \right) \hat{u} \left(H_0^{(i)} \right) \hat{u} \left(H_s - H_0^{(i)} \right) \tag{3.24}$$

where $\eta_H^{(i)}$ is for a hemispherical upper surface, and $\eta_P^{(i)}$ for a planar upper surface. The constant R_c is the radius of the cylindrical control volume. The upper surface of the control volume consists of either a hemispherical surface with radius R_s and origin $\mathbf{b}_0$, or a planar surface located a height H_s above $\mathbf{b}_0$.

For defining the heat input spacial profile inside the control volume, a translating point $\mathbf{b}$ is defined as:

$$\mathbf{b} = \{0, -(L_0 + L), 0\} \tag{3.25}$$

where L varies with time. Relative to $\mathbf{b}$, the distance $R^{(i)}$ and the height $H^{(i)}$ are then defined as

$$R^{(i)} = \left[\left(\mathbf{c}^{(i)} - \mathbf{b} \right)^T \left(\mathbf{c}^{(i)} - \mathbf{b} \right) \right]^{1/2} \tag{3.26}$$

$$H^{(i)} = \left(\mathbf{c}^{(i)} - \mathbf{b} \right)^T \hat{\mathbf{y}} \tag{3.27}$$

The heat input into a particle is then calculated by

$$\dot{U}^{inp(i)} = q m_0^{(i)} \exp\left(-\frac{1}{\ell} \left\langle R_s - R^{(i)} \right\rangle \right) \eta_H^{(i)}, \qquad \text{hemispherical} \tag{3.28}$$

$$\dot{U}^{inp(i)} = q m_0^{(i)} \exp\left(-\frac{1}{\ell} \left\langle H_s - H^{(i)} \right\rangle \right) \eta_P^{(i)}, \qquad \text{planar} \tag{3.29}$$

where q is a power per unit mass heat input and ℓ is a heating depth. In the macroscale simulations, the upper surface of the control volume was initialized in contact with the sample surface. The heating profile was then propagated down through the material as ablation proceeded. A schematic of the heat input is shown in Figure 3.1.

The evolution of the variable L evolves to translate the heating profile downwards through the control volume. The following functional form was considered for L:

$$L = L(M_{frg}, Q, H_{py}, A_0, \rho_0) \tag{3.30}$$

where M_{frg} is the total system fragmented mass loss, Q is the total system heat input, A_0 is the area of the upper face of the sample in the reference configuration, and ρ_0 is the material reference density. The functional forms for L that were considered in this work are discussed in more detail in the preliminary analysis and model validation sections.

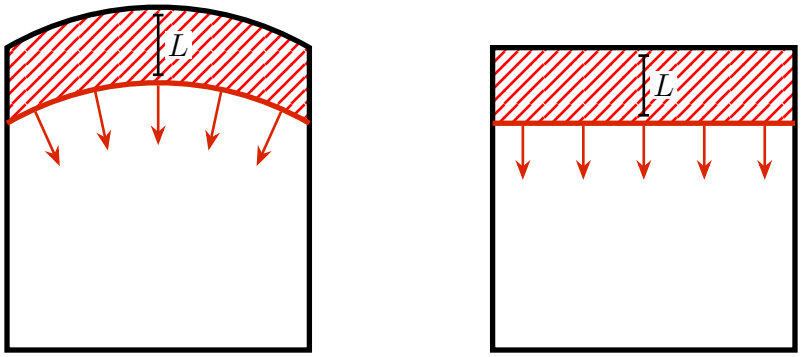

(a) Radial geometry (b) Planar geometry

Figure 3.1: Macroscale heat input schematic. Above the heating surface in the shaded region, the particles receive a constant per unit mass heat input; below the heating surface, the particles receive an exponentially spatially decaying per unit mass heat input, where the decay direction is denoted by the red arrows.

3.6 Particle Kinematics

The particle kinematics in the macroscale is taken from previous work [73, 146] and briefly described here. A particle based density interpolation is used for calculating volumetric change in the particles. For the ellipsoidal particles, the density interpolation is expressed as a function of the ellipsoidal coordinates $\zeta^{(i,j)}$ which are calculated by

$$\zeta^{(i,j)} = \left(\mathbf{r}^{(i,j)^T}\hat{\mathbf{H}}^{(j)}\mathbf{r}^{(i,j)}\right)^{1/2}, \quad \mathbf{r}^{(i,j)} = \mathbf{c}^{(i)} - \mathbf{c}^{(j)} \tag{3.31}$$

where

$$\hat{\mathbf{H}}^{(j)} = \mathbf{R}^{(j)}\mathbf{H}^{(j)}\mathbf{R}^{(j)T} \tag{3.32}$$

with

$$\mathbf{H}^{(j)} = \begin{bmatrix} 2\beta h_1^{(j)} & 0 & 0 \\ 0 & 2\beta h_2^{(j)} & 0 \\ 0 & 0 & 2\beta h_3^{(j)} \end{bmatrix}^{-2} \tag{3.33}$$

In the above, $h_k^{(j)}$ are the semi-major axes of an ellipsoid and β is a constant which allows for close packing in the reference configuration. The rotation matrix $\mathbf{R}^{(j)}$ relates a vector described in a fixed coordinate system ($\mathbf{r}$) to a corresponding vector described in a body fixed co-rotating frame as ($\hat{\mathbf{r}}$)

$$\hat{\mathbf{r}} = \mathbf{R}^{(j)T}\mathbf{r} \tag{3.34}$$

The rotation matrix $\mathbf{R}^{(i)}$ is expressed as a function of the particle euler coordinates as

$$\mathbf{R}^{(j)} = \mathbf{E}^{(j)}{\mathbf{G}^{(j)}}^T \tag{3.35}$$

where

$$\mathbf{E}^{(j)} = \begin{bmatrix} -e_1^{(j)} & e_0^{(j)} & -e_3^{(j)} & e_2^{(j)} \\ -e_2^{(j)} & e_3^{(j)} & e_0^{(j)} & -e_1^{(j)} \\ -e_3^{(j)} & -e_2^{(j)} & e_1^{(j)} & e_0^{(j)} \end{bmatrix} \tag{3.36}$$

$$\mathbf{G}^{(j)} = \begin{bmatrix} -e_1^{(j)} & e_0^{(j)} & e_3^{(j)} & -e_2^{(j)} \\ -e_2^{(j)} & -e_3^{(j)} & e_0^{(j)} & e_1^{(j)} \\ -e_3^{(j)} & e_2^{(j)} & -e_1^{(j)} & e_0^{(j)} \end{bmatrix} \tag{3.37}$$

The angular velocity of the particles $\boldsymbol{\omega}^{(j)}$ expressed in a body fixed co-rotating frame is related to the euler parameters velocities as

$$\boldsymbol{\omega}^{(j)} = 2\mathbf{G}^{(j)}\dot{\mathbf{e}}^{(j)}, \quad \dot{\mathbf{e}}^{(j)} = \frac{1}{2}{\mathbf{G}^{(j)}}^T\boldsymbol{\omega}^{(j)} \tag{3.38}$$

where

$$\mathbf{G}^{(j)}\mathbf{G}^{(j)^T} = \mathbf{I} \tag{3.39}$$

From the above relations, the ellipsoidal coordinate velocities can be written

$$\dot{\zeta}^{(i,j)} = \frac{1}{\zeta^{(i,j)}} \left[\left(\hat{\mathbf{H}}^{(j)} \mathbf{r}^{(i,j)} \right)^T \dot{\mathbf{r}}^{(i,j)} + \left(\mathbf{H}^{(j)} \hat{\mathbf{r}}^{(i,j)} \times \hat{\mathbf{r}}^{(i,j)} \right)^T 2\mathbf{G}^{(j)} \dot{\mathbf{e}}^{(j)} \right] \tag{3.40}$$

where $\hat{\mathbf{r}}^{(i,j)} = \mathbf{R}^{(j)} \mathbf{r}^{(i,j)}$.

The volumetric compression of the particles is calculated by

$$\frac{\rho^{(i)}}{\rho_0^{(i)}} = 1 + \frac{1}{N^{(i)}} \sum_{j=1}^{n_p} \left[\left(\frac{\zeta_0^{(i,j)}}{\zeta^{(i,j)}} \right)^3 - 1 \right] W^{(i,j)} \tag{3.41}$$

where $N^{(i)}$ is the number of near neighbors for a particle in the reference configuration, $\zeta_0^{(i,j)}$ is the ellipsoidal coordinate in the reference configuration, and $W^{(i,j)}$ is a weighting function which ensures that only neighboring particles interact,

$$W^{(i,j)} = (1 - \delta_{ij}) \hat{u} \left[1 - \frac{\zeta^{(i,j)}}{\zeta_0^{(i,j)}} \left(\frac{\rho^{(j)}}{\rho_0^{(j)}} \right)^{\frac{1}{3}} \right] \tag{3.42}$$

The preceding calculations are used for computing particle compression. The rate of change of the particle compression appears in the particle internal energy evolution and is used in the calculation of generalized forces and torques. The rate of change of the particle compression is formulated as

$$\frac{\dot{\rho}^{(i)}}{\rho_0^{(i)}} = -\frac{3}{N^{(i)}} \sum_{j=1}^{n_p} \left(\frac{\zeta_0^{(i,j)}}{\zeta^{(i,j)}} \right)^3 \frac{\dot{\zeta}^{(i,j)}}{\zeta^{(i,j)}} W^{(i,j)} \tag{3.43}$$

3.7 Hamiltonian Formulation

The total kinetic co-energy of the system is simply the sum of the particle kinetic co-energies

$$T^*(\dot{\mathbf{c}}^{(i)}, \dot{\mathbf{e}}^{(i)}, \mathbf{e}^{(i)}, m^{(i)}) = \sum_{i=1}^{n_p} \left(\frac{1}{2} m^{(i)} \dot{\mathbf{c}}^{(i)^T} \dot{\mathbf{c}} + 2 m^{(i)} \dot{\mathbf{e}}^{(i)^T} \mathbf{G}^{(i)^T} \mathbf{J}^{(i)} \mathbf{G}^{(i)} \dot{\mathbf{e}} \right) \quad (3.44)$$

where $m^{(i)}\mathbf{J}^{(i)}$ is the moment of inertia tensor for a particle. The conjugate momenta are

$$\mathbf{p}^{(i)} = \frac{\partial T^*}{\partial \dot{\mathbf{c}}^{(i)}} = m^{(i)} \dot{\mathbf{c}}^{(i)} \quad (3.45)$$

$$\mathbf{g}^{(i)} = \frac{\partial T^*}{\partial \dot{\mathbf{e}}^{(i)}} = 4 m^{(i)} \mathbf{G}^{(i)^T} \mathbf{J}^{(i)} \mathbf{G}^{(i)} \dot{\mathbf{e}}^{(i)} \quad (3.46)$$

The kinetic energy is then defined via the Legendre Transform

$$T = \sum_{i=1}^{n_p} \left(\dot{\mathbf{c}}^{(i)^T} \mathbf{p}^{(i)} + \dot{\mathbf{e}}^{(i)^T} \mathbf{g}^{(i)} \right) - T^* \quad (3.47)$$

which has the canonical form

$$T(\mathbf{p}^{(i)}, \mathbf{g}^{(i)}, \mathbf{e}^{(i)}, m^{(i)}) = \sum_{i=1}^{n_p} \left(\frac{\mathbf{p}^{(i)^T} \mathbf{p}^{(i)}}{2 m^{(i)}} + \frac{1}{8 m^{(i)}} \mathbf{g}^{(i)^T} \mathbf{G}^{(i)^T} \mathbf{J}^{(i)^{-T}} \mathbf{G}^{(i)} \mathbf{g}^{(i)} \right) \quad (3.48)$$

The kinetic co-energy has the total differential

$$dT^* = \sum_{i=1}^{n_p} \left(\mathbf{p}^{(i)^T} d\dot{\mathbf{c}}^{(i)} + \mathbf{g}^{(i)^T} d\dot{\mathbf{e}}^{(i)} + \frac{\partial T^{*^T}}{\partial \mathbf{e}^{(i)}} d\mathbf{e}^{(i)} + \frac{\partial T^*}{\partial m^{(i)}} dm^{(i)} \right) \quad (3.49)$$

From the Legendre transform (equation 3.47), the kinetic energy has the following total differential

$$dT = \sum_{i=1}^{n_p} \left(\dot{\mathbf{c}}^{(i)^T} d\mathbf{p}^{(i)} + \mathbf{p}^{(i)^T} d\dot{\mathbf{c}}^{(i)} + \dot{\mathbf{e}}^{(i)^T} d\mathbf{g}^{(i)} + \mathbf{g}^{(i)^T} d\dot{\mathbf{e}}^{(i)} \right) - dT^* \tag{3.50}$$

$$dT = \sum_{i=1}^{n_p} \left(\dot{\mathbf{c}}^{(i)^T} d\mathbf{p}^{(i)} + \dot{\mathbf{e}}^{(i)^T} d\mathbf{g}^{(i)} - \frac{\partial T^{*^T}}{\partial \mathbf{e}^{(i)}} d\mathbf{e}^{(i)} - \frac{\partial T^{*^T}}{\partial m^{(i)}} dm^{(i)} \right) \tag{3.51}$$

From the canonical form (equation 3.48), the total differential can also be written

$$dT = \sum_{i=1}^{n_p} \left(\frac{\partial T^T}{\partial \mathbf{p}^{(i)}} d\mathbf{p}^{(i)} + \frac{\partial T^T}{\partial \mathbf{g}^{(i)}} d\mathbf{g}^{(i)} + \frac{\partial T^T}{\partial \mathbf{e}^{(i)}} d\mathbf{e}^{(i)} + \frac{\partial T^T}{\partial m^{(i)}} dm^{(i)} \right) \tag{3.52}$$

from which the following relations are obtained

$$\frac{\partial T}{\partial \mathbf{e}^{(i)}} = -\frac{\partial T^*}{\partial \mathbf{e}^{(i)}}, \quad \frac{\partial T}{\partial m^{(i)}} = -\frac{\partial T^*}{\partial m^{(i)}} \tag{3.53}$$

$$\dot{\mathbf{e}}^{(i)} = \frac{\partial T}{\partial \mathbf{g}^{(i)}}, \quad \dot{\mathbf{c}}^{(i)} = \frac{\partial T}{\partial \mathbf{p}^{(i)}} \tag{3.54}$$

Employing the above relations, the following partial derivatives are evaluated [146]:

$$w^{(i)} = -\frac{\partial T}{\partial m^{(i)}} = \frac{1}{2} \dot{\mathbf{c}}^{(i)^T} \dot{\mathbf{c}^{(i)}} + 2 \dot{\mathbf{e}}^{(i)^T} \mathbf{G}^{(i)^T} \mathbf{J}^{(i)} \mathbf{G}^{(i)} \dot{\mathbf{e}}^{(i)} \tag{3.55}$$

$$\mathbf{k}^{(i)} = -\frac{\partial T}{\partial \mathbf{e}^{(i)}} = 4 m^{(i)} \dot{\mathbf{G}}^{(i)^T} \mathbf{J}^{(i)} \dot{\mathbf{G}}^{(i)} \mathbf{e}^{(i)} \tag{3.56}$$

The system Hamiltonian consists of the sum of the system kinetic (T) and potential (V) energies,

$$H = T + V \tag{3.57}$$

The system potential energy is the sum of the particle internal energies and elastic energy stored in the elements

$$V = \sum_{i=1}^{n_p} U^{(i)} + \sum_{i=1}^{n_e} V_0^{e(i)} \psi^{(i)} + \sum_{i=1}^{n_p} \sum_{j=1}^{n_p} \alpha_{ij} V_0^{f(i,j)} \psi^{(i,j)} \tag{3.58}$$

where the boolean α_{ij} determines whether a fiber element connects particles i and j, and the fiber volume $V_0^{f(i,j)}$ is simply the average of the associated particle volumes,

$$V_0^{f(i,j)} = \frac{1}{2}\left(\nu_0^{(i)} + \nu_0^{(j)}\right) \tag{3.59}$$

The system potential energy has the functional form

$$V = V\left(U^{(i)}, \mathbf{c}^{(i)}, \mathbf{e}^{(i)}, d^{(j)}, D^{(i)}, \mathbf{E}^{p(j)}\right) \tag{3.60}$$

which defines the generalized conservative forces

$$\frac{\partial V}{\partial U^{(i)}} = 1 \tag{3.61}$$

$$\frac{\partial V}{\partial \mathbf{c}^{(i)}} = \sum_{j=1}^{n_e} V_0^{e(j)} \mathbf{S}^{(j)} : \frac{\partial \mathbf{E}^{(j)}}{\partial \mathbf{c}^{(i)}} + \sum_{j=1}^{n_p} \alpha_{ij} V_0^{f(i,j)} \sigma^{(i,j)} \frac{\partial \epsilon^{(i,j)}}{\partial \mathbf{c}^{(i)}} \tag{3.62}$$

$$\frac{\partial V}{\partial \mathbf{e}^{(i)}} = \sum_{j=1}^{n_p} \alpha_{ij} V_0^{f(i,j)} \sigma^{(i,j)} \frac{\partial \epsilon^{(i,j)}}{\partial \mathbf{e}^{(i)}} \tag{3.63}$$

The strain energy release rates due to damage evolution in the elements are

$$\frac{\partial V}{\partial d^{(j)}} = -V_0^{e(j)} \mu^{(j)} tr\left(\mathbf{E}^{e(j)^T} \mathbf{E}^{e(j)}\right) = -\Gamma^{d(j)} \tag{3.64}$$

$$\frac{\partial V}{\partial D^{(i)}} = -\sum_{j=1}^{n_p} \alpha_{ij} V_0^{f(i,j)} \frac{1}{4} E^{(i,j)} \langle \epsilon^{e(i,j)} \rangle^2 = -\Gamma^{D(i)} \tag{3.65}$$

The stress associated with plastic evolution in the elements are

$$\frac{\partial V}{\partial \mathbf{E}^{p(j)}} = -V_0^{e(j)} \mathbf{S}^{(j)} \tag{3.66}$$

3.7.1 Virtual Work

Forces that arise due to the evolution of the particle masses must be accounted for in the formulation of the virtual work. Similar to the mesoscale model, the virtual work is considered as the sum of an internal and external portion [70, 89].

$$\delta W = \delta W^{int} + \delta W^{ext} \tag{3.67}$$

where the internal virtual work is associated with the forces arising from particle mass evolution. The internal virtual work is formulated as

$$\delta W^{int} = \sum_{i=1}^{n_p} \Bigg[\dot{m}^{(i)} \left(\dot{\mathbf{c}}^{(i)^T} \delta \mathbf{c}^{(i)} + 4 \left(\mathbf{G}^{(i)^T} \mathbf{J}^{(i)} \mathbf{G}^{(i)} \dot{\mathbf{e}}^{(i)} \right)^T \delta \mathbf{e}^{(i)} \right) - \delta m^{(i)} \left(\dot{\mathbf{c}}^{(i)^T} \dot{\mathbf{c}}^{(i)} + 4 \dot{\mathbf{e}}^{(i)^T} \mathbf{G}^{(i)^T} \mathbf{J}^{(i)} \mathbf{G}^{(i)} \dot{\mathbf{e}}^{(i)} \right) \Bigg] \tag{3.68}$$

which balances the rate of change of kinetic energy in the particles due to mass loss. It is noted that the internal virtual work performs no net work on the system, as the above yields zero when the variations are taken to be physical ($\delta \mathbf{c}^{(i)} = \dot{\mathbf{c}}^{(i)} dt$, $\delta \mathbf{e}^{(i)} = \dot{\mathbf{e}}^{(i)} dt$, $\delta m^{(i)} = \dot{m}^{(i)} dt$). The external virtual work is

$$\delta W^{ext} = \sum_{i=1}^{n_p} \left(h^{ext(i)} \delta m^{(i)} + \mathbf{f}^{ext(i)^T} \delta \mathbf{c}^{(i)} + 2 \mathbf{M}^{ext(i)^T} \mathbf{G}^{(i)} \delta \mathbf{e}^{(i)} \right) \tag{3.69}$$

where $h^{ext(i)}$ is an external enthalpy, and $\mathbf{f}^{ext(i)}$ and $\mathbf{M}^{ext(i)}$ account for external forces and torques that may be exerted on the particles.

3.7.2 Nonholonomic Constraints

The nonholonomic constraints include the evolution of the particle internal energy, which is

$$\dot{U}^{(i)} = \dot{U}^{wrk(i)} + \dot{U}^{irr(i)} - \dot{U}^{con(i)} + \dot{U}^{inp(i)} + \dot{U}^{trc(i)} \tag{3.70}$$

where $\dot{U}^{wrk(i)}$ is associated with volumetric deformation of the particles, $\dot{U}^{irr(i)}$ with viscous dissipation between particles and damage evolution and plastic evolution in the elements, $\dot{U}^{con(i)}$ with heat conduction between the particles, $\dot{U}^{inp(i)}$ with external heating of the particles, and $\dot{U}^{trc(i)}$ is associated with transpiration cooling in the particles. Power flow in the particles due to volumetric deformation is

$$\dot{U}^{wrk(i)} = m^{(i)} \frac{P^{(i)}}{\rho^{(i)2}} \dot{\rho}^{(i)} \tag{3.71}$$

The irreversible power in the particles includes viscous dissipation between particles and damage and plastic evolution in the elements

$$\begin{aligned} \dot{U}^{irr(i)} =& \mathbf{f}^{v(i)^T} \dot{\mathbf{c}}^{(i)} + \mathbf{M}^{v(i)^T} 2\mathbf{G}^{(i)} \dot{\mathbf{e}}^{(i)} + \sum_{j=1}^{n_e} \phi^{(i,j)} \Gamma^{d(j)} \dot{d}^{(j)} + \Gamma^{D(i)} \dot{D}^{(i)} + \\ & \sum_{j=1}^{n_e} \phi^{(i,j)} V_0^{e(j)} tr\left(\mathbf{S}^{(j)^T} \dot{\mathbf{E}}^{p(j)} \right) \end{aligned} \tag{3.72}$$

where $\mathbf{f}^{v(i)}$ and $\mathbf{M}^{v(i)}$ are a viscous force and viscous torque,

$$\mathbf{f}^{v(i)} = \sum_{j=1}^{n_p} \tau^{(i,j)} \left(\dot{\mathbf{c}}^{(i)} - \dot{\mathbf{c}}^{(j)} \right) \tag{3.73}$$

$$\mathbf{M}^{v(i)} = \sum_{j=1}^{n_p} m^{(i,j)} \mathbf{R}^{(i)^T} \left(2\mathbf{R}^{(i)} \mathbf{G}^{(i)} \dot{\mathbf{e}}^{(i)} - 2\mathbf{R}^{(j)} \mathbf{G}^{(j)} \dot{\mathbf{e}}^{(j)} \right) \tag{3.74}$$

and $\tau^{(i,j)}$ and $m^{(i,j)}$ are viscosity coefficients. Numerical conduction between particles has the form

$$\dot{U}^{con(i)} = \sum_{k=1}^{n_p} \kappa^{(i,j)}(\theta^{(i)} - \theta^{(j)}) \tag{3.75}$$

where $\kappa^{(i,j)}$ is a numerical conduction coefficient. The transpiration cooling in the particles is formulated as

$$\dot{U}^{trc(i)} = \left(u^{(i)} + \frac{P^{(i)}}{\rho^{(i)}} + h_{dec} \right) \dot{m}^{(i)} \tag{3.76}$$

where the energy ejected from the particle is defined as the sum of a particle enthalpy and a decomposition enthalpy h_{dec}.

3.7.3 Hamilton's Equations

The system level model is obtained by combining the macroscale Hamiltonian with the canonical Hamilton's equations, virtual work expression, and nonholonomic constraints describing the evolution of the particle internal energies, particle masses, element plastic and accumulated plastic strain, and element damage. A holonomic constraint for the particle euler parameters is also present,

$$\mathbf{e}^{(i)^T} \mathbf{e}^{(i)} = 1 \tag{3.77}$$

The canonical Hamilton's equations are

$$\dot{\mathbf{p}}^{(i)} = -\frac{\partial V}{\partial \mathbf{c}^{(i)}} + \mathbf{q}^{c(i)}, \quad \dot{\mathbf{c}}^{(i)} = \frac{\mathbf{p}^{(i)}}{m^{(i)}}, \quad \dot{\mathbf{g}}^{(i)} = -\frac{\partial V}{\partial \mathbf{e}^{(i)}} + \mathbf{k}^{(i)} + \mathbf{q}^{e(i)},$$

$$\dot{\mathbf{e}}^{(i)} = \frac{1}{4}\mathbf{G}^{(i)^T}\mathbf{J}^{(i)^{-1}}\mathbf{G}^{(i)}\mathbf{g}^{(i)}, \quad 0 = w^{(i)} + q^{m(i)}, \quad 0 = -\frac{\partial V}{\partial U^{(i)}} + q^{U(i)},$$

$$0 = -\frac{\partial V}{\partial \mathbf{E}^{p(j)}} + \mathbf{Q}^{Ep(j)}, \quad 0 = -\frac{\partial V}{\partial d^{(j)}} + q^{d(j)}, \quad 0 = -\frac{\partial V}{\partial D^{(i)}} + q^{D(i)} \tag{3.78}$$

where $\mathbf{q}^{c(i)}$, $\mathbf{q}^{e(i)}$, $q^{m(i)}$, $q^{U(i)}$, $\mathbf{Q}^{Ep(j)}$, $q^{d(j)}$, and $q^{D(i)}$ are generalized non conservative forces. Introducing Lagrange multipliers $\gamma^{m(i)}$, $\gamma^{U(i)}$, $\mathbf{X}^{p(j)}$, $\gamma^{d(j)}$, and $\gamma^{D(i)}$ for the nonholonomic constraints, and a Lagrange multiplier $\gamma^{e(i)}$ for the holonomic euler parameter constraint, the generalized forces are

$$\begin{aligned}
\mathbf{q}^{c(i)} =& 3\sum_{j=1}^{n_p}\left(\frac{m^{(i)}\rho_0^{(i)}}{N^{(i)}}\frac{P^{(i)}}{\rho^{(i)2}}\frac{\zeta_0^{(i,j)3}}{\zeta^{(i,j)5}}\hat{\mathbf{H}}^{(j)}W^{(i,j)}\gamma^{U(i)} + \right. \\
& \left.\frac{m^{(j)}\rho_0^{(j)}}{N^{(j)}}\frac{P^{(j)}}{\rho^{(j)2}}\frac{\zeta_0^{(j,i)3}}{\zeta^{(j,i)5}}\hat{\mathbf{H}}^{(i)}W^{(j,i)}\gamma^{U(j)}\right)\mathbf{r}^{(i,j)} - \mathbf{f}^{v(i)}\gamma^{U(i)} + \\
& \dot{m}^{(i)}\dot{\mathbf{c}}^{(i)} + \mathbf{f}^{ext(i)}
\end{aligned} \tag{3.79}$$

$$\begin{aligned}
\mathbf{q}^{e(i)} =& 3\sum_{j=1}^{n_p}\frac{m^{(j)}\rho_0^{(j)}}{N^{(j)}}\frac{P^{(j)}}{\rho^{(j)2}}\frac{\zeta_0^{(j,i)3}}{\zeta^{(j,i)5}}2\mathbf{G}^{(i)^T}\left(\mathbf{H}^{(i)}\hat{\mathbf{r}}^{(i,j)}\times\hat{\mathbf{r}}^{(i,j)}\right)W^{(j,i)}\gamma^{U(j)} \\
& - 2\mathbf{G}^{(i)^T}\mathbf{M}^{v(i)}\gamma^{U(i)} + 4\dot{m}^{(i)}\mathbf{G}^{(i)^T}\mathbf{J}^{(i)}\mathbf{G}^{(i)}\dot{\mathbf{e}}^{(i)} + 2\mathbf{G}^{(i)^T}\mathbf{M}^{ext(i)} + \\
& \gamma^{e(i)}\mathbf{e}^{(i)}
\end{aligned} \tag{3.80}$$

$$q^{m(i)} = h^{ext(i)} - 2\,w^{(i)} - \left(u^{(i)} + \frac{P^{(i)}}{\rho^{(i)}} + h_{dec}\right)\gamma^{U(i)} + \gamma^{m(i)} \tag{3.81}$$

$$q^{U(i)} = \gamma^{U(i)} \tag{3.82}$$

$$\mathbf{Q}^{Ep(j)} = -V_0^{e(j)}\mathbf{S}^{(j)}\sum_{i=1}^{n_p}\phi^{(i,j)}\gamma^{U(i)} + \mathbf{X}^{p(j)} \tag{3.83}$$

$$q^{d(j)} = -\Gamma^{d(j)} \sum_{i=1}^{n_p} \phi^{(i,j)} \gamma^{U(i)} + \gamma^{d(j)} \tag{3.84}$$

$$q^{D(i)} = -\Gamma^{D(i)} \gamma^{U(i)} + \gamma^{D(i)} \tag{3.85}$$

Substituting the above into the degenerate canonical Hamilton equations, the Lagrange multipliers associated with the nonholonomic constraints can be solved for in closed form.

$$\gamma^{U(i)} = 1, \quad \gamma^{m(i)} = u^{(i)} + \frac{P^{(i)}}{\rho^{(i)}} + h_{dec} + w^{(i)} - h^{ext(i)}$$
$$\mathbf{X}^{p(j)} = \mathbf{0}, \quad \gamma^{d(j)} = 0, \quad \gamma^{D(i)} = 0 \tag{3.86}$$

The generalized forces and torques due to particle interactions can then be written

$$\begin{aligned}\mathbf{q}^{c(i)} =& 3 \sum_{j=1}^{n_p} \left(\frac{m^{(i)} \rho_0^{(i)}}{N^{(i)}} \frac{P^{(i)}}{\rho^{(i)2}} \frac{\zeta_0^{(i,j)3}}{\zeta^{(i,j)5}} \hat{\mathbf{H}}^{(j)} W^{(i,j)} + \right. \\ & \left. \frac{m^{(j)} \rho_0^{(j)}}{N^{(j)}} \frac{P^{(j)}}{\rho^{(j)2}} \frac{\zeta_0^{(j,i)3}}{\zeta^{(j,i)5}} \hat{\mathbf{H}}^{(i)} W^{(j,i)} \right) \mathbf{r}^{(i,j)} - \mathbf{f}^{v(i)} + \dot{m}^{(i)} \dot{\mathbf{c}}^{(i)} + \mathbf{f}^{ext(i)}\end{aligned} \tag{3.87}$$

$$\begin{aligned}\mathbf{q}^{e(i)} =& 3 \sum_{j=1}^{n_p} \frac{m^{(j)} \rho_0^{(j)}}{N^{(j)}} \frac{P^{(j)}}{\rho^{(j)2}} \frac{\zeta_0^{(j,i)3}}{\zeta^{(j,i)5}} 2\mathbf{G}^{(i)T} \left(\mathbf{H}^{(i)} \hat{\mathbf{r}}^{(i,j)} \times \hat{\mathbf{r}}^{(i,j)} \right) W^{(j,i)} \\ & - 2\mathbf{G}^{(i)T} \mathbf{M}^{v(i)} + 4\dot{m}^{(i)} \mathbf{G}^{(i)T} \mathbf{J}^{(i)} \mathbf{G}^{(i)} \dot{\mathbf{e}}^{(i)} + \\ & 2\mathbf{G}^{(i)T} \mathbf{M}^{ext(i)} + \gamma^{e(i)} \mathbf{e}^{(i)}\end{aligned} \tag{3.88}$$

The method employed for treating the remaining Lagrange multiplier $\gamma^{e(i)}$ due to the holonomic euler parameter constraint (equation 3.77) is taken from previous work [146] and briefly described here. An angular momentum vector $\mathbf{h}^{(i)} = m^{(i)} \mathbf{J}^{(i)} \boldsymbol{\omega}^{(i)}$ is introduced, which can be related to the conjugate

momentum vector $\mathbf{g}^{(i)}$ as

$$\mathbf{h}^{(i)} = m^{(i)}\mathbf{J}^{(i)}\boldsymbol{\omega}^{(i)} = \frac{1}{2}\mathbf{G}^{(i)}\mathbf{g}^{(i)} \tag{3.89}$$

The time derivative of $\mathbf{h}^{(i)}$ is then

$$\dot{\mathbf{h}}^{(i)} = \frac{1}{2}\dot{\mathbf{G}}^{(i)}\mathbf{g}^{(i)} + \frac{1}{2}\mathbf{G}^{(i)}\left(-\frac{\partial V}{\partial \mathbf{e}^{(i)}} + \mathbf{k}^{(i)} + \mathbf{q}^{e(i)}\right) \tag{3.90}$$

The above can be re-written by noting that the skew symmetric matrix $\boldsymbol{\Omega}^{(i)}$ associated with the angular velocity $\boldsymbol{\omega}^{(i)}$ as

$$\boldsymbol{\Omega}^{(i)}\mathbf{r} = -\boldsymbol{\omega}^{(i)} \times \mathbf{r} \tag{3.91}$$

is related to the euler parameter velocities by

$$\boldsymbol{\Omega}^{(i)} = 2\mathbf{G}^{(i)}\dot{\mathbf{G}}^{(i)^T} = -2\dot{\mathbf{G}}^{(i)}\mathbf{G}^{(i)^T} \tag{3.92}$$

Using the above relation, the following can be derived

$$\dot{\mathbf{G}}^{(i)}\mathbf{g}^{(i)} = \mathbf{G}^{(i)}\mathbf{k}^{(i)} = -\boldsymbol{\Omega}^{(i)}\mathbf{h}^{(i)} \tag{3.93}$$

The time derivative of $\mathbf{h}^{(i)}$ can then be written

$$\dot{\mathbf{h}}^{(i)} = -\boldsymbol{\Omega}^{(i)}\mathbf{h}^{(i)} - \frac{1}{2}\mathbf{G}^{(i)}\frac{\partial V}{\partial \mathbf{e}^{(i)}} + \frac{1}{2}\mathbf{G}^{(i)}\mathbf{q}^{e(i)} \tag{3.94}$$

Finally, the Lagrange multiplier $\gamma^{e(i)}$ is eliminated by the identity

$$\mathbf{G}^{(i)}\mathbf{e}^{(i)} = 0 \tag{3.95}$$

allowing $\dot{\mathbf{h}}^{(i)}$ to be written as

$$\dot{\mathbf{h}}^{(i)} = -\boldsymbol{\Omega}^{(i)}\mathbf{h}^{(i)} - \frac{1}{2}\mathbf{G}^{(i)}\frac{\partial V}{\partial \mathbf{e}^{(i)}} + \mathbf{q}^{(i)} \tag{3.96}$$

where $\mathbf{q}^{(i)}$ is

$$\begin{aligned}
\mathbf{q}^{(i)} =& \frac{1}{2}\mathbf{G}^{(i)}\mathbf{q}^{e(i)} \\
\mathbf{q}^{(i)} =& 3\sum_{j=1}^{n_p} \frac{m^{(j)}\rho_0^{(j)}}{N^{(j)}} \frac{P^{(j)}}{\rho^{(j)2}} \frac{\zeta_0^{(j,i)3}}{\zeta^{(j,i)5}} \left(\mathbf{H}^{(i)}\hat{\mathbf{r}}^{(i,j)} \times \hat{\mathbf{r}}^{(i,j)}\right) W^{(j,i)} \\
& - \mathbf{M}^{v(i)} + 2\dot{m}^{(i)}\mathbf{J}^{(i)}\mathbf{G}^{(i)}\dot{\mathbf{e}}^{(i)} + \mathbf{M}^{ext(i)}
\end{aligned} \tag{3.97}$$

The final Hamilton equations are then

$$\dot{\mathbf{p}}^{(i)} = -\frac{\partial V}{\partial \mathbf{c}^{(i)}} + \mathbf{q}^{c(i)} \tag{3.98}$$

$$\dot{\mathbf{c}}^{(i)} = \frac{\mathbf{p}^{(i)}}{m^{(i)}} \tag{3.99}$$

$$\dot{\mathbf{h}}^{(i)} = -\mathbf{\Omega}^{(i)}\mathbf{h}^{(i)} - \frac{1}{2}\mathbf{G}^{(i)}\frac{\partial V}{\partial \mathbf{e}^{(i)}} + \mathbf{q}^{(i)} \tag{3.100}$$

$$\dot{\mathbf{e}}^{(i)} = \frac{1}{2m^{(i)}}\mathbf{G}^{(i)^T}\mathbf{J}^{(i)^{-1}}\mathbf{h}^{(i)} \tag{3.101}$$

which combined with the evolution equations for the particle internal energies, particle masses, element plastic and accumulated plastic strain and element damage, constitute the system level equations.

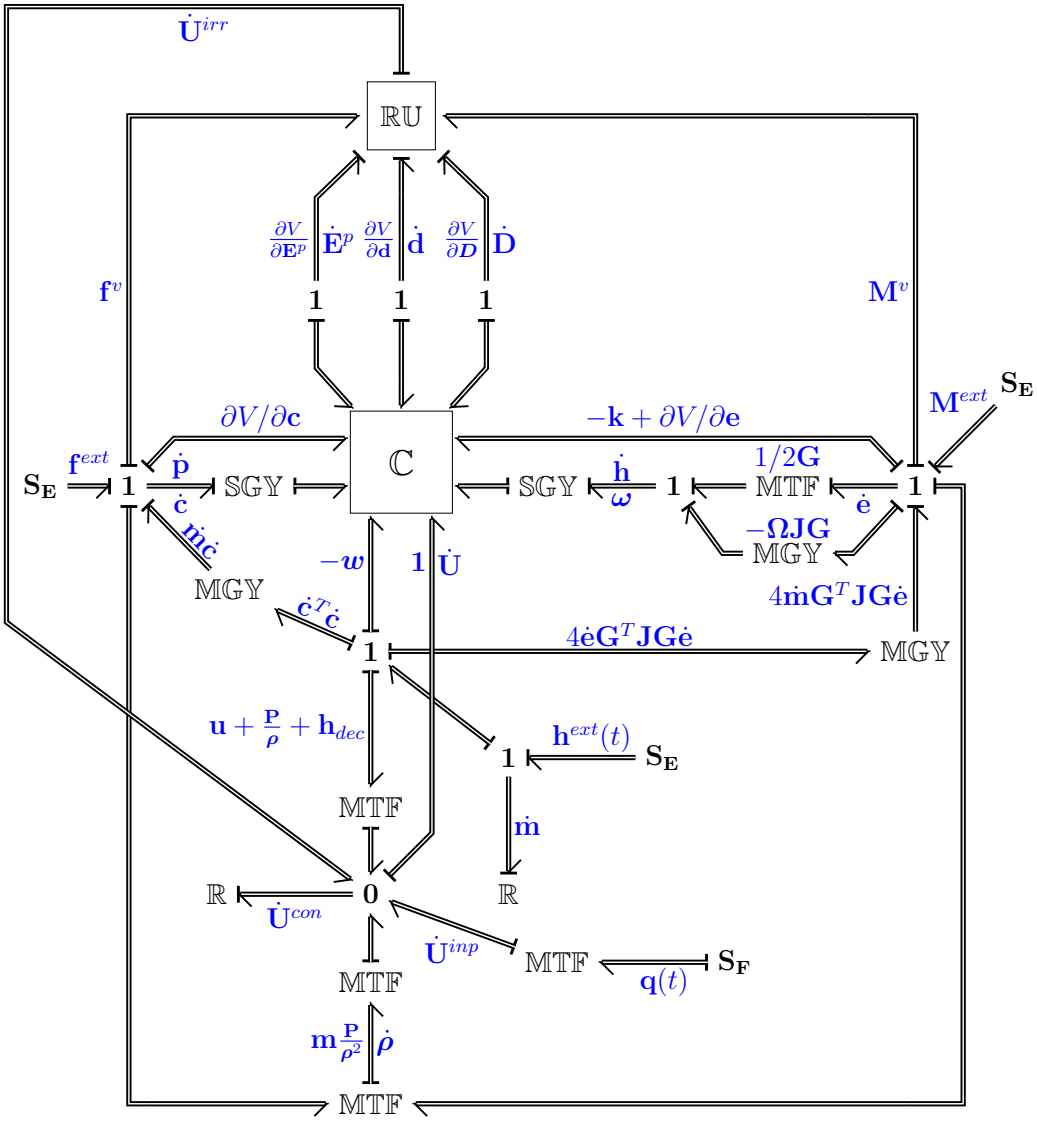

Figure 3.2: Macroscale model bond graph. The particle internal energies are treated as generalized coordinates where the associated efforts are unity. This has also been employed in previous work by Hean and Fahrenthold [54, 70].

3.8 Preliminary Analysis

As described in section 3.5, a per unit mass heat input is applied to the particles residing within a heating control volume. The heat input has an exponentially decaying spatial profile described by a moving surface which translates through the control volume, propagating the heat input profile. Propagation of the heating profile based on the total fragmented mass loss was first considered:

$$L = \hat{L}\frac{M_{frg}}{A_0\,\rho_0} \tag{3.102}$$

where L describes the translation of the heating surface (see equation 3.25), and $\hat{L}$ is a dimensionless surface translation constant. The above aims to propagate the heat input with the erosion of the material. However, the heat input propagation behavior was sensitive to particle sizes and exhibited poor convergence with particle resolution. A second expression based on the total system heat input was thus considered, which is used for all the preliminary simulations presented in the following sections:

$$L = \hat{L}\frac{Q}{H_{py}\,\rho_0\,A_0} \tag{3.103}$$

In implementing the above, once a particle is spalled off from the bulk material due to the failure of its associated elements, an aerodynamic loading is applied to the fragmented particle to transport it out of the heating volume.

Validation of the macroscale model is based on comparing simulation predictions of mass loss at a given heat input to experimental mass loss mea-

surements. Experimental methods, however, cannot make direct measurements of the actual heat flux on the material [129] and generally report experimental heat flux conditions as a "cold wall" heat flux measured by an actively cooled calorimeter [158]. For performing comparison to experiment, an experimental heat input is defined in this work as the cold wall heat load minus the re-radiated heat load:

$$Q_{cw} - Q_{rr} = (q_{cw} - q_{rr})\, AT \tag{3.104}$$

where q_{cw} is the reported experimental cold wall heat flux, A the projected area, T the exposure time, and q_{rr} an estimated re-radiated flux. The re-radiated flux is calculated as

$$q_{rr} = \epsilon \sigma \theta_{sur}^4 \tag{3.105}$$

where ϵ is the material emissivity, σ is Stefan-Boltzmann's constant, and θ_{sur} is the reported experimental surface temperature. In subtracting the re-radiated heat load from the cold wall heat load, re-radiation is then excluded in the macroscale model. Further details regarding the above calculation are provided in the appendix for each validation test case.

The following sections present simulations for three fiber reinforcement architectures: a 3-D, 2-D and short fiber architecture. Each architecture is differentiated by how the fiber bar element connectivities are selected. In previous research on the simulation of fabrics [133, 144], the fabric weave pattern was explicitly represented by the bar elements and particles. In this dissertation,

since the particle centers of mass define the vertices of hexahedral elements and tension only bar elements, the bar elements approximately capture the architecture of the fiber reinforcement and do not explicitly represent weave patterns. The macroscale program is parallelized with hybrid OpenMP-MPI. Previous work has analyzed the code performance in more detail [72] where maximizing shared memory was observed to produce the best performance, as particle methods require that each particle's time varying near neighbor set be tracked, resulting in substantial computational cost for the associated message passing. The preliminary simulations presented in the following sections were conducted on two nodes (Intel Xeon Phi 7250) with OpenMP parallelization on each node and message passing between nodes, requiring 10-33 wall clock hours.

3.8.1 Ablation Simulation for a Carbon Fiber Reinforced Phenolic Composite

This section presents the macroscale ablation simulation of a carbon fiber reinforced phenolic composite. The composite parameters are the same as the mesoscale simulation (section 2.8.1), with a composite density of 1450 kg/m^3 and resin mass fraction of 0.375, which are representative of the material tested by Pesci et al. [125], who conducted experimental plasma torch ablation tests of a carbon fiber reinforced phenolic composite under various heat fluxes and exposure times (see Appendix A).

The test article geometry consists of a cylinder with a hemispherical

cap, having a sample radius of 0.5 cm and a total height of 1.3 cm. A schematic of the test article from Ref [125] is provided in Figure A.1. The authors performed testing under three cold wall heat fluxes (0.626, 0.903, 1.379 MW/m^2) with four exposure times for each flux (30, 50, 70, 90 s). Total mass loss was measured by weighing the samples prior to and after testing. The reported test conditions, mass loss, and calculated values of Q_{cw} and Q_{rr} are listed in Table A.1, where Q_{cw} and Q_{rr} are calculated by equations A.1 and A.2. The authors did not measure surface temperature, which is needed for the calculation of the re-radiated heat load Q_{rr}. In this research, the surface temperatures are estimated based on other plasma torch experiments in the literature conducted by Silva et al. [43], who conducted ablation tests of tape wrapped carbon phenolic at similar heat fluxes of 0.626, 0.903 and 1.376 MW/m^2, and are listed in Table A.1. A plot of the experimental mass loss versus the calculated $Q_{cw} - Q_{rr}$ is shown in Figure A.2.

Figure 3.3 shows the initial configuration in the macroscale ablation simulation. The fiber reinforcement is modeled with a 3-D geometry where the fiber bar elements are visualized in black. The ablated configuration at a heat input of 15 kJ is shown in Figure 3.4. As mentioned, experimental methods cannot directly measure the heat flux on the material; the preceding section defines an experimental heat input as the cold wall minus re-radiated heat load $Q_{cw} - Q_{rr}$. At a given total mass loss, the simulation heat input was observed to be consistently lower than the value of $Q_{cw} - Q_{rr}$. Match between the simulation heat input and $Q_{cw} - Q_{rr}$, shown in Figure 3.5, requires very

high resin and fiber specific heats in the macroscale model. Table 3.2 lists the material properties used in the multiscale model.

3.8.2 Ablation Simulation for PICA (Phenolic Impregnated Carbon Ablator)

This section presents the macroscale ablation simulation of PICA (phenolic impregnated carbon ablator). The composite parameters are the same as the mesoscale simulation (section 2.8.2), with a composite density of 274 kg/m^3 and a resin mass fraction of 0.38 [114]. Tran et al. conducted arc-jet testing of PICA under various heat fluxes and exposure times with varying sample geometries (see Appendix B). The sample geometries were cylindrical with a flat surface, having diameters of 1, 2, 3, and 4 inches (2.54, 5.08, 7.62, 10.16 cm). Cold wall heat fluxes ranged from 426–3362 W/cm^2. Table B.2 lists the arc-jet test cases reported in Ref [158], including the sample diameters, cold wall fluxes, exposure times, surface temperatures and total mass loss. Table B.3 includes the calculated values of Q_{cw} and Q_{rr}.

In order to achieve the experimental heat flux range, the sample diameters were varied by a factor of four in the experimental tests (see Table B.2). Figure B.2 shows a plot of the experimental mass loss versus the cold wall minus re-radiated heat load $Q_{cw} - Q_{rr}$ in which the mass loss versus heat input behavior is observed to be test article size dependent. A more uniform trend, though with still significant scatter, can be achieved by normalizing the total mass loss as M/D^n, where M is the total mass loss, D is the sample

diameter, and n is an exponent. This behavior is also qualitatively reproduced by the macroscale model. A dimensional analysis for this relation is presented in appendix B. Figure B.3 shows a plot of the normalized experimental mass loss versus $Q_{cw} - Q_{rr}$ with n set to a value of 1.47.

The initial configuration for the 10.16 cm diameter model in the macroscale ablation simulation is shown in Figure 3.6. PICA uses Fiberform, a commercial insulation material with a short chopped carbon fiber architecture [158], as the fiber substrate. Reflective of the structure of Fiberform, the fiber bar elements are selected as having random lengths and orientations. Since the fibers lack cohesive connectivity, the fibers are released from the bulk material once the surrounding elements are ablated, which is reflective of arc-jet experiments of PICA in which exposed fibers are observed to spallate from the surface of the material [95, 128]. The ablated configuration at a heat input of 0.85 MJ is shown in Figure 3.7. Similar to the ablation simulations of the high density carbon phenolic material presented in the preceding section, match between the simulation heat input and the experimental cold wall minus re-radiated heat load $Q_{cw} - Q_{rr}$ at a given total mass loss, shown in Figures 3.8 and 3.9, requires very high resin and fiber specific heats in the macroscale model. Table 3.2 lists the material properties used in the multiscale model.

3.8.3 Ablation Simulation for a Carbon Fiber Reinforced Cyanate Ester Composite

This section presents the macroscale ablation simulation of a carbon fiber reinforced cyanate ester composite. The composite parameters are the same as the mesoscale simulation (section 2.8.3), with a composite density of 1710 kg/m^3 and resin mass fraction of 0.114, which are representative of the material tested by Nahar [119], who conducted oxyacetylene torch ablation tests of a carbon fiber reinforced cyanate ester material. The test article geometry is a cylinder with a radius of 1.5 cm and height of 1.27 cm. The oxyacetylene tests were conducted according to ASTM E 285 [10]. The heat flux was estimated by the author from the torch conditions as 1000 W/cm^2, though no calorimeter measurements were reported. The total mass loss was measured at 0.588 g at an exposure time of 28 s. A summary of the sample parameters and oxyacetylene torch test results are listed in Table C.1. A surface temperature is not reported, which is needed for the calculation of the re-radiated heat load Q_{rr}. The surface temperature in this research is estimated as 2273 K from published oxyacetylene torch ablation experiments in the literature conducted on the same experimental apparatus on a fully dense carbon phenolic material [77]. An additional issue is that the flame diameter is significantly smaller than the sample diameter. In this research, a rough estimate of the experimental cold wall minus re-radiated heat load $Q_{cw} - Q_{rr}$ was made by assuming a Gaussian radial distribution for the heat flux based on the literature [104, 135, 154]. The heating radius is estimated

from the ablation test images provided in Ref [119]. The estimated values of Q_{cw} and $Q_{cw}-Q_{rr}$ are 17.6 and 15.2 kJ respectively and are listed in Table C.1, with the details of the calculations described in the appendix (see appendix C).

The initial configuration for the ablation problem is shown in Figure 3.10. The fiber reinforcement is modeled with a 2-D geometry, reflecting the material's laminate architecture. The ablated configuration at a heat input of 14.8 kJ is shown in Figure 3.11. Similar to the ablation simulations of the carbon phenolic materials presented in the preceding sections, match between the simulation heat input and the experimental cold wall minus re-radiated heat load $Q_{cw} - Q_{rr}$ at a given total mass loss requires very high resin and fiber specific heats in the macroscale model. Table 3.5 compares the simulated total mass loss versus experiment. Table 3.4 lists the material properties used in the multiscale model.

In the oxyacetylene experiments, minimal recession was observed with mass loss resulting primarily from the ablation of the resin matrix. This is reflected in the simulation in which there is no bulk mass removal. As an extension to more severe ablation conditions, a simulation was also conducted with a total heat input of 238 kJ, shown in Figure 3.12, which results in a total mass loss of 7.81 g and significant ablation of the fiber.

3.8.4 Summary

This section presents the simulations of three materials with different fiber reinforcement architectures: a 3-D, 2-D and short fiber architecture. For each case, the total simulated mass loss versus the total heat input into the material is compared to published experimental results. In comparing simulation to experiment, the simulation heat input is equated with the cold wall minus re-radiated heat load $Q_{cw} - Q_{rr}$.

Table 3.1 shows a comparison of the three materials (carbon reinforced phenolic, carbon reinforced cyanate ester, and PICA) on the resin heat of pyrolysis H_{py} computed from the mesoscale simulation results, and the effective heat of ablation H_{eff} computed from the macroscale simulation results as the total heat input divided by the total mass loss. The total mass loss in the macroscale model includes both resin and fiber mass loss. The H_{eff} metric has relevance in previous literature [157, 158] where material performance in experimental arc-jet ablation tests was similarly assessed based on an energy per unit mass ablation quantity. As seen in Table 3.1, the carbon reinforced cyanate ester material has a higher computed resin heat of pyrolysis H_{py} than the carbon reinforced phenolic material and PICA. However, as discussed in the mesoscale model (see section 2.8.3), the high resin heat of pyrolysis for the carbon cyanate ester composite is due primarily to the low resin weight loading, which results in a significant portion of the heat input into the material being spent on heating the carbon. In the macroscale model, the carbon reinforced cyanate ester is predicted to have a similar effective of heat ablation H_{eff} to

the carbon reinforced phenolic. Since the ablation experiments for the carbon cyanate ester composite had negligible carbon ablation [119], the macroscale model is used to extend beyond the experimental test range in order to compare the carbon cyanate ester composite with the other materials. Out of the three materials, PICA is predicted to have the best performance in terms of H_{eff}.

At a given total mass loss, the simulation heat input tends to be lower than the value of $Q_{cw} - Q_{rr}$, requiring very high resin and fiber specific heats in the macroscale model to obtain a match between the two quantities. The preliminary results thus suggest that the simulation heat input is not an accurate physical equivalent to the experimental cold wall minus re-radiated heat load. This matter may be explained by the fact that experimental cold wall heat fluxes overestimate the actual heat flux on the material [83, 127, 129]. For estimating the actual heat flux, the literature generally estimates a so-called "hot wall" heat flux (q_{hw}) as $q_{hw} = q_{cw}(1 - h_w/h_r)$ [83, 127] where h_r is a recovery enthalpy and h_w is an estimated fluid enthalpy at the solid surface. The correlation aims to relate the convective heat flux from a cold surface to a hot surface, which is taken to be a better estimate of the actual heat flux on the material. The preliminary results suggest that a simulation hot wall heat input is essentially being compared to an experimental cold wall heat input. Thus, to compare simulation to experiment, the following section presents the formulation of a cold wall heat input model.

Table 3.1: Comparison of the three ablative materials presented in sections 3.8.1 to 3.8.3 (carbon reinforced phenolic, PICA, and carbon reinforced cyanate ester) on the computed resin heat of pyrolysis H_{py} and effective heat of ablation H_{eff}.

	H_{py}^{a} (MJ/kg)	H_{eff}^{b} (MJ/kg)
Carbon reinforced phenolic	1.4	27
PICA	1.4	43
Carbon reinforced cyanate ester	4.3	30[c]

[a] The resin heat of pyrolysis H_{py} is computed from the mesoscale simulation results (see sections 2.8.1 to 2.8.3).
[b] The effective heat of ablation H_{eff} is computed from the macroscale simulation results as the total heat input divided by the total mass loss.
[c] The H_{eff} value is computed for the simulation case with significant carbon ablation, which extends beyond the experimental ablation test [119] in which only a thin layer of matrix material was removed.

Table 3.2: Comparison of macroscale and mesoscale material properties for a carbon fiber reinforced phenolic composite.

material property	Macroscale	Mesoscale
fiber specific heat c_{v_f}	2000 J/kgK	771 J/kgK
resin specific heat c_{v_r}	2720 J/kgK	1674 J/kgK
heat of decomposition h_{dec}^{a}	0	293 kJ/kg
heat of pyrolysis H_{py}	2 MJ/kg	1.42 MJ/kg
fiber failure internal energy u_f^{fib}	10.08 MJ/kg	na

[a] The difference between the meso and macroscale value of 293 kJ/kg for h_{dec} is less than 1% of both the simulation and experimental values for the ratio of heat input to total mass loss.

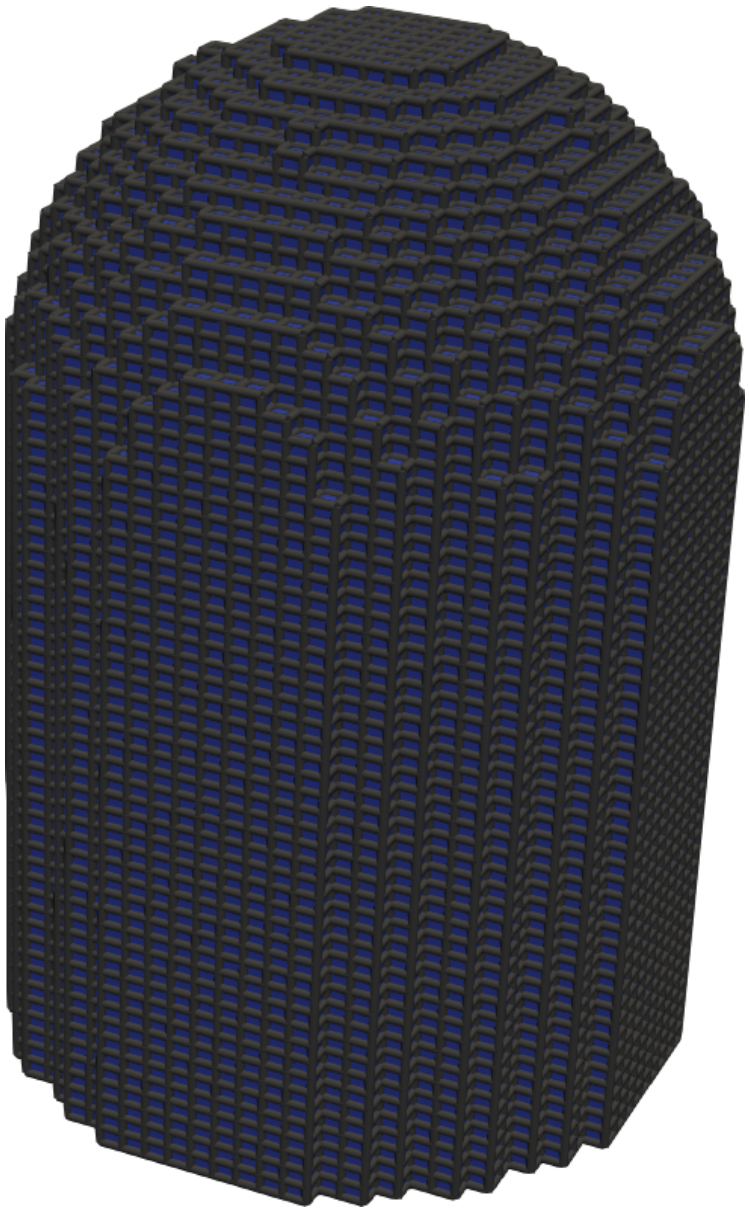

Figure 3.3: Ablation simulation of a carbon fiber reinforced phenolic composite, showing the initial unablated configuration.

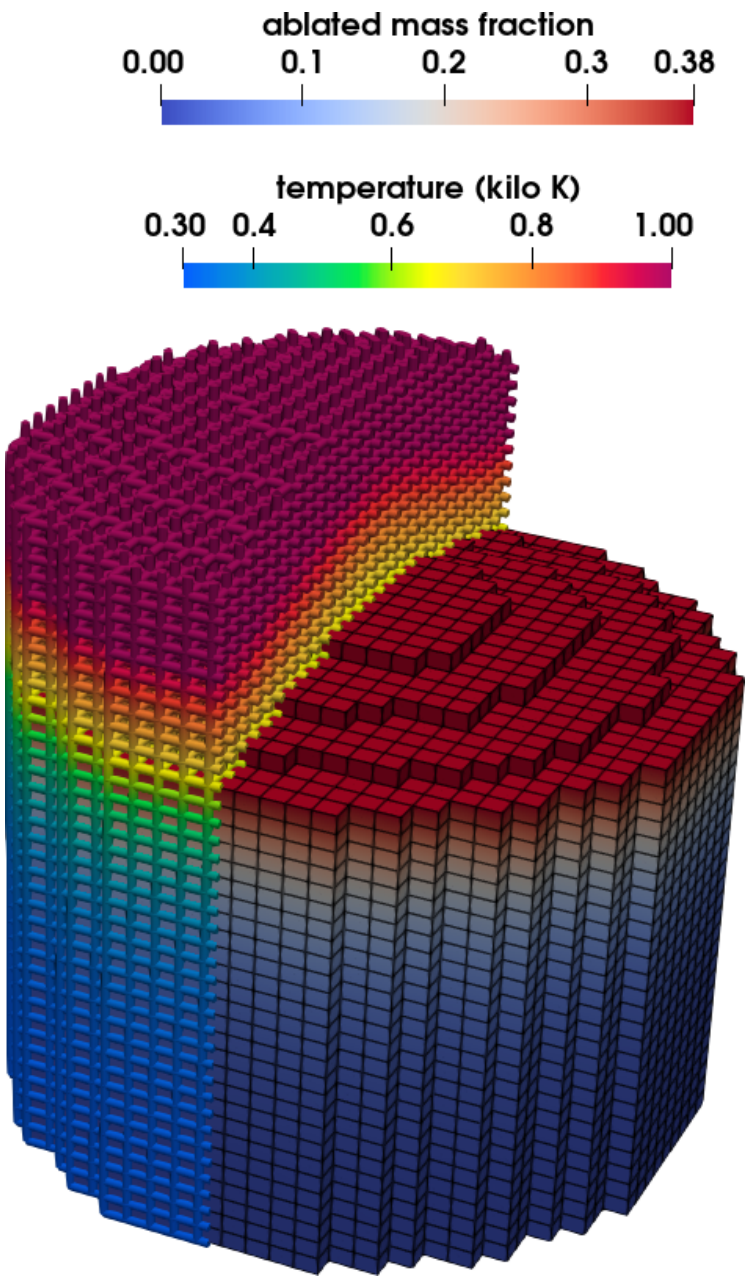

Figure 3.4: Ablation simulation of a carbon fiber reinforced phenolic composite, showing the ablated configuration at a heat input of 15 kJ.

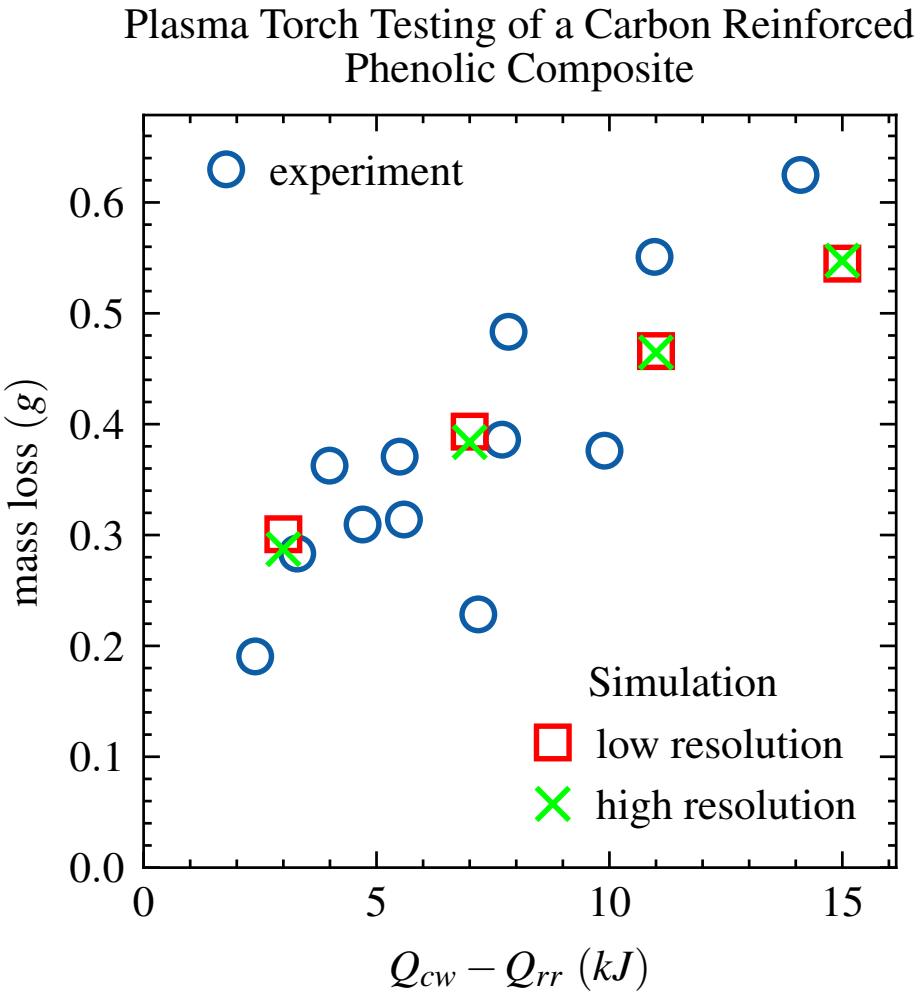

Figure 3.5: Ablation simulation of a carbon fiber reinforced phenolic composite, showing simulation versus experiment on total mass loss versus heat input. The low and high resolution simulations are with 30 and 60 elements across the sample height respectively.

Table 3.3: Comparison of macroscale and mesoscale material properties for PICA (phenolic impregnated carbon ablator).

material property	Macroscale	Mesoscale
fiber specific heat c_{v_f}	2000 J/kgK	771 J/kgK
resin specific heat c_{v_r}	2720 J/kgK	1674 J/kgK
heat of decomposition h^{a}_{dec}	0	293 kJ/kg
Heat of pyrolysis H_{py}	1 MJ/kg	1.41 MJ/kg
fiber failure internal energy u_f^{fib}	10.08 MJ/kg	na

[a] The difference between the meso and macroscale value of 293 kJ/kg for h_{dec} is less than 1% of both the simulation and experimental values for the ratio of heat input to total mass loss.

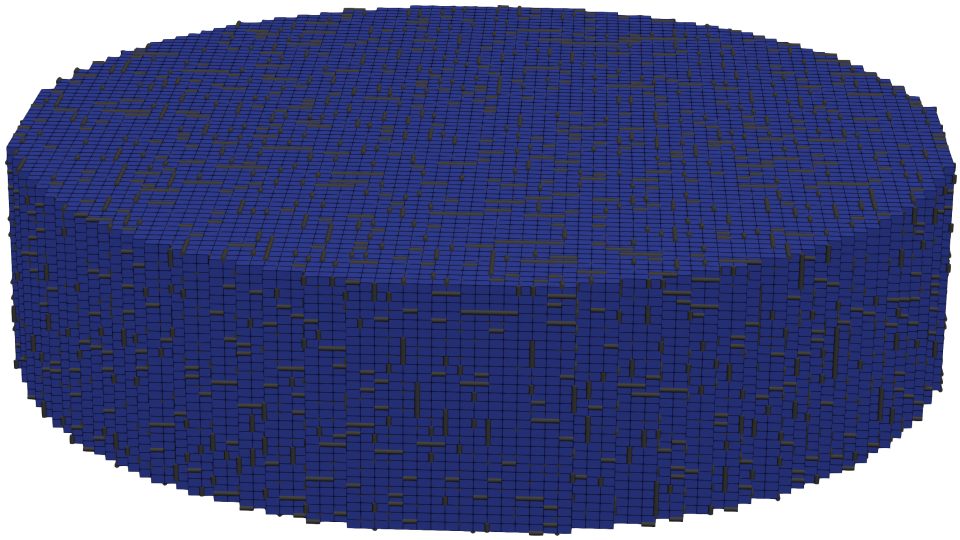

Figure 3.6: PICA (Phenolic Impregnated Carbon Ablator) 10.16 cm diameter model, showing hexahedral and bar element plot in initial configuration.

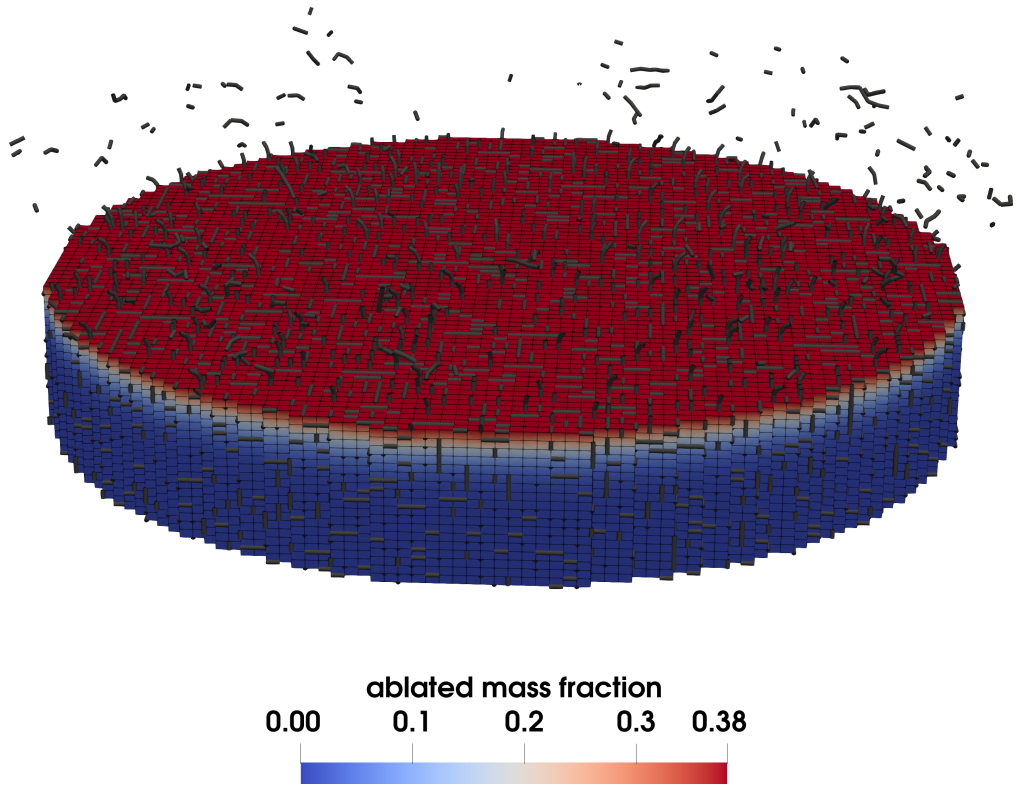

Figure 3.7: PICA (Phenolic Impregnated Carbon Ablator) 10.16 cm diameter model, showing ablated geometry at a heat input of 0.85 MJ. Elements are colored on ablated mass fraction.

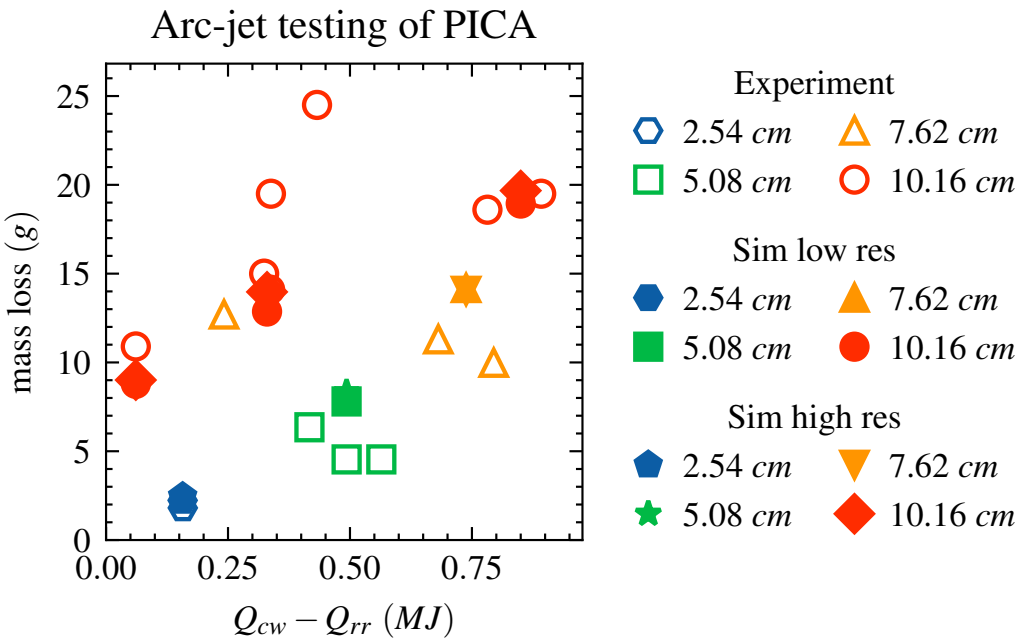

Figure 3.8: Arc-jet testing of PICA (Phenolic Impregnated Carbon Ablator), showing mass loss versus cold wall minus re-radiated heat loads ($Q_{cw} - Q_{rr}$). The low and high resolution simulations were 14 and 28 elements across the model height respectively.

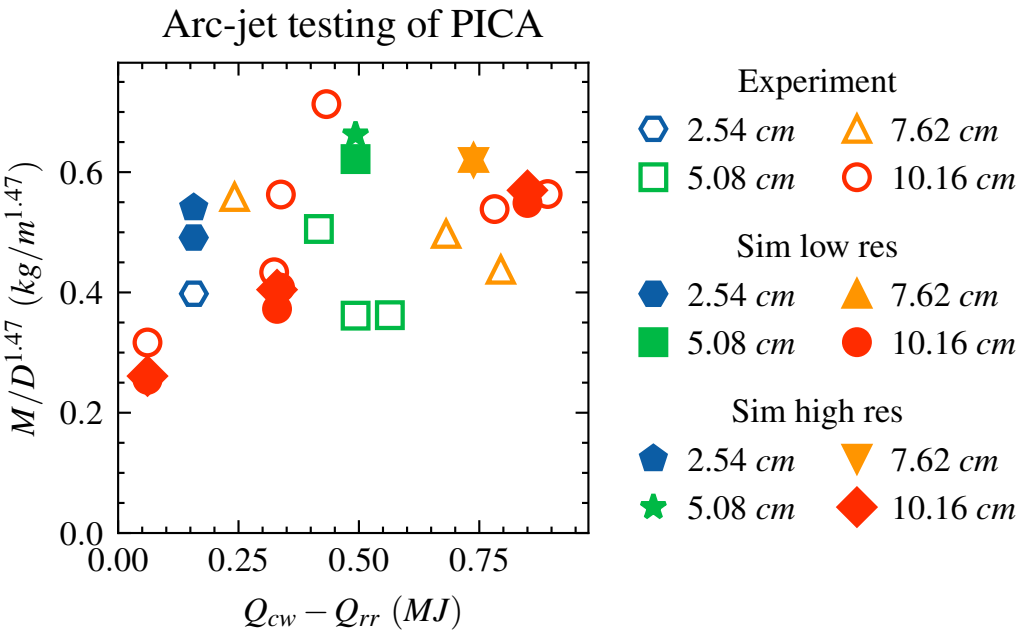

Figure 3.9: Arc-jet testing of PICA (Phenolic Impregnated Carbon Ablator), showing $\Delta m/D^{1.47}$ versus cold wall minus re-radiated heat loads ($Q_{cw} - Q_{rr}$). The higher resolution simulations are 28 elements across the model height, and the lower resolutions run are 14 elements across the model height.

Table 3.4: Comparison of macroscale and mesoscale material properties for a carbon fiber reinforced cyanate ester composite.

material property	Macroscale	Mesoscale
fiber specific heat c_{v_f}	2000 J/kgK	771 J/kgK
resin specific heat c_{vr}	2720 J/kgK	1200 J/kgK
heat of decomposition h^{a}_{dec}	0	-47 kJ/kg
heat of pyrolysis H_{py}	11.76 MJ/kg	4.32 MJ/kg
fiber failure internal energy u_f^{fib}	10.02 MJ/kg	na

[a] The difference between the meso and macroscale value of 47 kJ/kg for h_{dec} is less than 1% of both the simulation and experimental values for the ratio of heat input to total mass loss.

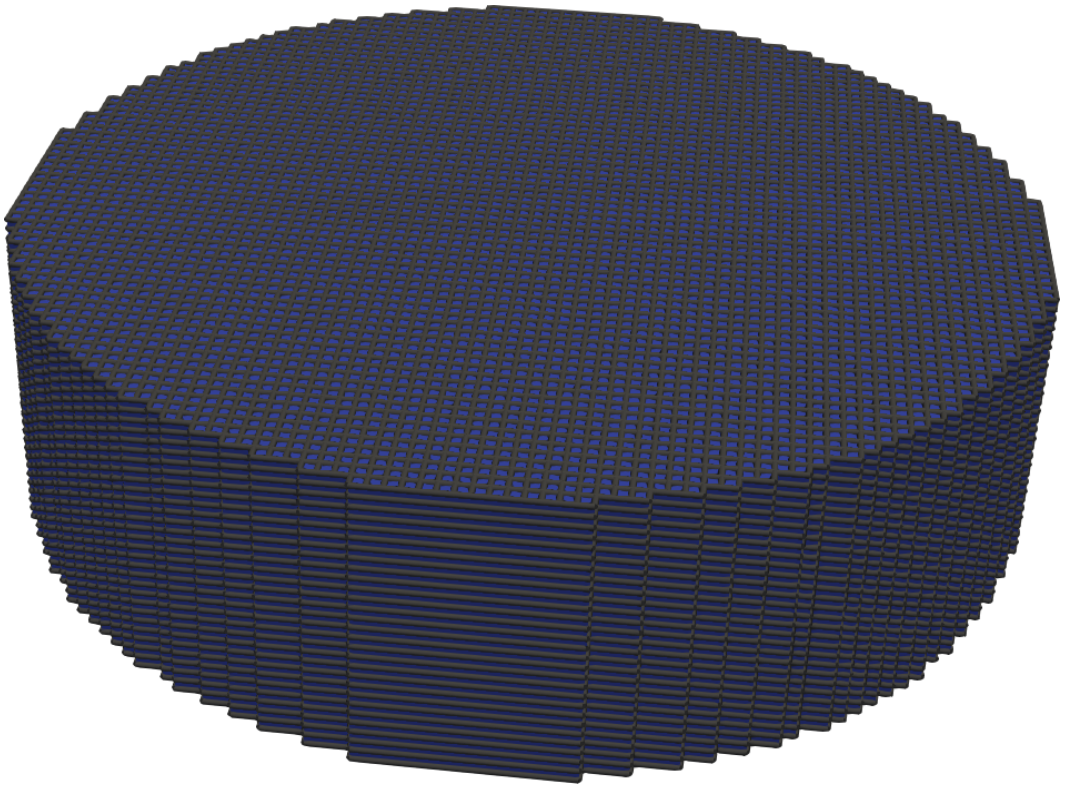

Figure 3.10: Carbon cyanate ester ablation problem, showing hexahedral and bar element plot in initial configuration.

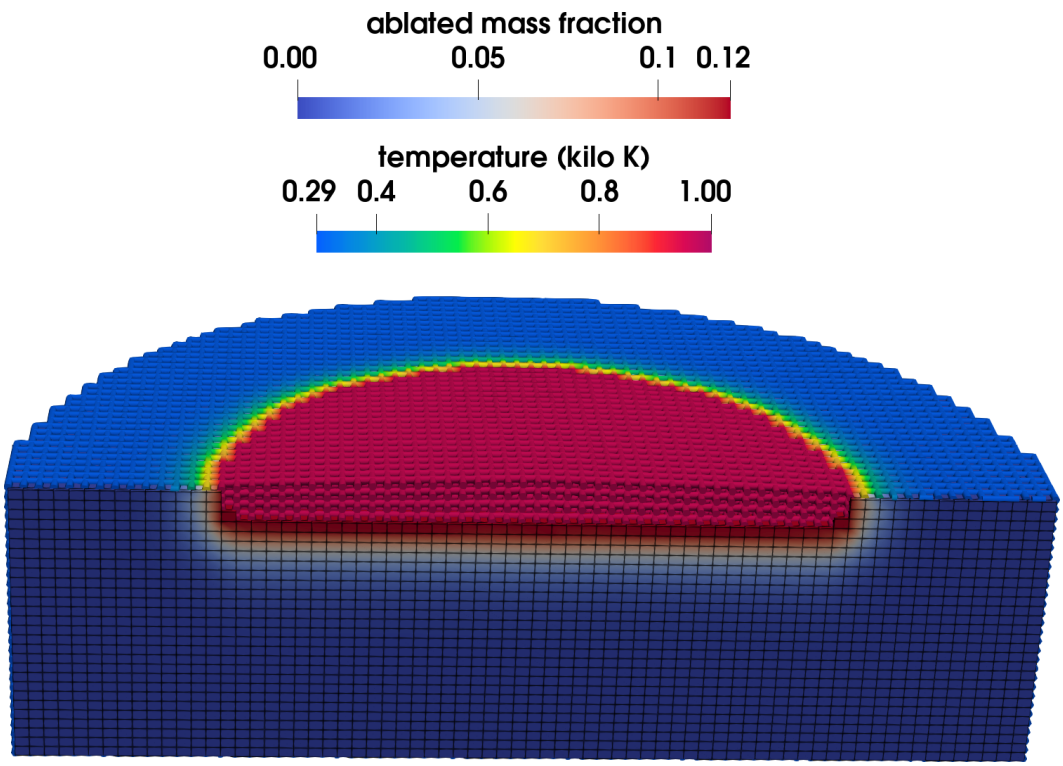

Figure 3.11: Carbon cyanate ester ablation problem, showing sectioned ablated geometry at a heat input of 14.8 kJ. Fibers are colored on temperature, elements are colored on ablated mass fraction.

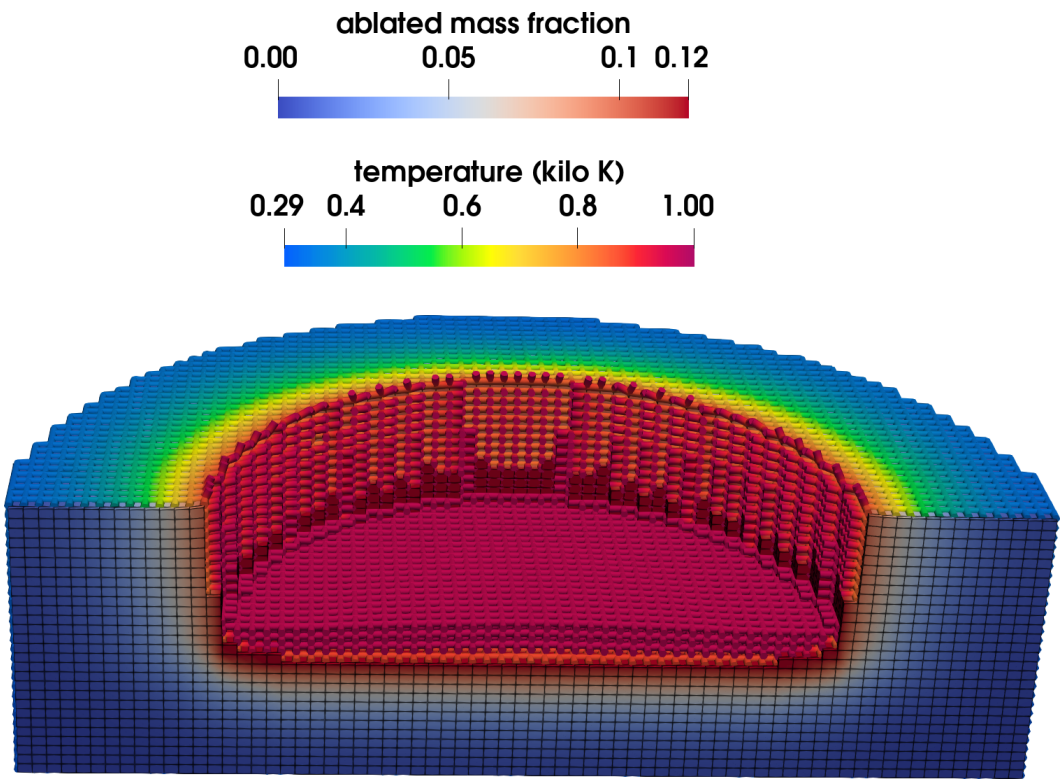

Figure 3.12: Carbon cyanate ester ablation problem, showing sectioned ablated geometry at a heat input of 238 kJ. Fibers are colored on temperature, elements are colored on ablated mass fraction.

Table 3.5: Carbon cyanate ester ablation problem, showing simulation versus experimental results on total mass loss and heat load ($Q_{cw} - Q_{rr}$). The low and high resolution simulations are with 14 and 28 elements across the sample height respectively.

	$Q_{cw} - Q_{rr}$	Δm	$(Q_{cw} - Q_{rr})/\Delta m$
Experiment	15.2 kJ	0.588 g	25.8 MJ/kg
Simulation high res	14.8 kJ	0.516 g	28.7 MJ/kg
Simulation low res	15.0 kJ	0.532 g	28.20 MJ/kg

3.9 Model Validation

The preliminary simulation results suggest a simulation cold wall heat input model must be formulated to compare simulation to experiment. This section thus develops a cold wall heat input model which can be directly incorporated into the macroscale model.

A cold wall heat input is defined in the macroscale model as the total heat load applied inside the heating control volume. In order to record the heat load, the spalled off particles are left inside the heating volume rather than being transported out. The fragmented particles inside the heating volume then record a cold wall heat input. The cold wall model is implemented by removing the aerodynamic loading on the fragmented particles; the heating profile is also propagated at a constant velocity.

Validation simulations are performed for the high density carbon fiber reinforced phenolic composite presented in section 3.8.1. The experimental heat input is defined as before in the preliminary analysis as the cold wall minus re-radiated heat load $Q_{cw} - Q_{rr}$; however, the simulation cold wall heat input is now used for comparison to experiment. The simulation results, shown in Figure 3.13, have a much-improved match with experiment and good convergence with particle resolution. Match with experiment is also achieved using very reasonable properties for the resin and fiber specific heats. Table 3.7 lists the material properties used in the multiscale model. The ablated configuration at a heat input of 15 kJ is shown in Figures 3.14 to 3.16.

A comparison of the ablated profiles for the cold wall and hot wall models is shown in Figure 3.19 where, in the hot wall model, an aerodynamic loading is applied to the fragmented particles to transport them out of the heating volume. As shown in Figure 3.19, the ablated profiles have no observable difference. This verifies that the cold wall and hot wall models differ only in the total recorded system heat input and not in the other ablation kinematics. Figure 3.17 compares the system heat input between the hot wall and cold wall models, where the hot wall heat input is predicted to be roughly half of the cold wall heat input. Since experiments cannot directly measure the hot wall heat load, an advantage of the macroscale model is thus that it can directly incorporate an estimation of the hot wall heat load.

In order to include full thermomechanical coupling in the macroscale model, the externally applied loading rates are amplified (on the order of 10^4) so that the total applied thermal load occurs over a much shorter time than is typical of ablation experiments. In order to determine the sensitivity of the macroscale model to the applied loading rates, a series of simulations are conducted where the per unit mass heat input, heating surface velocity, and resin ablation rate constant (equation 3.1) are varied by a factor of four. The simulation parameters are listed in Table 3.6, and the simulation results for mass loss versus heat input are shown in Figure 3.20. As seen in Figure 3.20, negligible difference is observed in the simulation results for simulations conducted using different system rates. A sensitivity study on the use of amplified rates cannot be performed at the long time scales of ablation experiments. However, within

the feasible simulation time scales, the presented results suggest that applying an equal thermal load across varying simulation times has a negligible effect on the simulation results.

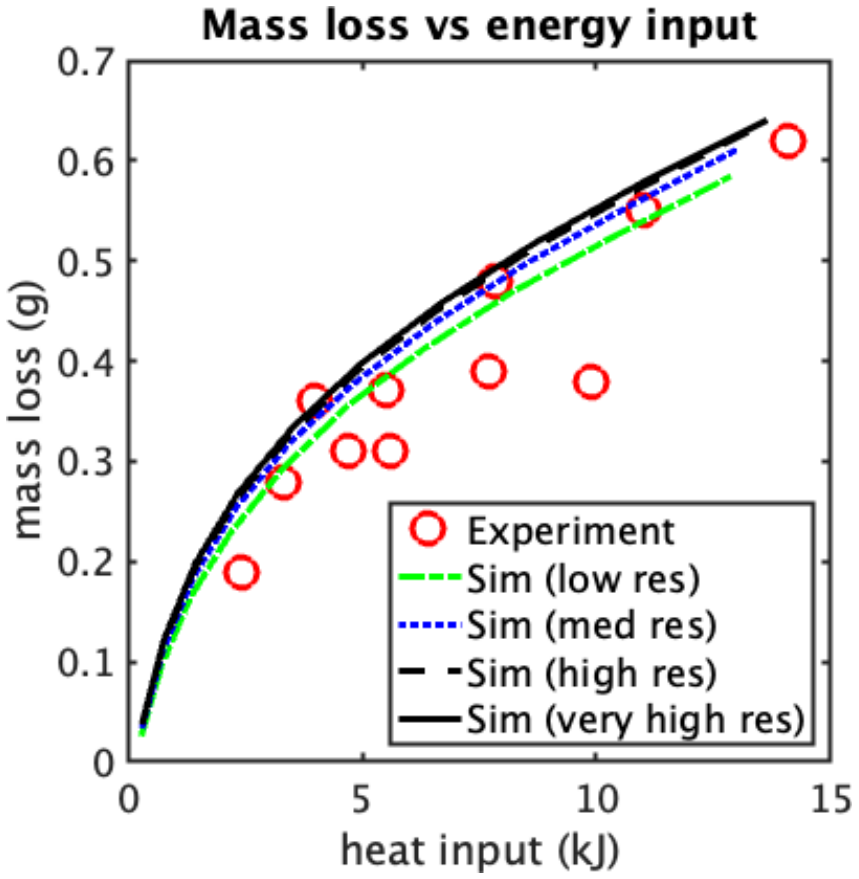

Figure 3.13: Comparison of macroscale simulation results at various model resolutions versus plasma torch test data (Ref [125]) on the ablation of a carbon reinforced phenolic composite. The model resolutions correspond to 30, 60, 90 and 120 elements across the sample height.

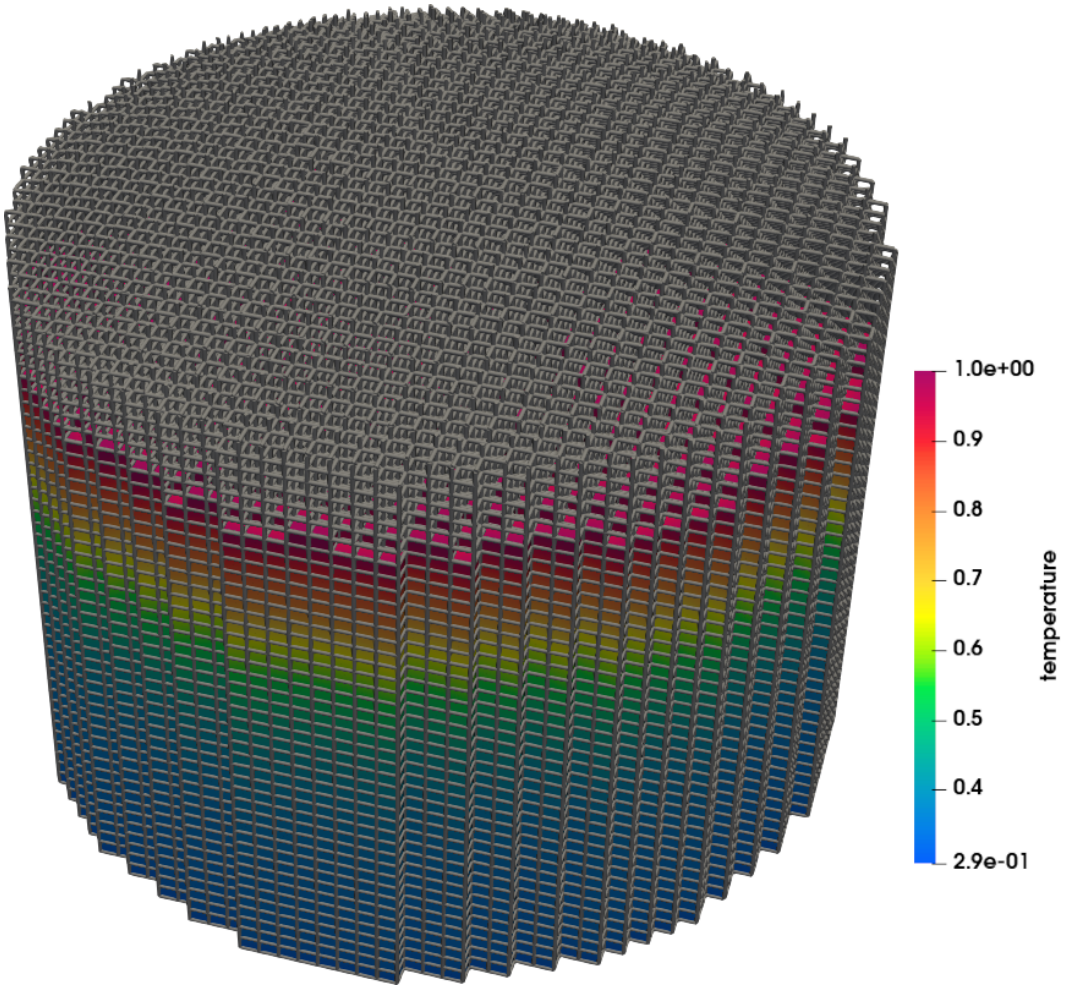

Figure 3.14: Macroscale simulation of a carbon reinforced phenolic composite, showing the ablated configuration. Elements are colored on temperature while the fiber reinforcement is visualized in grey.

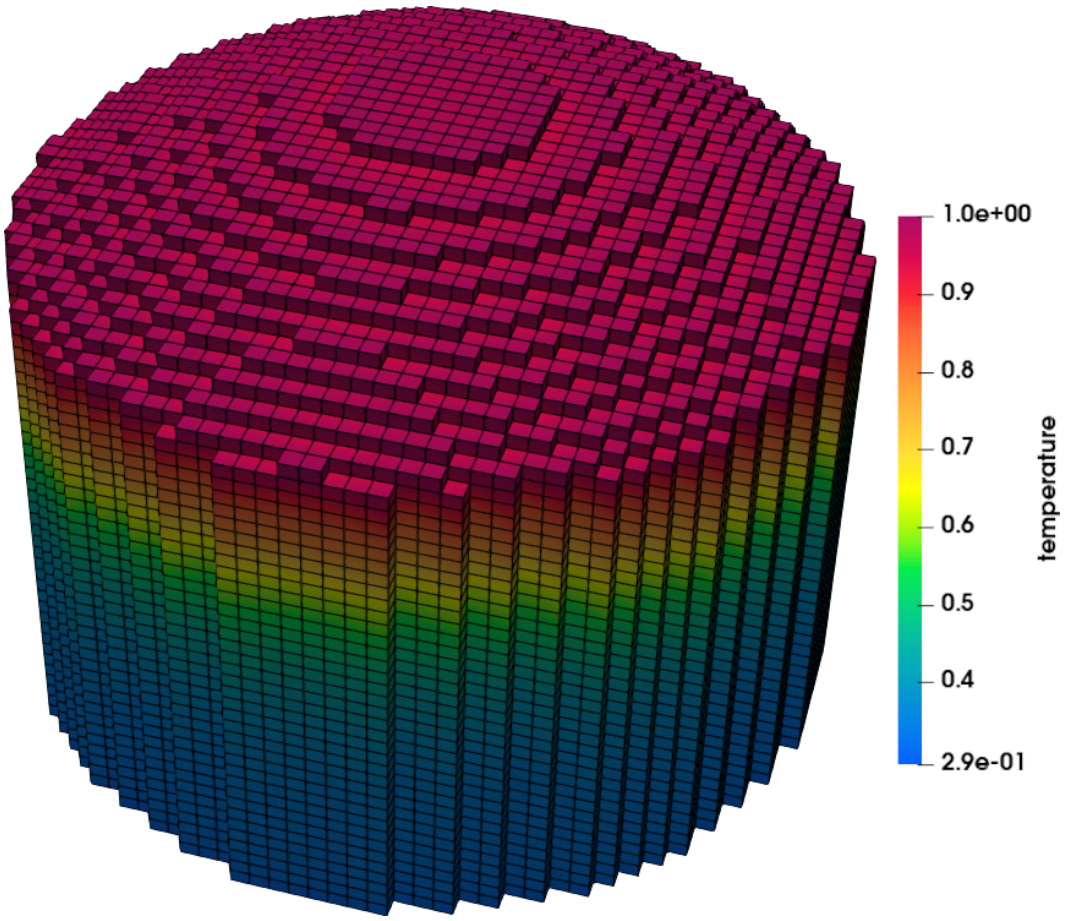

Figure 3.15: Macroscale simulation of a carbon reinforced phenolic composite, showing the ablated configuration with visualization of only the matrix elements. Elements are colored on temperature.

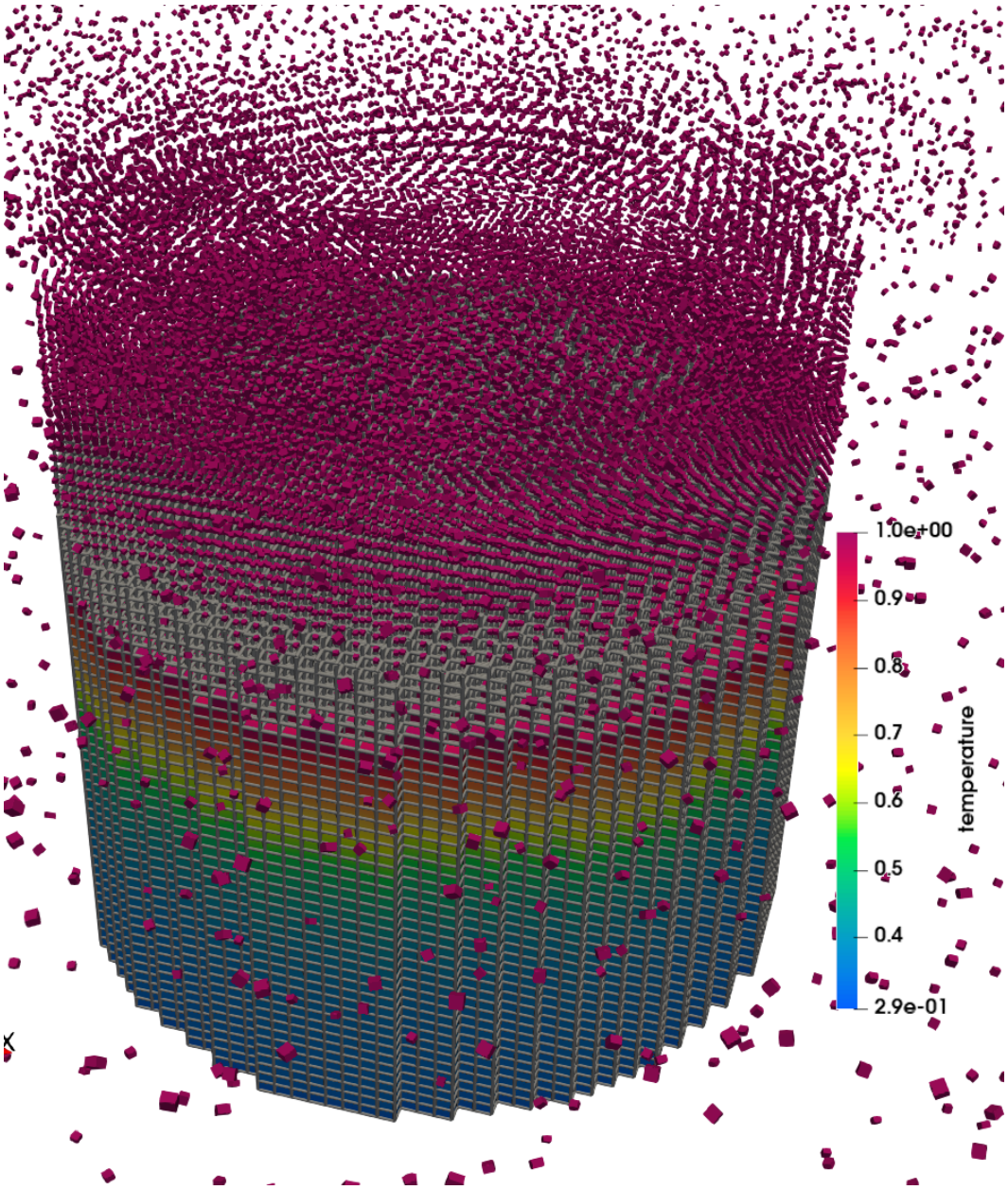

Figure 3.16: Macroscale simulation of a carbon reinforced phenolic composite, showing the ablated configuration with visualization of the fragmented particles. Elements are colored on temperature while the fiber reinforcement is visualized in grey.

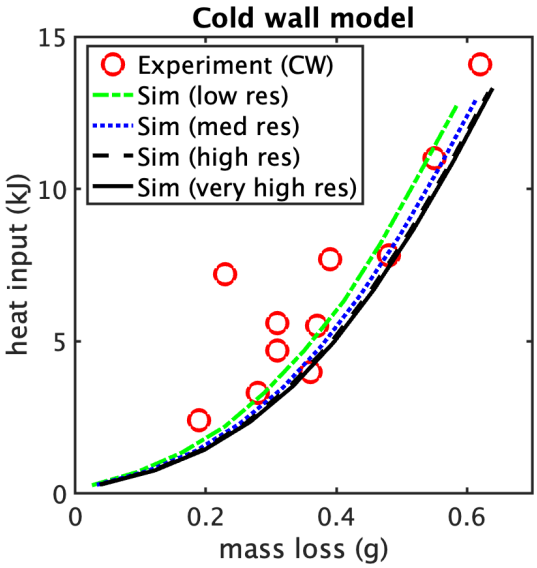

(a) Simulation cold wall heat input versus mass loss.

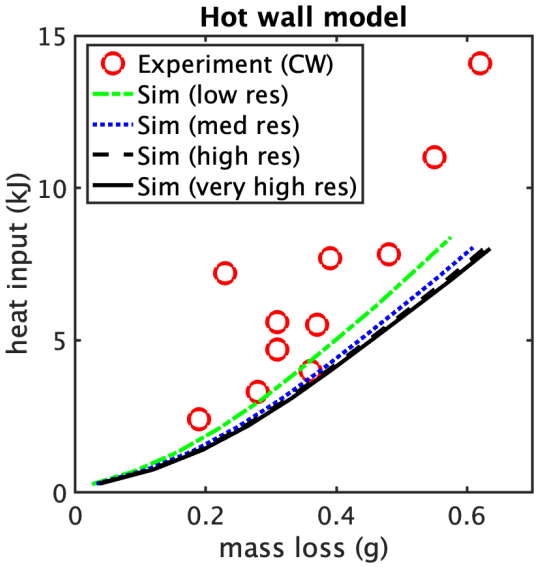

(b) Simulation hot wall heat input versus mass loss.

Figure 3.17: Simulation hot wall and cold wall heat input versus mass loss for a carbon phenolic reinforced composite. The hot wall and cold wall model refer to the case with and without aerodynamic loading on the fragmented particles respectively. The experimental data for mass loss versus $Q_{cw} - Q_{rr}$ is from Ref [125].

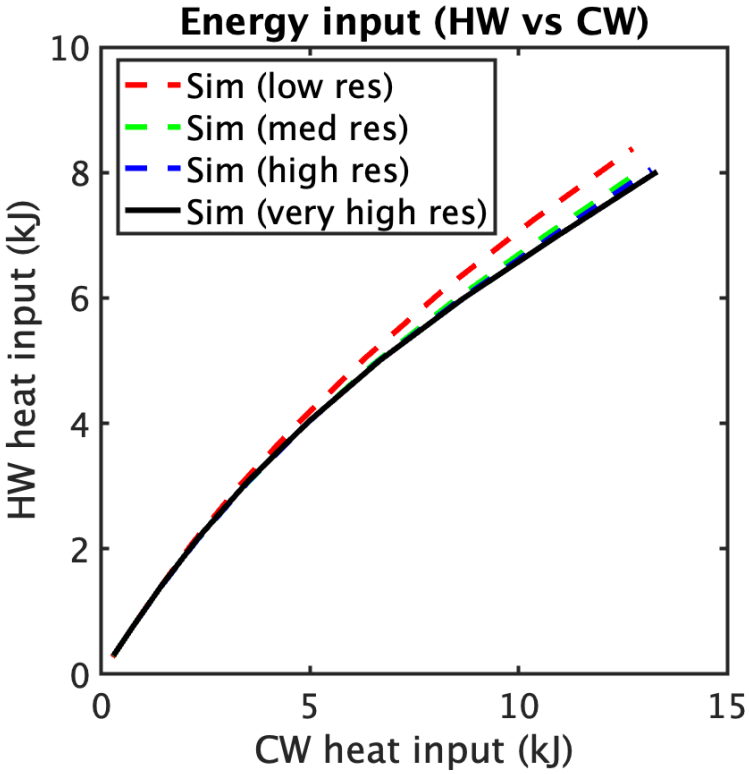

Figure 3.18: Plot of hot wall versus cold wall heat input for the ablation simulation of a carbon phenolic reinforced composite. The model resolutions correspond to 30, 60, 90 and 120 elements across the sample height.

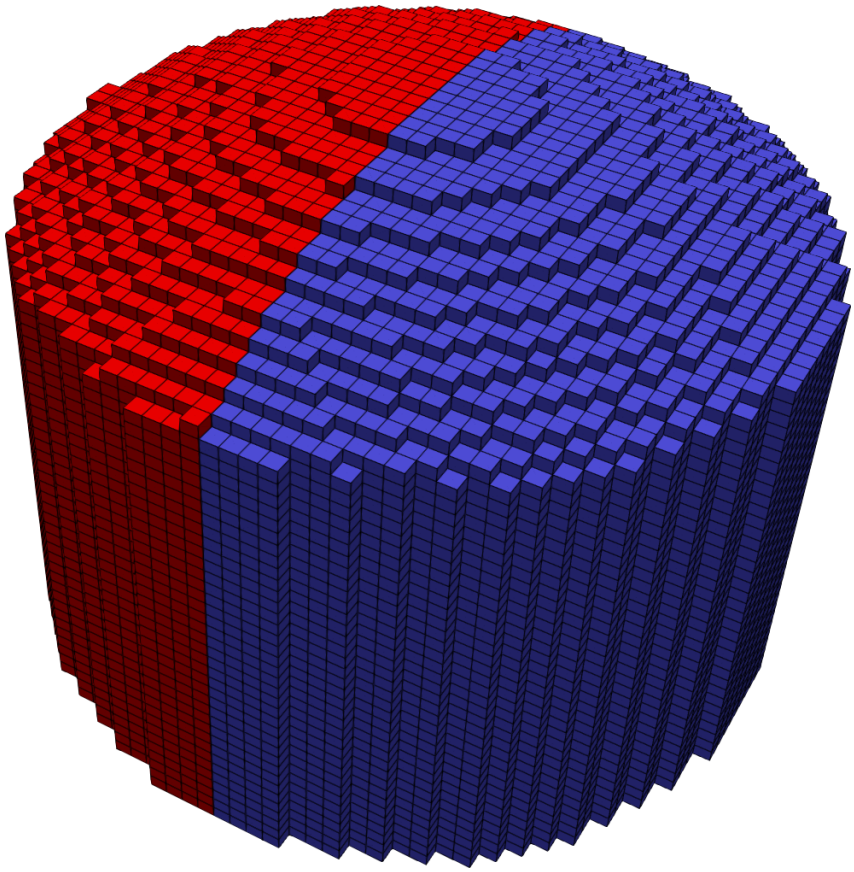

Figure 3.19: Macroscale simulation of a carbon reinforced phenolic composite, comparing the ablated configuration with and without external mechanical loading on fragmented particles.

Table 3.6: Rate parameters for series of simulations for a carbon fiber reinforced phenolic composite.

q $(MJ/\mu s\, kg)$	$1/\tau$ $(1/\mu s)$	$\dot{L}$ $(cm/\mu s)$
1.25	0.025	0.00125
2.5	0.05	0.0025
5.0	0.1	0.005

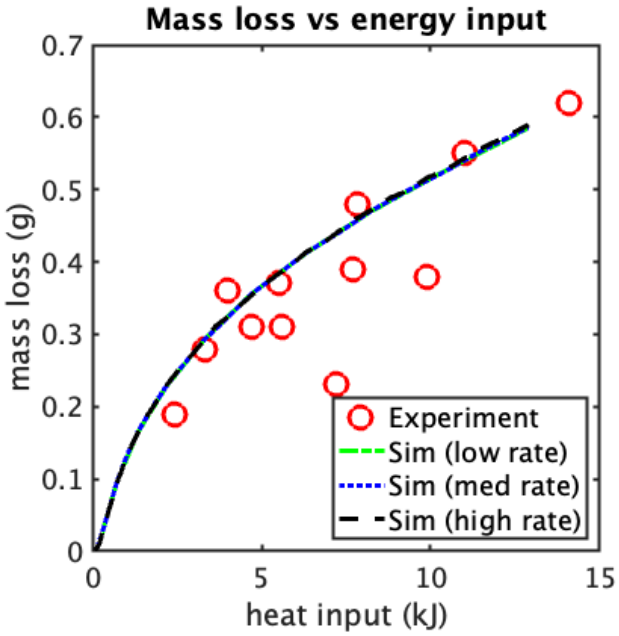

Figure 3.20: Comparison of simulations of a carbon reinforced phenolic composite at various loading rates (see Table 3.6). Experimental data is from Ref [125].

Table 3.7: Comparison of macroscale cold wall model and mesoscale model material properties for a carbon fiber reinforced phenolic composite.

material property	Macroscale	Mesoscale
fiber specific heat c_{v_f}	720 J/kgK	771 J/kgK
resin specific heat c_{v_r}	1464 J/kgK	1674 J/kgK
heat of decomposition h_{dec}^{a}	0	293 kJ/kg
heat of pyrolysis H_{py}	5 MJ/kg	1.49 MJ/kg
fiber failure internal energy u_f^{fib}	1.91 MJ/kg	na

[a] The difference between the meso and macroscale value of 293 kJ/kg for h_{dec} is less than 1% of both the simulation and experimental values for the ratio of heat input to total mass loss.

Chapter 4

Conclusions and Recommendations for Future Work

This work extends the state of the art in thermal ablation modeling by introducing the first integrated multiscale ablation model. The model has three levels of interest: nano, meso, and macroscale. At the nanoscale, reactive molecular dynamic simulations are performed of resin pyrolysis where the RMD simulations and pyrolysis chemical kinetics are taken from previous work [15, 16, 162]. The mesoscale model then incorporates the resin pyrolysis chemistry developed from the RMD simulation results into a one-dimensional fully coupled chemical-thermomechanical model of resin pyrolysis in a resin and fiber composite. A resin heat of pyrolysis is then computed from the mesoscale simulation results, which is incorporated into a resin mass loss model at the macroscale. The macroscale model then simulates in three dimensions the ablation of the resin and fiber and the resulting ablator geometry evolution in a fully coupled thermomechanical simulation.

The meso and macroscale models employ the hybrid particle element method in constructing a detailed model of the solid. This research extends previous work on the hybrid particle element method by the addition of variable mass particles and a description of the resin and fiber composite archi-

tecture in the macroscale model. A significant benefit to the hybrid particle element method is its ability to explicitly capture the the solid erosion and surface recession in the particle-element kinematics through a seamless particle and element based description of the material in an energy conserving formulation. In summary, the significant contributions of this research may be stated as follows: (1) it presents a multiscale strategy for coupling the three primary scales of interest: nano, meso and macro scale, (2) as part of the multiscale strategy, it incorporates a mesoscale model which simulates the fully coupled chemical-thermomechanical ablation problem, serving to integrate the temporally and spatially disparate nano and macro scales, (3) it enforces conservation of mass and energy in the formulation of the state variable evolution equations at each scale, and (4) it includes explicit modeling of solid erosion effects through a hybrid particle element composite model at the macroscale.

The one-dimensional mesoscale model is presented in Chapter 2. The model extends previous research on hybrid particle element with chemical reactions by the addition of variable mass particles, where the particle mass evolution is coupled to the RMD chemical kinetics, accounting for mass loss due to resin pyrolysis. The resin heat of pyrolysis computed from the mesoscale simulation results is compared to published bomb calorimetry experiments to validate the mesoscale model. For incorporation into the macroscale model, the resin heat of pyrolysis computed from the mesoscale simulation results is used in the formulation of a resin mass loss model at the macroscale.

The three-dimensional macroscale model is presented in Chapter 3.

The model extends previous work on hybrid particle element by the addition of variable mass particles and by combining particles, hexahedral elements, and tension only bar elements to construct a model of the resin and fiber composite architecture. Mass loss at the macroscale includes mass loss in the particles due to resin pyrolysis and the spalling of the particles due to element failure. Validation is performed by comparison to experiment on total mass loss versus heat input. A new approach is also developed for performing model validation which allows for incorporating the estimation of hot wall heat loads.

Some possible directions for future work are mentioned here. As described in section 3.8, an attempt at propagating the heat input profile with the fragmented mass encountered poor convergence with particle resolution. Future work may thus consider further addressing this matter by developing a robust heat input model that adaptively responds to the eroded geometry. Future work may also consider loosely coupling the presented multiscale model to a CFD solver. A sensitivity study on the parameters in the multiscale model, such as the resin heat of pyrolysis used for integrating the meso and macro scales, may be conducted to fit the simulation results better to experiment. Models describing the mechanical property degradation of the composite might also be developed. This may include, for example, additional state variables that describe a reduction in material stiffness as a function of the stress, strain, or temperature history [48]. Lastly, a conduction model might be incorporated into the multiscale model, where a strategy would have to be developed for bridging the disparate mechanical and conduction timescales.

Appendices

Appendix A

Plasma Torch Test Data for a Carbon Fiber Reinforced Phenolic Composite

Pesci et al. performed plasma torch testing of a carbon fiber reinforced phenolic composite [125]. The material has a composite density of 1400–1500 kg/m^3 and a resin mass fraction of 0.35–0.4 with a hemispherical cap geometry, having a total height of 1.3 cm with a radius of .5 cm (shown in Figure A.1). The authors performed testing under three cold wall heat fluxes (0.626, 0.903, 1.379 MW/m^2) with four exposure times for each flux (30, 50, 70, 90 s). Experimentally measured values were the total mass loss obtained by weighing samples prior and after testing. The test conditions and results reported in the paper are listed in Table A.1.

From the reported experimental parameters, a cold wall heat load Q_{cw} is estimated in this thesis as

$$Q_{cw} = q_{cw} A T, \quad A = \pi r^2 \tag{A.1}$$

where q_{cw} is the cold wall heat flux reported in the paper, A the projected area, and T the exposure time. A re-radiated heat load is also estimated as

$$Q_{rr} = q_{rr} A T, \quad q_{rr} = \epsilon \sigma \theta_{surf}^4 \tag{A.2}$$

where q_{rr} is a re-radiated flux, ϵ emissivity, and θ_{surf} is surface temperature. The authors do not report emissivity or surface temperature. For equation A.2, the emissivity is estimated from the literature as 0.9 [158] for carbon phenolic. The surface temperatures are based on plasma torch experiments conducted by Silva et al. [43], who conducted ablation tests of tape wrapped carbon phenolic at similar heat fluxes of 0.626, 0.903 and 1.376 MW/m^2. The surface temperatures and computed values for q_{rr}, Q_{cw} and Q_{hw} are also listed in Table A.1. A plot of the experimental mass loss versus $Q_{cw} - Q_{rr}$ is shown in Figure A.2.

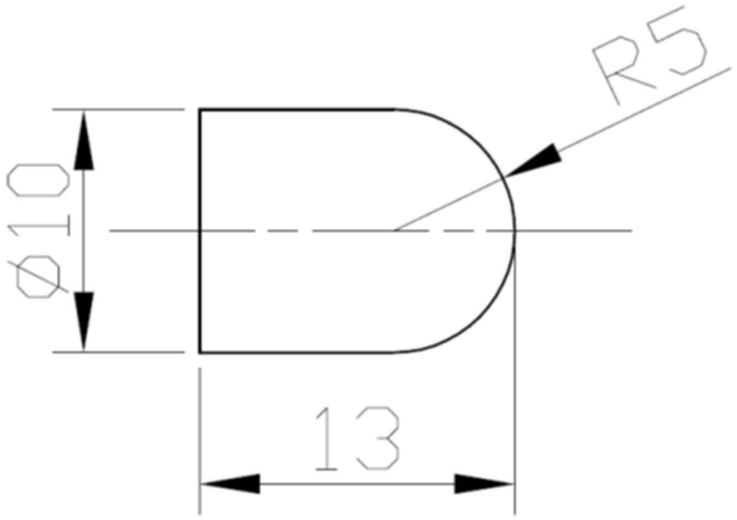

Figure A.1: Test article geometry for plasma torch testing of a carbon fiber reinforced phenolic composite. The above figure is from Ref [125]. All units are in mm.

Table A.1: Plasma torch testing of a carbon fiber reinforced phenolic composite [125]. The first three columns are estimated from Figure 6 in Ref [125].

Exposure Time (s)	q_{cw} (W/cm^2)	Mass loss (g)	θ^{a}_{surf} (K)	q^{b}_{rr} (MW/m^2)	$Q^{\dagger}_{cw}$ (kJ)	$Q^{\dagger}_{rr}$ (kJ)	$Q_{cw} - Q_{rr}$ (kJ)
30	62.6	0.19	1232	0.118	2.95	0.555	2.4
50	62.6	0.36	1232	0.118	4.92	0.925	3.99
70	62.6	0.31	1232	0.118	6.88	1.29	5.59
90	62.6	0.23	1232	0.118	8.85	1.66	7.19
30	90.3	0.28	1412	0.203	4.26	0.957	3.3
50	90.3	0.37	1412	0.203	7.09	1.6	5.5
70	90.3	0.39	1412	0.203	9.93	2.23	7.7
90	90.3	0.38	1412	0.203	12.8	2.87	9.89
30	137.9	0.31	1650	0.378	6.5	1.78	4.7
50	137.9	0.48	1650	0.378	10.8	2.97	7.83
70	137.9	0.55	1650	0.378	15.2	4.16	11.0
90	137.9	0.62	1650	0.378	19.5	5.35	14.1

[a] The surface temperature θ_{surf} is estimated based upon plasma torch experiments in the literature for carbon phenolic under similar conditions [43].

[b] q_{rr}, Q_{cw} and Q_{rr} are calculated from equations A.1 and A.2.

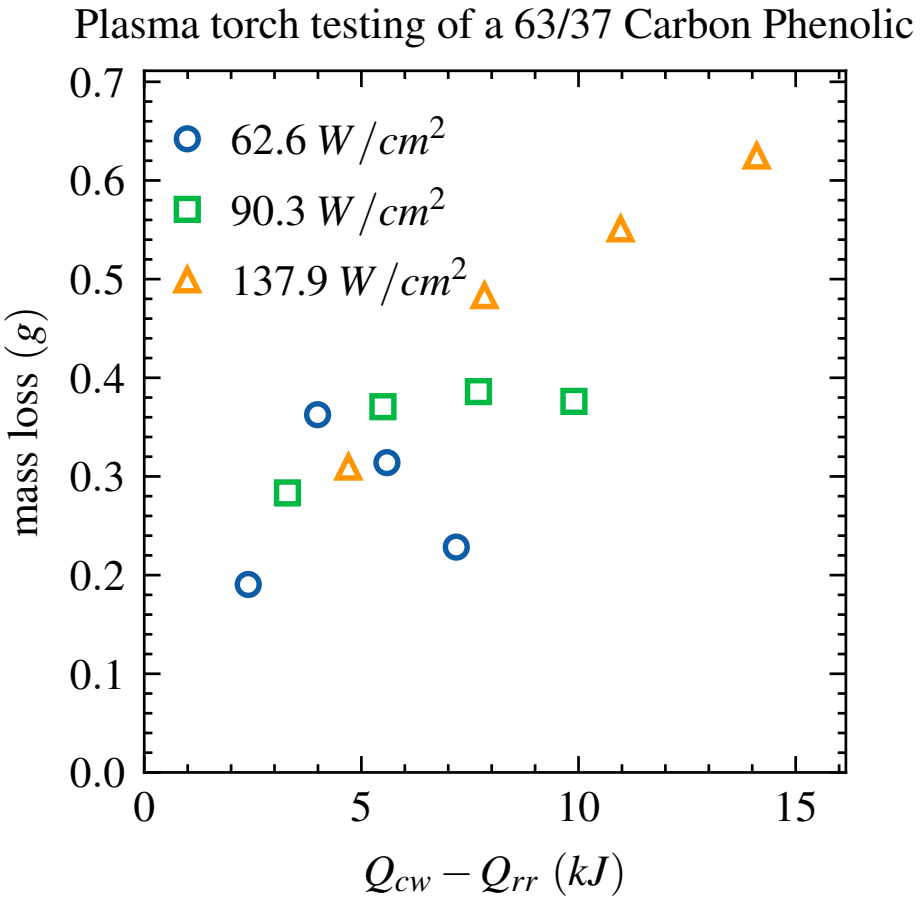

Figure A.2: Plasma torch testing of a carbon fiber reinforced phenolic composite [125]. The above figure shows the experimental mass loss versus $(Q_{cw} - Q_{rr})$, where Q_{cw} and Q_{rr} are calculated by equations A.1 and A.2. The uncertainty in the experimental mass loss reported by the authors were based on the instrument used for weighing the samples before and after the plasma torch tests ($\pm 0.07\ g$) [125].

Appendix B

Arc-Jet Test Data for PICA (Phenolic Impregnated Carbon Ablator)

Tran et al. performed arc-jet testing of PICA (Phenolic Impregnated Carbon Ablator) [158]. The material has a composite density of 274 kg/m^3 and a resin weight loading of 0.38 [114]. The sample geometries were cylindrical with a flat surface having diameters of 1–4 inches. A schematic of the samples are shown in Figure B.1. Cold wall heat fluxes ranged from 426–3362 W/cm^2. Table B.2 lists the arc-jet test cases reported in Ref [158], including the sample diameters, cold wall fluxes, exposure times, surface temperatures and total mass loss. Table B.3 includes the calculated values of Q_{cw} and Q_{rr}, where Q_{cw} and Q_{rr} are calculated as in the preceding section by equations A.1 and A.2. Figure B.2 shows a plot of the experimental mass loss versus the calculated $Q_{cw} - Q_{rr}$. As seen in the plot, the data does not appear to fall onto a single curve, especially for the varying diameter samples. It is observed that normalizing the total mass loss as $\Delta m/D^n$, where Δm is mass loss, D the sample diameter, and n an exponent, produces a plot better resembling a single curve. A plot with n set to a value of $n = 1.47$ is shown in Figure B.3.

The authors note that for the smaller diameter samples (1–3 inches),

the calorimeter cold wall heat flux measurements were adjusted for sample diameter, converting the heat flux readings from a 4 inch diameter calorimeter to the smaller sample diameters. The cold wall heat flux was assumed to scale inversely with the square root of the sample diameter based on the following stagnation point heat transfer correlation developed by Fay and Riddell [55, 74, 158]:

$$q_{cw} = C\Delta h \left(\frac{P}{R}\right)^{1/2} \tag{B.1}$$

where Δh is the stagnation enthalpy potential (recovery enthalpy of the free stream minus enthalpy at the material surface), P the stagnation pressure, C a heat transfer coefficient, and R the sample radius.

Based on the above relation, a dimensional analysis is presented here for the relation $\Delta m/D^n$ versus $(Q_{cw} - Q_{rr})$. We begin by postulating that the total mass loss is a function of the following form

$$\Delta m = f(q_{cw}, q_{rr}, R, \Delta h, C, P, H, \tau) \tag{B.2}$$

where H is an effective heat of ablation which accounts for the material properties in a lumped form, and τ is the exposure time. The above quantities can be expressed in three fundamental units kg, m and s as shown in Table B.1. Thus, five dimensionless parameters can be constructed from the eight function arguments, which, building from Ref [74], are chosen as

$$\pi_{cw} = q_{cw}R\frac{1}{H^{3/2}C^2}, \quad \pi_{rr} = q_{rr}R\frac{1}{H^{3/2}C^2}, \quad \pi_\tau = \tau P\frac{1}{H^{1/2}C^2},$$

$$\pi_p = PR\frac{1}{C^2H}, \quad \pi_f = q_{cw}\frac{1}{C\Delta h}\left(\frac{R}{P}\right)^{1/2} \tag{B.3}$$

where the last dimensionless variable π_f is simply the Fay-Riddell heat transfer correlation (equation B.1) and is equal to one. The total mass loss is non-dimensionalized as

$$\pi_m = \frac{\Delta m}{R^n} H^{n-2} C^{2n-6} P^{2-n} \tag{B.4}$$

Employing the Buckingham Pi-theorem [24], equation B.2 can be written in the following form

$$\pi_m = g(\pi_{cw}, \pi_{rr}, \pi_\tau, \pi_p) \tag{B.5}$$

We additionally postulate that the function g can be written as

$$\pi_m = g((\pi_{cw} - \pi_{rr})\pi_\tau \pi_p) \tag{B.6}$$

from which we write

$$\frac{\Delta m}{R^n} = H^{2-n} C^{6-2n} P^{n-2} g\left((Q_{cw} - Q_{rr}) P^2 \frac{1}{C^6 H^3}\right) \tag{B.7}$$

For constant heat transfer coefficient, stagnation pressure, and constant material with varying model radii, an argument can be made, based on dimensional analysis, that $\Delta m/R^n$ and $(Q_{cw} - Q_{rr})$ are the variables of interest. Hiester et al. notes that for the fluid properties of air, the heat transfer coefficient C is approximately constant in the range of arc-jet test conditions [74]. The stagnation pressure P in the PICA ablation tests varies (see Table B.2). It is understood that the pressure may contribute to spallation of the material [159]. However, for experimental arc-jet testing of PICA, spallation is estimated to be around 5% [12]. It is suggested in the current analysis that variations in

the stagnation pressure has two effects: one on the cold wall heat flux, and then second order mechanical effects. The total mass loss is thus assumed to depend on the heat input $Q_{cw} - Q_{rr}$ and the sample size, excluding variations on the stagnation pressure.

Table B.1: Dimensional analysis of arc-jet test data for PICA.

Variable	Units	Fundamental Units
Δm	kg	kg
q_{cw}	W/m^2	kg/s^3
q_{rr}	W/m^2	kg/s^3
R	m	m
H	J/kg	m^2/s^2
Δh	J/kg	m^2/s^2
C	$W\,kg/m^{3/2}\,J\,Pa^{1/2}$	$kg^{1/2}/m$
P	Pa	kg/ms^2
τ	s	s

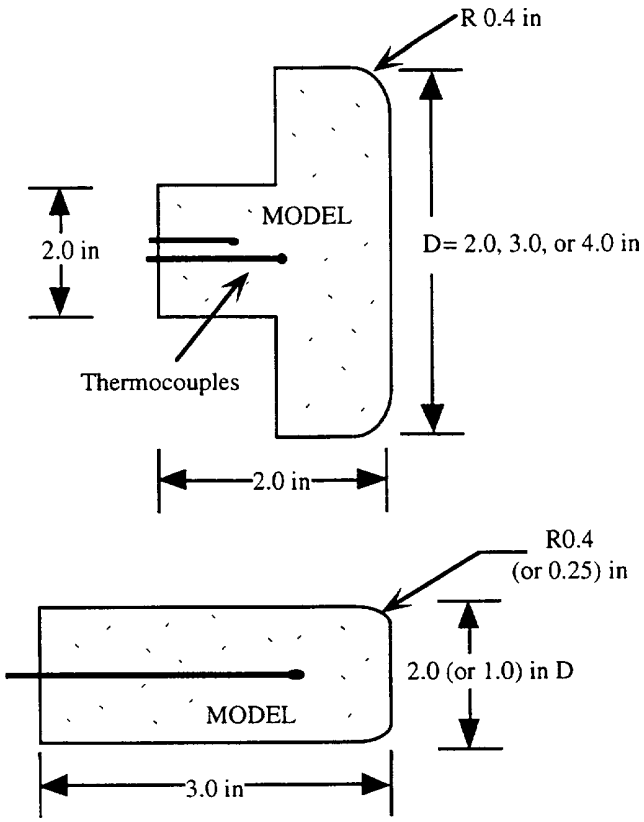

Figure B.1: Schematic of model geometries used in the Arc-jet testing of PICA (Phenolic Impregnated Carbon Ablator) from Ref [158].

Table B.2: Arc-jet testing of PICA (Phenolic Impregnated Carbon Ablator). The following data is from Ref [158].

Sample ID	Diameter (cm)	q_{cw} (W/cm^2)	Exposure Time (s)	θ_{surf} (K)	Mass loss (g)	P^{a} (kPa)
PICA-M4-A	2.555	3362	10	2755	1.814	43.57
PICA-M1-1	5.098	1136	25	2811	6.350	21.278
PICA-M5-26	5.090	1902	17	2700	4.536	34.451
PICA-M6-27	5.098	2158	14	3033	4.536	43.57
PICA-M2-6	7.630	483	25	2700	12.701	30.398
PICA-M2-7	7.628	1209	25	3311	11.340	34.451
PICA-M2-5	7.645	1363	17	2866	9.979	43.57
PICA-M3-10	10.104	426	25	2533	24.494	43.57
PICA-M3-8	10.152	454	25	2755	14.969	11.146
PICA-M3-11	10.142	511	25	2866	14.061	21.278
PICA-21G-PS	10.163	568	25	2978	19.504	42.556
PICA-M3-12	10.114	568	11	3144	10.886	42.556
PICA-M3-9	10.140	852	25	3089	18.597	43.57
PICA-M3-14	10.152	965	22	3089	19.504	43.57

[a] Stagnation pressure

Table B.3: Arc-jet testing of PICA (Phenolic Impregnated Carbon Ablator [158]), including calculated values of Q_{cw} and Q_{rr}.

Sample ID	Diameter (cm)	Mass loss (g)	q_{rr}^{a} (W/cm^2)	Q_{cw}^{a} (MJ)	Q_{rr}^{a} (MJ)	$Q_{cw} - Q_{rr}$ (MJ)
PICA-M4-A	2.555	1.814	294	0.172	0.015	0.157
PICA-M1-1	5.098	6.35	319	0.579	0.163	0.417
PICA-M5-26	5.090	4.536	271	0.658	0.094	0.564
PICA-M6-27	5.098	4.536	432	0.617	0.123	0.493
PICA-M2-6	7.630	12.701	271	0.552	0.31	0.242
PICA-M2-7	7.628	11.34	613	1.382	0.701	0.681
PICA-M2-5	7.645	9.979	345	1.064	0.269	0.795
PICA-M3-10	10.104	24.494	210	0.854	0.421	0.432
PICA-M3-8	10.152	14.969	294	0.919	0.595	0.324
PICA-M3-11	10.142	14.061	345	1.032	0.696	0.336
PICA-21G-PS	10.163	19.504	401	1.151	0.813	0.338
PICA-M3-12	10.114	10.886	499	0.502	0.441	0.061
PICA-M3-9	10.140	18.597	464	1.719	0.938	0.782
PICA-M3-14	10.152	19.504	464	1.719	0.827	0.892

[a] q_{rr}, Q_{cw} and Q_{rr} are calculated from equations A.1 and A.2 where the re-radiated flux is calculated from the experimental surface temperatures. The emissivity is also taken from the experimental reference with a value of 0.9.

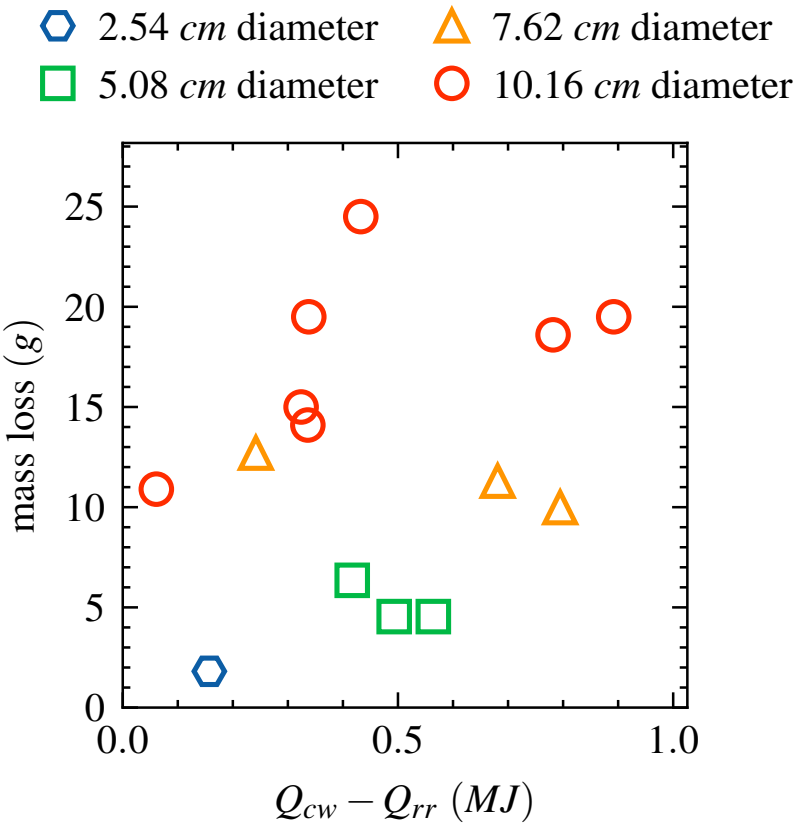

Figure B.2: Arc-jet testing of PICA (Phenolic Impregnated Carbon Ablator). The above figure shows the experimental mass loss versus $(Q_{cw} - Q_{rr})$, where Q_{cw} and Q_{rr} are calculated by equations A.1 and A.2.

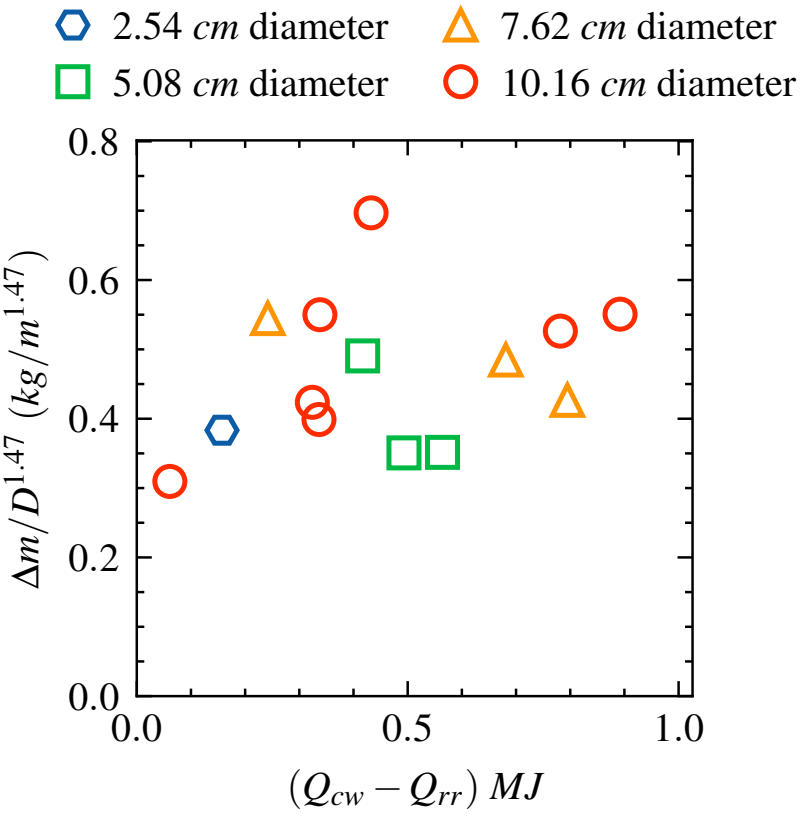

Figure B.3: Arc-jet testing of PICA (Phenolic Impregnated Carbon Ablator). The above figure shows the mass loss normalized by $D^{1.47}$ versus $(Q_{cw} - Q_{rr})$, where Q_{cw} and Q_{rr} are calculated by equations A.1 and A.2.

Appendix C

Oxyacetylene Torch Ablation Test Data for a Carbon Fiber Reinforced Cyanate Ester Composite

The author conducted oxyacetylene torch testing, as part of a masters thesis, of a carbon fiber reinforced cyanate ester composite with a composite density of 1710 kg/m^3. The resin mass fraction is not reported for the ablation test articles. It is estimated here from the constituent densities of cyanate ester (1250 kg/m^3) and carbon fiber (1800 kg/m^3) with a value of 0.114. The ablation article has a cylindrical geometry with a diameter and thickness of 3.0 cm and 1.27 cm respectively. The oxyacetylene tests were conducted according to ASTM E 285 [10]. The heat flux was estimated in the masters thesis from the torch conditions as 1000 W/cm^2, though no calorimeter measurements were reported. The total mass loss was measured at 0.588 g. Minimal surface recession was observed at under one millimeter measured by a dial gauge. A summary of the sample parameters and oxyacetylene torch test results are listed in Table C.1.

From the ablation images provided in the thesis, the flame diameter is significantly smaller than the sample diameter. In this research, the radial distribution of the torch heat flux is estimated as having a Gaussian distribution

based on the literature [104, 135, 154]. A functional form similar to Ref [104] is employed,

$$q_{cw} = q_0 \exp\left(-5\frac{r^2}{R^2}\right) \tag{C.1}$$

where q_0 is the maximum heat flux, r the distance from the torch center line, and R an effective heating radius. The above profile qualitatively matches CFD temperature simulation results of oxyacetylene torch ablation tests in literature [154]. From the ablation test image provided in the thesis, R is estimated as 1 cm. The cold wall heat load is then calculated as

$$\begin{aligned} Q_{cw} =& T q_0 2\pi \int_0^{1.5} \exp\left(-5r^2\right) r dr \\ Q_{cw} =& 28 * 1000 * \frac{\pi}{5}\left(1 - \exp(-5 * 1.5^2)\right) \\ Q_{cw} =& 17.6\ kJ \end{aligned} \tag{C.2}$$

For computing the re-radiated heat load Q_{rr}, it is assumed that the re-radiated flux follows a similar radial profile where $q_0 = \epsilon\sigma\theta_{surf}^4$. A surface temperature is not reported in the masters thesis. For calculating Q_{rr}, the surface temperature is estimated as 2273 K from published oxyacetylene torch ablation experiments in the literature conducted on the same experimental apparatus on a fully dense carbon phenolic material [77]. The emissivity is estimated from the literature as 0.9 [158]. The calculated values of Q_{cw} and Q_{rr} are listed in Table C.1.

Table C.1: Sample parameters and oxyacetylene torch ablation test results of a carbon fiber reinforced cyanate ester composite [119]. Q_{cw} and Q_{rr} are calculated assuming a Gaussian heating profile as described in equation C.2.

Sample parameters	
Diameter	3.0 cm
Thickness	1.27 cm
Density	1710 kg/m^3
Resin mass fraction[a]	0.114
OTB Test	
Heat flux[b]	1000 W/cm^2
Surface temperature[c]	2273 K
Exposure time	28 s
Mass loss	0.588 g
Q_{cw}	17.6 kJ
$Q_{cw} - Q_{rr}$	15.2 kJ

[a] The resin weight loading is computed in this thesis from the reported constituents and composite densities, assuming a porosity of zero.

[b] The heat flux in the paper was estimated by the author based on the oxyacetylene torch conditions, though calorimeter measurements were not reported.

[c] The surface temperature was not reported. A surface temperature is estimated in this thesis from published oxyacetylene torch ablation experiments in the literature conducted on the same experimental apparatus on a fully dense carbon phenolic material [77].

Appendix D

Mesoscale Program User Guide

D.1 Overview

The mesoscale program employs the hybrid particle-finite element method to perform a one-dimensional simulation of resin pyrolysis in a resin and fiber composite. The following sections describe the code compilation, input file, and code output.

D.2 Code Compilation

The program can be compiled with any C compiler for serial execution or parallel execution with OpenMP support. Table D.1 lists the compilation commands for the GCC compiler. The listed commands generate an executable titled `parallel` or `serial`, corresponding to compilation with or without OpenMP parallelization.

Table D.1: Compilation commands for the mesoscale program.

parallel	`gcc meso.c -lm -fopenmp -O3 -o parallel`
serial	`gcc meso.c -lm -O3 -o serial`

D.3 Units

SI units are employed:

mass	kilograms
length	meters
time	seconds
energy	Joules
temperature	Kelvin
velocity	meters per second
species concentration	moles per meters cubed

D.4 Input File Description

The program reads all simulation parameters from the input file `meso.inp`. The file format and example input files are provided at the end of this user guide. The input file consists of the following sections:

Control: This section specifies the simulation time duration, the number of printouts generated during the simulation, the domain length, and the number of particles in the domain. A buffer region is appended to the backside of the domain to prevent the reflection of mechanical waves, where the size of the buffer region is automatically computed by the program. A flag is included that permits the user to explicitly set the buffer region size. In order to reduce the computational cost, the buffer region employs a particle grading that successively increases the particle sizes by a constant factor (capped by a maximum factor) to reduce the number of particles; the default grading parameters may also be tuned by the user.

Loading: This section specifies the heat flux applied on the particles,

and the heating depth, which controls the heat flux profile.

Resin: This section specifies the resin density, sound speed, Grüneisen parameter, specific heat, and reference temperature.

Fiber: This section specifies the fiber density, sound speed, Grüneisen parameter, specific heat, and reference temperature.

Material: This section specifies the composite density, resin mass fraction, and fiber mass fraction. The program computes the composite porosity based on these quantities. For a fully dense material, the user can input a negative value for the composite density, in which case the program will compute the composite density assuming zero porosity. This section also specifies the resin shear modulus, yield stress, ultimate strength, failure accumulated plastic strain, fracture strain, and failure temperature. A flag is included where the program will adjust the resin shear modulus, yield stress, and ultimate strength by a factor of $(1 - \phi)$ to account for the composite porosity (ϕ).

Species: This section specifies the number of chemical species, the chemical species molar masses, and whether the simulation is conducted in an air or vacuum environment.

Reaction Rate Constants: This section specifies the number of chemical reactions and the reaction rate parameters. The chemical reactions have the following form:

$$\frac{\mathrm{d}}{\mathrm{d}t}C_i = \sum_{j=1}^{N_r} \xi^{(j)} \left(\nu^{(i,j)} - \hat{\nu}^{(i,j)}\right) \tag{D.1}$$

where C_i are species concentrations (moles per volume), N_r is the number of reactions, and $\nu^{(i,j)}$ and $\hat{\nu}^{(i,j)}$ are the product and reactant stoichiometric coefficients for species i in reaction j respectively. The reaction rates $\xi^{(j)}$ are defined as:

$$\xi^{(j)} = k^{(j)} f^{(j)}(\theta) \prod_{i=1}^{N_s} C_i^{\alpha^{(i,j)}} \tag{D.2}$$

where $k^{(j)}$ are the reaction rate constants, N_s is the number of species, $\alpha^{(i,j)}$ the reaction exponents, and $f^{(j)}(\theta)$ are temperature dependent functions. The program supports three functional forms for $f^{(j)}(\theta)$:

$$f^{(j)}(\theta) = \left[1 + \exp\left(\frac{\theta - \theta^{(j)}}{\theta^{(j)}}\right)\right]^{-1} \qquad \text{type 0} \tag{D.3a}$$

$$f^{(j)}(\theta) = 1 - \left[1 + \exp\left(\frac{\theta - \theta^{(j)}}{\theta^{(j)}}\right)\right]^{-1} \qquad \text{type 1} \tag{D.3b}$$

$$f^{(j)}(\theta) = 1 \qquad \text{type 2} \tag{D.3c}$$

It is assumed in the mesoscale program that only one reaction consumes the resin species, referred to in this user guide as the disassociation reaction.

Reaction Stoichiometric Matrix: This section specifies the reaction stoichiometry. The stoichiometric coefficients are input as the matrix $\nu^{(i,j)} - \hat{\nu}^{(i,j)}$.

Reaction Exponent Matrix: This section specifies the reaction exponents. The exponents are input as the matrix $\alpha^{(i,j)}$.

Pyrolysis: This section specifies the parameters associated with resin decomposition, including the resin decomposition enthalpy, resin pyrolysis temperature, and maximum extent of resin pyrolysis. The program automatically initializes a gas control volume associated with each particle in which

the gas species are assumed to reside. A flag is included that allows the user to explicitly set the gas control volume size as a factor of the particle volume.

D.5 Code Output

The program writes to files particle and element quantities where all files are written in text format. Table D.2 lists the output files and associated quantities. The program writes to the file `ablation` at each printout the following eight quantities: 1) simulation time, 2) time step, 3) total mass loss, 4) total heat input, 5) total system energy, 6) total system mass, 7) exact system energy, and 8) exact system mass. The exact system mass and energy are obtained by integrating the power flow and mass flow entering and leaving the system. The last four quantities can be used to verify the conservation of mass and energy.

For files which contain time dependent quantities, the printout index is appended to the filenames to distinguish between printouts. The time stamps at each printout uniformly divide the simulation time duration.

At the conclusion of the simulation, the total number of particles (including buffer particles), wall time, run time, and number of threads used, if compiled with OpenMP support, are written to the file `meso.runtime`.

Table D.2: Mesoscale program output filenames and associated descriptions. All files are written in text format. The printout index is appended to the filenames to distinguish between printouts.

File Name	Simulation Quantity
`ablation`	system energy (J), mass (kg), and simulation time (s)
`gasvol`[†]	particle gas control volume (m^3)
`def`	particle volumetric compression
`den`	particle density (kg/m^3)
`diam`[†]	particle diameters (m)
`dmg`	element damage
`efp`	element accumulated plastic strain
`ie`	particle specific internal energy (J/kg)
`m`	particle mass (kg)
`pe`	particle pressure (Pa)
`pegas`	particle gas pressure (Pa)
`qflux`	particle heat flux (W/m^2)
`qinp`	particle heat input rate (W)
`rpv`	particle resin extent of pyrolysis
`sm`	particle species masses (kg)
`strain`	element elastic strain
`stress`	element stress (Pa)
`te`	particle temperature (K)
`v`	particle velocity (m/s)
`x`	particle position (m)

[†] The particle diameters and gas control volumes are time independent and are thus written once at the start of the simulation. All other files are generated at each printout where the printout index is appended to the filenames.

D.6 Input File Format

In the following, "default" values provided for entry fields must be entered by the user.

Line	Columns	Data Type	Description
Control			
1	–	–	blank (optional section title)
2	1-12	float	dimensionless time step factor, default=10.0
2	12-24	float	simulation stop time (s)
2	24-36	float	number of print outs
3	1-12	float	domain length, excluding buffer (m)
3	12-24	float	number of particles in domain, excluding buffer
4	1-12	integer	flag to set buffer length (yes=1, no=0), default=0
4	12-24	float	buffer length (m)
5	1-12	float	particle grading factor, default=1.1
5	12-24	float	maximum particle grading, default=100.0
Loading			
1	–	–	blank (optional section title)
2	1-12	float	heat flux (W/m^2-s)
2	12-24	float	heating depth (m)
Resin			
1	–	–	blank (optional section title)
2	1-12	float	resin density (kg/m^3)

Continued on next page

3	1-12	float	resin sound speed (m/s)
3	12-24	float	resin Grüneisen parameter
4	1-12	float	resin specific heat ($J/kg\text{-}K$)
4	12-24	float	resin reference temperature (K)

Fiber

1	–	–	blank (optional section title)
2	1-12	float	fiber density (kg/m^3)
3	1-12	float	fiber sound speed (m/s)
3	12-24	float	fiber Grüneisen parameter
4	1-12	float	fiber specific heat ($J/kg\text{-}K$)
4	12-24	float	fiber reference temperature (K)

Material

1	–	–	blank (optional section title)
2	1-12	float	composite density (kg/m^3)
2	12-24	float	resin mass fraction
2	24-36	float	fiber mass fraction
3	1-12	float	resin shear modulus (Pa)
3	12-24	float	resin yield stress (Pa)
3	24-36	float	resin ultimate strength (Pa)
4	1-12	float	resin failure accumulated plastic strain
4	12-24	float	resin failure elastic strain
4	24-36	float	resin failure temperature (K)
5	1-12	integer	flag to scale elastic properties (yes=1, no=0), default=1
6	1-12	float	dimensionless numerical viscosity, default=1.0

Continued on next page

6	12-24	float	dimensionless numerical conduction, default=10^{-4}

Species

1	–	–	blank (optional section title)
2	1-12	integer	number of species
2	12-24	integer	resin species index (index from zero)
3	1-12	integer	air case boolean (in air=1, in vacuum=0)
3	12-24	integer	oxygen species index (index from zero)
3	24-36	integer	nitrogen species index (index from zero)
N_s rows follow with one row for each species			
–	1-12	string	species name
–	12-24	float	species molar mass (kg)

Reaction Rate Constants

1	–	–	blank (optional section title)
2	1-12	integer	number of reactions
2	12-24	integer	disassociation reaction index (index from zero)

Three rows follow with N_r columns per row. Each column corresponds to a chemical reaction. Each entry composes 12 spaces.

3	–	float	reaction rate constant $k^{(j)}$ $(1/s)(mol/m^3)^{1-m^{(j)}}$, $m^{(j)} = \sum_{i=1}^{N_s} \alpha^{(i,j)}$
4	–	integer	temperature function type (0, 1, or 2)
5	–	float	temperature parameter $\theta^{(j)}$ (K)

Continued on next page

Reaction Stoichiometric Matrix

1	–	–	blank (optional section title)

N_s rows follow with N_r columns per row. Each row corresponds to a chemical species, and each column to a chemical reaction. Each entry composes 12 spaces.

–	–	float	product minus reactant stoichiometric coefficient for associated species and reaction $(\nu^{(i,j)} - \hat{\nu}^{(i,j)})$

Reaction Exponent Matrix

1	–	–	blank (optional section title)

N_s rows follow with N_r columns per row. Each row corresponds to a chemical species, and each column to a chemical reaction. Each entry composes 12 spaces.

–	–	float	reaction exponent for associated species and reaction $(\alpha^{(i,j)})$

Pyrolysis

1	–	–	blank (optional section title)
2	1-12	float	resin pyrolysis temperature (K)
2	12-24	float	resin decomposition enthalpy (J/kg)
2	24-36	float	maximum extent of resin pyrolysis
3	1-12	float	dimensionless gas convection coefficient, default=10^6
4	1-12	integer	flag to set gas control volume (yes=1, no=0), default=0
4	12-24	float	dimensionless gas control volume

D.7 Input File Examples

Pyrolysis simulation of a high density carbon phenolic material in air:

```
CONTROL
        10.0    20.00e-9         100
        4e-6         800
           0
         1.1       100.0
LOADING
     7.25e10     5.00e-8
RESIN
      1250.0
      2370.0         1.3
      1674.0       300.0
FIBER
      1800.0
      2687.0        0.26
       771.0       300.0
MATERIAL
      1450.0       0.375       0.625
      5.79e9     136.0e6     272.0e6
        0.25        10.0       500.0
           1
         1.0        1e-4
SPECIES
          11           0
           1           2           3
       C6H6O     94.0e-3
           N     14.0e-3
          O2     32.0e-3
          N2     28.0e-3
         CO2     44.0e-3
          OH     17.0e-3
          CO     28.0e-3
           H      1.0e-3
           C     12.0e-3
           O     16.0e-3
         H2O     18.0e-3
REACTION RATE CONSTANTS
           6           0
 1.01997e+09 6.95552e+07 1.02167e+03 1.96735e+06 4.47335e+05 2.09225e+00
           2           0           0           0           0           0
           0  2.1183e+03  1.6411e+03  3.1660e+03  3.1660e+03  1.6411e+03
```

```
REACTION STOICHIOMETRIC MATRIX
        -1.0         0.0         0.0         0.0         0.0         0.0
        48.0        -2.0         0.0         0.0         0.0         0.0
        -7.0         0.0         0.0         0.0         0.0         0.0
       -24.0         1.0         0.0         0.0         0.0         0.0
 1.66667e-01         0.0         0.0         0.0         0.0         1.0
 1.66667e-01         0.0        -1.0         1.0         0.0         0.0
         1.0         0.0         0.0         0.0         1.0        -1.0
 5.833333333         0.0        -1.0        -1.0         0.0         0.0
 4.833333333         0.0         0.0         0.0        -1.0         0.0
        13.5         0.0         0.0        -1.0        -1.0        -1.0
         0.0         0.0         1.0         0.0         0.0         0.0
REACTION EXPONENT MATRIX
      0.5013         0.0         0.0         0.0         0.0         0.0
         0.0      1.7596         0.0         0.0         0.0         0.0
      0.5014         0.0         0.0         0.0         0.0         0.0
      0.5002         0.0         0.0         0.0         0.0         0.0
         0.0         0.0         0.0         0.0         0.0         0.0
         0.0         0.0      1.6617         0.0         0.0         0.0
         0.0         0.0         0.0         0.0         0.0      1.9433
         0.0         0.0      1.3069      1.1893         0.0         0.0
         0.0         0.0         0.0         0.0     0.28855         0.0
         0.0         0.0         0.0     0.87235      1.9198      1.5637
         0.0         0.0         0.0         0.0         0.0         0.0
PYROLYSIS
       500.0       293e3        0.99
         1e6
           0
```

Pyrolysis simulation of a high density carbon phenolic material in vacuum:

```
CONTROL
        10.0    20.00e-9         100
        4e-6         800
           0
         1.1       100.0
LOADING
     7.25e10     5.00e-8
RESIN
      1250.0
      2370.0         1.3
      1674.0       300.0
FIBER
      1800.0
      2687.0        0.26
       771.0       300.0
MATERIAL
      1450.0       0.375       0.625
      5.79e9     136.0e6     272.0e6
        0.25        10.0       500.0
           1
         1.0        1e-4
SPECIES
           8           0
           0
       C6H6O     94.0e-3
           H      1.0e-3
           C     12.0e-3
           O     16.0e-3
          C2     24.0e-3
          CH     13.0e-3
          CO     28.0e-3
         CH2     14.0e-3
REACTION RATE CONSTANTS
           5           0
 1.05040e+13 1.76789e+06 1.33713e+07 1.41897e+08 8.38106e+05
           2           0           0           1           0
           0      2000.0      2000.0      2000.0      2000.0
```

```
REACTION STOICHIOMETRIC MATRIX
        -1.0         0.0         0.0         0.0         0.0
       5.225         0.0         0.0        -1.0        -1.0
         5.0        -1.0        -2.0        -1.0         0.0
         0.9        -1.0         0.0         0.0         0.0
         0.1         0.0         1.0         0.0         0.0
       0.625         0.0         0.0         1.0        -1.0
         0.1         1.0         0.0         0.0         0.0
       0.075         0.0         0.0         0.0         1.0
REACTION EXPONENT MATRIX
      0.5687         0.0         0.0         0.0         0.0
         0.0         0.0         0.0     0.66341    0.023431
         0.0      1.4697      1.6300     0.49622         0.0
         0.0     0.50613         0.0         0.0         0.0
         0.0         0.0         0.0         0.0         0.0
         0.0         0.0         0.0         0.0       2.000
         0.0         0.0         0.0         0.0         0.0
         0.0         0.0         0.0         0.0         0.0
PYROLYSIS
       500.0       293e3        0.99
         1e6
           0
```

```
CONTROL
        10.0    20.00e-9         100
        4e-6         800
           0
         1.1       100.0
LOADING
     1.37e10     5.00e-8
RESIN
      1250.0
      2370.0         1.3
      1674.0       300.0
FIBER
      1800.0
      2687.0        0.26
       771.0       300.0
MATERIAL
       274.0       0.380       0.620
      5.79e9     136.0e6     272.0e6
        0.25        10.0       500.0
           1
         1.0        1e-4
SPECIES
          11           0
           1           2           3
       C6H6O     94.0e-3
           N     14.0e-3
          O2     32.0e-3
          N2     28.0e-3
         CO2     44.0e-3
          OH     17.0e-3
          CO     28.0e-3
           H      1.0e-3
           C     12.0e-3
           O     16.0e-3
         H2O     18.0e-3
REACTION RATE CONSTANTS
           6           0
 1.01997e+09 6.95552e+07 1.02167e+03 1.96735e+06 4.47335e+05 2.09225e+00
           2           0           0           0           0           0
           0  2.1183e+03  1.6411e+03  3.1660e+03  3.1660e+03  1.6411e+03
```

```
REACTION STOICHIOMETRIC MATRIX
        -1.0         0.0         0.0         0.0         0.0         0.0
        48.0        -2.0         0.0         0.0         0.0         0.0
        -7.0         0.0         0.0         0.0         0.0         0.0
       -24.0         1.0         0.0         0.0         0.0         0.0
 1.66667e-01         0.0         0.0         0.0         0.0         1.0
 1.66667e-01         0.0        -1.0         1.0         0.0         0.0
         1.0         0.0         0.0         0.0         1.0        -1.0
 5.833333333         0.0        -1.0        -1.0         0.0         0.0
 4.833333333         0.0         0.0         0.0        -1.0         0.0
        13.5         0.0         0.0        -1.0        -1.0        -1.0
         0.0         0.0         1.0         0.0         0.0         0.0
REACTION EXPONENT MATRIX
      0.5013         0.0         0.0         0.0         0.0         0.0
         0.0      1.7596         0.0         0.0         0.0         0.0
      0.5014         0.0         0.0         0.0         0.0         0.0
      0.5002         0.0         0.0         0.0         0.0         0.0
         0.0         0.0         0.0         0.0         0.0         0.0
         0.0         0.0      1.6617         0.0         0.0         0.0
         0.0         0.0         0.0         0.0         0.0      1.9433
         0.0         0.0      1.3069      1.1893         0.0         0.0
         0.0         0.0         0.0         0.0     0.28855         0.0
         0.0         0.0         0.0     0.87235      1.9198      1.5637
         0.0         0.0         0.0         0.0         0.0         0.0
PYROLYSIS
       500.0       293e3        0.99
         1e6
           0
```

```
CONTROL
        10.0    20.00e-9         100
        4e-6         800
           0
         1.1       100.0
LOADING
     1.37e10     5.00e-8
RESIN
      1250.0
      2370.0         1.3
      1674.0       300.0
FIBER
      1800.0
      2687.0        0.26
       771.0       300.0
MATERIAL
       274.0       0.380       0.620
      5.79e9     136.0e6     272.0e6
        0.25        10.0       500.0
           1
         1.0        1e-4
SPECIES
           8           0
           0
       C6H6O     94.0e-3
           H      1.0e-3
           C     12.0e-3
           O     16.0e-3
          C2     24.0e-3
          CH     13.0e-3
          CO     28.0e-3
         CH2     14.0e-3
REACTION RATE CONSTANTS
           5           0
 1.05040e+13 1.76789e+06 1.33713e+07 1.41897e+08 8.38106e+05
           2           0           0           1           0
           0      2000.0      2000.0      2000.0      2000.0
```

```
REACTION STOICHIOMETRIC MATRIX
        -1.0         0.0         0.0         0.0         0.0
       5.225         0.0         0.0        -1.0        -1.0
         5.0        -1.0        -2.0        -1.0         0.0
         0.9        -1.0         0.0         0.0         0.0
         0.1         0.0         1.0         0.0         0.0
       0.625         0.0         0.0         1.0        -1.0
         0.1         1.0         0.0         0.0         0.0
       0.075         0.0         0.0         0.0         1.0
REACTION EXPONENT MATRIX
      0.5687         0.0         0.0         0.0         0.0
         0.0         0.0         0.0     0.66341    0.023431
         0.0      1.4697      1.6300     0.49622         0.0
         0.0     0.50613         0.0         0.0         0.0
         0.0         0.0         0.0         0.0         0.0
         0.0         0.0         0.0         0.0       2.000
         0.0         0.0         0.0         0.0         0.0
         0.0         0.0         0.0         0.0         0.0
PYROLYSIS
       500.0       293e3        0.99
         1e6
           0
```

```
CONTROL
        10.0    20.00e-9         100
        4e-6         800
           0
         1.1       100.0
LOADING
     8.57e10     5.00e-8
RESIN
      1250.0
      1425.0        0.11
      1200.0       300.0
FIBER
      1800.0
      2687.0        0.26
       771.0       300.0
MATERIAL
        -1.0       0.114       0.886
      1.16e9      55.0e6     110.0e6
        0.25        10.0       700.0
           1
         1.0        1e-4
SPECIES
          11           0
           1           2           3
  C17H14N2O2    278.0e-3
           N     14.0e-3
          O2     32.0e-3
          N2     28.0e-3
         CO2     44.0e-3
          OH     17.0e-3
          CO     28.0e-3
           H      1.0e-3
           C     12.0e-3
           O     16.0e-3
         H2O     18.0e-3
REACTION RATE CONSTANTS
           6           0
 8.29853e+09 3.19006e+10 7.43240e+09 1.18212e+02 5.08995e+06 9.58208e+06
           2           0           0           0           0           0
           0  3.6251e+03  2.3503e+03  3.3310e+03  3.3310e+03  2.3503e+03
```

```
REACTION STOICHIOMETRIC MATRIX
        -1.0         0.0         0.0         0.0         0.0         0.0
       125.0        -2.0         0.0         0.0         0.0         0.0
       -19.5         0.0         0.0         0.0         0.0         0.0
       -61.5         1.0         0.0         0.0         0.0         0.0
         0.5         0.0         0.0         0.0         0.0         1.0
         0.5         0.0        -1.0         1.0         0.0         0.0
         3.0         0.0         0.0         0.0         1.0        -1.0
        13.5         0.0        -1.0        -1.0         0.0         0.0
        13.5         0.0         0.0         0.0        -1.0         0.0
        36.5         0.0         0.0        -1.0        -1.0        -1.0
         0.0         0.0         1.0         0.0         0.0         0.0
REACTION EXPONENT MATRIX
      0.5527         0.0         0.0         0.0         0.0         0.0
         0.0  1.2473e+00         0.0         0.0         0.0         0.0
      0.5237         0.0         0.0         0.0         0.0         0.0
      0.4407         0.0         0.0         0.0         0.0         0.0
         0.0         0.0         0.0         0.0         0.0         0.0
         0.0         0.0  6.5733e-01         0.0         0.0         0.0
         0.0         0.0         0.0         0.0         0.0  5.0601e-01
         0.0         0.0  6.2490e-01  1.8920e+00         0.0         0.0
         0.0         0.0         0.0         0.0  1.1321e+00         0.0
         0.0         0.0         0.0  9.7954e-01  9.8697e-01  1.4584e+00
         0.0         0.0         0.0         0.0         0.0         0.0
PYROLYSIS
       700.0     -47.0e3        0.99
         1e6
           0
```

Pyrolysis simulation of a carbon cyanate ester material in vacuum

```
CONTROL
        10.0    20.00e-9         100
        4e-6         800
           0
         1.1       100.0
LOADING
     8.57e10     5.00e-8
RESIN
      1250.0
      1425.0        0.11
      1200.0       300.0
FIBER
      1800.0
      2687.0        0.26
       771.0       300.0
MATERIAL
        -1.0       0.114       0.886
      1.16e9      55.0e6     110.0e6
        0.25        10.0       700.0
           1
         1.0        1e-4
SPECIES
          10           0
           0
  C17H14N2O2    278.0e-3
           H      1.0e-3
           C     12.0e-3
           N     14.0e-3
           O     16.0e-3
          C2     24.0e-3
          N2     28.0e-3
          CH     13.0e-3
          CO     28.0e-3
         CH2     14.0e-3
REACTION RATE CONSTANTS
           6           0
 3.88441e+12 9.73592e+04 5.17522e+06 4.91996e+06 3.93672e-03 1.12672e+07
           2           0           0           1           0           0
         0.0      1002.0      1002.0       998.6       998.6      1000.1
```

```
REACTION STOICHIOMETRIC MATRIX
        -1.0         0.0         0.0         0.0         0.0         0.0
      12.375         0.0         0.0        -1.0        -1.0         0.0
        13.0        -1.0        -2.0        -1.0         0.0         0.0
        1.75         0.0         0.0         0.0         0.0        -2.0
        1.75        -1.0         0.0         0.0         0.0         0.0
      1.0625         0.0         1.0         0.0         0.0         0.0
       0.125         0.0         0.0         0.0         0.0         1.0
       1.625         0.0         0.0         1.0        -1.0         0.0
        0.25         1.0         0.0         0.0         0.0         0.0
         0.0         0.0         0.0         0.0         1.0         0.0
REACTION EXPONENT MATRIX
         0.5         0.0         0.0         0.0         0.0         0.0
         0.0         0.0         0.0      0.3791       2.000         0.0
         0.0      0.5785      1.9907      1.0806         0.0         0.0
         0.0         0.0         0.0         0.0         0.0      1.9759
         0.0      1.9996         0.0         0.0         0.0         0.0
         0.0         0.0         0.0         0.0         0.0         0.0
         0.0         0.0         0.0         0.0         0.0         0.0
         0.0         0.0         0.0         0.0       2.000         0.0
         0.0         0.0         0.0         0.0         0.0         0.0
         0.0         0.0         0.0         0.0         0.0         0.0
PYROLYSIS
       700.0     -47.0e3        0.99
         1e6
           0
```

D.8 Plot Script

The following Matlab script plots the quantities described in Table D.2 with respect to the particles' reference configuration (position at time zero). The buffer region, which is appended to the backside of the domain to prevent the reflection of mechanical waves, is excluded in the plots, where the buffer region consists of particles with a negative spatial position in the reference configuration. Following the plot script, the figures for the pyrolysis simulation of high density carbon phenolic in air are provided. The corresponding input file is given in the preceding section. Since the pyrolysis reactions occur rapidly at the heating front, the gas species densities tend to have a step response centered around the heating profile. Thus, only the oxygen species spatial profile is shown in the following figures, though the following script plots all of the species present in the simulation.

```
clear all;

% printout index
N = 100;

% directory containing simulation output files
direc = "../";

x      = load(sprintf('%s/x_000', direc));
ie     = load(sprintf('%s/ie_%03d', direc, N));
def    = load(sprintf('%s/def_%03d', direc, N));
dmg    = load(sprintf('%s/dmg_%03d', direc, N));
den    = load(sprintf('%s/den_%03d', direc, N));
pe     = load(sprintf('%s/pe_%03d', direc, N));
efp    = load(sprintf('%s/efp_%03d', direc, N));
rpv    = load(sprintf('%s/rpv_%03d', direc, N));
stress = load(sprintf('%s/stress_%03d', direc, N));
te     = load(sprintf('%s/te_%03d', direc, N));
v      = load(sprintf('%s/v_%03d', direc, N));
qflux  = load(sprintf('%s/qflux_%03d', direc, N));
qinp   = load(sprintf('%s/qinp_%03d', direc, N));
m      = load(sprintf('%s/m_%03d', direc, N));

gasvol = load(sprintf('%s/gasvol', direc));
pegas  = load(sprintf('%s/pegas_%03d', direc, N));

smfilename = sprintf('%s/sm_%03d', direc, N);
file = fopen(smfilename);
species_names = fgetl(file);
species_names = split(strtrim(species_names));
fclose(file);
species = readmatrix(smfilename, 'NumHeaderLines', 1);

massOut = zeros(1, N);
heatInp = zeros(1, N);
for i=1:N
    file = fopen(sprintf('%s/ablation_%03d', direc, i));
    line = fgetl(file);
    while line~=-1
        if contains(line, 'total mass loss')
            line = split(strtrim(line));
            massOut(i) = str2double(line{end});
        end
        if contains(line, 'total heat input')
            line = split(strtrim(line));
```

```
            heatInp(i) = str2double(line{end});
        end
        line = fgetl(file);
    end
    fclose(file);
end

% element centroid position
xe = (x(1:end-1) + x(2:end)).*.5;

% exclude buffer region in plots
ind  = x>=0;
inde = xe>=0;

x     = x(ind);
xe    = xe(inde);

ie    = ie(ind);
pe    = pe(ind);
rpv   = rpv(ind);
den   = den(ind);
def   = def(ind);
dmg   = dmg(inde);
efp   = efp(inde);
stress= stress(inde);
te    = te(ind);
v     = v(ind);
qflux = qflux(ind);
qinp  = qinp(ind);
m     = m(ind);

pegas = pegas(ind);
species = species(ind, 1:end);
gasvol = gasvol(ind);

size = [684, 496];
layout = "loose";
linewidth = 1;

fig = figure();
fig.Position(3:4) = [336, 315];
plot(massOut.*1e3, heatInp.*1e-3, 'LineWidth', linewidth);
xlabel('mass out (g)', 'Interpreter', 'latex');
ylabel('heat input (kJ)', 'Interpreter', 'latex');
title('heat input (kJ) vs mass out (g)', 'Interpreter', 'latex');
```

```
setLim(gca, massOut.*1e3, heatInp.*1e-3);
savefig(fig, 'fig1')

fig = figure();
tiledlayout(2,2, "TileSpacing", layout);
fig.Position(3:4) = size;

ax = nexttile;
plot(ax, x.*1e6, ie.*1e-3, 'LineWidth', linewidth);
xlabel(ax, 'X ($\mu$m)', 'Interpreter', 'latex');
ylabel(ax, 'internal energy (kJ/kg)', 'Interpreter', 'latex');
title(ax, 'internal energy (kJ/kg) vs position ($\mu$m)', ...
      'Interpreter', 'latex');
setLim(ax, x.*1e6, ie.*1e-3);

ax = nexttile;
plot(ax, x.*1e6, pe.*1e-6, 'LineWidth', linewidth);
xlabel(ax, 'X ($\mu$m)', 'Interpreter', 'latex');
ylabel(ax, 'pressure (MPa)', 'Interpreter', 'latex');
title(ax, 'pressure (MPa) vs position ($\mu$m)', ...
      'Interpreter', 'latex');
setLim0(ax, x.*1e6, pe.*1e-6);

ax = nexttile;
plot(ax, x.*1e6, rpv, 'LineWidth', linewidth);
xlabel(ax, 'X ($\mu$m)', 'Interpreter', 'latex');
ylabel(ax, 'resin extent of pyrolysis', 'Interpreter', 'latex');
title(ax, 'resin extent of pyrolysis vs position ($\mu$m)', ...
      'Interpreter', 'latex');
setLim(ax, x.*1e6, rpv);

ax = nexttile;
plot(ax, x.*1e6, den, 'LineWidth', linewidth);
xlabel(ax, 'X ($\mu$m)', 'Interpreter', 'latex');
ylabel(ax, 'density (kg/m$^3$)', 'Interpreter', 'latex');
title(ax, 'density (kg/m$^3$) vs position ($\mu$m)', ...
      'Interpreter', 'latex');
setLim0(ax, x.*1e6, den);

savefig(fig, 'fig2')

fig = figure();
tiledlayout(2,2, "TileSpacing", layout);
fig.Position(3:4) = size;
```

```
ax = nexttile;
plot(ax, x.*1e6, def, 'LineWidth', linewidth);
xlabel(ax, 'X ($\mu$m)', 'Interpreter', 'latex');
ylabel(ax, 'volumetric compression', 'Interpreter', 'latex');
title(ax, 'volumetric compression vs position ($\mu$m)', ...
      'Interpreter', 'latex');
setLim(ax, x.*1e6, def);

ax = nexttile;
plot(ax, xe.*1e6, dmg, 'LineWidth', linewidth);
xlabel(ax, 'X ($\mu$m)', 'Interpreter', 'latex');
ylabel(ax, 'element damage', 'Interpreter', 'latex');
title(ax, 'element damage vs position ($\mu$m)', ...
      'Interpreter', 'latex');
setLim(ax, xe.*1e6, dmg);

ax = nexttile;
plot(ax, xe.*1e6, efp, 'LineWidth', linewidth);
xlabel(ax, 'X ($\mu$m)', 'Interpreter', 'latex');
ylabel(ax, 'accumulated plastic strain', 'Interpreter', 'latex');
title(ax, 'accumulated plastic strain vs position ($\mu$m)', ...
      'Interpreter', 'latex');
setLim(ax, xe.*1e6, efp);

ax = nexttile;
plot(ax, xe.*1e6, stress.*1e-6, 'LineWidth', linewidth);
xlabel(ax, 'X ($\mu$m)', 'Interpreter', 'latex');
ylabel(ax, 'stress (MPa)', 'Interpreter', 'latex');
title(ax, 'stress (MPa) vs position ($\mu$m)', ...
      'Interpreter', 'latex');
setLim(ax, xe.*1e6, stress.*1e-6);

savefig(fig, 'fig3')

fig = figure();
tiledlayout(2,2, "TileSpacing", layout);
fig.Position(3:4) = size;

ax = nexttile;
plot(ax, x.*1e6, te, 'LineWidth', linewidth);
xlabel(ax, 'X ($\mu$m)', 'Interpreter', 'latex');
ylabel(ax, 'temperature (K)', 'Interpreter', 'latex');
title(ax, 'temperature (K) vs position ($\mu$m)', ...
      'Interpreter', 'latex');
setLim(ax, x.*1e6, te);
```

```
ax = nexttile;
plot(ax, x.*1e6, v, 'LineWidth', linewidth);
xlabel(ax, 'X ($\mu$m)', 'Interpreter', 'latex');
ylabel(ax, 'velocity (m/s)', 'Interpreter', 'latex');
title(ax, 'velocity (m/s) vs position ($\mu$m)', ...
      'Interpreter', 'latex');
setLim(ax, x.*1e6, v);

ax = nexttile;
plot(ax, x.*1e6, qflux.*1e-9, 'LineWidth', linewidth);
xlabel(ax, 'X ($\mu$m)', 'Interpreter', 'latex');
ylabel(ax, 'heat flux J/ns-m$^2$', 'Interpreter', 'latex');
title(ax, 'heat flux (J/ns-m$^2$) vs position ($\mu$m)', ...
      'Interpreter', 'latex');
setLim(ax, x.*1e6, qflux.*1e-9);

ax = nexttile;
plot(ax, x.*1e6, qinp.*1e-9./(m.*1e3), 'LineWidth', linewidth);
xlabel(ax, 'X ($\mu$m)', 'Interpreter', 'latex');
ylabel(ax, 'heat input J/ns-g', 'Interpreter', 'latex');
title(ax, 'heat input (J/ns-g) vs position ($\mu$m)', ...
      'Interpreter', 'latex');
setLim(ax, x.*1e6, qinp.*1e-9./(m.*1e3));

savefig(fig, 'fig4')

fig = figure();
fig.Position(3:4) = [336, 315];
plot(x.*1e6, pegas.*1e-6, 'LineWidth', linewidth);
xlabel(gca(), 'X ($\mu$m)', 'Interpreter', 'latex');
ylabel(gca(), 'gas pressure (MPa)', 'Interpreter', 'latex');
title('gas pressure (MPa) vs position ($\mu$m)', ...
      'Interpreter', 'latex');
setLim0(gca(), x.*1e6, pegas.*1e-6);
savefig(fig, 'fig5')

file = fopen(sprintf('%s/meso.inp', direc));
for i=1:23
   line = fgetl(file);
end
line = split(strtrim(line));
ns = str2num(line{1});
resin_index = str2num(line{2}) + 1;
```

```
for i=1:ns
   if i~=resin_index
       fig = figure();
       fig.Position(3:4) = [336, 315];
       plot(x.*1e6, species(1:end,i)./gasvol, 'LineWidth',
          linewidth);
       xlabel(gca(), 'X ($\mu$m)', 'Interpreter', 'latex');
       ylabel(gca(), 'density (kg/m$^3$)', ...
              'Interpreter', 'latex');
       title(species_names{i});
       setLim0(gca(), x.*1e6, species(1:end,i)./gasvol);
       savefig(fig, species_names{i})
   end
end

% set plot limits
function setLim(ax, x, y)
    xmin = min(x);
    ymin = min(y);
    xmax = max(x);
    ymax = max(y);
    xint = xmax - xmin;
    yint = ymax - ymin;
    xlim(ax, [xmin-.05*xint, xmax+.05*xint]);
    ylim(ax, [ymin-.05*yint, ymax+.05*yint]);
end

% set plot limits with ylimit set to zero
function setLim0(ax, x, y)
    xmin = min(x);
    ymin = 0;
    xmax = max(x);
    ymax = max(y);
    xint = xmax - xmin;
    yint = ymax - ymin;
    xlim(ax, [xmin-.05*xint, xmax+.05*xint]);
    ylim(ax, [ymin-.05*yint, ymax+.05*yint]);
end
```

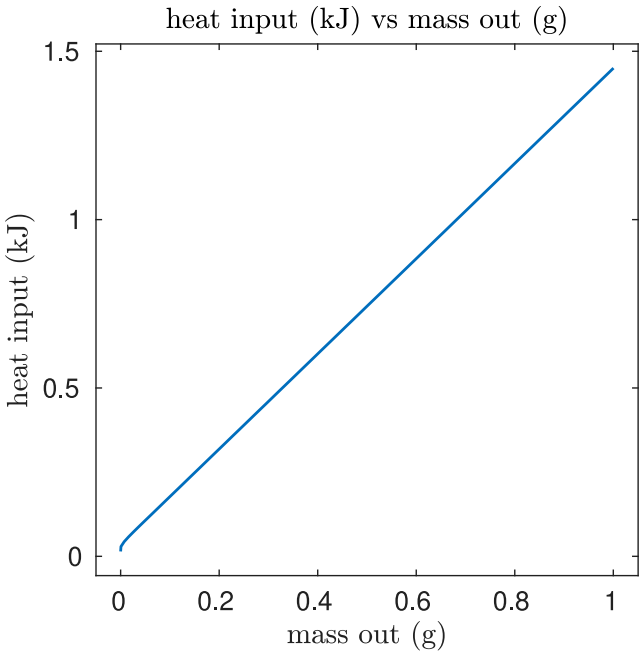

Figure D.1: Pyrolysis simulation of a high density carbon phenolic material in an air environment, showing total heat input versus mass loss.

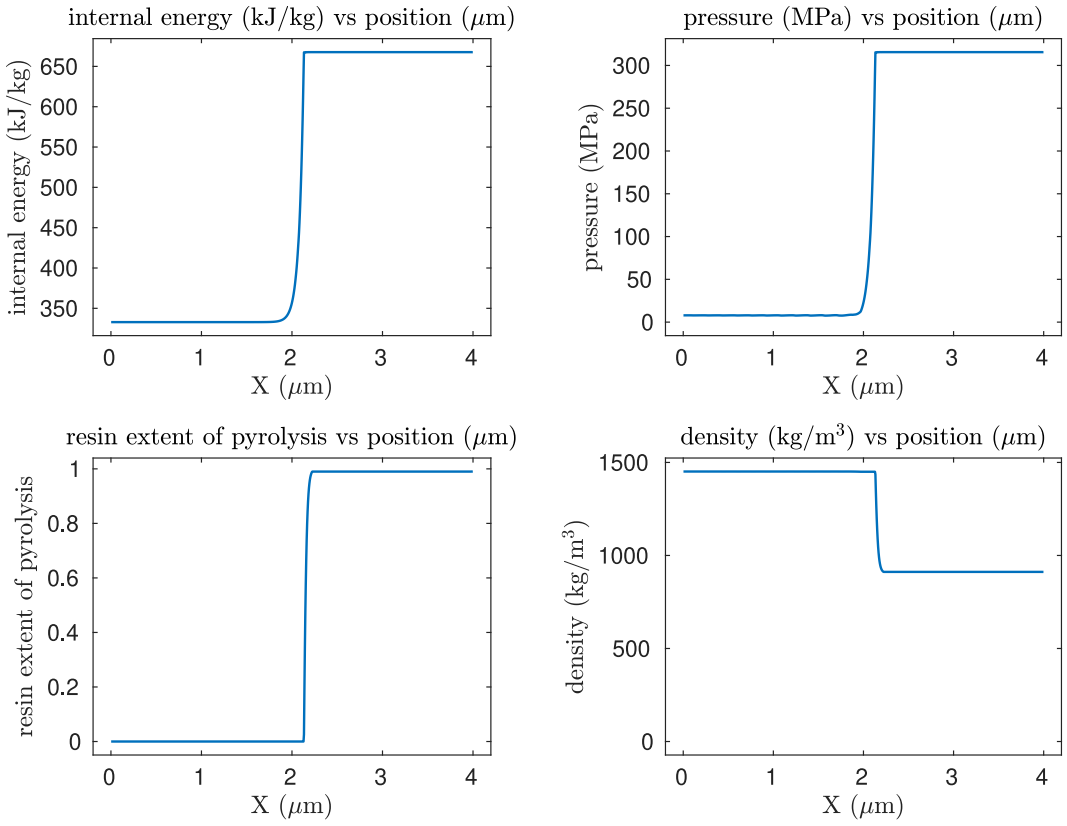

Figure D.2: Pyrolysis simulation of a high density carbon phenolic material in an air environment, showing the internal energy, pressure, extent of pyrolysis, and density spatial profiles.

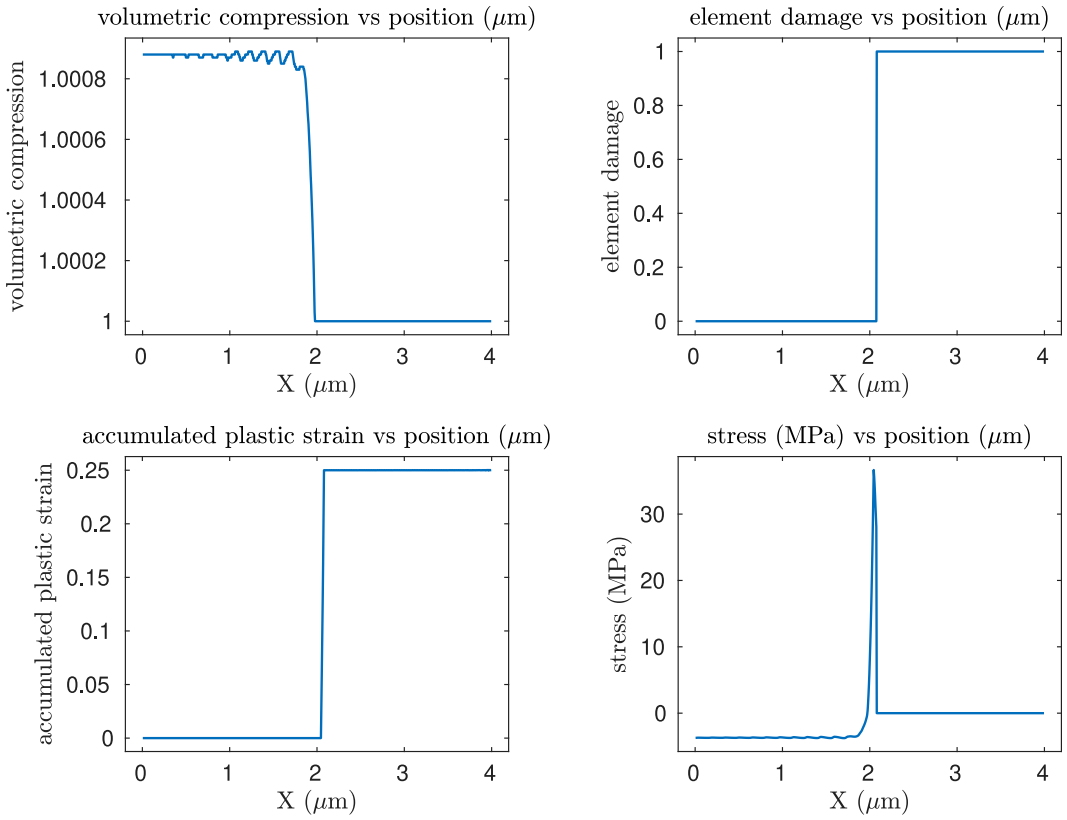

Figure D.3: Pyrolysis simulation of a high density carbon phenolic material in an air environment, showing the volumetric compression, damage, accumulated plastic strain, and stress spatial profiles.

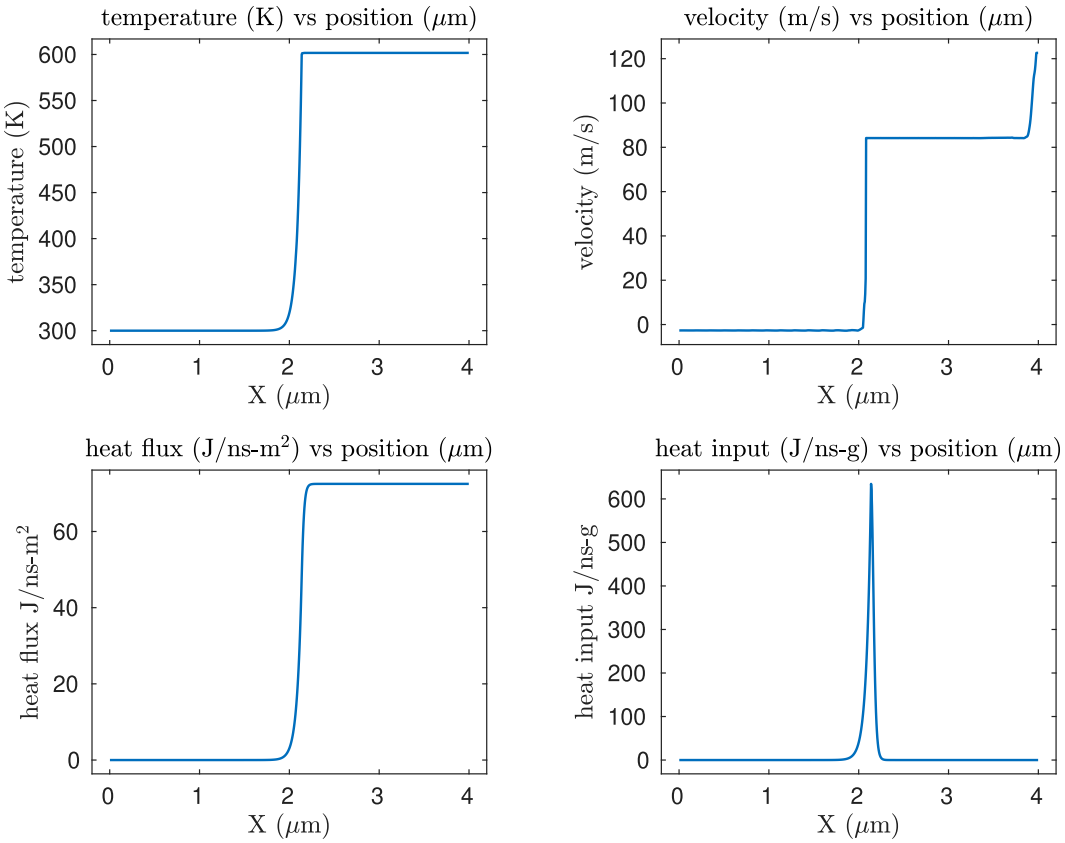

Figure D.4: Pyrolysis simulation of a high density carbon phenolic material in an air environment, showing the temperature, velocity, and heat input spatial profiles.

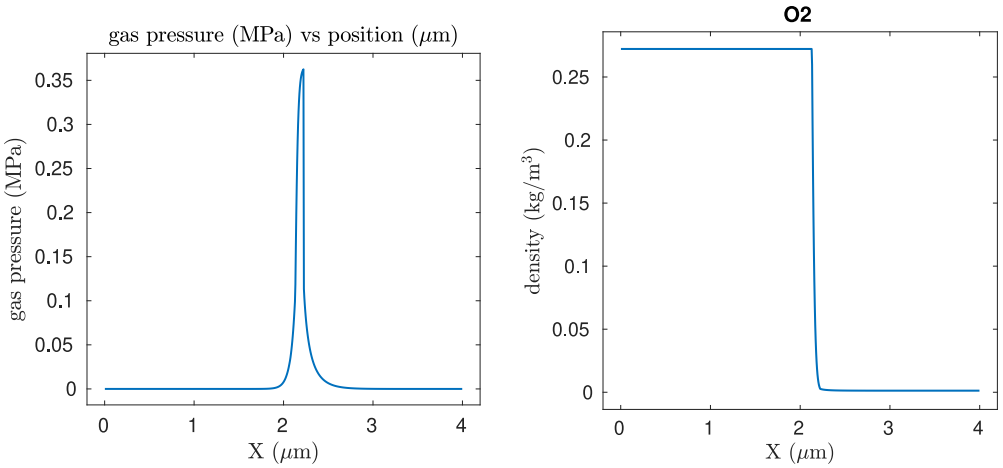

Figure D.5: Pyrolysis simulation of a high density carbon phenolic material in an air environment, showing the total gas pressure and oxygen density spatial profile.

Bibliography

[1] J. Abrahamson. Graphite sublimation temperatures, carbon arcs and crystallite erosion. *Carbon*, 12(2), 1974.

[2] Hannah Alpert, Milad Mahzari, David Saunders, Joshua Monk, and Todd R. White. Inverse Estimation of Mars 2020 Entry Aeroheating Environments Using MEDLI2 Flight Data. *AIAA 2022 Scitech Forum*, 2022.

[3] Adam Amar, Nathan Calvert, and Benjamin Kirk. Development and verification of the charring ablating thermal protection implicit system solver. *49th AIAA Aerospace Sciences Meeting including the New Horizons Forum and Aerospace Exposition*, 2011.

[4] Adam J. Amar, Ben F. Blackwell, and J. R. Edwards. Development and verification of a one-dimensional ablation code including pyrolysis gas flow. *Journal of Thermophysics and Heat Transfer*, 23(1):59–71, 2009.

[5] Adam J. Amar, A. Brandon Oliver, Benjamin S. Kirk, Giovanni Salazar, and Justin Droba. Overview of the charring ablator response (CHAR) code. *46th AIAA Thermophysics Conference*, 2016.

[6] Adam J. Amar, Justin Cooper, A. Brandon Oliver, Giovanni Salazar, and Lucas Agricola. Mesh Deformation Boundary Conditions for Three-Dimensional Ablation Solvers. *AIAA Science and Technology Forum and Exposition, AIAA SciTech Forum 2022*, 2022.

[7] R. Anzalone, B. W. Barr, R. R. Upadhyay, and O. A. Ezekoye. Use of a quasi-steady ablation model for design sensitivity with uncertainty propagation. *Journal of Thermal Science and Engineering Applications*, 2017.

[8] Ahilan Appar, Rakesh Kumar, and Srujan K. Naspoori. Conjugate flow-thermal analysis of a hypersonic reentry vehicle in the rarefied flow regime. *Physics of Fluids*, 34, 2022.

[9] Yvan Aspa, Jean R. Lachaud, Gérard L Vignoles, and Michel Quintard. Simulation of C/C composites ablation using a VOF method with moving reactive interface. *ECCM12 proceedings*, 2006.

[10] ASTM E285-08. Standard Test Method for Oxyacetylene Ablation Testing of Thermal Insulation Materials. ASTM International, West Conshohocken, PA, 2020. w.astm.org.

[11] Prashanth Badrinarayanan, Ben Mac Murray, and Michael R. Kessler. Zirconium tungstate reinforced cyanate ester composites with enhanced dimensional stability. *Journal of Materials Research*, 24(7):2235–2242, 2009.

[12] Sean C.C. Bailey, Dominik Bauer, Francesco Panerai, Scott C. Splinter, Paul M. Danehy, J. Matthew Hardy, and Alexandre Martin. Experimental analysis of spallation particle trajectories in an arc-jet environment. *Experimental Thermal and Fluid Science*, 93(January):319–325, 2018.

[13] Michael Barnhardt, Aaron Brandis, Michael Wright, and Monica Hughes. Recent advances in modeling and simulation of entry systems at nasa. Nasa technical report, NASA, 2019.

[14] Eugene P. Bartlett, Robert M. Kendall, and Roald A. Rindal. A Unified Approximation for Mixture Transport Properties for Multi-component Boundary-Layer Applications. Technical Report CR 1063, NASA, 1968.

[15] J. Bass and E. Fahrenthold. Nonholonomic Hamiltonian method for molecular dynamics simulations of reacting shocks. *AIP Conference Proceedings*, 1793(070011), 2017.

[16] J. L. Bass. *Nonholonomic Hamiltonian Method for Reacting Molecular Dynamics*. PhD thesis, University of Texas at Austin, August 2017.

[17] Charles W. Bauschlicher, Tingting Qi, Evan J. Reed, Antonin Lenfant, John W. Lawson, and Tapan G. Desai. Comparison of ReaxFF, DFTB, and DFT for phenolic pyrolysis. 2. Elementary reaction paths. *Journal of Physical Chemistry A*, 117(44):11126–11135, 2013.

[18] Robin A. S. Beck. Ablative Thermal Protection Systems Fundamentals. Presented at Thermal and Fluids Analysis Workshop, Huntsville, Al-

abama, August 2017. https://ntrs.nasa.gov/api/citations/20170011453/downloads/20170011453.pdf.

[19] Abhishek S. Bhesania, Parvesh Kamboj, Sai Abhishek Peddakotla, and Rakesh Kumar. In-depth analysis of reaction kinetics parameters of phenolic resin using molecular dynamics and unsupervised machine learning approach. *Computational Materials Science*, 206, January 2022.

[20] Abhishek S. Bhesania, Rakesh Kumar, and Vaibhav K. Arghode. Ablative Thermal Response for Two-Dimensional Axisymmetric Problems. *Journal of Thermophysics and Heat Transfer*, 2022.

[21] Daniele Bianchi, Francesco Nasuti, and Emanuele Martelli. Navier-stokes simulations of hypersonic flows with coupled graphite ablation. *Journal of Spacecraft and Rockets*, 47(4):554–562, 2010.

[22] Arnaud Borner, Francesco Panerai, and Nagi N. Mansour. High temperature permeability of fibrous materials using direct simulation Monte Carlo. *International Journal of Heat and Mass Transfer*, 106:1318–1326, 2017.

[23] Ian D. Boyd. Interdisciplinary Hypersonics Research in Academia. Hypersonic Weapons Summit, April, 2021. https://dsiac.org/wp-content/uploads/2021/05/Boyd-DSIAC-Talk_15-Sept-211.pdf.

[24] E. Buckingham. On Physically Similar Systems: Illustrations of the Use of Dimensional Analysis. *Physical Review*, 4, 1914.

[25] Vincent Calard, Celeste Pereira, Antonio Vavouliotis, Stefan Forero, Laurent Pambaguian, and Fellicitas Hepp. Thermal, Electrical And Mechanical Properties Of Carbon Nanotube Reinforced Cyanate Ester Polymer. `http://esmat.esa.int/materials\_news/isme09/pdf/4-New/S6\%20-\%20Calard.pdf`.

[26] Samuel Y. Chen and Iain D. Boyd. Chemical equilibrium analysis of silicon carbide oxidation in oxygen and air. *Journal of the American Ceramic Society*, 2019.

[27] T. B.Y. Chen, A. C.Y. Yuen, B. Lin, L. Liu, A. L.P. Lo, Q. N. Chan, J. Zhang, S. C.P. Cheung, and G. H. Yeoh. Characterisation of pyrolysis kinetics and detailed gas species formations of engineering polymers via reactive molecular dynamics (ReaxFF). *Journal of Analytical and Applied Pyrolysis*, 153, 2020.

[28] Y. K. Chen and F. S. Milos. Two-dimensional implicit thermal response and ablation program for charring materials. *Journal of Spacecraft and Rockets*, 38(4):473–481, 2001.

[29] Yih Kanq Chen and Tahir Gökçen. Evaluation of finite-rate gas/surface interaction models for carbon-based ablator. *Journal of Spacecraft and Rockets*, 53(1):143–152, 2016.

[30] Yih-Kanq Chen and Tahir Gökçen. Evaluation of Sublimation Kinetics for Phenolic Impregnated Carbon Ablator. *Journal of Spacecraft and Rockets*, 2022.

[31] Yih Kanq Chen, Tahir Gökçen, and Karl T. Edquist. Two-dimensional ablation and thermal response analyses for mars science laboratory heat shield. *Journal of Spacecraft and Rockets*, 52(1):134–143, 2015.

[32] Yih-Kanq Chen, Frank S. Miles, and Tahir Gökçen. Loosely coupled simulation for two-dimensional ablation and shape change. *Journal of Spacecraft and Rockets*, 2010.

[33] Yih Kanq Chen and Frank S. Milos. Ablation and thermal response program for spacecraft heatshield analysis. *Journal of Spacecraft and Rockets*, 36(3), 1999.

[34] Yih Kanq Chen and Frank S. Milos. Effects of Nonequilibrium Chemistry and Darcy-Forchheimer Pyrolysis Flow for Charring Ablator. *Journal of Spacecraft and Rockets*, 50(2):256–269, 2013.

[35] Yih Kanq Chen and Frank S. Milos. Multidimensional finite volume fully implicit ablation and thermal response code. *Journal of Spacecraft and Rockets*, 55(4):914–927, 2018.

[36] Gary C. Cheng, Balaji Shankar Venkatachari, and Ioana Cozmuta. Multi-scale simulations of in-depth pyrolysis of charring ablative thermal protection material. *Computers and Fluids*, 45(1):191–196, 2011.

[37] O. Chiantore, M. Lazzari, and M. Fontana. Thermal Decomposition of Phenol-Formaldehyde Foundry Resins. *International Journal of Polymer Analysis and Characterization*, 1995.

[38] Robert Chiodi, Kelly Stephani, Marco Panesi, and Daniel J. Bodony. CHyPS: A High-Order Material Response Solver for Ablative Thermal Protection Systems. *AIAA Science and Technology Forum and Exposition, AIAA SciTech Forum 2022*, 2022.

[39] R. M. Christensen. Properties of carbon fibers. *Journal of the Mechanics and Physics of Solids*, 42(4):681–695, 1994.

[40] CIDRA Precision Services - Machining of Materials. (2023, March 09). Silica - Fused Silica (Silicon Dioxide). AZoM. Retrived on April 03, 2023 from `https://www.azom.com/article.aspx?ArticleID=1387`.

[41] Ronald Keith Clark. An analysis of a charring ablator with thermal nonequilibrium, chemical kinetics, and mass transfer. NASA Technical Note D-7180. NASA, Hampton, 1973.

[42] Joffrey Coheur, Alessandro Turchi, Pierre Schrooyen, and Thierry E. Magin. Development of a unified model for flow-material interaction applied to porous charring ablators. *47th AIAA Thermophysics Conference, 2017*, 2017.

[43] Sônia Fonseca Costa e Silva, Humberto Araújo Machado, and Edison Bittencourt. Effect of the fiber orientation relatively to the plasma flow direction in the ablation process of a carbon-phenolic composite. *Journal of Aerospace Technology and Management*, 7(1):43–52, 2015.

[44] M A Covington, J M Heinemann, H E Goldstein, Y.-K Chen, I Terrazas-Salinas, J A Balboni, Olejniczak, and E R Martinez. Performance of a Low Density Ablative Heat Shield Material. *Journal of Spacecraft and Rockets*, 45(2), 2008.

[45] Peter G. Cross. Coupled simulations of finite-rate ablation with pyrolysis in rocket nozzles. *Journal of Thermophysics and Heat Transfer*, 2020.

[46] Peter G. Cross and Iain D. Boyd. Two-dimensional modeling of ablation and pyrolysis with application to rocket nozzles. *Journal of Spacecraft and Rockets*, 54(1):212–224, 2017.

[47] Peter G. Cross and Iain D. Boyd. Conjugate analyses of ablation in rocket nozzles. *Journal of Spacecraft and Rockets*, 56(5):1593–1610, 2019.

[48] David Z. Dang, Eric C. Stern, and Iain D. Boyd. Data-Driven Analysis of the Stiffness Degradation of a Woven Thermal Protection System. *Journal of Spacecraft and Rockets*, 2022.

[49] John A. Dec, Robert D. Braun, and Bernard Laub. Ablative thermal response analysis using the finite element method. *Journal of Thermophysics and Heat Transfer*, 2012.

[50] Bruno Dias, Aleksander L. Zibitsker, Jeremie B. Meurisse, and Nagi N.

Mansour. Towards a flow-material unified solver for heatshield modeling. *AIAA SciTech 2023 Forum*, 2023.

[51] D. Dixit, R. Pal, G. Kapoor, and M. Stabenau. 6 - lightweight composite materials processing. In Ashok Bhatnagar, editor, *Lightweight Ballistic Composites (Second Edition)*, Woodhead Publishing Series in Composites Science and Engineering, pages 157–216. Woodhead Publishing, second edition edition, 2016.

[52] Mark E. Ewing, Daron A. Isaac, H. Heath Dewey, Cory W. Smith, Zachary D. Harman, and David T. Walker. Multidimensional Modeling of Ablation Heat Transfer. *Journal of Thermophysics and Heat Transfer*, 2023.

[53] Mark E. Ewing, Travis S. Laker, and David T. Walker. Numerical modeling of ablation heat transfer. *Journal of Thermophysics and Heat Transfer*, 27(4):615–632, 2013.

[54] Eric P. Fahrenthold and Charles R. Hean. Discrete Lagrange equations for thermofluid systems. *Journal of Dynamic Systems, Measurement and Control, Transactions of the ASME*, 130, 2008.

[55] J. A. Fay and F. R. Riddell. Theory of Stagnation Point Heat Transfer in Dissociated Air. *Journal of the Aerospace Sciences*, 25(2):73–85, 1958.

[56] Joseph C. Ferguson, Francesco Panerai, Arnaud Borner, and Nagi N.

Mansour. PuMA: the Porous Microstructure Analysis software. *SoftwareX*, 7:81–87, 2018.

[57] Joseph C. Ferguson, Francesco Panerai, Jean R. Lachaud, and Nagi N. Mansour. Theoretical study on the micro-scale oxidation of resin-infused carbon ablators. *Carbon*, 121:552–562, 2017.

[58] Joseph C. Ferguson, Francesco Panerai, Jean R. Lachaud, Alexandre Martin, Sean C.C. Bailey, and Nagi N. Mansour. Modeling the oxidation of low-density carbon fiber material based on micro-tomography. *Carbon*, 96:57–65, 2016.

[59] L. Formaggia and F. Nobile. A stability analysis for the arbitrary Lagrangian Eulerian formulation with finite elements. *East-West Journal of Numerical Mathematics*, 7(2):105–131, 1999.

[60] Rui Fu, Haoyue Weng, Jonathan F. Wenk, and Alexandre Martin. Thermomechanical Coupling for Charring Ablators. *Journal of Thermophysics and Heat Transfer*, 32(2):369–379, 2018.

[61] Rui Fu, Haoyue Weng, Jonathan F. Wenk, and Alexandre Martin. Thermal Expansion for Charring Ablative Materials. *Journal of Thermophysics and Heat Transfer*, 34(1):57–65, 2020.

[62] Xueqiong Fu. Nanostructure, Plastic Deformation, and Influence of Strain Rate Concerning Ni/Al2O3 Interface System Using a Molecular Dynamic Study (LAMMPS). *Nanomaterials*, 2023.

[63] Luciano Garelli, Rodrigo R Paz, Mario A Storti, Cristian García Bauza, Pablo Lotito, Lisandro Parente, and Marcelo Vénere. Geometric conservation law in ALE formulations. *Mecánica Computacional*, XXVIII(November):1477–1488, 2009.

[64] Tahir Gökçen, Yih-Kanq Chen, Kristina A. Skokova, and Frank S. Milos. Computational analysis of arc-jet stagnation tests including ablation and shape change. *Journal of Thermophysics and Heat Transfer*, 24(4):694–707, 2010.

[65] Rene F. B. Goncalves, Koshun Iha, and Jose A. F. F. Rocco. Reactive Molecular Dynamic Simulation and Chemical Kinetic Evaluation of Combustion of Triethylaluminium (TEA). *Quim. Nova*, 41(5):507–511, 2018.

[66] Dennis Grady. Differential Hugoniot and experimental estimate of the Grüneisen parameter for SiO_2. In *AIP Conference Proceedings*, 1998.

[67] Abdurrahman Günday. A method for distributed sensing of temperature, strain and weight formations employing the acoustic velocity and Bulk modulus of fused silica. *Optik*, 252(October 2021):168489, 2022.

[68] Abhilash Harpale, Saurabh Sawant, Rakesh Kumar, Deborah Levin, and Huck Beng Chew. Ablative thermal protection systems: Pyrolysis modeling by scale-bridging molecular dynamics. *Carbon*, 130:315–324, 2018.

[69] Bruce Hartmann. Ultrasonic properties of phenolic and poly(phenylquinoxaline) polymers. *Journal of Applied Polymer Science*, 19(12):3241–3255, 1975.

[70] Charles R. Hean and Eric P. Fahrenthold. Discrete Lagrange equations for reacting thermofluid dynamics in arbitrary Lagrangian–Eulerian frames. *Computer Methods in Applied Mechanics and Engineering*, 313:303–320, 2017.

[71] Bernd Helber, Alessandro Turchi, James B. Scoggins, Annick Hubin, and Thierry E. Magin. Experimental investigation of ablation and pyrolysis processes of carbon-phenolic ablators in atmospheric entry plasmas. *International Journal of Heat and Mass Transfer*, 2016.

[72] R. J. Hernandez. *Hybrid Particle-Element for a General Hexahedral Mesh*. PhD thesis, University of Texas at Austin, 2009.

[73] R. J. Hernandez and E. P. Fahrentold. Hybrid particle-element method for an unstructured hexahedral mesh. *International Journal for Numerical Methods in Engineering*, 94:1191–1215, 2013.

[74] Nevin K. Hiester and Carroll F. Clark. Comparative evaluation of ablating materials in arc plasma jets. Nasa cr-1207, Stanford Research Institute, December 1968.

[75] Roy Hogan, Ben F. Blackwell, and R. J. Cochran. Application of moving grid control volume finite element method to ablation problems. *Journal of Thermophysics and Heat Transfer*, 10(2):312–319, 1996.

[76] Jürgen Horbach, Walter Kob, and Kurt Binder. Specific heat of amorphous silica within the harmonic approximation. *Journal of Physical Chemistry B*, 103(20):4104–4108, 1999.

[77] Yanan Hou, Colin Yee, Wei Li, Joseph H. Koo, Liguo Li, Ben Rech, William Fahy, Hao Wu, and Jarrod J. Buffy. A novel ablative material for thermal protection system: Carbon fiber/polysiloxane composites. *Aerospace Science and Technology*, 129:107822, 2022.

[78] Sergio Fraile Izquierdo, Federico Semeraro, and Marcos Acín. Multi-Scale Analysis of Effective Mechanical Properties of Porous 3D Woven Composite Materials. *AIAA Science and Technology Forum and Exposition, AIAA SciTech Forum 2022*, 2022.

[79] Revathi Jambunathan, Deborah A. Levin, Arnaud Borner, Joseph C. Ferguson, and Francesco Panerai. Prediction of thermal protection system material permeability and hydraulic tortuosity factor using Direct Simulation Monte Carlo. *AIAA Aerospace Sciences Meeting, 2018*, 2018.

[80] Fenghui Jiang, J. L. de Ris, and M. M. Khan. Absorption of thermal energy in pmma by in-depth radiation. *Fire Safety Journal*, 2009.

[81] Joe Boylan (2001, May 29). Carbon - Graphite Materials. AZoM. Retrived on April 05, 2023 from `https://www.azom.com/article.aspx?ArticleID=516`.

[82] M. S. Kandelousi and D. D. Ganji. *Hydrothermal Analysis in Engineering Using Control Volume Finite Element Method*, chapter Control volume finite element method (CVFEM), pages 1–12. Academic Press, 2015.

[83] Sumio Kato, Keiichi Okuyama, Kenta Gibo, Takuma Miyagi, Toshiyuki Suzuki, Kazuhisa Fujita, Takeharu Sakai, Seiji Nishio, and Akihiro Watanabe. Thermal Response Simulation of Ultra Light Weight Phenolic Carbon Ablator by the Use of the Ablation Analysis Code. *Transactions of the Japan Society for Aeronautical and Space Sciences, Aerospace Technology Japan*, 2012.

[84] Robert M. Kendall. A General Approach to the Thermochemical Solution of Mixed Equilibrium-Nonequilibrium, Homogeneous or Heterogeneous Systems. Technical Report CR 1064, NASA, June 1968.

[85] Robert M. Kendall and Eugene P. Bartlett. Nonsimilar Solution of the Multicomponent Laminar Boundary Layer by an Integral-Matrix Method. *AIAA Journal*, 6(6), June 1968.

[86] Robert M. Kendall, Eugene P. Bartlett, Roald A. Rindal, and Carl B. Moyer. An Analysis of the Coupled Chemically Reacting Boundary Layer and Charring Ablator, Part 1 Summary Report. Technical Report CR-1060, NASA, 1968.

[87] Robert M. Kendall, Roald A. Rindal, and Eugene P. Bartlett. Thermochemical Ablation. *AIAA Thermophysics Specialist Conference*, 1965.

[88] H. Kolsky. *Stress Waves in Solids*. Dover, New York, 1963.

[89] J. C. Koo and E. P. Fahrenthold. Discrete Hamilton's equations for arbitrary Lagrangian-Eulerian dynamics of viscous compressible flow. *Computer Methods in Applied Mechanics and Engineering*, 2000.

[90] David W. Kuntz, Basil Hassan, and Donald L. Potter. Predictions of Ablating Hypersonic Vehicles Using an Iterative Coupled Fluid/Thermal Approach. *Journal of Thermophysics and Heat Transfer*, 15(2):129–139, 2001.

[91] J. Lachaud, A. Martin, I. Cozmuta, and B. Laub. Ablation Workshop Test Case, Ver. 1.1, Feb. 2011. Schmisseur, J., *4rth Ablation Workshop*, Albuquerque, NM, March 2011.

[92] J. Lachaud, J. B. Scoggins, T. E. Magin, M. G. Meyer, and N. N. Mansour. A generic local thermal equilibrium model for porous reactive materials submitted to high temperatures. *International Journal of Heat and Mass Transfer*, 108:1406–1417, 2017.

[93] J. Lachaud and G. L. Vignoles. A Brownian motion technique to simulate gasification and its application to C/C composite ablation. *Computational Materials Science*, 44(4):1034–1041, 2009.

[94] Jean Lachaud, Ioana Cozmuta, and Nagi N. Mansour. Multiscale approach to ablation modeling of phenolic impregnated carbon ablators. *Journal of Spacecraft and Rockets*, 47(6):910–921, 2010.

[95] Jean Lachaud and Nagi N. Mansour. Porous-material analysis toolbox based on openfoam and applications. *Journal of Thermophysics and Heat Transfer*, 28(2):191–202, 2014.

[96] Jean Lachaud, Tom Van Eekelen, James B. Scoggins, Thierry E. Magin, and Nagi N. Mansour. Detailed chemical equilibrium model for porous ablative materials. *International Journal of Heat and Mass Transfer*, 90:1034–1045, 2015.

[97] Jean R. Lachaud, Thierry E Magin, Ioana Cozmuta, and Nagi N. Mansour. A short review of ablative-material response models and simulation tools. *7th Aerothermodynamics Symposium*, 2011.

[98] Michael Ladacki, Janet V. Hamilton, and Samuel N. Conz. Heat of pyrolysis of resin in silica-phenolic ablator. *AIAA Journal*, 4(10):1798–1802, 1966.

[99] Bernard Laub. Ablator modeling: why not much has changed over the past 45+ years. 4th AF/SNL/NASA ablation workshop, Albuquerque, NM, March 2011. `https://ntrs.nasa.gov/api/citations/20110012046/downloads/20110012046.pdf`.

[100] Sangyup Lee. *Nonholonomic Hamiltonian method for multiscale simulation of reacting shocks physics*. PhD thesis, University of Texas at Austin, 2017.

[101] Sangyup Lee and Eric P. Fahrenthold. Multiscale simulation of shock to detonation in condensed phase explosives. *Journal of Applied Physics*, 132(175901), 2022.

[102] Cyril Levet, Jean R. Lachaud, Virginie Ducamp, Régis Memes, Jacques Couzi, Julien Mathiaud, Adrien P. Gillard, P. Weisbecker, and Gérard L. Vignoles. High-flux sublimation of a 3D carbon/carbon composite: Surface roughness patterns. *Carbon*, 173:817–831, 2021.

[103] Jing Li and Stanislav I. Stoliarov. Measurement of kinetics and thermodynamics of the thermal degradation for charring polymers. *Polymer Degradation and Stability*, 106:2–15, 2014.

[104] Weijie Li, Zhongwei Zhang, Mengdie Zhu, Jun Zhang, Zhichao Dong, Haiming Huang, and Jun Liang. Heat insulation and ablation resistance performance of continuous fiber reinforced composites with integrated gradient fabric. *Polymer Composites*, 43(4):2375–2383, 2022.

[105] Qiang Liu, Shixiang Liu, Yadong Lv, Ping Hu, Yajiang Huang, Miqiu Kong, and Guangxian Li. Atomic-scale insight into the pyrolysis of polycarbonate by ReaxFF-based reactive molecular dynamics simulation. *Fuel*, 287(January 2020), 2021.

[106] J. H. Lundell and R. R. Dickey. Response of Heat-Shield Materials To Intense Laser Radiation. *Progress in Astronautics and Aeronautics*, 64:193–209, 1978.

[107] Alexandre Martin and Iain D. Boyd. Non-Darcian behavior of pyrolysis gas in a thermal protection system. *Journal of Thermophysics and Heat Transfer*, 24(1):60–68, 2010.

[108] Alexandre Martin and Iain D. Boyd. Strongly coupled computation of material response and nonequilibrium flow for hypersonic ablation. *Journal of Spacecraft and Rockets*, 52(1):89–104, 2015.

[109] Chad August McCoy. "the sound velocity and grüneisen parameter of fused silica, periclase, and polystyrene shocked to tpa pressures". Master's thesis, University of Rochester, Rochester, New York, 2016.

[110] Jeremie B.E. Meurisse, Georgios Bellas Chatzigeorgis, Patricia Ventura Diaz, Brody K. Bessire, Francesco Panerai, and Nagi N. Mansour. Equilibrium model for the ablation response of silicone-coated PICA. *International Journal of Heat and Mass Transfer*, 201, 2023.

[111] Jeremie B.E. Meurisse, Jean R. Lachaud, Francesco Panerai, Chun Tang, and Nagi N. Mansour. Multidimensional material response simulations of a full-scale tiled ablative heatshield. *Aerospace Science and Technology*, 76:497–511, 2018.

[112] Claudio Miccoli, Alessandro Turchi, Pierre Schrooyen, Domenic D'Ambrosio, and Thierry Magin. Detailed Modeling of Cork-Phenolic Ablators in Preparation for the Post-flight Analysis of the QARMAN Re-entry CubeSat. *Aerotecnica Missili & Spazio*, 2021.

[113] F. S. Milos and Y. K. Chen. Ablation, thermal response, and chemistry program for analysis of thermal protection systems. *Journal of Spacecraft and Rockets*, 50(1):137–149, 2013.

[114] Frank S. Milos, Matthew J. Gasch, Dinesh K. Prabhu, and G. Russell. Conformal Phenolic Impregnated Carbon Ablator Arcjet Testing, Ablation, and Thermal Response. In *Journal of Spacecraft and Rockets*, volume 52, pages 804–812. American Institute of Aeronautics and Astronautics Inc., 2015.

[115] Frank S. Milos and Y. K. Ghent. Comprehensive model for multicomponent ablation thermochemistry. In *35th Aerospace Sciences Meeting and Exhibit*. American Institute of Aeronautics and Astronautics Inc, AIAA, 1997.

[116] Hosein Molavi, Iraj Pourshaban, Ali Hakkaki-Fard, Mehdi Molavi, Anahita Ayasoufi, and Ramin K. Rahmani. Inverse identification of thermal properties of charring ablators. *Numerical Heat Transfer, Part B: Fundamentals*, 56(6):478–501, 2009.

[117] Joshua Monk, Jay D. Feldman, Milad Mahzari, Jose A. Santos, Todd R. White, Dinesh K. Prabhu, and Hannah Alpert. MEDLI2 Material Response Model Development and Validation. In *AIAA SCITECH 2022 Forum*, 2022.

[118] C. B. Moyer and R. A. Rindal. An Analysis of the Coupled Chemically Reacting Boundary Layer and Charring Ablator, Part II, Finite

Difference Solution for the In-Depth Response of Charring Materials Considering Surface Chemical and Energy Balances. Technical Report CR-1061, NASA, 6 1968.

[119] Aziza Gul Nahar. High temperature performance of carbon fiber reinforced cyanate ester composites filled with nano-ceramics. M.S. Thesis, Texas State University, July 2021.

[120] Lauge Fuglsang Nielsen. Strength and Stiffness of Porous Materials. *Journal of the American Ceramic Society*, 1990.

[121] L. N. Nikitin and É. E. Said-Galiev. Ablation of Polymers and Composites When Exposed to CO2 Laser Radiation (Review). *Mechanics of Composite Materials*, 28:97–114, 1992.

[122] W. F. Noh. Errors for calculation of strong shocks using an artificial viscosity and an artificial heat flux. *Journal of Computational Physics*, 1978.

[123] Francesco Panerai, Joseph C. Ferguson, Jean R. Lachaud, Alexandre Martin, Matthew J. Gasch, and Nagi N. Mansour. Micro-tomography based analysis of thermal conductivity, diffusivity and oxidation behavior of rigid and flexible fibrous insulators. *International Journal of Heat and Mass Transfer*, 108, 2017.

[124] Y. K. Park and E. P. Fahrenthold. A kernel-free particle-finite element method for hypervelocity impact simulation. *International Journal for*

Numerical Methods in Engineering, 63:737–759, 2005.

[125] Pedro Guilherme Silva Pesci, Humberto Araújo Machado, Homero de Paula e Silva, Cristian Cley Paterniani Rita, Gilberto Petraconi Filho, and Edson Cocchieri Botelho. Numerical-Experimental Analysis of a Carbon-Phenolic Composite via Plasma Jet Ablation Test. *Materials Research Express*, 5(6), 2018.

[126] Savio Poovathingal, Thomas E. Schwartzentruber, Vanessa J. Murray, Timothy K. Minton, and Graham V. Candler. Finite-rate oxidation model for carbon surfaces from molecular beam experiments. *AIAA Journal*, 55(5):1644–1658, 2017.

[127] Robert L. Potts. Application of integral methods to ablation charring erosion, A review. *Journal of Spacecraft and Rockets*, 1995.

[128] Kristen J. Price, Francesco Panerai, Colby G. Borchetta, J. Matthew Hardy, Alexandre Martin, and Sean C.C. Bailey. Arc-jet measurements of low-density ablator spallation. *Experimental Thermal and Fluid Science*, 133(June 2021):110544, 2022.

[129] Clayton A. Pullins and Tom E. Diller. Direct measurement of hot-wall heat flux. *Journal of Thermophysics and Heat Transfer*, 26, 2012.

[130] Fei Qin, Li Na Peng, Jiang Li, and Guo Qiang He. Numerical simulations of multiscale ablation of carbon/carbon throat with morphology effects. *AIAA Journal*, 55(10):3476–3485, 2017.

[131] Christopher T. Quinn, Daniel N. Pickard, and Raul Radovitzky. A Discontinuous-Galerkin, Lagrangian Thermo-chemo-mechanical Material Response Solver for the Analysis of Ablative Thermal Protection Systems. *AIAA SciTech 2023 Forum*, 2023.

[132] Robert J. Rabb and Eric P. Fahrenthold. Impact dynamics simulation for multilayer fabrics. *International Journal for Numerical Methods in Engineering*, pages 537–557, 2010.

[133] Robert J. Rabb and Eric P. Fahrenthold. Simulation of large fragment impacts on shear-thickening fluid Kevlar fabric Barriers. *Journal of Aircraft*, 48(6):2059–2067, 2011.

[134] Roald A. Rindal. An Analysis of the Coupled Chemically Reacting Boundary Layer and Charring Ablator, Part VI, An Approach for Characterizing Charring Ablator Response with In-Depth Coking Reactions. Technical Report CR 1065, NASA, June 1968.

[135] N. N. Ryalkin. Calculation of heat processes in welding. Paper given at 42nd Annual Meeting of the American Welding Society, 1960. Moscow, U.S.S.R.

[136] Michael N. Sakano, Ahmed Hamed, Edward M. Kober, Nicolo Grilli, Brenden W. Hamilton, Md Mahbubul Islam, Marisol Koslowski, and Alejandro Strachan. Unsupervised Learning-Based Multiscale Model of Thermochemistry in 1,3,5-Trinitro-1,3,5-triazinane (RDX). *Journal of Physical Chemistry A*, 124(44):9141–9155, 2020.

[137] Saurabh S. Sawant, Pooja Rao, Abhilash Harpale, Huck Beng Chew, and Deborah A. Levin. Multi-scale thermal response modeling of an AVCOAT-like thermal protection material. *International Journal of Heat and Mass Transfer*, 133:1176–1195, 2019.

[138] Pierre Schrooyen, Koen Hillewaert, Thierry E. Magin, and Philippe Chatelain. Fully implicit Discontinuous Galerkin solver to study surface and volume ablation competition in atmospheric entry flows. *International Journal of Heat and Mass Transfer*, 2016.

[139] Joseph C. Schulz, Eric C. Stern, Suman Muppidi, Grant E. Palmer, Olivia Schroeder, and Alexandre Martin. Development of a three-dimensional, unstructured material response design tool. *AIAA SciTech Forum - 55th AIAA Aerospace Sciences Meeting*, 2017.

[140] James B. Scoggins and Thierry E. Magin. Gibbs function continuation for linearly constrained multiphase equilibria. *Combustion and Flame*, 162(12):4514–4522, December 2015.

[141] Federico Semeraro, Joseph C. Ferguson, Marcos Acin, Francesco Panerai, and Nagi N. Mansour. Anisotropic analysis of fibrous and woven materials part 2: Computation of effective conductivity. *Computational Materials Science*, 186(July 2020):109956, 2021.

[142] Federico Semeraro, Joseph C. Ferguson, Francesco Panerai, Robert J. King, and Nagi N. Mansour. Anisotropic analysis of fibrous and wo-

ven materials part 1: Estimation of local orientation. *Computational Materials Science*, 2020.

[143] Shangcong Cheng. Medium Range Ordering Structure and Silica Glass Transition. *Glass Physics and Chemistry*, 45(2):91–97, 2019.

[144] Moss E. Shimek and Eric P. Fahrenthold. Impact dynamics simulation for multilayer fabrics of various weaves. *AIAA Journal*, 53(7):1793–1811, 2015.

[145] R. Shivarama and E. P. Fahrenthold. An ellipsoidal particle-finite element method for hypervelocity impact simulation. *International Journal for Numerical Methods in Engineering*, 59:737–753, 2004.

[146] Ravishankar Shivarama and Eric P. Fahrenthold. Hamilton's equations with euler parameters for rigid body dynamics modeling. *Journal of Dynamic Systems, Measurement and Control*, 126(1):124–130, 2004.

[147] Mairead Stackpoole, Steve Sepka, Ioana Cozmuta, and Dean Kontinos. Post-flight evaluation of stardust sample return capsule forebody heatshield material. *46th AIAA Aerospace Sciences Meeting and Exhibit*, 2008.

[148] A P Stepovik. Measurement of the Gruneisen coefficient of some anisotropic carbon materials. *Journal of Applied Mechanics and Technical Physics*, 46(6):911–917, 2005.

[149] J. Summerscales. Bulk modulus of carbon fibers. *Journal of Materials Science Letters*, 19(1):15–16, 2000.

[150] Toshiyuki Suzuki, Takeharu Sakai, and Tetsuya Yamada. Calculation of thermal response of ablator under arcjet flow condition. *Journal of Thermophysics and Heat Transfer*, 2007.

[151] George F. Sykes, Jr. Decomposition Characteristics of a Char-Forming Phenolic Polymer Used for Ablative Composites. NASA Technical Note D-3810, Langley Research Center, 2 1967.

[152] Vahid Tahmasbi and Sahar Noori. Application of Levenberg–Marquardt Method for Estimation of the Thermophysical Properties and Thermal Boundary Conditions of Decomposing Materials. *Heat Transfer Engineering*, 2020.

[153] Vahid Tahmasbi and Sahar Noori. Multidimensional Numerical Analysis of the Thermal Behavior and Pyrolysis Gas Flow Inside an Orthotropic Porous Material. *Journal of Heat Transfer*, 2020.

[154] Yunlong Tang, Mengkun Yue, Jinsong Zhang, Yan Li, Xufei Fang, and Xue Feng. Revealing thermal ablation mechanisms of C/SiC with in situ optical observation and numerical simulation. *Journal of the European Ceramic Society*, 40(12):3897–3905, 2020.

[155] Francisco Torres-Herrador, Joffrey Coheur, Francesco Panerai, Thierry E. Magin, Maarten Arnst, Nagi N. Mansour, and Julien Blondeau. Com-

petitive kinetic model for the pyrolysis of the Phenolic Impregnated Carbon Ablator. *Aerospace Science and Technology*, 100:105784, 2020.

[156] Francisco Torres-Herrador, Alessandro Turchi, Kevin M. Van Geem, Julien Blondeau, and Thierry E. Magin. Determination of heat capacity of carbon composites with application to carbon/phenolic ablators up to high temperatures. *Aerospace Science and Technology*, 108:106375, 2021.

[157] Huy Tran, Christine Johnson, Daniel Rasky, Frank Hui, and Ming Hsu. Silicone impregnated reusable ceramic ablators for Mars follow-on missions. AIAA, Paper 96-1819, June 1996.

[158] Huy Tran, Christine Johnson, Daniel Rasky, Frank Hui, Ming Hsu, and Y Chen. Phenolic Impregnated Carbon Ablators (PICA) for Discovery class missions. NASA Technical Memorandum 110440, National Aeronautics and Space Administration, April 1997.

[159] Ethiraj Venkatapathy, Bernard Laub, G. J. Hartman, J. O. Arnold, M. J. Wright, and G. A. Allen. Thermal protection system development, testing, and qualification for atmospheric probes and sample return missions. Examples for Saturn, Titan and Stardust-type sample return. *Advances in Space Research*, 2009.

[160] G. L. Vignoles, Y. Aspa, and M. Quintard. Modelling of carbon-carbon composite ablation in rocket nozzles. *Composites Science and Technology*, 70(9):1303–1311, 2010.

[161] Gerard L. Vignoles, Jean Lachaud, Yvan Aspa, and Jean Marc Goyhénèche. Ablation of carbon-based materials: Multiscale roughness modelling. *Special Issue on the 12th European Conference on Composite Materials, ECCM 2006*, 69(9):1470–1477, 2009.

[162] Jonathan Wang. Reacting molecular dynamics simulation of phenol and cyanate ester pyrolysis. Master's thesis, University of Texas at Austin, 2022.

[163] Quan De Wang, Jing Bo Wang, Juan Qin Li, Ning Xin Tan, and Xiang Yuan Li. Reactive molecular dynamics simulation and chemical kinetic modeling of pyrolysis and combustion of n-dodecane. *Combustion and Flame*, 158(2):217–226, 2011.

[164] Yeqing Wang, Timothy K. Risch, and Joseph H. Koo. Assessment of a one-dimensional finite element charring ablation material response model for phenolic-impregnated carbon ablator. *Aerospace Science and Technology*, 91:301–309, 2019.

[165] Zuo Jia Wang, Dong Jun Kwon, Ga Young Gu, Woo Il Lee, Jong Kyoo Park, K. Lawrence Devries, and Joung Man Park. Ablative and mechanical evaluation of CNT/phenolic composites by thermal and microstructural analyses. *Composites Part B: Engineering*, 60:597–602, 2014.

[166] R. W. Warfield and Eleonore G. Kayser. Specific Heat of Phenolic

Polymer. *Journal of Macromolecular Science, Part B*, 11(3):325–328, 1975.

[167] Peng Wen, Gang Tao, Douglas E. Spearot, and Simon R. Phillpot. Molecular dynamics simulation of the shock response of materials: A tutorial. *Journal of Applied Physics*, 131(5), 2022.

[168] Haoyue Weng, Ümran Düzel, Rui Fu, and Alexandre Martin. Geometric effects on charring ablator: Modeling the full-scale stardust heat shield. *Journal of Spacecraft and Rockets*, 2021.

[169] Haoyue Weng and Alexandre Martin. Multidimensional modeling of pyrolysis gas transport inside charring ablative materials. *Journal of Thermophysics and Heat Transfer*, 2014.

[170] Wikipedia. Beer-Lambert Law. `https://en.wikipedia.org/wiki/Beer%E2%80%93Lambert_law`. Accessed: 2023-06-05.

[171] M. R. Wool. Aerotherm Equilibrium Surface Thermochemistry Computer Program, Version 3. Volume 1. Program Description and Sample Problems. Tech. Rep. UM - 70 - 13, Aerotherm Corp. Mountain View CA, 1970.

[172] Xiaolong Xing, Xiaoru Niu, Yun Liu, Changhong Yang, Shujuan Wang, Yu Li, and Xinli Jing. In-depth understanding on the early stage of phenolic resin thermal pyrolysis through ReaxFF-molecular dynamics simulation. *Polymer Degradation and Stability*, 186, 2021.

[173] Xinrui Yang, Lin Jiang, and Mi Li. Modeling continuous laser ablation of glass fiber–reinforced epoxy resin plate with two–dimensional finite element. *Journal of Thermal Analysis and Calorimetry*, 2023.

[174] Li Chuan Zhou, Xiao Hao Sun, Ming Wei Chen, Yin Bo Zhu, and Heng An Wu. Multiscale modeling and theoretical prediction for the thermal conductivity of porous plain-woven carbonized silica/phenolic composites. *Composite Structures*, 215(January):278–288, 2019.

[175] Rui Zhou and Kaiping Yu. Hamilton's law of variable mass system and time finite element formulations for time-varying structures based on the law. *International Journal for Numerical Methods in Engineering*, 99, 2014.